A DETAILED STUDY OF THE FLOW FIELD OF A SUBMARINE AT LARGE ANGLE OF DRIFT

FINAL REPORT

David H. Bridges
Mississippi State University
Department of Aerospace Engineering
Mississippi State, MS 39762

May 2001

20010612 082   MSSU-ASE-01-1

DEPARTMENT OF AEROSPACE ENGINEERING

JOHN C. MCWHORTER, III, PH.D.
HEAD, DEPARTMENT OF AEROSPACE ENGINEERING

A. GEORGE BENNETT, PH.D.
DIRECTOR, RASPET FLIGHT RESEARCH LABORATORY

BRADLEY D. CARTER, PH.D.
INTERIM EXECUTIVE DIRECTOR, NSF ENGINEERING RESEARCH CENTER

COLLEGE OF ENGINEERING

A. WAYNE BENNETT, PH.D.
DEAN, COLLEGE OF ENGINEERING

LESIA CRUMPTON-YOUNG, PH.D.
ASSOCIATE DEAN, RESEARCH & INDUSTRIAL OUTREACH
COLLEGE OF ENGINEERING

For additional copies or information
address correspondence to:

Department of Aerospace Engineering
Mississippi State University
PO Box A
Mississippi State, MS 39762

Telephone (662) 325-3623
Fax (662) 325-7730

A DETAILED STUDY OF THE FLOW FIELD OF A SUBMARINE
AT LARGE ANGLE OF DRIFT

FINAL REPORT

David H. Bridges
Mississippi State University
Department of Aerospace Engineering
Mississippi State, MS 39762

May 2001

MSSU-ASE-01-1

Acknowledgments

Abstract

When a submarine executes a high-speed turn, the sail is placed at an angle of attack relative to the oncoming flow. Because the sail is essentially a low-aspect-ratio finite-span wing, it sheds a tip vortex. The flow field induced by the vortex creates higher pressures on the deck of the hull and lower pressures on the keel, creating a net downward force. Because this force is aft of the sail and the center of gravity of the submarine, a nose-up pitching moment is created, which can be a problem when the submarine is maneuvering in the shallow waters of littoral regions. Tests to examine the various features of such flows were conducted in the U. S. Navy's Large Cavitation Channel (LCC), located in Memphis, TN. A submarine model of length 22.7 ft was mounted in the LCC at angles of drift of 0, 5, and 9.5 degrees and was tested with the sail on and with the sail off. Tests were conducted at speeds up to 14.9 m/s (27 kts). Circumferential pressure distributions and laser Doppler velocimeter (LDV) surveys were obtained at two axial locations for each of the speeds and configurations tested. Body forces and moments were also measured using a 6-component force balance. The pressure distributions were integrated to obtain section vertical force coefficients, and the velocity data obtained from the LDV surveys were used to estimate the circulation of the tip vortex. The measured pressure distributions were consistent with the hypothesized mechanism by which the tip vortex changed the flow around the submarine, demonstrating higher pressures on the deck and lower pressures on the keel. The measured pitching moment and the sectional vertical force coefficients demonstrated the nonlinear variation with angle of drift predicted by the theory. The measured values of the circulation were in general agreement with values obtained by other researchers in similar experiments and with finite wing and potential flow theory predictions, although the measured circulation values were consistently somewhat higher than the values of other researchers or the values predicted by the theories. Reynolds number effects were minimal over the range of Reynolds number tested. The tests were conducted in two phases, and between the two phases, a trip ring located near the nose of the model was removed. There were some differences between the results of the two test phases that were considered significant, but most of these could be attributed to the change in the state of the boundary layer caused by the removal of the trip ring. Possible areas of future research include the investigation of methods of introducing vorticity of opposite sign to that of the tip vortex, such as small fins extending from the keel of the submarine, or the development of a control law that would use nose-down pitching moments generated by deflections of the bow or sail planes to counteract the nose-up pitching moment produced by the tip vortex.

Table of Contents

List of figures

List of symbols

a	Lift-curve slope for two-dimensional airfoil
AR_s	Aspect ratio of submarine sail = height of sail / chord of sail
AR_w	Aspect ratio of finite wing = square of wing span / wing planform area
c	Sail chord length
C_l	Rolling moment coefficient
C_m	Pitching moment coefficient
C_n	Yawing moment coefficient
C_p	Pressure coefficient
C_X	Axial force coefficient
C_Y	Side force coefficient
C_Z	Vertical force coefficient
c_l	Section lift coefficient
c_z	Section vertical force coefficient
Δc_z	Change in section vertical force coefficient
D	Submarine model hull diameter
F_V	Fraction of maximum velocity value used to obtain minimum velocity contour value
F_z	Vertical force per unit length
h	Sail height, measured from hull deck
L	Submarine model hull length
l	Rolling moment
L'	Lift per unit span
m	Pitching moment
N_{cont}	Number of contours between maximum and minimum contour levels in contour plots
n	Yawing moment
Δp	Pressure drop from reference pressure tap to pressure tap at point of measurement
R	Submarine model hull radius
Re_c	Crossflow Reynolds number, based on crossflow velocity component and hull diameter
Re_L	Reynolds number based on overall submarine hull length
U	Freestream velocity magnitude
u	Axial or streamwise velocity component
u_{max}	Maximum value of streamwise velocity component, used in contour plots
V_{max}	Resultant of maximum streamwise and transverse velocity components
w	Vertical velocity component (relative to test section floor)
w_{max}	Maximum value of vertical velocity component, used in contour plots
X	Axial force

x

x	Axial coordinate on hull centerline
Y	Side force
y	Vertical coordinate, measured from hull centerline
Z	Vertical force
α	Angle of attack
β	Drift or yaw angle
Γ	Circulation associated with vortex
γ	Non-dimensional circulation = circulation / (freestream velocity * hull length)
γ_{cv}	Non-dimensional circulation = circulation / (cross flow velocity component * hull diameter)
θ	Coordinate for circumferential location of pressure taps
ρ	Density

Subscripts

no sail	Quantity measured with sail not attached to model
ref	For pressure, reference value used to calculate pressure coefficient
sail	Quantity measured with sail attached to model
w	Quantity measured at wall

1. INTRODUCTION

1.1   Narrative Overview

1.1.1   Statement of work

When a submarine executes a high-speed turn, the sail of the submarine is placed at angle of attack. Since the sail in this condition is essentially a low-aspect ratio, finite-span wing, it sheds a tip vortex. This vortex modifies the pressure distribution on the rear of the submarine, causing a change in the pitching moment which in turn causes a change in the direction of motion of the submarine in the vertical plane as well as the horizontal plane. In the fall of 1995 the first author was awarded a grant by the Office of Naval Research under the 1995 Department of Defense Experimental Program to Stimulate Competitive Research (DEPSCoR) to conduct studies in the Large Cavitation Channel (LCC) of the Naval Surface Warfare Center, Carderock Division, located in Memphis, TN. The purpose of these studies was to examine the physical mechanisms associated with the tip vortex and the corresponding pressure distributions on the submarine. Additional funding in this grant was provided to renovate a small high-speed water tunnel facility at Mississippi State University, in order to examine various testing issues that have been encountered at the LCC but which did not warrant full-scale studies in the LCC.

1.1.2   Tests in the Large Cavitation Channel

The submarine tests in the LCC were conducted in two phases. The first phase of the tests were performed in October of 1996, and the second phase were performed in July of 1998. The measurements in the first phase consisted of laser Doppler velocimeter (LDV) surveys of the tip vortex flowfield and pressure readings taken around the circumference of the submarine model at two axial locations. Measurements were made at angles of drift of 0 deg and 9.5 deg and at a maximum free stream speed of almost 30 kts. The second phase was delayed due to repairs that had to be made to the motor of the LCC. During the time between the two test phases, some changes were made to the model, including the removal of a boundary layer trip ring on the nose of the model. When the second set of tests were run, force measurements were obtained using an internal force balance, in addition to the velocity and pressure measurements such as those obtained in the first tests. Measurements were made at drift angles of 0, 5, and 9.5 deg. In order to obtain the force measurements, a support that had attached one of the fins at the rear of the model to the LCC test section wall was removed, so that the flow speed had to be restricted to 18 kts for the 5 deg studies and 10 kts for

1

the 9.5 deg studies. During these tests, LDV surveys were also made of the boundary layer on the submarine hull. The results of the two test phases are presented in the body of this report.

1.1.3   Work on the Mississippi State University Water Tunnel

A small, high-speed water tunnel was constructed at Mississippi State University (MSU) in the mid-1960s. This tunnel was designed with a maximum test section speed of 50 ft/s (29.6 kts) and a maximum operating pressure of 60 psi in the test section. The tunnel had an axisymmetric test section that was 11 in (0.28 m) in diameter and 5 ft (1.52 m) long. Because the operating conditions closely approach those of the LCC, it was believed that the MSU tunnel would make an ideal support facility for the LCC, enabling the study of various issues that might arise during the operation of the LCC but that did not warrant full-scale investigations in the LCC, because of the large operating cost of the LCC. Two such issues which had already arisen were the impact of pressure tap hole diameter on pressure measurement accuracy and the best method for visualizing surface flows at the high speeds at which the LCC operates. In order to study these and other issues, funds were requested and granted for the renovation of the MSU tunnel, including a re-coating of the interior of the fiberglass tunnel walls and a new motor and drive system. Unfortunately, there were delays in the initial re-coating work on the tunnel and then problems with pressure measurements in the tunnel test section were discovered. When the tunnel was disassembled to examine the interior, it was discovered that the coating had come off in some locations. There were further delays in repairing this damage, so that the pressure tap and flow visualization studies were not completed. The work on the tunnel continues, however, and these studies will be completed after the tunnel is reassembled. The work completed on the tunnel to this point is described in Appendix A, which is a master's thesis written by Michael Lindsey, a graduate student who worked on the tunnel and performed the initial shakedown runs and pressure measurement studies.

1.1.4 Overview of Report

In the following chapter, previous studies related to the dynamics of submarine motion will be examined, with particular attention being paid to those studies that deal with the variation of the submarine pitching moment with angle of drift. Chapter 3 will give details of the experimental apparatus and procedure and will describe the test grid that was used for the tests. Chapter 4 will report the results of the first phase of tests in the LCC and will describe the pressure distributions and velocity fields that were measured. Chapter 5 will report the results of the second phase of tests, which included force measurements as well as surface pressure distributions and velocity field surveys, and will also make comparisons between the results of the two test phases. The conclusions and recommendations for future work will be contained in Chapter 6.

2. BACKGROUND

2.1   Basic Statement of Problem

As was stated in the Introduction, the basic problem being examined is the appearance of a moment in the horizontal plane that causes the nose of the submarine to rise whenever a high-speed turn is executed. The basic flow mechanisms have been known for some time. According to Feldman (1995),

> When the submarine is in a turning maneuver there is a distribution of angle of drift developed along the length of the hull. The local angle of drift is relatively small along the forebody, but is relatively large along the afterbody. Lift is developed on the bridge fairwater due to the local angle of drift. It is assumed that there is a bound vortex at the quarter chord of the bridge fairwater and a tip vortex which trails aft. An image vortex is located inside the hull. This system of vorticity sets up circulation around the hull which in combination with the local cross flow causes a hydrodynamic pressure difference to occur between the deck and keel. The normal force and pitching moment which result can be shown to vary with the angle of drift squared, at least for moderate angles of drift.

The difficulties in submarine control that arise during the maneuvers that create these flow features are described by Gruner and Payne (1992). Gruner and Payne describe the undesired forces and moments that are generated during a high-speed turn and point out that manual control under these conditions is highly difficult, if not impossible. They attribute the appearance of these control difficulties to the rise in speed as submarine design has advanced. More accurate control of a submarine during maneuvers became a more critical issue when more submarine missions began to be executed in shallow-water littoral regions. Wright (1995) defines the littoral zone as a region within 100 miles of the shoreline where the water is less than 100 fathoms (660 ft) deep. Wright also describes some of the missions that can be executed in this zone and discusses submarine design features that will be necessary to accomplish these missions. In addition to the features discussed by Wright, the need for pinpoint control capability in a shallow-water situation is obvious.

2.2   Previous Work on Submarines

As was discussed in the previous section, the issues that have caused attention to be focused on this particular aspect of submarine maneuvering have only arisen in relatively recent times. Some investigations have been conducted, to the point that the basic flow mechanisms underlying the control problems have been identified, as indicated by the quote from Feldman above. However, because of the sensitive nature of the work involving submarines, little of this

3

4

previous work is available in the open literature[1]. A few published studies are available, and these will be discussed here. Particular attention will be paid to results of these studies concerning variations of pitching moment with drift (or yaw) angle.

In order to create a submarine geometry that could be used for both experimental and computational studies, and hence provide data for validation of computational results, Groves *et al.* (1989) designed and constructed what became known as the Defense Advanced Research Projects Agency (DARPA) SUBOFF model. The hull for this geometry was axisymmetric and was designed so that it could be used with or without typical appendages, such as a sail or stern fins. Roddy (1990) tested the SUBOFF model in the David Taylor Model Basin (hereinafter referred to as "DTMB"). Roddy measured the forces and moments acting on the SUBOFF model for a range of configurations. The results are presented but not discussed in much detail. Roddy shows the variation of pitching moment with drift angle for the fully-appended SUBOFF configuration and for the configuration of bare hull plus sail only. Both show the nonlinear increase in pitching moment with angle of drift, as described by Feldman above. The pitching moment is essentially symmetric in angle of drift for the fully-appended configuration, but demonstrates some asymmetry for the bare-hull-plus-sail configuration at large drift angles. For large positive drift angles, the moment continues to increase more or less monotonically, but for large negative drift angles, the moment peaks and then begins to decrease. The reason for this asymmetry is not presented in the report. Jonnalagadda (1996; see also Jonnalagadda *et al.* 1997; Zierke 1997) computed the flow past the SUBOFF geometry using a Reynolds-averaged Navier-Stokes solver with a Baldwin-Lomax turbulence model for various combinations of appendages. These computations included the flow past the hull plus sail configuration at various angles of drift. Jonnalagadda's results are in general agreement with the pitching moment variations with angle of drift measured by Roddy, demonstrating the symmetric, nonlinear variation observed in the experiments. Jonnalagadda's results do not show the asymmetry at large angles of drift observed in the experiments.

Computational studies were also performed by Sung *et al.* (1996) on the SUBOFF, DTMB Body 1, Albacore, and DTMB Model 4156 geometries undergoing constant-radius turns, and the results were compared with experiments. The variation of pitching moment with pitch angle is shown for the two angles of yaw (drift) of 0 deg and 12 deg. At zero pitch (the orientation of interest in the current study), the moment is shown to have a large negative value at zero yaw and a large positive value at 12 deg yaw, for both the experimental and computational studies. It is not known why the large negative value occurs at zero pitch and zero yaw. However, the change in pitching moment from negative to positive (hence in the positive direction) for an increase in yaw angle is what one might expect.

Particle displacement velocimetry (PDV) measurements were made of the flow around a submarine model in the David Taylor Model Basin rotating arm facility by Liu and Fu (1994). The submarine model used in the experiments was Model 5484, and the reader is referred to Liu *et al.* (1993) for details of the model. These tests were conducted to

---

[1]At the beginning of this study, the first author was provided with some comments by Dr. Jerome P. Feldman of the Carderock Division, Naval Surface Warfare Center. The comments included a list of 14 references, 11 of which were marked "CONFIDENTIAL."

demonstrate the capability of the PDV system for measuring the flowfield of a submarine undergoing a turning motion. The model was towed at a nominal speed of 5 kts and at various pitch and yaw angles. Liu and Fu report, among other things, the circulations measured in the vortex wake of the submarine and how these values compare with theoretical predictions based on the angle of attack of the sail. Liu and Fu also report measurements of the sail vortex trajectory downstream of the sail and observations of the circumferential angles at which the flow separates from the hull. These results will be compared with the current observations later in this report.

Wetzel *et al.* (1993; see also Wetzel and Simpson 1998) investigated the effects of fins and jets in preventing or delaying crossflow separation on a submarine model. The model was a commercially-available 1/48-scale kit of a 688 Los Angeles-class submarine manufactured by Scale Shipyard in 1991. The sail was mounted on the hull with sailplanes but no stern appendages were used. The model was sting-mounted in the wind tunnel at Virginia Polytechnic Institute (VPI) and forces and moments were measured over a range of angles of drift. Various fin and jet configurations were studied to see which would prevent or delay crossflow separation. For the no-fin, no-jet case the variation of pitching moment with drift angle repeated the nonlinear variation observed by others (only positive angles of drift were tested, so no comment can be made concerning symmetry). There does appear to be one discrepancy with what might be expected and with other measurements. As the drift angle increased in the tests by Wetzel *et al.*, the pitching moment became more negative, indicating a larger nose-down pitching moment, according to the coordinate system diagrams in the report. Most investigators agree that a nose-up pitching moment is caused by the changes in the flow resulting from the vortex shed from the sail. The cause for the apparent discrepancy is unclear; Wetzel *et al.* attributed the nose-down pitching moment to interactions between the appendage wake and the body separation. The results with the vortex generators indicate that in general more attached flow caused an increase in the magnitude of the pitching moment coefficient for nonzero drift angles. Wetzel *et al.* also examined the impact of the fins and jets on the surface separation location using an oil flow technique. The effects of the vortex shed by the sail are not directly addressed, as no off-body flowfield measurements are reported.

2.3   Previous Work on Tip Vortices

Whenever a finite-length wing is placed at an angle of attack relative to the oncoming flow, it will generate and shed tip vortices. These vortices have a major impact on aircraft performance, since they lead to the quantity called induced drag. Further, recent incidents have also demonstrated the impact of these tip vortices on other aircraft. Light aircraft have been upset after encountering the trailing vortices of a large transport aircraft taking off or landing from an airport. The interaction between the vortex shed by the tip of a helicopter rotor and the helicopter fuselage is of great importance in helicopter design. Because of these various situations there exists a large body of literature on the tip vortex generated by a finite-length wing. Only a few of the most recent additions to this body will be addressed here; the reader is referred to the references in these articles for further study.

Chow *et al.* (1997) describe measurements made in a tip vortex near the wing tip which generated the vortex. Multi-hole pressure probes and triple-wire anemometers were used to measure the flowfield of a 0.75-aspect ratio semi-

span wing with a NACA 0012 airfoil section and a rounded (body of revolution) tip mounted at an angle of attack of 10 deg. They report axial velocity components as high as 1.77 times the freestream velocity, and resultant crossflow velocity magnitudes as high as 1.07 times the freestream velocity. They also report that the tip vortex moves up and slightly outboard with downstream distance, but this is attributed to the proximity of the wind tunnel walls. Measurements of a number of turbulence quantities are reported, and the effects of vortex "meander" on these measurements are addressed. The same geometry was used in computations by Dacles-Mariani *et al.* (1995) and the results are compared with the experiments.

The decay in time of vortices trailing from the wingtips of aircraft in flight is discussed by Sarpkaya (1998). Sarpkaya beings by reviewing some of the previous work on tip vortices, and then describes the results of experiments conducted on aircraft in field tests at the Memphis, Tennessee airport. The discussion centers primarily on turbulence quantities related to the vortices. Mean velocity profiles are plotted as functions of the inverse of the radial distance from the vortex core, and these plots are used to find the correct vortex core location. Once these are obtain, the radial circulation distribution is plotted. Sarpkaya makes note of the fluctuations shown in the circulation plots, even though the velocity plots are relatively smooth. The decay in the average vortex circulation with time is then discussed. Sarpkaya concludes that a turbulent vortex core does not exhibit solid body rotation. Rather, a turbulent exchange of mass, momentum and vorticity takes place between the outer region and the core, leading to a decay through an inertial mechanism that causes the turbulent vortex to behave quite differently from its laminar counterpart.

3. EXPERIMENTAL APPARATUS AND PROCEDURE

3.1   Facility

The experiments to be described in this report were all conducted in the Large Cavitation Channel (LCC), located in Memphis, Tennessee. This facility is part of the Carderock Division of the Naval Surface Warfare Center (NSWCCD) and was first made operational in 1991. The LCC has a test section that is 3.05 m (10 ft) high, 3.05 m (10 ft) wide, and 12.2 m (40 ft) long. The maximum test section speed is approximately 18 m/s (35 kts), and the pressurization range for the test section extends from 3.5 kPa (0.05 psia) to 415 kPa (60 psia). The freestream turbulence level is less than 0.5%. Details of the design, construction, and operation of this facility may be found in Etter and Wilson (1992; 1993).

3.2   Model

The model used in these experiments was a standard axisymmetric hull with a sail and four standard cruciform stern appendages. The hull length L was 6.92 m (272.36 in) and the diameter D was 0.623 m (24.54 in). The hull outline is shown in Figure 1 (figures are in a separate section immediately following the text of this report). The two stern appendages that formed the rudder had trailing edges that could be deflected. These were normally adjusted to be in line with the freestream flow direction, to minimize the loads on the rear of the model. The sail was 0.565 m (22.25 in) long and 0.321 m (12.63 in) high. The location of the sail is shown in Figure 1, while the sail's foil section is shown in Figure 2. The sail tip extended 0.019 m (0.75 in) above the sail and was elliptic in cross-section. The aspect ratio of the sail, computed using the flat sail height (*i.e.* not including the tip) and the sail length, was 0.57. The sail had an airfoil cross-section with a maximum thickness of 0.108 m (4.25 in) thick, yielding a thickness ratio of 0.2. The leading edge of the sail was located 1.24 m (48.7 in) from the nose, or $x/L = 0.18$. The model was suspended from the ceiling of the test section using a standard LCC strut arrangement with the pivot point located at $x/L = 0.22$. The angle of attack of the model could be varied by adjusting the mount on the strut. The sail was mounted on the side of the hull so that the flow past a submarine at angle of drift could be simulated. In the first phase of testing, angles of drift of 0 deg and 9.5 deg were used. In the second phase, angles of drift of 0, 5 and 9.5 deg were used. The maximum test section blockage with the model at the largest angle of drift was approximately 10%. Pressure taps were mounted in circumferential rings located at $x/L = 0.47$ and $x/L = 0.65$. The circumferential angular position ϕ of these taps was measured relative to the starboard side of the model when viewed from the stern looking forward, and ϕ was positive

in the counter-clockwise direction. This coordinate system is shown in Figure 3. It should be noted in this figure that the submarine has been rotated 90 deg from its actual mounting orientation in the tunnel (the strut was attached to the test section ceiling, as mentioned before). The taps were 0.318 cm (0.125 in) in diameter and spaced 10 deg apart in the circumferential direction, for a total of 36 taps at each axial location. The number of taps was limited by the space available in the conduits through the strut to the outside of the test section. During the second phase of tests, when the internal force balance was used to measure forces on the model, the limited amount of cable access from the interior of the model through the penetrator plate to the outside of the LCC test section meant that the leads for 10 taps had to be eliminated in order to make room for the balance electrical cable. Ten taps from the downstream ring were eliminated in the region 140 deg $\leq \phi \leq$ 230 deg.

During the first test phase, the model had a boundary layer trip ring located at $x/L = 0.05$. This ring was a wire with a diameter of 0.318 cm (0.125 in) that had been epoxied to the surface of the model's nose. Tests conducted on the hull by the staff of the LCC between the first and second phase of the tests indicated that this ring was introducing nonuniformities into the flow and so it was removed before the second phase of tests. Also during the first test phase, a support strut was used to tie the stern of the model to the test section wall. This support strut was welded to the wall and extended out to the vertical rudder on the side of the model. The strut had a biconvex airfoil section for three-quarters of its length. This terminated in a axisymmetric body whose axis was aligned with the freestream flow direction. A threaded shaft extended from this body and spanned the remainder of the distance to the rudder. The threaded shaft was used to adjust the length of the support strut. The strut was removed for the second phase of tests because force and moment measurements were going to be made using an internal force balance, and the strut would have interfered with these measurements. In order to ensure that the resulting forces and moments on the model did not exceed the balance limits nor create potential hazards for the model, the test section velocity was limited to 9.26 m/s (18 kts) at 5 deg drift and 5.14 m/s (10 kts) at 9.5 deg drift.

3.3   Instrumentation

3.3.1   Velocity measurements

In both phases of the experiments described in this report, the velocity field was measured using a Dantec laser Doppler velocimeter (LDV) system. This system and its use is described in detail by Blanton (1995b) and Blanton and Etter (1995). The focal length of the LDV probe was 1600 mm. The measurement volume was typically 0.3 mm in the direction perpendicular to the beam bisector and 10.1 mm in the direction parallel to the beam bisector. Two velocity components could be measured. One was the axial flow component u which corresponded to the freestream velocity direction in the LCC. The other component was the vertical component w (vertical with respect to the test section). Because of low data rates that occurred when attempts were made to measure the two components simultaneously, each component was measured separately. The LDV system was traversed through the velocity field and the u-velocity component was measured, and then the LDV probe was rotated 90 deg about its axis in the traverse mount and the w

velocity component was measured. The stated accuracy of the traverse system was 0.05 mm.

The velocity measurements were made on a grid of points perpendicular to the axis of the model and thus inclined to the freestream flow direction at the angle of drift being studied. The grids typically extended $0.5R$ to either side of the model and $0.5R$ above the sail, where R is the model radius (0.312 m or 12.27 in). The grid spacing was typically $0.1R$, yielding a grid with typically 500-600 points. Additionally, grids with a finer resolution, with a grid spacing of $0.05R$, were used to obtained detailed mappings of the flow in the vicinity of the vortex core. In the first test phase the grid planes were located at the same axial locations as the pressure tap rings ($x/L = 0.47$ and $x/L = 0.65$). The locations of the pressure tap rings had been chosen in part because of the availability of optical access for the LDV system at these locations. The LDV system had to be able to "see" the model through one of the test section windows. In the second phase, a change in the strut support mechanism which suspends the strut from the LCC test top meant that the model was mounted at a slightly different axial location in the test section, and so the grid planes had to be shifted slightly so as to remain within one of the test section windows. The exact locations will be noted in each of the velocity field plots. Because the model was at 9.5 deg drift for several of the tests and because the model was 6.92 m long, the lower portion of the model at the aft pressure tap location was below the bottom of the test section window and hence could not be "seen" by the LDV system. In those cases the bottom of the grid was cut off. However, the region which contained the sail vortex and thus was of primary interest remained in view.

In addition to the field surveys away from the model, some boundary layer surveys were conducted during the second phase of tests. These were done primarily to see if the crossflow separation could be detected. The LDV grids were typical boundary layer grids used by the LCC, with surveys conducted in the radial direction and with variable grid point spacing in the radial direction. These surveys also were typically done at the pressure tap locations.

3.3.2 Pressure measurements

The pressures in the first test phase were measured using a Viatran model 223 pressure transducer with a range of ±10 psid and an accuracy of 0.25% of full-scale, as stated by the manufacturer. For the second phase of tests, the transducer was replaced by a Viatran model 274 transducer with a range of ±5 psid and an uncertainty of 0.15% full-scale, as stated by the manufacturer. The reference port of the transducer was connected to a reference pressure tap located just upstream of the test section in the contraction, essentially at the end of the contraction. The pressure taps on the model and the test section walls were connected to a manifold system, and the output of each tap was routed to the other side of the transducer, so that each pressure measurement actually measured the pressure drop from the reference tap to the tap in question. The pressures were averaged from 1000 readings from the pressure transducer over a period of 1 s. Since there was some variation in the freestream pressure because of the presence of the model in the test section, the pressure from the wall tap nearest the pressure tap ring in question was used as the reference pressure for the results to be presented in this report. In the first test phase, the pressure tap ring at $x/L = 0.47$ and at $x/L = 0.65$ both lay between two wall taps and so the reference pressures for the rings were obtained from a linear interpolation between the closest two wall taps. In the second test phase, the pressure tap ring at $x/L = 0.47$ lay immediately opposite

a wall pressure tap, and so no interpolation was required for this reference pressure. The presence of the model in the test section also lead to a variation in the freestream velocity, and so the velocity used to compute the pressure coefficient at each pressure ring was the freestream velocity obtained from the LDV survey at each axial location. Each LDV survey began and ended with a velocity measurement at a point halfway between the model and the test section wall, away from the tip vortex. This velocity was used as the freestream velocity at the particular axial location.

3.3.3   Force measurements

The forces on the model were measured using a AMTI 6-component dynamometer. This device is an internal force balance that was attached between the strut and the model. It was set up to measure forces in all three directions and moments about all three axes. The balance was calibrated by a member of the NSWCCD staff who oversaw the setup and the initial use of the balance in the model at the LCC. The voltage outputs of the dynamometer were sampled 1000 times over a one-second interval by the same system that sampled the pressure voltages. The dynamometer voltages were converted to forces and moments using supplied calibration data.

3.4   Uncertainty Analysis

As discussed in the previous section, three variables were of primary interest in these experiments: velocities in the flowfield away from the model, pressures on the surface of the model, and forces acting upon the model. The uncertainty associated with each of these quantities will be discussed here. A detailed uncertainty analysis of pressure measurements in the LCC was performed by Blanton (1995a) using the techniques outlined in Coleman and Steele (1989; see also 1999). A separate analysis of the uncertainty in LDV velocity measurements was performed by Blanton and Etter (1995) using the same techniques. In most cases, the uncertainty was estimated using the formula

$$U_X = \sqrt{B_X^2 + P_X^2}$$

where X represents the variable being measured (velocity, pressure, or force), B_X represents the systematic uncertainty, and P_X represents the random uncertainty[2]. The random uncertainty is computed from the formula

$$P_X = KS_X$$

where S_X is the sample standard deviation of a set of N readings and K is the desired coverage factor. If the number of readings is greater than or equal to 10, then a value of K equal to 2 will provide coverage of 95% at a confidence level of 95%. The value U_X then represents the range around the reported single reading within which the true value of the

---

[2]There has been a revision of terminology in the new edition of Coleman and Steele (1999). Formerly, the "systematic uncertainty" was known as the "bias limit" or "bias error," and the "random uncertainty" was known as the "precision limit" or "precision error."

measured quantity will lie with 95% confidence. If the quantity in question is the mean of a set of readings, then the uncertainty is expressed as

$$U_{\bar{X}} = \sqrt{B_X^2 + KS_{\bar{X}}^2}$$

where

$$S_{\bar{X}} = \frac{S_X}{\sqrt{N}}$$

is the sample standard deviation of the mean. The uncertainty now represents the range around the reported mean reading within which the true value of the mean will lie, with 95% confidence. These uncertainties were computed for each of the raw data values obtained and then standard error propagation techniques were used to compute the same uncertainties for the quantities computed from the raw data values, such as the pressure, force and moment coefficients. Extensive use will be made of the information presented by Blanton (1995a) and Blanton and Etter (1995) in the analyses here.

3.4.1 Uncertainties in LDV velocity measurements

Since the LDV system that was used to measure the velocities in the flowfield was essentially the same as that discussed by Blanton and Etter (1995), their results may be used directly here. The systematic uncertainty was estimated to be 0.05 m/s, or 0.46% at a freestream speed of 10.4 m/s, and was assumed to come from uncertainties in the beam angle and laser wavelength. The precision limit was obtained from repeating 14 times a velocity traverse with 16 different spatial points. At each point during each traverse, the velocity was sampled 1000 times. The resulting random uncertainty was 0.09 m/s, or 0.8% at a freestream speed of 10.4 m/s. The total uncertainty in an individual velocity measurement was then estimated to be 0.1 m/s or 0.96% at a freestream speed of 10.4 m/s. This was shown to be within the manufacturer's claim of "typically 1%" accuracy in the velocity measurement. This value of the velocity uncertainty was used in the computation of pressure, force and moment coefficients.

3.4.2 Uncertainties in density

According to Blanton (1995a), the density was measured using the measured temperature of the water and a curvefit. The results of the curvefit were compared to the output of an Anton Paar DMA 35 density meter. The curvefit values all fell within the error bands associated with the manufacturer's specifications for the density meter. The systematic uncertainty was estimated from these measurements to be 0.001 g/cm^3 (0.002 slug/ft^3). The random uncertainty was estimated from readings taken during the current tests to be 0.0005 g/cm^3 (0.001 slug/ft^3). Therefore, the total uncertainty in the density was estimated to be 0.0011 gm/cm^3 (0.0022 slug/ft^3). This value was used in the computation of pressure, force and moment coefficients.

3.4.3 Uncertainties in pressure measurements and pressure coefficients

The pressure coefficient was computed from

$$C_p(\theta) = \frac{\Delta p(\theta) - \Delta p_w}{\frac{1}{2}\rho U^2}$$

where $\Delta p(\theta)$ is the pressure drop from the reference tap to the particular pressure tap on the model, and Δp_w is the pressure drop from the reference tap to the wall tap nearest the particular pressure tap ring. According to Coleman and Steele (1999), the uncertainty associated with the pressure coefficient computed in this manner is given by

$$U_{C_p}^2 = \sum_{i=1}^{J} \theta_i^2 B_i^2 + 2\sum_{i=1}^{J-1} \sum_{k=i+1}^{J} \theta_i \theta_k B_{ik} + \sum_{i=1}^{J} \theta_i^2 (2S_i)^2$$

where $\theta_i = \partial C_p / \partial x_i$, with $x_1 = \Delta p(\theta)$, $x_2 = \Delta p_w$, $x_3 = \rho$, and $x_4 = U$ (thus $J = 4$). The values B_i are the systematic uncertainties in each variable and the values B_{ik} are the correlated systematic uncertainties for each pair of variables. The values S_i are sample standard deviations of each variable.

There were two main sources of systematic uncertainty in the pressure measurements. One source was the error associated with the regression which was used to compute the pressure from the voltage output of the transducer. This was estimated during the test to be 0.03 psi (0.6% of full scale). The second source came from the use of a Druck DPI 601 pressure calibrator to calibrate the transducer. This calibrator had a range of 0-100 psi with an uncertainty of ±0.06 psi (0.6% of full-scale). However, this systematic error was a correlated error for the model and wall pressure measurements, and since the definition of C_p used the difference of these two pressures, this error was canceled. The resulting expression used for computing the uncertainty in the pressure coefficient was

$$U_{C_p} = C_p \left[\frac{2(B_{\Delta p})_{reg}^2 + 4S_{\Delta p}^2 + 4S_{\Delta p_w}^2}{(\Delta p - \Delta p_w)^2} + \frac{U_\rho^2}{\rho^2} + \frac{U_u^2}{U^2} \right]^{1/2}$$

In this expression, $(B_{\Delta p})_{reg}$ is the systematic error associated with the regression, $S_{\Delta p}$ and $S_{\Delta p_w}$ are the sample standard deviations of the model and wall pressure measurements, respectively, and U_ρ and U_U are the total uncertainties in the density and velocity measurements, as discussed above. The sample standard deviations tended to scale with the square of the velocity, as did the pressure difference in the denominator of the first term. The systematic error associated with the regression, on the other hand, was a fixed quantity. At lower speeds, this error tended to dominate the total uncertainty value. The resulting error bars will be discussed in more detail in the presentation of the data below.

3.4.4 Uncertainties in force measurements

No information was available on the systematic uncertainties that could be expected with the 6-component

internal balance. The balance was calibrated off-site and then checked after it was installed, and so it is reasonable to assume that the systematic errors were minimized by the calibration process. Because of the unsteadiness that existed in the flow, the random uncertainty tended to be somewhat large. The standard deviation of the pitching moment averaged over 1000 readings was generally 10% of the mean value. Only the random uncertainty in the force and moment measurements, along with the total uncertainties in density, velocity and model length, were used in the computation of the uncertainty in the force and moment coefficients. An estimate of 0.125 in was used as the uncertainty in L.

3.5   Test Grid

The conditions for each test are summarized in Tables 1 and 2 for the first test phase. In the first test, it was determined that a freestream velocity of 14.7 m/s (28.6 kts) was the maximum allowable speed that could be used without risking damage to the model or the strut. Tests were conducted at this speed and approximately half of this speed at 7.5 m/s (14.6 kts). The two angles of drift studied in the first phase were 0 deg and 9.5 deg. The model was tested with the sail (the so-called "sail on" configuration) and without the sail (the so-called "sail off" configuration). Table 1 records the conditions during each set of pressure measurements and Table 2 records the conditions for each LDV velocity survey. The pressure measurements were generally made during the LDV surveys, but since the LDV surveys generally took much longer, the conditions were recorded independently at the time of each pressure survey. In addition to the model configuration for each test, Table 1 records the LCC control set point for shaft speed in RPM, the corresponding set-point velocity in knots, the corresponding freestream speed in m/s as measured by the LDV system, the temperature in the test section in degrees Farenheit, the water density in slug/ft^3, and the test section pressure measured at the test top during each test in psi (the units of each of these quantities are the units as used in the operation of the LCC). The last two columns of Table 1 show Re_L, the Reynolds number based on the overall length L of 6.92 m and the freestream speed U, and Re_c, the crossflow Reynolds number based on the component of the freestream perpendicular to the axis of the model, $U \sin \beta$, and the diameter D of 0.623 m.

The conditions for each test in the second phase are summarized in Tables 3-5. Since forces were to be measured in the second phase, the support strut at the rear of the model had to be removed. Because of concerns about the resulting stability of the model, the maximum flow speeds were limited to nominally 9.26 m/s (18 kts) at 5 deg drift and 5.14 m/s (10 kts) at 9.5 deg drift. The model was again tested in "sail-on" and "sail-off" configurations. Table 3 lists the conditions for the pressure measurements, Table 4 lists the conditions for the velocity measurements, and Table 5 lists the conditions for the force measurements. As in the first test phase, the conditions for each pressure and force measurement were recorded independently at the time of each pressure and force measurement. The other quantities in Tables 3-5 are the same as for Tables 1-2, except that in Table 5, the values of the Reynolds number were computed using the reference LDV velocity instead of the local freestream velocity, as was the case for the pressure measurements.

14

Table 1 Test Conditions for Pressure Measurements, Phase I Tests

Test	Date	Sail	Drift angle	CCM set	CCM U	LDV U	Temp.	density	Ptop	ReL	Rec
			(deg)	(rpm)	(kts)	(m/s)	(deg F)	(slug/ft^3)	(psi)	(*10e-6)	(*10e-6)
AP1	5-Nov-96	on	9.5	44.9	27.3	14.76	76.1	1.934	50	112.5	1.67
AP2	5-Nov-96	on	9.5	23.8	14.0	7.64	77.7	1.934	50	59.4	0.88
AP3	6-Nov-96	on	9.5	44.9	27.3	14.85	79.8	1.934	50	118.6	1.76
AP4	7-Nov-96	off	9.5	23.76	14.0	7.64	84.3	1.934	50	64.4	0.96
AP5	7-Nov-96	off	9.5	44.9	27.3	14.76	84.6	1.934	50	124.9	1.86
AP6	13-Nov-96	on	0	44.9	27.5	14.9	85.1	1.934	50	126.8	0
AP7	13-Nov-96	off	0	44.9	27.5	14.9	88.1	1.934	50	131.4	0

Table 2 Test Conditions for Velocity Measurements, Phase I Tests

Test	Date	Sail	Drift	Traverse	Vel.	LDV grid	LDV U	CCM U	CCM set	Ptop	Temp.
			(deg)	(x/L)	comp.		(m/s)	(kts)	(RPM)	(psi)	(deg F)
AV01	5-Nov-96	on	9.5	0.47	u	coarse	14.76	27.3	44.9	50.0	76.1
AV02	5-Nov-96	on	9.5	0.47	u	coarse	7.64	14.0	23.76	50.0	77.7
AV03	5-Nov-96	on	9.5	0.47	w	coarse	7.64	14.0	23.76	50.0	78.1
AV04	6-Nov-96	on	9.5	0.47	w	coarse	14.85	27.3	44.9	50.0	78.4
AV05	6-Nov-96	on	9.5	0.47	w	fine	14.85	27.3	44.9	50.0	80.5
AV06	6-Nov-96	on	9.5	0.47	u	fine	14.85	27.3	44.9	50.0	80.9
AV07	6-Nov-96	on	9.5	0.65	u	coarse	14.85	27.3	44.9	50.0	82.3
AV08	6-Nov-96	on	9.5	0.65	w	coarse	14.85	27.3	44.9	50.0	83.8
AV09	7-Nov-96	off	9.5	0.65	u	coarse	14.86	27.3	44.9	50.0	84.6
AV10	7-Nov-96	off	9.5	0.65	w	coarse	14.86	27.3	44.9	50.0	86.1
AV11	7-Nov-96	off	9.5	0.47	w	coarse	7.6	14.0	23.76	50.0	87.0
AV12	7-Nov-96	off	9.5	0.47	w	coarse	14.86	27.3	44.9	50.0	87.0
AV13	7-Nov-96	off	9.5	0.47	u	coarse	7.6	14.0	23.76	50.0	88.1
AV14	8-Nov-96	off	9.5	0.47	u	coarse	14.93	27.3	44.9	50.0	86.9
AV15	13-Nov-96	on	0	0.47	w	coarse	14.79	27.3	44.9	50.0	85.4
AV16	13-Nov-96	on	0	0.47	u	coarse	14.79	27.3	44.9	50.0	87.0
AV17	13-Nov-96	off	0	0.47	u	coarse	14.87	27.3	44.9	50.0	88.1
AV18	13-Nov-96	off	0	0.47	w	coarse	14.87	27.3	44.9	50.0	89.8

Table 3 Test Conditions for Pressure Measurements, Phase II Tests

Test	Date	Sail	Drift	CCM set	CCM U	LDV U	Temp.	density	Ptop	ReL	Rec
			(deg)	(rpm)	(kts)	(m/s)	(deg F)	(slug/ft^3)	(psi)	(*10e-6)	(*10e-6)
BP1	14-Jul-98	on	5	29.1	17.6	9.18	79.0	1.934	48	72.6	0.57
BP2	16-Jul-98	on	9.5	16.6	9.50	5.14	81.5	1.933	48	41.9	0.62
BP3	18-Jul-98	off	5	29.0	17.5	9.18	82.1	1.933	48	75.4	0.59
BP4	20-Jul-98	off	9.5	16.6	9.64	5.15	82.4	1.933	48	42.4	0.63
BP5	21-Jul-98	off	0	33.1	20.2	10.5	82.9	1.933	48	87.0	0
BP6	21-Jul-98	off	0	16.7	10.2	5.25	82.9	1.933	48	43.5	0

Table 4 Test Conditions for Velocity Measurements, Phase II Tests

Test	Date	Sail	Drift	Traverse	Vel.	LDV grid	LDV U	CCM U	CCM Set	Ptop	Temp
			(deg)	x/L	comp.		(m/s)	(kts)	(RPM)	(psi)	(deg F)
BV01	14-Jul-98	on	5	0.47	u	coarse	9.33	17.6	29.1	48	78.8
BV02	15-Jul-98	on	5	0.47	w	coarse	9.29	17.6	29.1	48	79.2
BV03	15-Jul-98	on	5	0.47	u	fine	9.36	17.6	29.1	48	80.5
BV04	15-Jul-98	on	5	0.47	w	fine	9.39	17.6	29.1	48	80.5
BV05	17-Jul-98	on	5	0.59	u	fine	9.38	17.6	29.0	48	81.6
BV06	15-Jul-98	on	5	0.59	w	fine	9.39	17.6	29.1	48	81.2
BV07	16-Jul-98	on	9.5	0.48	u	coarse	5.24	9.50	16.6	48	81.5
BV08	16-Jul-98	on	9.5	0.48	w	coarse	5.23	9.50	16.6	48	81.5
BV09	16-Jul-98	on	9.5	0.48	u	fine	5.25	9.47	16.6	48	81.6
BV10	16-Jul-98	on	9.5	0.48	w	fine	5.24	9.47	16.6	48	81.6
BV11	16-Jul-98	on	9.5	0.48	u	bnd.layer	5.24	9.50	16.6	48	81.6
BV12	16-Jul-98	on	9.5	0.48	w	bnd.layer	5.24	9.50	16.6	48	81.6
BV13	17-Jul-98	on	9.5	0.62	u	coarse	5.29	9.42	16.6	48	81.3
BV14	17-Jul-98	on	9.5	0.62	w	fine	5.28	9.44	16.6	48	81.2
BV15	17-Jul-98	on	9.5	0.62	u	bnd.layer	5.29	9.47	16.6	48	81.2
BV16	17-Jul-98	on	9.5	0.62	w	bnd.layer	5.29	9.47	16.6	48	81.2
BV17	18-Jul-98	off	5	0.47	u	bnd.layer	9.42	17.5	29.0	48	82.2
BV18	18-Jul-98	off	5	0.47	w	bnd.layer	9.41	17.5	29.0	48	82.2
BV19	20-Jul-98	off	5	0.48	u	bnd.layer	5.27	9.68	16.6	48	82.4
BV20	20-Jul-98	off	5	0.48	w	bnd.layer	5.27	9.68	16.6	48	82.4
BV21	20-Jul-98	off	5	0.62	u	bnd.layer	5.31	9.61	16.6	48	82.6
BV22	20-Jul-98	off	5	0.62	w	bnd.layer	5.30	9.61	16.6	48	82.6

Table 5 Test Conditions for Force Measurements, Phase II Tests

Test	Date	Sail	Drift	CCM set	CCM U	Ref. LDV U	Temp.	density	Ptop	ReL	Rec
			(deg)	(rpm)	(kts)	(m/s)	(deg F)	(slug/ft^3)	(psi)	(*10e-6)	(*10e-6)
BF1	15-Jul-98	1	5	29.4	17.7	9.172	79.0	1.934	48.0	72.5	0.569
BF2	16-Jul-98	1	9.5	16.8	9.49	5.142	81.5	1.933	48.0	41.9	0.623
BF3	17-Jul-98	1	9.5	16.8	9.43	5.139	81.3	1.933	48.0	41.8	0.621
BF4	18-Jul-98	0	5	29.3	17.6	9.178	81.7	1.933	48.0	75.0	0.589
BF5	18-Jul-98	0	5	29.3	17.6	9.178	82.4	1.933	48.0	75.6	0.594
BF6	20-Jul-98	0	9.5	16.9	9.65	5.147	82.5	1.933	47.9	42.5	0.631
BF7	21-Jul-98	0	0	32.6	19.9	10.28	82.8	1.933	47.9	85.1	0
BF8	21-Jul-98	0	0	16.8	9.74	5.146	82.9	1.933	48.0	42.7	0

4. PHASE I RESULTS

4.1   Pressure Measurements

The pressure distributions obtained during the first phase of tests will be discussed first. In these results, the pressure coefficient as defined by

$$C_p(\theta) = \frac{p(\theta) - p_{ref}}{\frac{1}{2}\rho U^2}$$

will be presented. The variable θ, the circumferential location of an individual pressure tap, is defined in Figure 1, as previously discussed. The reference pressure p_{ref} was obtained from an interpolation between the nearest wall taps, as discussed in Section 3.3.2. Figure 4 shows a typical distribution of the pressure acting on the test section wall as a function of axial distance. There is an obvious acceleration and deceleration of the flow due to the blockage effect of the model in the tunnel test section. The use of p_{ref} as discussed above was made in an attempt to remove as much of this blockage effect from the presentation of the data as possible. Similarly, the velocity U in the definition of the pressure coefficient above was taken as the value at the particular location of each pressure tap ring and measured halfway between the tunnel wall and model, as discussed previously. These measures were taken in order to obtain the most realistic representation of the "freestream" possible.

Figure 5 shows the pressure coefficient distribution for the model at zero drift and with no sail attached, hence a completely symmetric configuration with respect to the oncoming flow (excepting the strut at $\theta = 180$ deg), at both of the axial pressure measurement locations. The variations for each set of taps is attributed to minor surface imperfections in the model. Even though the local freestream pressure has been used in the definition of the pressure coefficient, the values at $x/L = 0.65$ are lower than those at $x/L = 0.47$, indicating some local acceleration of the flow in the vicinity of the hull. This acceleration can probably be attributed to the growth of the boundary layer on the model with increasing axial distance.

Figure 6 shows the pressure coefficient distributions at the two axial locations for the model with no sail but now inclined at a drift angle of 9.5 deg. These data were collected at the "half-speed" condition of 7.64 m/s. The large error bars are the result of the large bias error discussed in section 3.4.2. Figure 7 shows the pressure distributions

17

obtained at the "high-speed" condition of 14.8 m/s. Note that the error bars are considerably smaller here, due to the fact that the error is inversely proportional to the square of the velocity. As will be shown later, the flow shows very little dependence on Reynolds number over the range of Reynolds number studied. It can be argued that while at low speeds the errors appear quite large, the results at the higher speeds and the invariance with Reynolds number mean that the mean values at the lower speeds can be relied upon perhaps more than the error bars would indicate.

The pressure distributions indicated by Figures 6 and 7 are similar to the pressures around an inclined cylinder and are thus to be expected. There is a high-pressure region on the windward side of the hull, pressure minima on the two sides of the hull, and another pressure maximum on the leeward side. It should be noted that the leeward-side pressures in the vicinity of $\theta = 180$ deg are somewhat higher than one might expect in a separated region, but the reader should recall that this portion of the hull is in the wake of the support strut, which attaches to the hull at $\theta = 180$ deg. The comparison between this flow and the inclined cylinder will be examined again in a later section. The pressures at the downstream axial location are again lower than those at the upstream location, as they were for the zero-drift case.

Figures 8 and 9 demonstrate what happen when the sail is added to the model at 9.5 deg drift. The pressures on the "top" of the hull (0 deg $< \theta < 180$ deg) increase and the pressures on the "bottom" of the hull (180 deg $< \theta < 360$ deg) decrease. Again we have the large error bars at the lower speed and smaller errors at the higher speed, and the generally lower pressures at the downstream axial location. The progression just followed is shown in Figures 10 and 11 for the two axial locations: zero drift and no sail first, then the drift angle is set to 9.5 deg, and finally the sail is added. The symmetric pressure distribution for the no-sail case is seen first, and then the asymmetric distribution appears when the sail is added (note that error bars in these and all subsequent figures discussed in this section have been removed for clarity).

Figures 12 through 15 demonstrate the Reynolds number invariance of the flow. There are some slight variations with Reynolds number. Note in Figures 12 through 15 the (minor) changes with Reynolds number occur in the regions of the suction "peaks." As will be shown later with the LDV surveys, in these regions the flow is attached. An increase in Reynolds number generally leads to an increase in the magnitude of the "peaks." It is thought that the increase in Reynolds number produces a decrease in the boundary layer thickness so that the flow conforms more to the body and the pressure distribution approaches the form it would take in an inviscid or potential flow.

It was recognized from the beginning that the presence of the strut would probably interfere with the measurements, and perhaps seriously. In order to remove the effects of the strut as much as possible, it was decided to examine the changes in the flow variables produced when the sail was added to the model at angle of drift. Figures 16 through 18 illustrate these changes. These figures show the quantity $\Delta C_p(\theta)$, defined as

$$\Delta C_p(\theta) = C_{p,\,sail}(\theta) - C_{p,\,no\,sail}(\theta)$$

or the pressure coefficient at a particular point when the sail is attached minus the pressure coefficient at the same point with no sail attached. Figures 16 through 18 illustrate the fact that adding the sail produces higher pressures on the top

of the submarine (0 deg < θ < 180 deg) and lower pressures on the bottom of the submarine (180 deg < θ < 360 deg). Since this asymmetry in the pressure distribution only occurs aft of the sail and to a greater extent aft of the submarine's center of gravity than ahead of it, the higher pressures on the top and the lower pressures on the bottom lead to a nose-up pitching moment. Figure 18 illustrates the development of the pressure asymmetry with increasing axial distance. The magnitude seems to decrease slightly and the peak in the positive pressure moves slightly in the circumferential direction. The shift in peak could be due to the change in circumferential location of the tip vortex relative to the submarine, so that the peak is attempting to "track" the tip vortex. Other than that shift and some peculiarities of the downstream distribution in the vicinity of θ = 180 deg, the two $\Delta C_p(\theta)$ distributions are rather similar.

These $\Delta C_p(\theta)$ distributions may be integrated to yield estimates of the change in the local vertical force coefficient per unit length. If the coefficient of change in vertical force Δc_z is defined as

$$\Delta c_z = \frac{\Delta F_z}{\frac{1}{2}\rho U^2 R}$$

where ΔF_z is the change in vertical force per unit length when the sail is added and $R = D/2$ is the radius of the submarine, then the exact integral

$$\Delta c_z = \int_0^{2\pi} \Delta C_p(\theta) \sin\theta \, d\theta$$

may be computed numerically using some scheme such as the trapezoid rule. Since the density of measured ΔC_p values is relatively small (only 36 values over the circumference of the hull), the trapezoid rule was deemed sufficient to compute the coefficients for the purpose of indicating trends. The $\Delta C_p(\theta)$ distributions in Figures P12 and P13 were integrated, yielding the following values:

Nominal U	x/L	Δc_z
(m/s)		
7.64	0.47	0.0877
7.64	0.65	0.0805
14.8	0.47	0.0956
14.8	0.65	0.0895

These numbers seem to be in general agreement. They are consistent in that the magnitude of the change in force coefficient increases with increasing Reynolds number, again perhaps due to the effects of a thinner boundary layer discussed earlier. They are also consistent in that the values at the downstream location are smaller than those at the upstream location, reflecting the decrease in magnitude of the pressure differences demonstrated in Figures 16 and 17. These results will be revisited at the end of the next chapter.

4.2   Velocity Measurements

The velocity measurements will be presented first as contour plots of the components of the velocity field. The velocity measurements will then be used to extract information about the position of the vortex core and estimates of the circulation associated with the tip vortex.

4.2.1   Velocity Contours

The results of the velocity flowfield measurements are shown in Figures 19 through 36. These are contour plots of the streamwise (u) and transverse (w) velocity components measured on grids perpendicular to the axis of the submarine. The transverse velocity component is the vertical component of the flow velocity (*i.e.* the velocity component in the direction perpendicular to the floor and ceiling of the test section). What are shown in these plots are true views of the measurement grid (*i.e.* sighted along the axis of the submarine) and values of the velocity components that are streamwise and transverse relative to the test section (*i.e.* the components of the velocity parallel to and perpendicular to the axis of the model were not computed). The highest level contour in each plot corresponds to the maximum value of the velocity component measured on that grid, and not the freestream velocity. This value of either u_{max} or w_{max} is reported on each figure. The minimum level contour for the streamwise velocity component corresponds to a fraction F_V of the maxmimum value measured for the grid. For example, in Figure 19, the maximum streamwise velocity value was $u_{max} = 17.141$ m/s and so the maximum contour level corresponds to that value. The fraction for this plot was set at $F_V = 0.75$, and so the minimum contour level corresponds to $F_V * u_{max} = 0.75*17.141$ m/s, or 12.856 m/s. The fraction for each plot is reported on the plot. This value changes from plot to plot in order to emphasize the features of each particular flowfield. The intermediate levels were obtained by taking the difference between the minimum and maximum values chosen and dividing by the number of contours N_{cont}, in most cases 10. The value of N_{cont} is reported in each plot. For the transverse velocity plots, the maximum contour level again corresponds to the maximum value measured on that grid. The minimum level is taken as the negative of the maximum level, since for most of these plots there were both positive and negative values of the transverse velocity measured. Positive values are represented by solid lines and negative values by dashed lines (no negative values of the streamwise velocity component were measured). It will generally be obvious where the maximum values of either velocity component occur in a particular plot.

As stated before, the coordinates y and z in these plots are fixed to the model. The origin for y and z is the model centerline. The model itself is represented by the semi-circle in each plot. The coordinates are rotated so that the sail (not shown in the plots) extends out from the model to the right, or in the positive y-direction. This represents a view from the stern looking toward the bow along the axis of model as it was mounted in the LCC test section. In this view the cross-flow component of the freestream velocity would be directed vertically in the positive z-direction. The sail was approximately 1 model radius high, and so in each of these plots it would lie on the y-axis between $y/R = 1$ and $y/R = 2$. The rather jagged contour near the model is an artifact of the contour plotting routine used. The "corners" on these contours represent the measurement locations closest to the model surface. The primary purpose of these plots is to aid in detecting features of the flow, in particular the vortex location and an idea of the size of the vortex core.

It should be noted that the velocity measurements upon which these plots are based were time averages and do not take into account vortex "meander." Also, the grids were somewhat sparse, in order to cover the flowfield in a reasonable amount of time. Therefore it is possible (and likely) that velocity measurements were not made exactly at or near the vortex core, and so the maximum velocity measured was not necessarily the maximum velocity in the flowfield. Thus the apparent peaks in velocity in the contours shown in these plots do not necessarily indicate the precise positions of the vortex core.

Figure 19 shows the streamwise velocity contours for the model at 9.5 deg drift with the sail on, measured at the axial location $x/L = 0.47$, and at a freestream speed of 14.76 m/s (recall that this is the local freestream value, measured at the same axial location as the velocity survey grid). The tip vortex is clearly visible, lying slightly above the sail tip location at $(y/R, z/R) \approx (2, 0)$. Note that the maximum measured value u_{imax} was 17.141 m/s, for a value of u_{max}/U of 1.16. Figure 20 shows the transverse velocity contours at the same location. As will be shown in detail later, the vortex essentially aligns itself with the freestream velocity direction. Since these are the vertical velocity components measured across the vortex, the contours in the vicinity of the vortex take on the appearance of the classical dipole distribution. The maximum value v_{max} for this survey was 7.525 m/s, for a value $v_{max}/U = 0.510$. The z-component of velocity was not measured, and so its maximum value is not known. However, an idea of the strength of the vortex as measured by the magnitude of its velocity may be found from the resultant of the u and w velocity components: $V_{max} = (u_{max}^2 + w_{max}^2)^{1/2} = 18.7$ m/s, or $V_{max}/U = 1.27$. The variations in velocity magnitude indicated by the contours at the top of the figure near $y = 0$ are a result of the wake of the strut that supports the model from the ceiling of the test section.

Figures 21 and 22 show the contours for a survey done on a finer grid in the vicinity of the vortex core. In these surveys the grid spacing was decreased from $0.1R$ to $0.05R$. Figure 21 shows that the streamwise maximum value increased slightly to $u_{max} = 17.575$ m/s, and Figure 22 shows that the transverse maximum value increased significantly, to $v_{max} = 11.245$ m/s, as a result of capturing values closer to the core with the finer grid. The maximum resultant value was $V_{max} = 20.9$ m/s, or $V_{max}/U = 1.41$. While these maximum values do not quite approach the value 2.07 indicated by the results in Chow *et al.* (1997), they still demonstrate a substantial acceleration of the flow as a result of the formation of the tip vortex. Figure 21 also indicates perhaps some of the wake flow of the sail being drawn into the vortex. This will be discussed in more detail later. Figure 22 indicates the rapid change from the maximum positive value of w to the right of the almost-vertical dividing contour at $(y/R, z/R) \approx (1.93, 0.64)$ to the maximum negative value at $(y/R, z/R) \approx (1.82, 0.64)$. This is again typical of what one would expect in making a cut across a vortex in this manner.

Figures 23 and 24 show the velocity contours measured at the same locations and for the same model configuration as in Figures 19 - 22, but at the "half-speed" condition of $U = 7.64$ m/s. Very little change between the flows may be noted. The lack of Reynolds number effect in the contour plots parallels the lack of Reynolds number effect on the pressure distributions discussed earlier. In this flow, the resultant velocity ratio V_{max}/U was 1.28, producing approximately the same velocity scale as that measured on the coarse grid for the "full-speed" condition of $U = 14.76$ m/s.

Figures 25 and 26 show the velocity contours for the same model configuration as in the previous plots but measured at the axial location $x/L = 0.65$. These contours show the displacement of the vortex core relative to the model as it aligns itself with the freestream. The u-velocity contours in Figure 25 also indicate a migration of the sail wake around the hull of the submarine (the "thumb" of contours in the vicinity $(y/R, z/R) \approx (1.4, 0.6)$. Recall that the model is inclined to the flow. The sail wake seems to be "wrapping" itself around the model, aligning itself with the local flow direction.

Figures 27 through 32 show measurements made for the model at a drift angle of 9.5 deg with the sail off, for comparison purposes. Figures 27 and 28 show the results for u and w at the axial location $x/L = 0.47$ and a freestream speed of $U = 14.93$ m/s. The u-component results indicate an essentially constant value over the field, and the v-component results in Figure 28 indicate a mild acceleration at the side of the model, with a maximum in the vicinity of $(y/R, z/R) \approx (1.1, 0)$, as one would expect for amounts to an inclined cylinder. The results at $x/L = 0.65$ are shown in Figures 29 and 30 and indicate the same features as exist at the upstream location. The results at the "half-speed" condition of $U = 7.6$ m/s are shown in Figures 31 and 32 and indicate no major variations with Reynolds number.

In order to obtain the results shown in Figures 33 and 34, the model was placed at 0 deg drift and the sail was replaced. The sail wake shows up well in the u-component contours of Figure 33, obtained at $x/L = 0.47$. The contours are not completely symmetric, and the apparent "feature" in the w-component contours in Figure 34, in the vicinity of $(y/R, z/R) \approx (1.9, 0)$ indicate the possibility of a slight misalignment of the model at zero angle of drift. The apparent random nature of the rest of the w-component contours simply indicate the random fluctuations (in space) in the freestream. The maximum contour level is at a value of 0.536 m/s, or 3.6% of the freestream velocity. The majority of the contours are below that level, near the value of the acceptable transverse velocity fluctuation for the LCC.

Finally, Figures 35 and 36 show the results for the model at zero drift and with no sail. The streamwise component indicates essentially uniform flow in the freestream, with only the wake of the sail showing any discernible disturbance. The transverse velocity contours in Figure 36 show again the small, random distribution of w-component velocities.

4.2.2 Vortex Trajectories and Circulations

Two additional results that were extracted from the velocity field measurements were vortex core positions and estimates of the strength of the tip vortex. As described in the previous section, the velocity components available from the LDV system were the streamwise velocity component u and the transverse velocity component w. Because the other transverse velocity component v (the component perpendicular to the vertical walls of the tunnel test section) was not available, the usual vorticity calculations could not be performed. Therefore, in order to obtain at least an estimate of the circulation associated with the vortex, two different procedures were used. As will be seen shortly, the vortex shed from the tip of the sail aligned itself generally with the freestream velocity direction shortly after leaving the trailing edge of the sail. The tangential velocity component associated with a point vortex in a two-dimensional potential flow is given by

$$V_\theta = -\frac{\Gamma}{2\pi r}$$

where r is the radial distance measured from the center of the vortex (a positive circulation is usually associated with a clockwise tangential velocity, hence the minus sign). If a measurement of the transverse velocity component w had been made on a horizontal line, perpendicular to the tunnel wall, that passed through the center of the vortex, then because the vortex was essentially aligned with the freestream velocity, the component w would have been the tangential velocity component associated with the vortex (see Figure 37). In that case, assuming an axisymmetric flow around the vortex core, the integral for the circulation around a circle of radius R centered on the vortex core would have yielded

$$\Gamma = \oint V \cdot ds = 2\pi R V_\theta = 2\pi R w$$

(the minus sign has been dropped for convenience). In other words, the product of the radius measured from the center of the vortex and the transverse velocity component would have approached a constant. In some cases this appeared to work well, as is shown in Figure 38. In other situations, the method did not work as well, for a couple of reasons. First, note the distinction in Figure 38 between the circulation values calculated inboard of the vortex ($y < y_v$) and those calculated outside the vortex ($y > y_v$). Note that the outboard values are approaching a constant value, as one might expect, but that the inboard values are increasing with increasing distance away from the vortex. Recall that the tip vortex is shed by the sail at angle of attack (as it is when the yaw angle is nonzero). In addition to generating the tip vortex, the sail is also deflecting the flow downward, giving it a net nonzero velocity in the z-direction. This is illustrated in Figure 39, which shows the w-velocity component values measured at a single z-location. The position of the vortex is obvious from the rapid change in sign of the velocity component, and the intermediate value is evidence of the viscous vortex core. For y values inboard of the vortex, the flow is not approaching a zero velocity but a relatively constant negative velocity, so that from the circulation computation given by the formula above, a steadily increasing value of the circulation is obtained. It was evident from this sort of result that attempts to model the tip vortex as a potential vortex in order to determine the circulation would have to make use of data obtained only from outboard of the vortex position.

It was also recognized that the lines of the traverse grid did not necessarily intersect the vortex core. The finest grid resolution used had a spacing of $0.05R$, so the core could have been missed by as much as $0.025R$ in the y- and z-directions. If the traverse in the y- and z-directions did not pass through the vortex core, then both the magnitudes of the w-velocity component and the distances r used to compute the circulation would have been in error. Additionally, it became obvious from an examination of the velocity data that the influence of the sail and the body itself, as well as viscous effects inside the vortex core, had the capability of "corrupting" the data used to obtain the location and circulation of the inviscid vortex from the potential flow model. Therefore the following procedure was developed in

order to analyze the data. The expression for the velocity induced by a potential vortex given above was used to compute the vertical velocity component induced at the point (y, z) by a point vortex located at (y_v, z_v):

$$w = \frac{\Gamma}{2\pi} \frac{y - y_v}{(y - y_v)^2 + (z - z_v)^2}$$

A program was written to extract from a given data set $w(y)$ at a fixed location $z = z_m$ and $w(z)$ at a fixed location $y = y_m$. These velocity data were read into a Mathcad file and the values of y_v, z_v and Γ were adjusted manually until the curves for $w(y)$ and $w(z)$ generated by the formulae

$$w(y) = \frac{\Gamma}{2\pi} \frac{y - y_v}{(y - y_v)^2 + (z_m - z_v)^2}, \qquad w(z) = \frac{\Gamma}{2\pi} \frac{y_m - y_v}{(y_m - y_v)^2 + (z - z_v)^2}$$

simultaneously gave the best possible fit (from a visual inspection). Velocity data $w(y)$ and $w(z)$ for two new values of y_m and z_m were then read in and the values of y_v, z_v and Γ were adjusted again to yield the best fit. This procedure was repeated until data could be read in and an acceptable curvefit computed without readjusting the values of y_v, z_v and Γ. In this manner the position and circulation of the vortex were obtained simultaneously. One of the benefits of this procedure was that the data points could be weighed during the curvefit process and "corrupted" values could be ignored. Examples of these curvefits for $\beta = 9.5$ deg, $U = 14.9$ m/s and $x/L = 0.47$ are shown in Figure 40. This figure also shows the regions where the velocity data departed from the potential flow curve, generally inboard of the vortex and below. The curvefits tended to be rather sensitive to the values of y_v, z_v and particularly Γ, as one might expect when trying to fit data to a singular function. It was found that often the best fits did not always come from locations very close to the core but somewhat farther away, where the effects of viscosity on the induced velocities seemed to be somewhat less. It was also found that often an overall "bias" velocity value had to be added to the expressions given above to obtain a proper fit, implying an overall mean w value that was not zero. These were small, however, and tended to be 2-4% of the freestream velocity or less. The difficulties of applying some sort of uncertainty analysis to this procedure are obvious, and none was attempted. Based on the variations observed by the author during the curvefits, the uncertainties in y_v and z_v were estimated to be on the order of $0.02R$, and the uncertainty in Γ was estimated to be on the order of 20%.

The vortex trajectory data are shown in Figure 41. Included in this figure are vortex locations measured by Liu and Fu (1994). Liu and Fu measured the flowfield around a submarine model undergoing a constant-radius turn in the Rotating Arm Basin located at the Carderock Division of the Naval Surface Warfare Center (NSWCCD). Liu and Fu used Model 5484, which is described in detail in Liu, Beglin and Fu (1993). There were significant differences between the model used by Liu and Fu and the model in the current study, as well as the basic flow itself, but since the study by Liu and Fu is one of the few available in the open literature that examined many of the same flow phenomena

that are being examined in the current study, it was decided that a comparison would be worthwhile to see if the flows were generally similar.

Since the sail on the model used by Liu and Fu was located at a different x/L, their vortex locations were shifted by the difference in x/L values for the trailing edges of the sails (the trailing edge of their sail was located at $x/L = 0.325$, while the trailing edge of the sail in the current study was located at $x/L = 0.258$). The tops of the sails in both studies were located at $y/L \approx 0.045$, and so no vertical shift was added. No other changes were made to the values reported by Liu and Fu. Two different vortex trajectories from Liu and Fu are shown, one for an angle of yaw of 8 deg and one for an angle of yaw of 16 deg. Liu and Fu report that for an angle of yaw of 8 deg, the angle of attack measured at the sail varied between 0.843 deg at the leading edge and 3.672 deg at the trailing edge, with a value of 2.964 deg at the quarter-chord of the sail. At a yaw angle of 16 deg, the angle of attack measured at the sail varied from 8.432 deg at the leading edge of the sail to 11.41 deg at the trailing edge, with a value of 10.663 deg at the quarter-chord. Although their yaw angle of 8 deg was closer to the yaw angle in the current study (9.5 deg), the angles measured at the sail for a yaw angle of 16 deg were actually closer to the yaw angle in the current study, which was constant over the length of the sail, hence the inclusion of both trajectories here.

The data from both studies show that the tip vortex does in fact align itself generally with the freestream direction. For the current study, the angle between the vortex projection in the x-z plane and the x-axis (the view in the top diagram of Figure 41) is 11.8 deg (recall the angle of attack of the sail is 9.5 deg). The total included angle between the vortex and the x-axis is 12.1 deg. For the case of 8 deg yaw in the study by Liu and Fu, the angle between the vortex projection in the x-z plane and the x-axis is 13.5 deg and the total included angle is also 13.5 deg. For the case of 16 deg yaw, the angle between the vortex projection in the x-z plane and the x-axis is 16.3 deg and the total included angle is 16.5 deg. There seems to be a larger discrepancy for the case of 8 deg yaw than for the other two cases. However, the vortex trajectory as shown in Liu and Fu for the case of 8 deg yaw is not as regular as the case of 16 deg yaw; there are more "kinks" in the trajectory. The current data seem to be consistent with the results of Liu and Fu in yielding angles that are slightly larger than the drift angle. In all cases, the vortex moves closer to the body in the x-z plane, which could be expected. The vortices trailing from the wings of an airplane tend to move closer together, and it is possible using inviscid lifting-line theory to predict the final separation distance, which is always less than the wing span (see *e.g.* Pope 1951, pp. 227ff.). If we imagine the vorticity wrapped around the hull of the submarine to be the other "tip vortex" in the pair, then the movement of the sail tip vortex toward the hull makes sense. We will return to this concept of the vorticity around the hull shortly.

The results for the circulation values are tabulated below. The dimensionless circulation values γ and γ_{cv} are defined in the following manner:

$$\gamma = \frac{\Gamma}{UL}, \quad \gamma_{cv} = \frac{\Gamma}{U \sin\beta\, D}$$

where Γ is the dimensional circulation, U is the freestream velocity, L is the model length, β is the drift angle, and D

is the model diameter. The first definition is the standard definition, while the second defines the dimensionless variable in terms of the crossflow-relevant quantities, the crossflow velocity component $U \sin \beta$ and the model diameter D.

Test	Grid	U (m/s)	x/L	Γ (m²/s)	γ	γ_{cv}
AV04	Coarse	14.9	0.47	1.84	0.018	1.2
AV05	Fine	14.9	0.47	1.83	0.018	1.2
AV03	Coarse	7.64	0.47	0.95	0.018	1.2
AV08	Coarse	14.9	0.65	2.02	0.019	1.3

The column labeled "Grid" indicates the spacing between grid points used in the LDV survey. For the "coarse" grids, the spacing was $0.1R$ (where R is the model radius), and for the "fine" grids, the spacing was $0.05R$.

The results for the circulation estimates were quite consistent. The circulations measured using the coarse and fine grids differed only slightly at $x/L = 0.47$, and the circulation measured at the downstream position $x/L = 0.65$ was only slightly larger than the upstream value. The "half-speed" measurement made at $U = 7.64$ m/s resulted in a circulation approximately half that of the other values, and the dimensionless value was equal to the others.

Unfortunately, the values measured here were not as consistent with values reported by Liu and Fu (1994) or with theoretical predictions. In their study, Liu and Fu obtained a particle Doppler velocimetry (PDV) measurement of the wake of the sail. This survey provided a "snapshot" of the flow in a plane behind the sail, with both in-plane velocity components available. Using these components, Liu and Fu were able to perform a standard contour integration to obtain the circulation associated with the sail tip vortex. Liu and Fu report a value $\gamma = 0.014$ at a yaw angle of 16 deg, with a corresponding angle of attack at the quarter-chord of their model of 10.663 deg, close to the current value of 9.5 deg. The value reported by Liu and Fu agrees well with a value obtained from airfoil theory. It is worthwhile to consider briefly this theory and some of its implications.

The Kutta-Joukowski theorem predicts that the lift per unit span L' for a two-dimensional airfoil is given by the following well-known formula:

$$L' = \rho U \Gamma$$

where ρ is the fluid density, U is the freestream velocity, and Γ is the total circulation contained within the airfoil contour. If we use the standard definition of the section lift coefficient c_l, then the lift coefficient and the circulation may be related in the following manner:

$$c_l = \frac{L'}{1/2\rho U^2 c} = \frac{\rho U \Gamma}{1/2\rho U^2 c} = \frac{2\Gamma}{Uc} = \frac{2\Gamma}{UL} \cdot \frac{L}{c} = 2\left(\frac{L}{c}\right)\gamma$$

This equation is significant because the lift coefficient is also related to the angle of attack of the airfoil through the

following formula (assuming a symmetric airfoil where the zero-lift angle of attack is zero):

$$c_l = a\,\alpha = a\,\beta$$

where a is the two-dimensional lift-curve slope for the airfoil and α is the angle of attack, which in the current study is the angle of drift or yaw β. Thus the circulation around the airfoil may be related to the angle of drift through the following formula:

$$\gamma = \frac{1}{2}\left(\frac{c}{L}\right) a\,\beta$$

If we make the assumption that the circulation in the tip vortex is equal to the circulation bound to the sail at angle of attack (because it is at angle of drift), then this formula yields a prediction for the dimensionless circulation in the tip vortex. Theoretical and empirical values of a for low-aspect ratio airfoils may be found in various references (*e.g.* Jones 1946, Hoerner 1971). The value that Jones reports for a is

$$a = \frac{\pi}{2} AR_w$$

where AR_w is the aspect ratio of the finite wing. For typically rectangular planform submarine sails, the aspect ratio AR_s would normally be defined as h/c, where h is the distance the sail protrudes from the hull and c is the length of the sail in the spanwise direction. From the perspective of finite wing theory, the sail is actually *half* of the wing, and so the relationship between the two values of the aspect ratio is $AR_w = 2AR_s$. Wald (1967) in his theoretical work on the lift produced by submarine appendages, defines the aspect ratio as $2h^2/S$, where S is the planform area of one fin. For a rectangular-planform fin, such as a sail, this reduces to $AR = 2h/c = 2AR_s$, as just pointed out. Therefore, using this value of the lift-curve slope with the common definition of the aspect ratio, the relationship between the dimensionless circulation and the angle of drift is

$$\gamma = \frac{\pi}{2}\left(\frac{c}{L}\right) AR_s\,\beta$$

In the current study, the values were $\beta = 9.5$ deg $= 0.166$ rad, $AR_2 = h/c = 0.57$, and $c/L = 0.0817$, yielding a value for the circulation of $\gamma = 0.012$, which is considerably smaller than the value $\gamma = 0.018$ obtained through the analysis of the velocity data described above. Using the values $\beta = 10.663$ deg $= 0.186$ rad, $AR_s = 0.62$, and $c/L = 0.076$, which are the values in the study by Liu and Fu (1994) corresponding to the case of 16 deg yaw and a measured angle of attack of 10.663 deg at the sail quarter-chord, one obtains $\gamma = 0.0137$, which agrees well with their experimentally-determined

value of $\gamma = 0.014$. A value predicted by theory that falls a little closer to the value in the current study may be obtained by using the results of Wald (1967) for a single fin. For a single fin with an aspect ratio less than one, Wald reports a lift-curve slope given by

$$a = \pi \, AR_s \, J_1$$

where J_1 is given by

$$J_1 = \frac{4}{\pi}\left(\frac{R}{h}\right)^2 \left\{ \frac{1}{2}(t+1)^2 \left[\frac{\pi}{2} + \sin^{-1}\sqrt{\frac{t-1}{t+1}} \right] - \pi - (3-t)\sqrt{\frac{1}{2}(t-1)} \right\}, \quad t = \frac{1}{2}\left(\frac{R+h}{R} + \frac{R}{R+h} \right)$$

Using the values for the model in the current study, $J_1 = 1.36$ so that $a = 2.435$ and the value of the circulation predicted by the theory is $\gamma = 0.0165$, still lower than the measured value of 0.018. Even though the estimated uncertainty would include the Liu and Fu values and the theoretical values within the error bands of the current circulation values, it is not known why the values in the current study are consistently somewhat higher than the values measured by Liu and Fu or predicted by theory.

The circulation associated with the sail tip vortex may be used along with airfoil theory in one final calculation. If we assume that the circulation in the vortex is equivalent to the circulation around the sail (thought of now as an airfoil at angle of attack), then we may also assume that an equivalent amount of circulation exists around the submarine hull. Coney (1985) made measurements of the circulation along a contour around the sail mounted at angle of attack on a submarine hull and of the circulation around the submarine hull and found that the ratio of the two values of the circulation was very close to one. As a result of this we can think of the vorticity attached to the submarine as something akin to a classical horseshoe vortex, where the base of the horseshoe is bound to the sail, one leg is the sail tip vortex, and the other is actually enlarged and wrapped around the submarine hull (a description identical to that in the quote from Feldman (1995) at the beginning of Section 1.1). It is this argument that allows us to equate the circulation in the tip vortex with the circulation bound to the sail and the circulation around the submarine hull.

We can use the Kutta-Joukowski theorem along with the circulation around the hull and the crossflow velocity component to compute the vertical force per unit length acting on the hull that contributes to the pitching moment:

$$F_z = \rho(U\sin\beta)\Gamma \Rightarrow c_z = \frac{F_z}{\frac{1}{2}\rho U^2 R} = \frac{\rho(U\sin\beta)(U\sin\beta D\gamma_{cv})}{\frac{1}{2}\rho U^2 \frac{D}{2}} = 4\gamma_{cv}\sin^2\beta$$

For small angles, $\sin\beta \approx \beta$ and so $c_z \approx 4\gamma_{cv}\beta^2$, illustrating the dependence of the vertical force coefficient on the *square* of the drift angle, as discussed in Section 1.1. Using the value of $\gamma_{cv} = 1.2$ obtained in the current study, the

corresponding value of c_z is 0.13. This value may be compared to the values for Δc_z obtained by integrating the pressure distributions in Section 4.1. Those values were obtained by integrating the difference in pressure coefficient values between the submarine with sail at angle of attack and the submarine with no sail at angle of attack, in order to minimize the effects caused by the presence of the strut. However, since the no-sail case should result in zero vertical force (and hence zero pitching moment), the c_z values obtained from the theoretical considerations described above should be essentially the same as the Δc_z values obtained from the integrations. The results of the integrations varied, but the values of Δc_z ranged from 0.08 to 0.096, still somewhat lower than the value of 0.13 computed using the measured circulation. If Wald's value for a is used to compute the circulation and this value is then used to compute the force coefficient, the result is $c_z = 0.12$, which is still slightly higher than the value obtained from integrating the pressure coefficients.

5. PHASE II RESULTS

5.1 Overview

Between the first and second phases of these tests, some changes were made to the model. The trip ring, which had been located at $x/L = 0.05$, was removed. In other tests with this model the staff of the LCC had concluded that the trip ring introduced asymmetries in the circumferential distribution of flow properties, in particular the boundary layer profiles, and so the ring was removed. The model was also painted flat black in the region of the x/L locations for LDV surveys, in order to decrease reflections from the model and thus increase data acquisition rates. The sting and sting support mechanism were replaced with a new sting mechanism that allowed a continuous variation in the model angle of attack. This produced a slight shift in the streamwise location of the model relative to the LCC test section and so the positions of the LDV surveys had to be altered slightly so that the survey planes remained accessible optically through the LCC test section windows. In each of the following sections, the results of Phase II will be presented first, and then a comparison between the results of the two phases will be presented.

5.2 Pressure Measurements

The same definition of the pressure coefficient used in Chapter 4 will be used here. The wall tap locations relative to the model were corrected for the model shift, so that the wall tap closest to the particular presssure tap ring was used as the reference pressure in the pressure coefficient definition.

The results for the sail-off configuration at 0 deg drift are shown in Figure 42. As in Phase I, the variations in pressure coefficient were attributed to small imperfections in the model surface. The gap in the data at $x/L = 0.65$ for 135 deg $< \theta < 240$ deg is the result of the omission of the pressure tubes for 10 pressure taps in order to make room for the force balance cable, as discussed before. This figure also reveals some acceleration of the flow between $x/L = 0.47$ and $x/L = 0.65$, as observed in the tests in Phase I. A word concerning the seemingly large error bars is in order here. As was discussed in Section 3.4 on uncertainty analysis, an uncorrelated systematic uncertainty of 0.3 psi was associated with the regression used to obtain pressure values from the output of the pressure transducer. At higher speeds, the pressure difference used in computing the pressure coefficient is relatively large, and so the regression error makes a relatively small contribution. However, in the tests in Phase II, the tunnel velocities had to be kept somewhat low, since the stern of the model was no longer restrained. The lower velocities resulted in lower pressure differences

30

and hence the relative contribution from the regression error was larger, resulting in the larger error bars as seen in Figure 42. Typically the larger the angle of drift, the smaller the tunnel velocity that could be obtained. A few tests were conducted in which the tunnel speed was allowed to vary over a greater range for a fixed model configuration. Data were obtained at the lower and higher speeds and compared. Figure 43 is an example of this. This figure shows the pressure distribution obtained for a sail-off configuration at 0 deg drift, the same configuration shown in Figure 43. The data in Figure 43 were obtained at a tunnel speed twice that for the data shown in Figure 42. The error bars are significantly smaller. Figure 44 compares the data from these two tests and demonstrates that the mean values are essentially the same. Similar results were obtained in other tests which will be discussed below. The conclusion is that the mean values for the pressure coefficient may be considered to be more reliable than a quick glance at the error bars would indicate. In the basic presentation of the data, multiple runs will be included to emphasize the repeatability of the data.

Figures 45 and 46 show the pressure distributions obtained for a sail-off configuration at 5 deg of drift. The data demonstrate the roughly symmetric pressure distribution similar to that of a yawed circular cylinder, with suction "peaks" at $\theta = 90$ deg and $\theta = 270$ deg, where the flow has experienced the maximum accleration. Similar variations show up at $\beta = 9.5$ deg, as shown in Figures 47 and 48. Note that these measurements were made at the lowest tunnel velocity and thus have the largest error bars.

Figures 49 and 50 show the pressure distributions obtained for a sail-on configuration at $\beta = 5$ deg. The cause for the abrupt "dip" in C_p around $\theta = 140$ deg for $x/L = 0.47$ is not known. This "dip" can be seen in other Phase II pressure distributions, although it is generally much smaller (see e.g. Figure PB03). It is possible that it was caused by a surface imperfection introduced during a model change. The pressure distributions for a sail-on configuration at $\beta = 9.5$ deg are shown in Figures 51 and 52.

The changes in the pressure distributions as the model geometry changed are shown in Figures 53 through 56. In Figure 53, the pressure distributions at $x/L = 0.47$ are shown for the sail-off, $\beta = 0$ deg configuration, followed by the sail-off, $\beta = 5$ deg configuration, and then the sail-on, $\beta = 5$ deg configuration. The same progression is shown in Figure 54 for the pressure distributions at $x/L = 0.65$, and the same pair of progressions for $\beta = 9.5$ deg are shown in Figures 55 and 56. Recall that the pressure data is presented in this manner in order to emphasize the effects of adding the sail, and thus minimize the effects of the strut. While the changes are not as clear at $\beta = 5$ deg as they are at $\beta = 9.5$ deg, the pressure distributions do show an increase in pressure on top of the hull and a decrease in pressure on the bottom of the hull, changes which would create a nose-up pitching moment. In general the data seemed to be less well organized at $\beta = 5$ deg than it was at $\beta = 9.5$ deg, as can be seen by comparing Figures 54 and 56 in particular.

The circumferential variations of $\Delta C_p = C_{p,sail} - C_{p, no sail}$ for $\beta = 5$ deg and $\beta = 9.5$ deg are shown in Figures 57 and 58. Figure 57 does in fact show that at both x/L positions, the pressure on top of the hull (0 deg $< \theta <$ 180 deg) becomes larger and the pressure on the bottom of the hull (180 deg $< \theta <$ 360 deg) becomes smaller when the sail is added (except for the abrupt variation around $\theta = 140$ deg discussed above). Figures 59 and 60 demonstrate the development of the pressure difference with angle of drift for the two x/L locations. These distributions seem to indicate

a nonlinear variation of the change in pressure distribution with angle of drift. As noted in the Phase I experiments, the peak pressure difference moves slightly with increasing axial distance down the model, in such a manner that it appears to be "following" the tip vortex.

The ΔC_p distributions for $x/L = 0.47$ were integrated using the procedure discussed in Section 4.1 to obtain values of Δc_z (the distributions at $x/L = 0.65$ were not integrated because of the large gap caused by the removal of the the 10 taps). The two different runs were averaged and the resulting pressure coefficient differences were integrated. The results are tabulated below and plotted in Figure 61 (in this figure it is assumed that $\Delta c_z = 0$ at $\beta = 0$). This figure demonstrates the nonlinear variation of the change in sectional vertical force coefficient with drift angle. The result for $\beta = 9.5$ deg was in general agreement with the values obtained in Phase I; a more complete comparison of the results is deferred until the next section.

β	Nominal U	Δc_z
(deg)	(m/s)	
5	9.18	0.0321
9.5	5.15	0.0877

5.2.1 Comparison of Phase I and Phase II pressure measurement results

Figure 62 shows the pressure distributions at $x/L = 0.47$ from both Phase I and Phase II for the model at zero angle of drift and with the sail off. Results for two different speeds are included for the Phase II results. It can be seen that in some regions there is good agreement between the data, and other regions the agreement is not so good. Error bars have been omitted from this figure for clarity. Generally the results are in better agreement in the region 180 deg $\leq \phi \leq 360$ deg. Figure 63 compares results for the same conditions at $x/L = 0.65$, and in these cases the agreement is not as good as at $x/L = 0.47$. The Phase II results seem to be shifted from the Phase I results. Numerous checks of the data were made to ensure that the correct reference pressures were being used. In general it is believed that the differences between the results for the two test phases were caused by the removal of the trip ring between Phase I and Phase II. The primary effect of this removal would be to change the characteristics of the boundary layer at the pressure tap locations by affecting the initial conditions of the boundary layer development. It would be expected that the removal of the trip ring would delay transition and the subsequent thickening of the boundary layer. The trip ring itself could contribute to a thicker boundary layer if it were too large by introducing a wake component to the boundary layer profile. It should also be kept in mind that the Phase II tests were generally run at lower speeds than the Phase I tests, because of the necessity of leaving the stern of the model unrestrained for the force measurements. The lower Reynolds number in Phase II would also tend to delay transition. Of course, the lower Reynolds number would in general mean a thicker boundary layer at a downstream point, and so these two Re effects might offset somewhat. Any surface imperfection would have its influence increased or diminished according to how the boundary layer thickness changed at the location of the imperfection, with a particular surface imperfection expected to have a larger effect in a thinner boundary layer. The results in Figures 62 and 63 would demonstrate these effects most dramatically, since at zero drift

angle the boundary layer at the pressure tap rings has developed from the nose of the model. Figure 64 also supports this argument. This figure shows the results at $x/L = 0.47$ for the two different phases with the model at $\beta = 9.5$ deg and the sail off. With the model inclined to the freestream, the boundary layer develops from the attachment streamline on the windward side of the model. The surface streamline which crosses the pressure tap location originates on this attachment line and not at the nose, and so the influence of conditions at the nose of the model on the state of the boundary layer at the pressure tap location is reduced. The two curves in Fig. PAB03 lie almost on top of each other. Figure 65 shows the results at $x/L = 0.65$. The "shift" between the two phases is still present but is less pronounced than in the zero drift angle case.

Figures 66 and 67 show the results at the two x/L locations for the model at $\beta = 9.5$ deg with the sail on. As before, the results are in fairly good agreement at $x/L = 0.47$ and less so at $x/L = 0.65$. It should be noted, however, that in one region in Figure 67, 270 deg $\leq \phi \leq$ 360 deg, the results of the two test phases are in good agreement even at $x/L = 0.65$. In this region the effect of the tip vortex shed by the sail is to accelerate the flow, creating the pressure minimum at $\phi \approx 280$ deg. It is possible here that the acceleration of the flow has the effect of thinning the boundary layer to the point that the flow conforms to the body shape and the pressures approach the distribution they would have in potential flow, overriding any local effects caused by surface imperfections. That the differences between the pressure distributions from the two different test phases are the result of boundary layer effects is suggested even more strongly by Figures 68 and 69. These figures show the differences in the values of the pressure coefficients between the "sail-off" and "sail-on" configurations, isolating the effects of adding the sail. The region 0 deg $\leq \phi \leq$ 180 deg is where the boundary layer would tend to be thick, because of the adverse pressure gradient induced by the tip vortex, and would perhaps even separate in the cross-flow plane in some cases. In this region the addition of the sail causes an increase in the pressure on the surface. The region 180 deg $\leq \phi \leq$ 360 deg is where the addition of the sail causes a decrease in the surface pressure and the local flow acceleration might be expected to thin the boundary layer. It can be seen in these two figures that in the "thick boundary layer" region, where the effects of boundary layer - surface imperfection interactions would be minimal, the distributions of pressure coefficient difference are almost identical, even at $x/L = 0.65$ (Fig. 69), and that the differences in the two difference distributions tend to show up in the "thin boundary layer" region, where surface imperfection - boundary layer interactions would be more pronounced (note that while the "sail-on" curves showed good agreement in this region, the "sail-off" curves showed some discrepancies, and the curves in Figures 68 and 69 result from taking the difference between the "sail-on" and "sail-off" C_p values). The reasons for local differences, particularly the "spike" in the pressure distribution around $\phi = 160$ deg in the Phase II results shown in Fig. 68, are still not clear, although these could also be due to larger surface imperfections introduced to the model between the two test phases that overrode smaller differences in the state of the boundary layer.

Phase	Nominal U (m/s)	Δc_z
I	14.8	0.096
I	7.64	0.088
II	5.15	0.089

The results of integrating the pressure difference distributions to obtain values of Δc_y are compared in the table above. Since the pressure distributions at $x/L = 0.65$ were not integrated in Phase II tests because of the gap left by the taps that had to be omitted, only the values obtained from the integrations at $x/L = 0.47$ are compared. The results compare fairly well, with the Phase II value lying between the two Phase I values and very close to the Phase I "low-speed" value.

5.3   Force Measurements

The results of the force measurements are presented in Figures 70 through 75. The force balance was mounted at the pivot point of the model mount, and so the forces and moments shown were measured about that point. The force balance was fixed to the model and aligned with the model axes, and so the force components shown correspond to the body-fixed coordinate system. The axial force X is in the direction of the model axis and is positive toward the bow. The side force Y is positive in the starboard direction, and the vertical force Z is positive down, in the direction of the keel. The moments l, m and n are in the positive directions about the x, y, and z axes as determined by the right-hand rule. The forces are normalized by the dynamic pressure and the square of the model length to form the force coefficients C_X, C_Y and C_Z, and the moments are normalized by the dynamic pressure and the cube of the model length to form the moment coefficients C_l, C_m and C_n. The reference velocity measured by the LDV system at the entrance to the test section was used to compute the dynamic pressure. In Figures 70-75 the force and moment coefficients are shown as functions of the angle of drift β. Again, because of the unavoidable presence of the support strut, two sets of data are shown in each figure, one for the "sail-off" configuration and one for the "sail-on" configuration, to demonstrate the effects of adding a sail. In the second phase of testing, in which the forces and moments were measured, the model was not tested in a zero drift angle, sail-on configuration, and so no force measurements were made for that configuration. The conditions for each point are listed in each figure; these correspond to the conditions described in Table 5 of Section 3.5. It should be noted that since the speed had to be limited at the higher drift angle, each point on each figure essentially corresponds to a different model/flow condition. Also, the lower speeds at the higher drift angle led to the generally larger error bands at the higher drift angle. As the model configuration was altered, primarily when the drift angle was changed, the rudders on the model were adjusted to minimize the loads on the model and strut, particularly the yawing moment. Generally the rudders were aligned with the freestream direction. Since no systematic study was performed to determine the effects of the rudder position on the forces and moments, and since these effects were assumed to be minimal on the pitching moment and the lift force, the two primary quantities of interest in this study, most attention will be focused on these two quantities. The results for the other forces will be

presented and commented upon briefly. The current results will be compared with the results of the studies performed by Wetzel *et al.* (1993) and Wetzel and Simpson (1998) discussed in Section 1.2.

Figure 70 shows the variation of the pitching moment coefficient C_m with angle of drift. For the "sail-off" configuration, the pitching moment began at zero, as one might expect, and then became slightly more negative as the β increased. The reason for this variation is unclear. However, when the sail was added, the pitching moment demonstrated a nonlinear positive increase, as arguments previously discussed would suggest. As has been shown by the pressure measurements made in this study, the presence of the tip vortex creates a pressure distribution that results in a "down" force on the submarine aft of the sail, leading to a nose-up pitching moment. Wetzel *et al.* (1993) reported a nose-*down* increase in pitching moment as β increased, and attributed this variation to an interaction between the appendage wake and the flow separation from the body. The current studies had nominally the same geometry and the same reference point for the forces and moments, and so the reason for the discrepancy between the current results and those of Wetzel *et al.* are unclear. The magnitudes of the pitching moment coefficients measured in the current study and reported by Wetzel are in general agreement. The maximum value of C_m measured in the current study was approximately 0.0007 at β = 9.5 deg. Wetzel *et al.* report a value of approximately -0.004 at a drift angle of 10 deg.

Figure 71 shows the variation of the vertical force coefficient C_z with β. Again, for the "sail-off" configuration there was a slight increase in the negative direction as β increased which is unexplained. When the sail was added, C_z demonstrated a nonlinear increase in the positive direction. Recall the mechanism for the nonlinear variation. The circulation of the sail tip vortex is proportional to the sail angle of attack, in this case the drift angle β. The circulation bound to the hull is assumed to be equal and opposite to the tip vortex circulation. Then, according to the Kutta-Joukowski theorem, the transverse (in this case vertical) force is proportional to the circulation and the crossflow velocity, which in this case is proportional to the sine of β and is therefore proportional to β itself for small β. This nonlinear variation shows up most clearly in the variation of C_z, since the model was mounted at a fixed angle of drift and therefore the entire model saw the same crossflow velocity component. This is the primary difference between the flow currently under consideration and the actual flowfield of a submarine executing a turn. The values reported by Wetzel *et al.* for C_z are also in general agreement with the current results. The maximum value of C_z in Figure 71 is approximately 0.002 at β = 9.5 deg; Wetzel *et al.* report a value of approximately 0.0015 at β = 10 deg.

The remainder of the force and moment results are shown in Figures 72 through 75. The axial force coefficient C_x shown in Figure 72 demonstrated both the most relative scatter in terms of the sizes of the error bands and the least consistency in terms of the changes between the "sail-off" and "sail-on" configurations. For the "sail-off" configuration, the value of C_x became more negative as β increased, indicating an increase in drag, as one might expect, but when the sail was added, C_x became less negative as β increased from 5 deg to 9.5 deg. However, it should be noted that these variations were small and within the error bands. Wetzel *et al.* report similar variations and values of C_x generally in the neighborhood of -0.001, as in the current study. The side force coefficient C_y shown in Figure 73 demonstrated the expected increase in the negative direction, as expected, with a larger increase for the "sail-on" configuration caused by the lift force generated by the sail. The maximum value measured was approximately -0.003 at β = 9.5 deg; Wetzel

et al. report a value of approximately -0.0055 at $\beta = 10$ deg. The variation of rolling moment coefficient shown in Figure 74 requires comment. As β increases, the lift force generated by the sail increases, creating presumably a negative rolling moment about the longitudinal axis of the submarine. The variation shown in Figure 74 indicates a positive increase in C_l as β increased. It is believed that this discrepancy is due to a minus sign associated with a calibration coefficient that was inadvertently omitted during the data reduction process. The general behavior illustrated in Figure 74 is reasonable: essentially no change in rolling moment with β for the "sail-off" configuration, as one might expect, and a significant increase in magnitude as β increased for the "sail-on" configuration. The maximum C_l value in the current study was approximately 0.00009 at $\beta = 9.5$ deg; Wetzel *et al.* report a value of -0.0001 at $\beta = 10$ deg. Finally, the variation of yawing moment coefficient C_n with β is shown in Figure 75. The variation of C_n with β is similar to that of Wetzel *et al.* both in general trends and in the fact that there is not a large change between the "sail-off" and "sail-on" configurations. Wetzel *et al.* do report a significantly larger magnitude for the yawing moment coefficient. In the current study, the maximum C_n is approximately -0.0011 at $\beta = 9.5$ deg, where Wetzel *et al.* report a value of approximately -0.004 at $\beta = 10$ deg. It should be noted that Wetzel *et al.* report that the rudders of their model were fixed for all tests, where the rudders in the current study were moved to minimize the loads on the model, as discussed above. This difference between the two configurations would likely show up most noticeably in the yawing moment coefficient, and so this could explain the differences in the current values and those reported by Wetzel *et al..*

5.4   Velocity Measurements

As in Section 4.2, the velocity measurements will be presented first as contour plots of the components of the velocity field. These plots will include surveys of the boundary layer on the model at various conditions. The velocity measurements will then be used to extract information about the position of the vortex core and estimates of the circulation associated with the tip vortex.

5.4.1   Velocity contours

The results of the velocity flowfield measurements are shown in Figures 76 through 97. Figures 76 through 88 are the contour plots for the general surveys, and Figures 89 through 97 are the results of the boundary layer surveys. The reader is referred to the beginning of Section 4.2.1 for a discussion of how these plots were constructed and what the variables represent.

Figure 76 shows the streamwise (u) velocity contours for the model with sail at $\beta = 5$ deg at the axial location $x/L = 0.47$ and a freestream speed of 9.33 m/s. The tip vortex shows up clearly at $(y/R, z/R) \approx (1.8, 0.4)$. The wake of the sail also appears just below the tip vortex and between the vortex and the model. Recall that the distortion in the contours at the top left of the figure ($y/R = 0$) was due to the wake of the strut. Figure 77 shows the transverse (w) velocity contours at the same location and condition. As was discussed in Section 4.2, because the vortex nearly aligns itself with the freestream direction, the vortex shows up in this plot as a classic dipole distribution. The maximum streamwise velocity measured on this grid was $u_{max} = 9.45$ m/s, yielding $u_{max}/U = 1.01$. The maximum transverse velocity measured was $w_{max} = 2.90$ m/s, yielding $w_{max}/U = 0.312$. The resultant maximum velocity ratio $V_{max}/U = (u_{max}^2 +$

$w_{max}^2)^{1/2}/U$ was 1.06. Figures 78 and 79 show the results of a detailed survey of the vortex at the same axial location and flow condition. The maximum velocity values were $u_{max}/U = 1.01$, $w_{max}/U = 0.348$, and $V_{max}/U = 1.07$. That this value is very close to the value obtained from the "coarse" grid is an indication that a point on the coarse grid happened to fall very close to the core of the vortex, or at least as close as did a point on the "fine" grid. Figures 80 and 81 show the results of surveys taken at $\beta = 5$ deg and at $x/L = 0.59$ (*i.e.* the downstream location). The "coarse" grid was used for the streamwise velocity component and the "fine" grid was used for the transverse velocity component (this was done in order to save time, since from the Phase I tests it was determined that the detailed survey of the transverse velocity component was most useful in determining vortex circulation values). The streamwise component survey (Figure 80) shows the migration of the vortex up relative to the submarine, an indication of the vortex aligning itself with the freestream direction and thus moving further away from the submarine with increasing axial distance. The transverse velocity contours again demonstrate the dipole distribution. The maximum velocity values were $u_{max}/U = 1.01$, $w_{max}/U = 0.360$, and $V_{max}/U = 1.07$ (this value computed using the values from the coarse grid for the streamwise velocity and the fine grid for the transverse velocity). The nearly-constant values for the maximum velocity ratio are an indication of the essentially constant vortex strength.

Figures 82 through 85 show the results of the velocity surveys for a sail-on configuration at $\beta = 9.5$ deg and $x/L = 0.48$. The first two figures show the results for the streamwise and transverse velocity components on the "coarse" grid and the second two the corresponding velocity components for the "fine" grid. The vortex is in approximately the same position as it was in the Phase I tests, but it does not appear to be as organized, at least in terms of the streamwise velocity component. The freestream speed here was 5.43 m/s, as opposed to a value of 14.76 m/s in the first phase of tests. There is evidence in Figure 82 of the sail wake. The resulting speed ratios were, for the coarse grid, $u_{max}/U = 1.04$, $w_{max}/U = 0.719$, and $V_{max}/U = 1.26$, and for the fine grid, $u_{max}/U = 1.18$, $w_{max}/U = 0.801$, and $V_{max}/U = 1.43$. Note the larger values for the higher angle of drift, indicating a stronger vortex, as one would expect. Note also that the fine grid did come closer to the vortex core. This values indicate a significant acceleration of the flow in the tip vortex.

Figures 86 and 87 shows the results for a sail-on configuration at $\beta = 9.5$ deg and $x/L = 0.62$. The first figure shows the contours for the streamwise velocity component on a coarse grid, and the second shows the transverse velocity components measured on a fine grid. The tip vortex is almost indistinguishable in the streamwise velocity component. The seeming lack of organization is again attributed to the relatively low velocity. The migration of the sail wake around the model hull is also apparent. The speed ratios were $u_{max}/U = 1.01$, $w_{max}/U = 0.794$, and $V_{max}/U = 1.29$. This is a smaller value than at $x/L = 0.48$, but note that the value from the coarse grid was used to compute u_{max}/U, and hence the true maximum in u at $x/L = 0.62$ was probably missed by the coarse grid.

As stated earlier, Figures 88 through 97 show the results of the boundary layer surveys. It should be noted that the boundary layer surveys were added to the test program at a later stage of the tests, when there was not sufficient time to make all the required model changes to create all the various model configurations, hence the boundary layer surveys at $\beta = 5$ deg were all with the sail off and the surveys at $\beta = 9.5$ deg were all with the sail on. Since the primary interest of these studies was crossflow separation, which at the low angles of drift studied would occur at circumferential

38

locations significantly far away from the region of the model surface most affected by the tip vortex, the variations introduced by the sail were taken to be of secondary importance which did not warrant a full study.

Figures 88 through 93 show the velocity contours for the boundary layer surveys conducted at $\beta = 5$ deg with no sail. The boundary layer surveys were performed primarily to see if there was any evidence of crossflow separation at the angles of drift that were used. Figures 88 and 89 contain the results for the streamwise and transverse velocity components at a freestream speed $U = 5.27$ m/s and axial location $x/L = 0.48$, and Figures 90 and 91 show the results for the streamwise and transverse velocity components at a freestream speed $U = 9.42$ m/s at the same axial location. Figures 92 and 93 show the results for the streamwise and transverse velocity components at a freestream speed $U = 5.31$ m/s and an axial location $x/L = 0.62$. Figure 88 shows some apparent thickening of the boundary layer at $\theta \approx 70$ deg (where θ is measured from the horizontal in this figure). There is no obvious indication of vortical flow in the transverse velocities shown in Figure 89, although the velocity contours do show a radial gradient in the transverse velocity near the wall which would indicate some vorticity in the streamwise direction. These features are less pronounced in Figures 90 and 91, where the higher speed has resulted in thinner boundary layers and a corresponding reduced tendency toward separation. Figures 92 and 93 do seem to show somewhat more obvious flow separation at $\theta \approx 50$ deg, along with more evidence of a vortical flow. The streamwise velocity component in Figure 92 seems to have a local minimum in this vicinity near the wall, and the transverse velocity component shows a more pronounced gradient in the same region.

Figures 94 through 97 show the results for the boundary layer velocity contours for the model with sail at $\beta = 9.5$ deg. Figures 94 and 95 show the streamwise and transverse velocity component contours at a freestream speed $U = 5.24$ m/s and axial location $x/L = 0.48$, and Figures 96 and 97 show the streamwise and transverse velocity component contours at a freestream speed $U = 5.29$ m/s and axial location $x/L = 0.62$. Figure 94 shows a pronounced thickening of the boundary layer in the region $\theta \approx 60$ deg. The gradient of the transverse velocity in the same region as shown in Figure 95 would indicate the presence of some streamwise vorticity in that region. These effects are even more pronounced at the downstream location, as shown by Figures 96 and 97. These figures also show the effects of the sail wake on the boundary layer and its tendency to "migrate" or wrap itself around the submarine in the direction of the crossflow velocity.

5.4.2   Vortex trajectories and circulations

The same procedure for obtaining vortex core positions and circulation values that was discussed in Section 4.2.2 was used in these tests, with similar results concerning the sensitivity of the values, the necessity of adding "bias" velocity values to obtain good fits, and the overall uncertainty of the results. It should be noted that all of these computations were performed using results from "fine" resolution LDV survey grids. Figures 98 and 99 show the vortex locations at drift angles of 5 deg and 9.5 deg, respectively, and the two vortex trajectories are compared directly in Fig. 100. At $\beta = 5$ deg, the angle between the vortex projection in the x-z plane and the x-axis (the view in the top diagram of Figure 98) was 8.11 deg, and the total included angle between the vortex and the x-axis was 8.13 deg. At $\beta = 9.5$ deg, the angle between the vortex projection in the x-z plane and the x-axis was 13.1 deg and the total included

angle was 13.2 deg. Figure 101 compares the Phase I and Phase II results for the vortex locations at $\beta = 9.5$ deg. These are seen to agree fairly well in general, although there are some discrepancies. These are most likely due to vortex "meander," in which the vortex position is not steady but varies somewhat slowly with time. The angles for both test phases and both angles of drift are summarized in the table below.

Phase	β (deg)	Projection Angle (deg)	Total Included Angle (deg)
II	5	8.11	8.13
I	9.5	11.8	12.1
II	9.5	13.1	13.2

As mentioned above, values were obtained for the dimensionless values of the vortex circulations γ and γ_{cv}, using the same definitions as before:

$$\gamma = \frac{\Gamma}{UL}, \qquad \gamma_{cv} = \frac{\Gamma}{U \sin\beta \, D}$$

These results are summarized in the table below, along with the corresponding results from the Phase I tests, so that all of the results are collected into one table. The last two columns are the values of γ predicted by low-aspect-ratio wing theory and Wald's theory, described in Section 4.4.2.

Phase	Test	β (deg)	U (m/s)	x/L	γ	γ_{cv}	γ_{wing}	γ_{Wald}
I	AV04	9.5	14.9	0.47	0.018	1.2	0.0121	0.0165
I	AV05	9.5	14.9	0.47	0.018	1.2	0.0121	0.0165
I	AV03	9.5	7.64	0.47	0.018	1.2	0.0121	0.0165
I	AV08	9.5	14.9	0.65	0.019	1.3	0.0121	0.0165
II	BV02	5	9.29	0.468	0.0065	0.84	0.0063	0.00868
II	BV04	5	9.39	0.468	0.0066	0.83	0.0063	0.00868
II	BV06	5	9.39	0.585	0.0071	0.9	0.0063	0.00868
II	BV08	9.5	5.23	0.475	0.017	1.1	0.0121	0.0165
II	BV10	9.5	5.24	0.475	0.017	1.2	0.0121	0.0165
II	BV14	9.5	5.28	0.618	0.017	1.1	0.0121	0.0165

The first observation that is apparent from this table is that γ seems to be nonlinear with respect to the drift angle β. The value of γ at $\beta = 5$ deg is slightly over a third of the value at $\beta = 9.5$ deg, and not the half that would be expected for a linear variation of circulation strength with drift angle. The results for Phase I and Phase II at $\beta = 9.5$ deg compare

fairly well, with the values of γ for Phase II being somewhat smaller and closer to the value predicted by Wald. It should also be noted that the "measured" values of γ at $\beta = 5$ deg compare more closely to the low-aspect-ratio wing theory value than the Wald value. It may be that even at these small angles, there is a difference that is picked up by the more-involved Wald theory. These values, along with the corresponding values from Liu and Fu (1994) are shown in Fig. 102. This figure illustrates the departure of the current results at $\beta = 9.5$ deg from the results of Liu and Fu and the low-aspect-ratio wing theory (which Liu and Fu's results follow to a drift angle of over 10 deg) but also demonstrates the consistency of the current results at $\beta = 9.5$ deg.

Note also in the preceding table the variation of the values of γ_{cv}, which are obtained by normalizing on the crossflow velocity component. If the circulation is proportional to the drift angle for small angles, then the normalization by $\sin \beta$ should remove the dependence on drift angle and the resulting dimensionless circulation should be approximately constant. The values for γ_{cv} in the table are close but not exactly the same, with $\gamma_{cv} \approx 0.85$ at $\beta = 5$ deg and $\gamma_{cv} \approx 1.2$ at $\beta = 9.5$ deg.

Phase	β (deg)	x/L	U (m/s)	$c_{z, exp}$	$c_{z, wing}$	$c_{z, Wald}$	$c_{z, int}$
I	9.5	0.47	14.9	0.13	0.0889	0.121	0.096
I	9.5	0.47	14.9	0.13	0.0889	0.121	-
I	9.5	0.47	7.64	0.13	0.0889	0.121	0.088
I	9.5	0.65	14.9	0.14	0.0889	0.121	0.090
II	5	0.468	9.29	0.026	0.0247	0.0336	0.032
II	5	0.468	9.39	0.025	0.0247	0.0336	-
II	5	0.585	9.39	0.027	0.0247	0.0336	x
II	9.5	0.475	5.23	0.12	0.0889	0.121	0.088
II	9.5	0.475	5.24	0.13	0.0889	0.121	-
II	9.5	0.618	5.28	0.12	0.0889	0.121	x

The results of computing the sectional vertical force coefficient from the vortex circulations estimated from the measured velocity fields are shown in the table above. As a reminder, the sectional side force coefficient is defined as follows:

$$c_z = \frac{F_z}{\frac{1}{2}\rho U^2 R}$$

where F_z is the vertical side force per unit length. In the table above, the value of c_z computed from the velocity field measurements is denoted by $c_{p, exp}$. The sectional side force coefficients computed using the low-aspect-ratio finite-wing

theory and Wald's calculations are denoted by $c_{z\,wing}$ and $c_{z\,Wald}$, respectively. These calculations are described in Section 4.4.2. It should be noted that for a given drift angle β these calculated values will not change. The values are repeated in the table merely for convenience. The last column contains the corresponding values of the sectional side force coefficient obtained by integrating the measured pressure distributions. These values are denoted by $c_{z\,int}$. Recall that these values were obtained by taking the difference in the pressure coefficient values with the sail on and the sail off and integrating that difference, so that each integration was actually the result of two separate runs. Therefore there is not a one-to-one correspondence between the test conditions for the coefficients computed from the circulations and the coefficients obtained from the pressure integrations. Hence in the table above, the values of $c_{p,\,int}$ are those that were obtained at the same nominal test conditions as the corresponding values of $c_{p,\,exp}$, and therefore are not repeated in the table, to emphasize this distinction. Recall also that because a number of pressure taps from the downstream tap ring had to be omitted in Phase II, no pressure integrations were computed at this location in Phase II. These conditions are denoted by an "x" in the table. Note finally that this table contains the results for both Phases I and II and therefore summarizes the results for all of the measurements.

This table demonstrates some interesting comparisons, to say the least. At the higher angle of drift ($\beta = 9.5$ deg), the values of $c_{z\,exp}$ agree closely to the values predicted by the results of Wald, as might have been expected, since the circulation values also agreed closely. The agreement is slightly better in the Phase II results. Note, however, that at $\beta = 9.5$ deg, the low-aspect-ratio finite wing predictions ($c_{z\,wing}$) agrees fairly well with the values obtained by integrating the pressure distributions. This agreement is consistent between the two phases. At the lower angle of drift ($\beta = 5$ deg), the values of $c_{z\,exp}$ agree closely to the values of $c_{z\,wing}$, again a result that might have been expected, since the circulation values also agreed relatively closely at $\beta = 5$ deg. Note in this case, however, the pressure integration values are in closer agreement with $c_{z\,Wald}$ than they are with $c_{z\,wing}$. Recall from earlier discussions that at $\beta = 9.5$ deg, the values of the circulation obtained from the measured velocity fields seemed to exceed the values measured by other investigators and the values obtained from the most common theory (the low-aspect-ratio finite-wing theory). These values led to values of $c_{z\,exp}$ that exceeded $c_{z\,wing}$. The agreement between $c_{z\,wing}$ and $c_{z\,int}$ at $\beta = 9.5$ deg would seem to confirm that the values of $c_{z\,exp}$ were being over-predicted. The reasons then for the almost complete reversal of the situation at $\beta = 5$ deg, where $c_{z\,exp}$ is in fairly good agreement with $c_{z\,wing}$ and $c_{z\,int}$ is in relatively close agreement with $c_{z\,Wald}$ are unknown. It is quite possible that in this case it is $c_{z\,int}$ that is most in error. The pressure distributions at the lower value of β were somewhat less well defined, and this combined with the large spacing between the pressure taps could have increased the error in the integration. Recall that because of the manner in which the vortex circulations were estimated from the velocity measurements, an uncertainty analysis was not performed for the circulation and subsequent force coefficient values. It may be that the error bars would account for the differences in the table above. However, the consistency of the results shown suggests that at least trends are being captured accurately, and perhaps the values themselves are closer to correct than might otherwise be expected.

6. CONCLUSIONS AND FUTURE WORK

6.1   Conclusions

The pressure distributions measured in these tests are consistent with the mechanism postulated by Feldman and others by which the tip vortex shed from the sail at angle of drift during a high speed turn causes an out-of-plane moment, in particular a pitching moment: the circulation associated with the vortex creates an equal and opposite circulation about the hull which results in a shift in the pressure distribution, increasing the pressure on the deck of the hull and decreasing the pressure on the keel. Since this net downward force acts primarily on the rear of the submarine, the net result is a nose-up pitching moment. The forces and moments measured in these tests were also in agreement with this theory.

The velocity field measurements demonstrated that the axial and tangential velocity components in the vortex core could reach very large values. The axial velocity component in some cases exceed the freestream value by 40%, and the maximum tangential velocity component was sometimes as large as the freestream velocity. The vortices generally aligned themselves with the freestream velocity direction, usually making an angle that was greater than the drift angle by 1 or 2 degrees.

Estimates of the circulation associated with the tip vortex were in general agreement with those measured by other investigators and with values predicted by finite wing and potential flow theory, although the values obtained from the measurements in these tests were consistently slightly higher than those obtained by other researchers. Estimates of the vertical force section coefficient obtained from the estimated circulation values were in general agreement with values obtained by integrating the measured pressure distributions. Both the vertical force section coefficients obtained from integrating the pressure distributions and the vertical force coefficients obtained by measuring the forces on the model exhibited the nonlinear variation with angle of drift predicted by the theories.

Over the range of Reynolds numbers at which tests were conducted in this investigation, the results showed very little dependence on Reynolds number. Doubling the Reynolds number had very little effect on either pressure distributions or velocity field measurements.

Boundary layer surveys conducted at 5 and 9.5 deg angles of drift indicated the presence of some streamwise vorticity in the boundary layer. However, there was no clear indication of crossflow separation and its associated vortical structures in the boundary layer measurements.

Between the two test phases, a trip ring was removed from the nose of the model. There were some differences

42

in the results between the two phases that were considered significant. Most of these changes were attributed to changes in the state of the boundary layer resulting from the removal of the trip ring.

6.2 Future work

The generation of the tip vortex during a non-coordinated turn, in which a velocity component perpendicular to the axis of the submarine exists, is unavoidable. The circulation associated with the vortex will cause the shift in pressures on the hull and lead to the uncommanded pitching moment. There seem to be only two methods of circumventing this problem.

The first method would be to introduce circulation of a sign opposite to that of the tip vortex. This could be done, for example, by using small fins located on the keel of the submarine. In their measurements of forces on a submarine model, Wetzel et al. (1993) and Wetzel and Simpson (1998) examined the effects of such fins on the flow past the submarine. However, they took the approach of determining which orientation of the fins would prevent crossflow separation on the keel of the model, and thus exacerbated the pitching moment situation. The figures in these two reports do in fact show an increase in pitching moment with angle of drift as they add the fins and change their orientation. In order to prevent the pitching moment from developing, or at least to reduce its magnitude, the fins need to be oriented in such a way that introduce vorticity of the opposite sign to that of the tip vortex, and thus in all likelihood hasten crossflow separation on the keel of the submarine. An investigation could be conducted into determining the fin orientation that reduces or eliminates the pitching moment.

The problem with using fins on the bottom of the submarine is that they would need to be retractable. The fins would not be needed when the submarine is moving in a straight line or turning at a slow rate. In these situations, the fins would only add to the drag (and probably the noise) of the submarine. Making the fins retractable introduces new problems that occur whenever the hull of the submarine has to be breached, and also introduces extra weight and space requirements in the form of the machinery that would be necessary to extend and retract the fins. Of the two, the space requirement is probably the greater evil on a submarine. The other method of dealing with the pitching moment problem avoids the problem of breaching the hull and adding equipment. This method is to develop a control law for the submarine such that the sail or bow planes are commanded to generate a nose-down pitching moment as the nose-up moment is created by the tip vortex. This would involve dynamic testing of a submarine model to determine at what rate the pitching moment develops as angle of drift changes. The model would have to be swept through a range of angle of drift beginning at $\beta = 0$, and either the forces or pressure distributions would have to be measured during the sweep. A similar study would have to be done to determine the response of the submarine to a bow- or sail-plane displacement. Once the behaviors of the pitching moments were known, a control law could be developed that would connect the two. If the time scales are small, this might involve the development of electronic or electro-mechanical control systems for the submarine. Larger time scales might allow the necessary control inputs to be entered by humans. The classified nature of submarine development limits the extent of speculation on how a submarine control system might be modified or developed.

44

References

Blanton, J. 1995 Uncertainty estimates of test section pressure and velocity in the Large Cavitation Channel. *AIAA Paper No. 95-3079, July 1995.*

Blanton, J. 1995 Laser Doppler velocimetry techniques in the Large Cavitation Channel. *Presented at the 24th American Towing Tank Conference, Texas A&M University, College Station, Texas, November 1995.*

Blanton, J. and Etter, R. 1995 Laser Doppler velocimetry on a body of revolution in the Large Cavitation Channel. *Presented at the 1995 ASME Fluids Engineering Division Summer Meeting: Symposium on Laser Anemometry, Hilton Head, South Carolina.*

Coleman, H. and Steele, W. 1989 Experimentation and uncertainty analysis for engineers. *New York: John Wiley & Sons, 1989.*

Coleman, H. and Steele, W. 1999 Experimentation and uncertainty analysis for engineers (2nd ed.). *New York: John Wiley & Sons, 1999.*

Coney, W. B. 1985 Circulation measurements about a body of revolution with an attached fin. *M. S. Thesis, Massachusetts Institute of Technology, June 1985.*

Chow, J., Zilliac, G., and Bradshaw, P. 1997 Mean and turbulence measurements in the near field of a wingtip vortex. *AIAA J., vol. 35, no. 10 (October 1997), pp. 1561-1567.*

Dacles-Mariani, J., Zilliac, G., Chow, J., and Bradshaw, P. 1995 Numerical/experimental study of a wingtip vortex in the near field. *AIAA J., vol. 33, no. 9 (September 1995), pp. 1561-1568.*

Etter, R. and Wilson, M. 1992 The large cavitation channel. *Presented at the 23rd American Towing Tank Conference, University of New Orleans, New Orleans, La., June 1992.*

Etter, R. and Wilson, M. 1993 Testing ship designs in a water tunnel. *Mechanical Engineering, October 1993, pp. 74-80.*

Feldman, J. P. 1995 Method of performing captive-model experiments to predict the stability and control characteristics of submarines. *Carderock Division, Naval Surface Warfare Center Report CRDKNSWC-HD-0393-25, June 1995.*

Groves, N., Huang, T., and Chang, M. 1989 Geometric characteristics of DARPA SUBOFF models. *David Taylor Research Center Report SHD-1298-01, March 1989.*

Gruner, W. P. and Payne, H. E., III 1992 Submarine maneuver control. *Proceedings of the United States Naval Institute, vol. 118, no. 7 (July 1992), pp. 56-60.*

Hoerner, S. F. 1971 Fluid-dynamic lift. *New Jersey: Hoerner Fluid Dynamics.*

Jones, R. T. 1946 Properties of low-aspect-ratio pointed wings at speeds below and above the speed of sound. *NACA Report No. 835.*

Jonnalagadda, R. 1996 Reynolds-averaged Navier-Stokes computation of forces and moments for appended SUBOFF configurations at incidence. *M. S. Thesis, Computational Engineering, Mississippi State University, May 1996.*

Jonnalagadda, R., Taylor, L., and Whitfield, D. 1997 Multiblock multigrid incompressible RANS computation of forces and moments on appended SUBOFF configurations at incidence. *AIAA Paper No. AIAA-97-0624.*

Liu, H., Beglin, G., and Fu, T. 1993 Implementation of PDV technology in the rotating arm facility. *David Taylor Model Basin Report CRDKNSWC/HD-1416-01, March 1993.*

Liu, H. and Fu, T. 1994 PDV measurement of vortical structures in the DTMB rotating arm facility. *Carderock Division, Naval Surface Warfare Center Report No. CRDKNSWC/HD-1416-02, September 1994.*

Pope, A. 1951 Basic wing and airfoil theory. *New York: McGraw-Hill.*

Roddy, R. F. 1990 Investigation of the stability and control characteristics of several configurations of the DARPA SUBOFF model (DTRC model 5470) from captive-model experiments. *David Taylor Research Center Report No. DTRC/SHD-1298-08, September 1990.*

Sarpkaya, T. 1998 Decay of wake vortices of large aircraft. *AIAA J., vol. 36, no. 9 (September 1998), pp. 1671-1679.*

Sung, C., Fu, T., Griffin, M., and Huang, T. 1996 Validation of incompressible flow computation of forces and moments on axisymmetric bodies undergoing constant radius turning. *Presented at the Twenty-First Symposium on Naval Hydrodynamics, Trondheim, Norway, 23-28 June 1996.*

Wald, Q. 1967 The hydrodynamic forces on fin-body combinations. *General Dynamics Electric Boat Division Report No. P-411-67-077, December 1967.*

Wetzel, T., Simpson, R., and Liapis, S. 1993 The effects of vortex generating fins and jets on the crossflow separation of a submarine in a turning maneuver. *Dept. of Aerospace and Ocean Engineering, Virginia Polytechnic Institute and State University Report No. VPI-AOE-195, May 1993.*

Wetzel, T. and Simpson, R. 1998 Effects of fin and jet vortex generators on the crossflow. *J. Aircraft, vol. 35, no. 3 (May-June 1998), pp. 370-379.*

Wright, J. E. 1995 Submarine design for the littorals. *Proceedings of the United States Naval Institute, vol. 121, no. 12 (Dec 1995), pp. 39-41.*

Zierke, W., ed. 1997 A physics-based means of computing the flow around a maneuvering underwater vehicle. *Pennsylvania State University Applied Research Laboratory Technical Report TR 97-0002, January 1997.*

This page intentionally left blank.
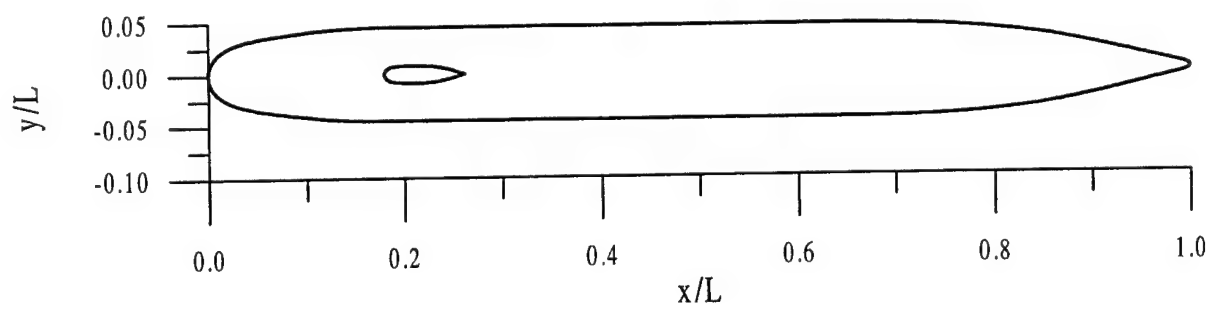
Figure 1 Submarine model hull geometry
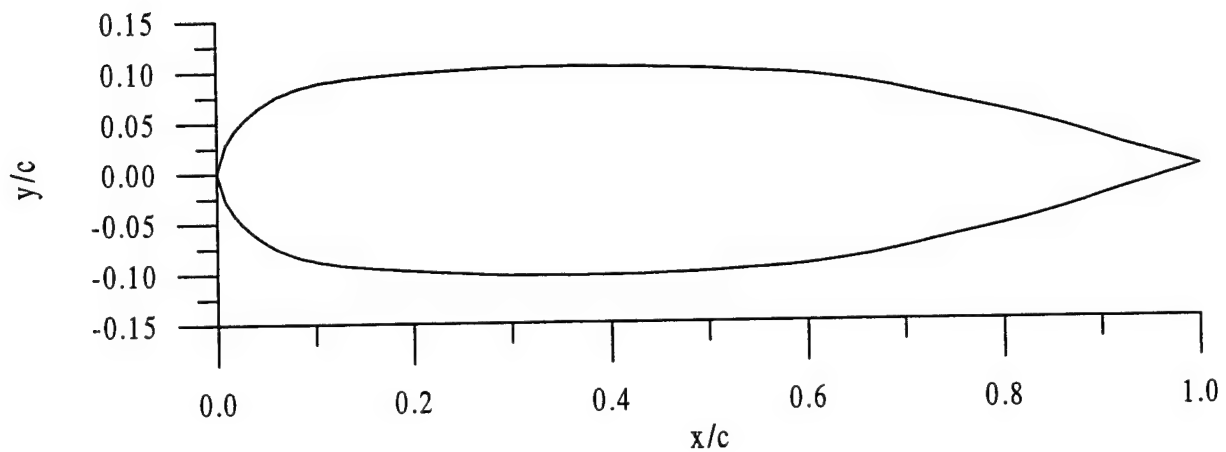
Figure 2 Sail foil section geometry

48
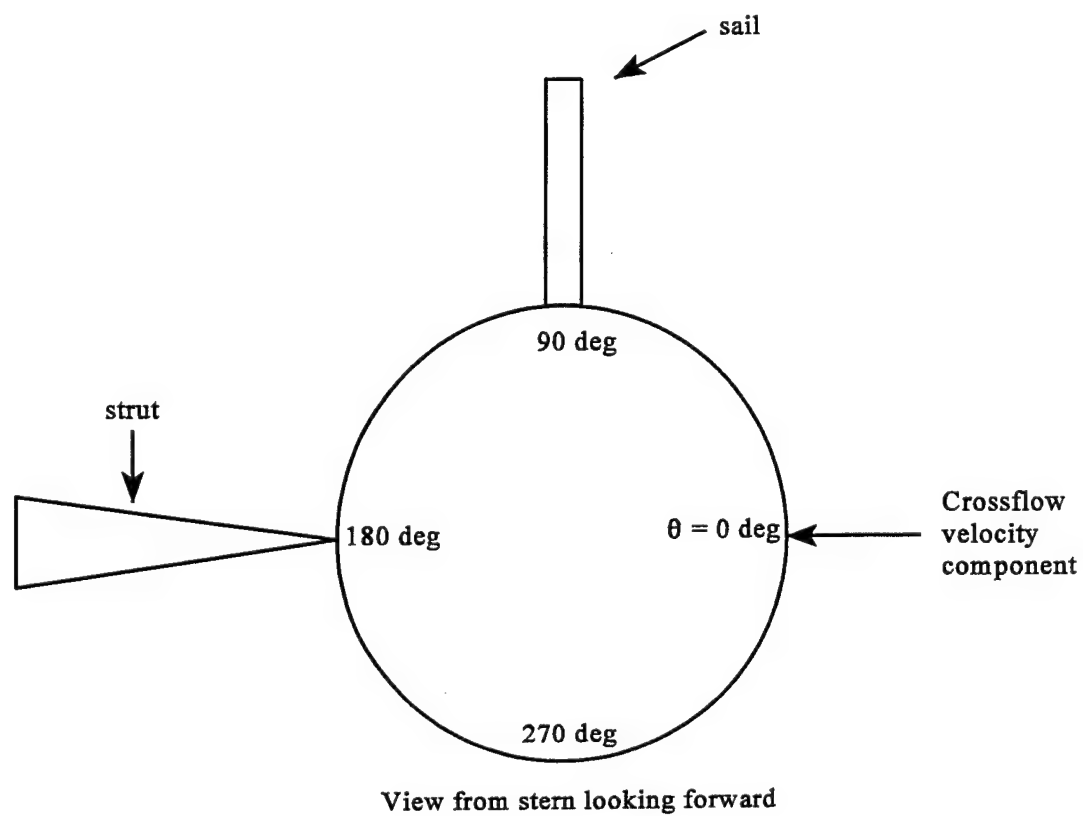
Figure 3 Coordinate system orientation diagram
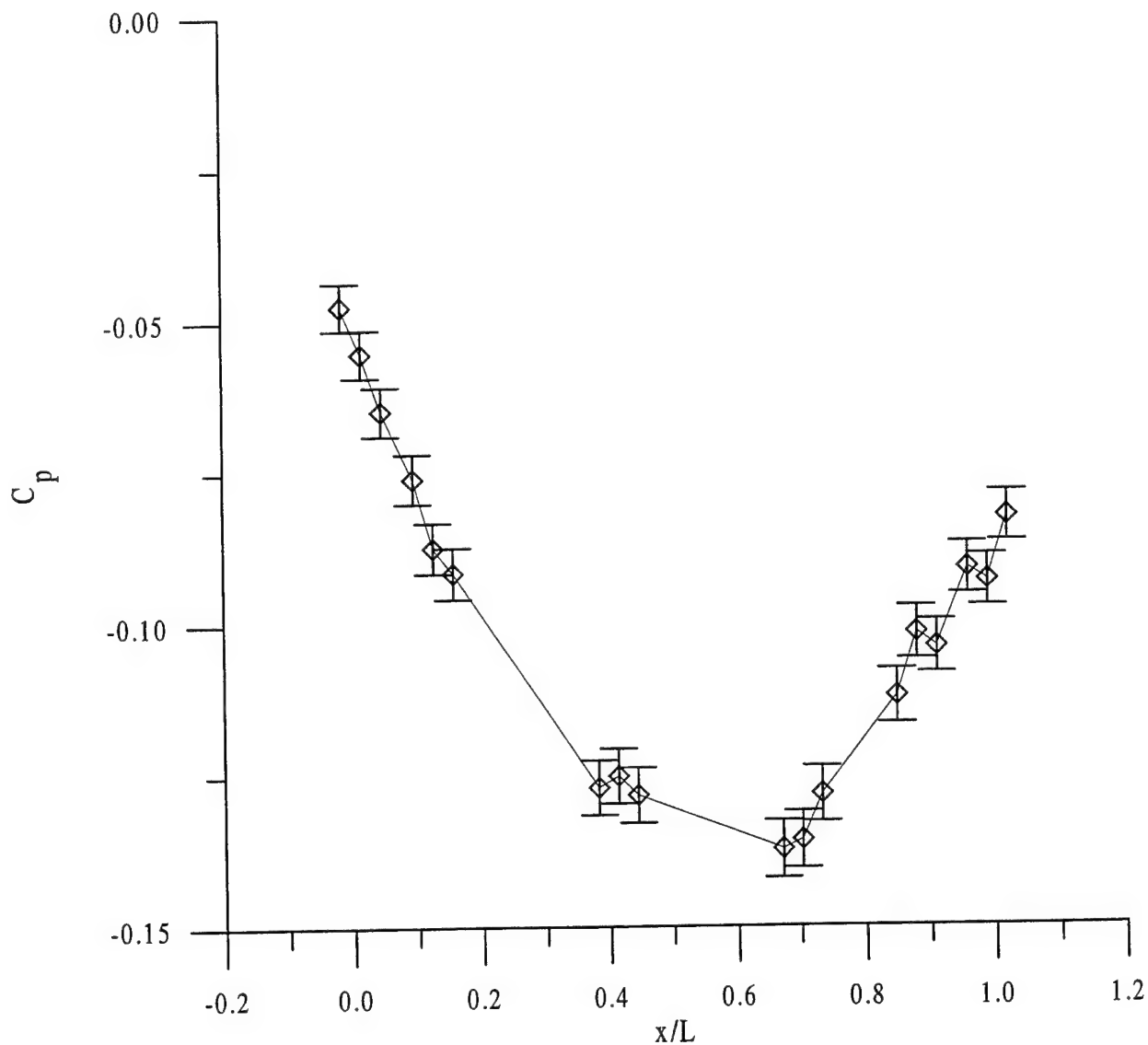
**Figure 4** Typical LCC wall pressure distribution: β = 9.5 deg, U = 14.9 m/s, sail on
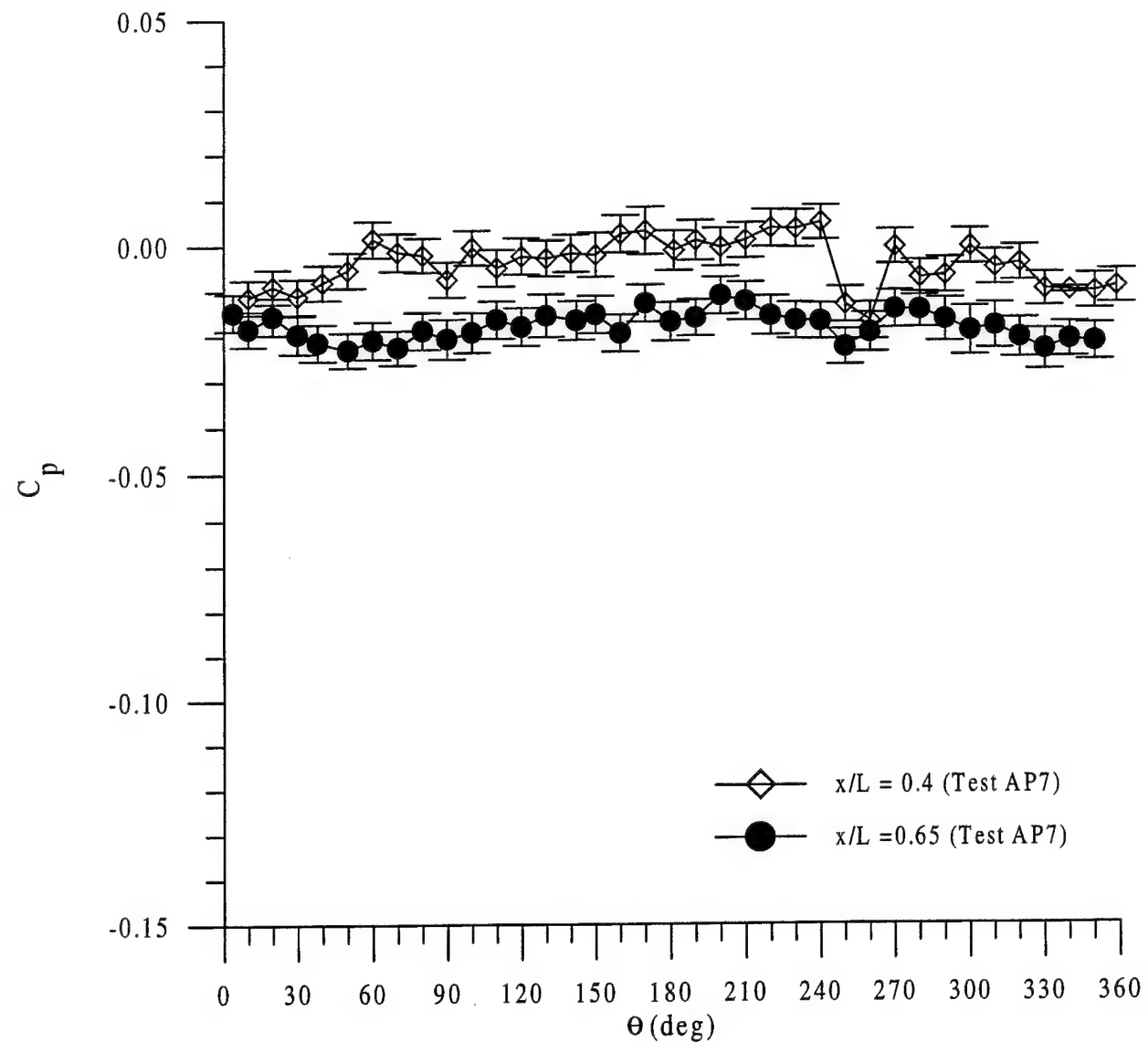
Figure 5 Circumferential pressure distribution: β = 0 deg, U = 14.9 m/s, sail off
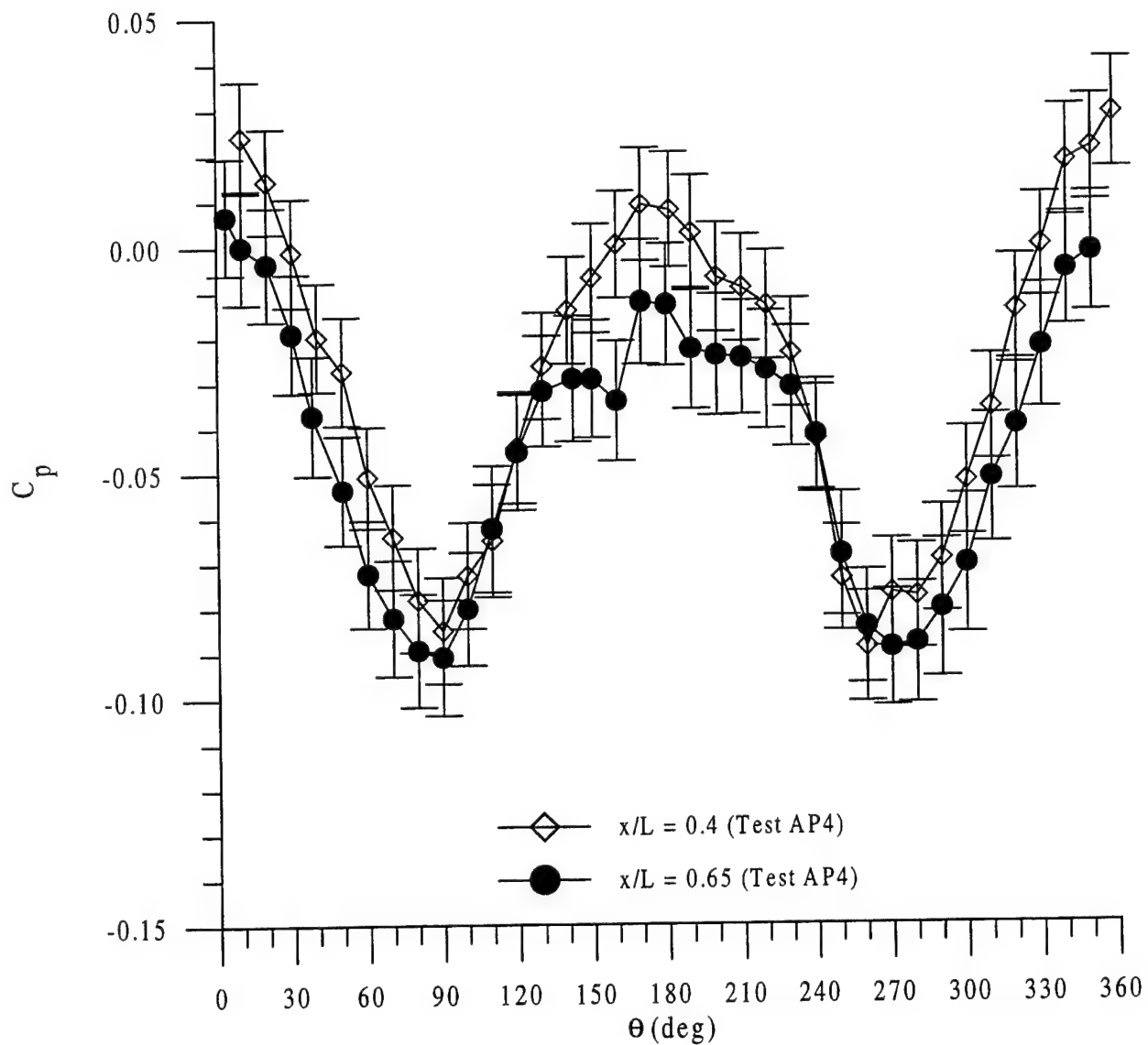
Figure 6 Circumferential pressure distributions: $\beta = 9.5$ deg, $U = 7.64$ m/s, sail off
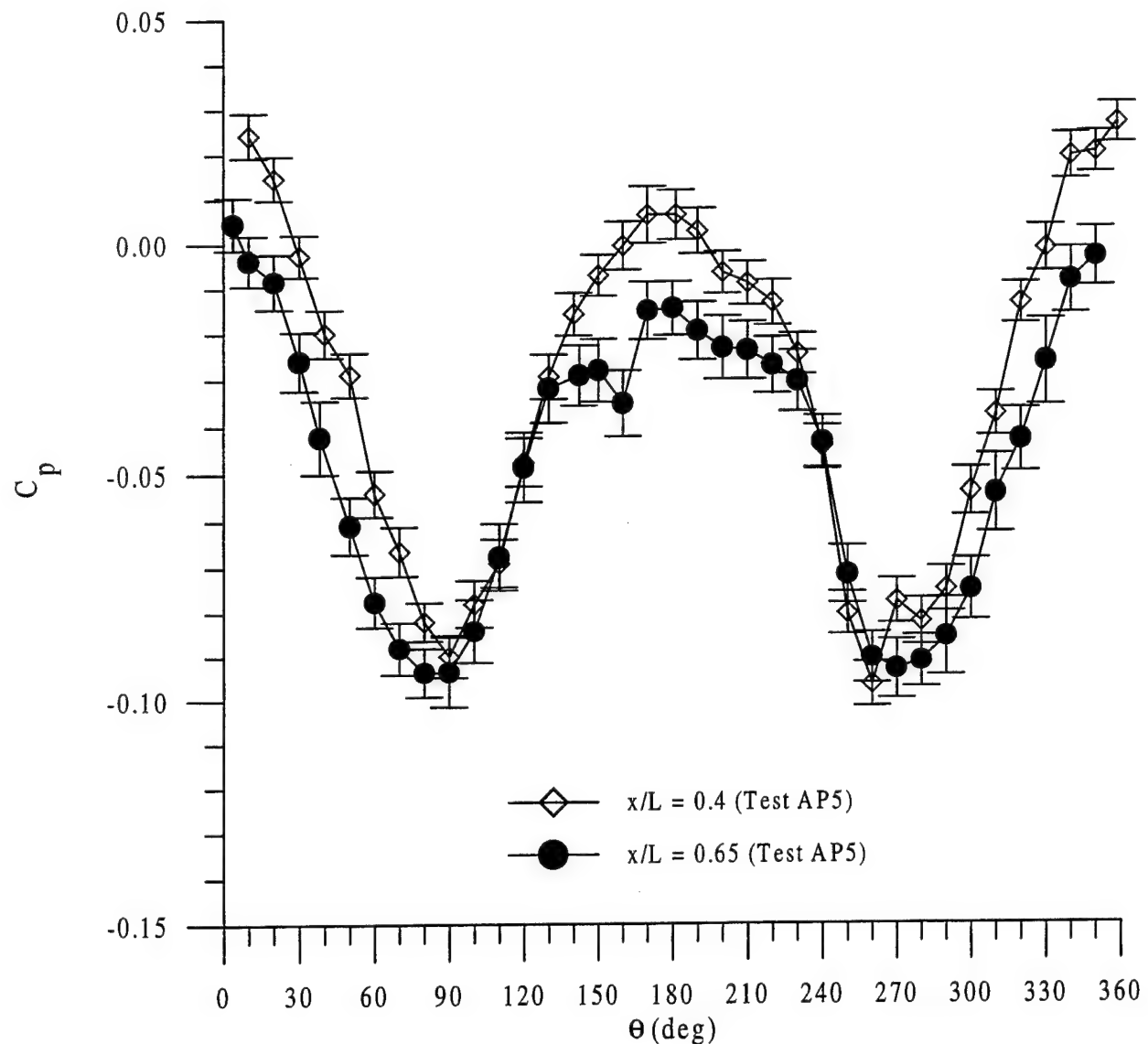
**Figure 7** Circumferential pressure distributions: $\beta = 9.5$ deg, $U = 14.8$ m/s, sail off
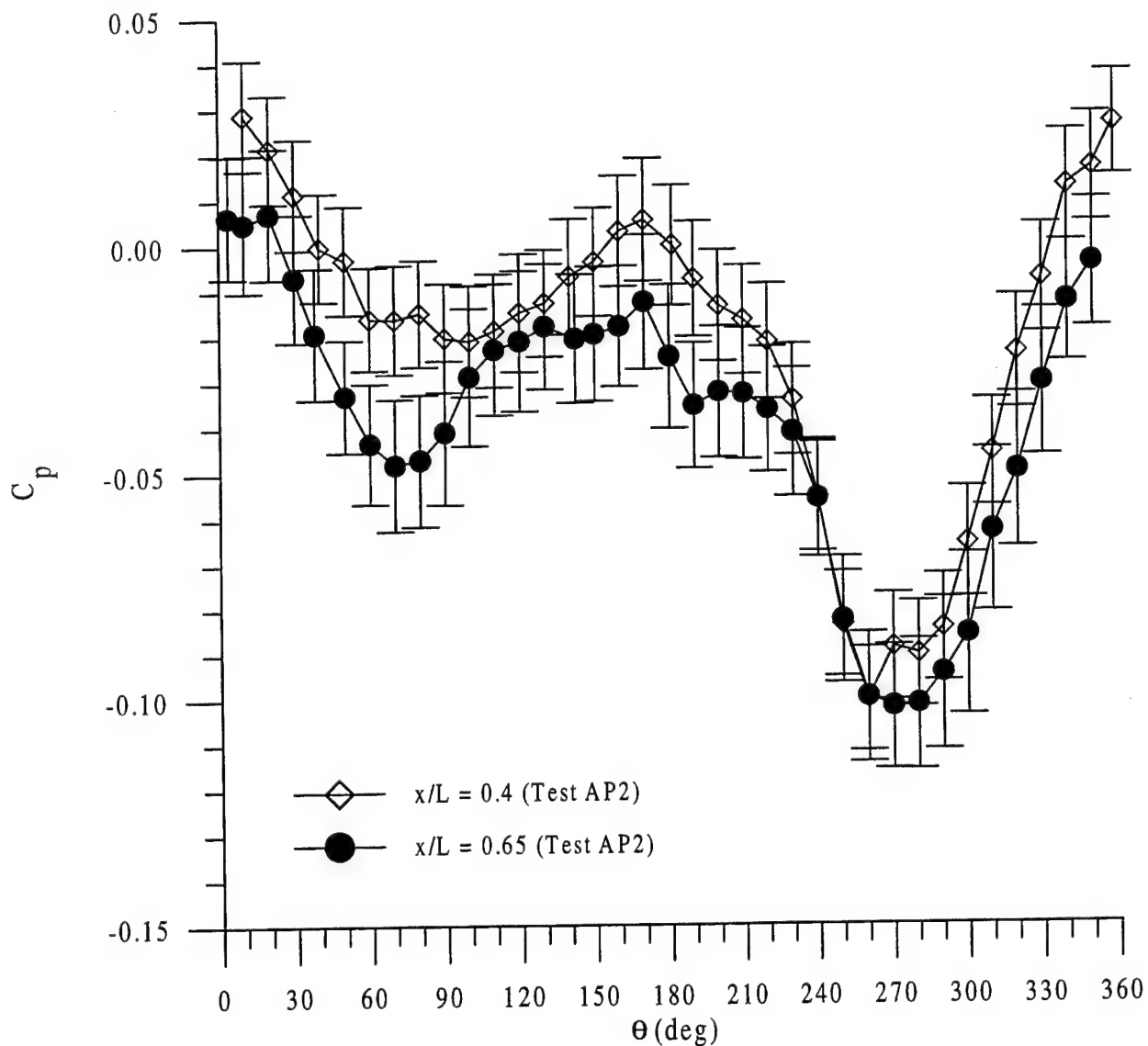
**Figure 8** Circumferential pressure distributions: $\beta = 9.5$ deg, $U = 7.64$ m/s, sail on
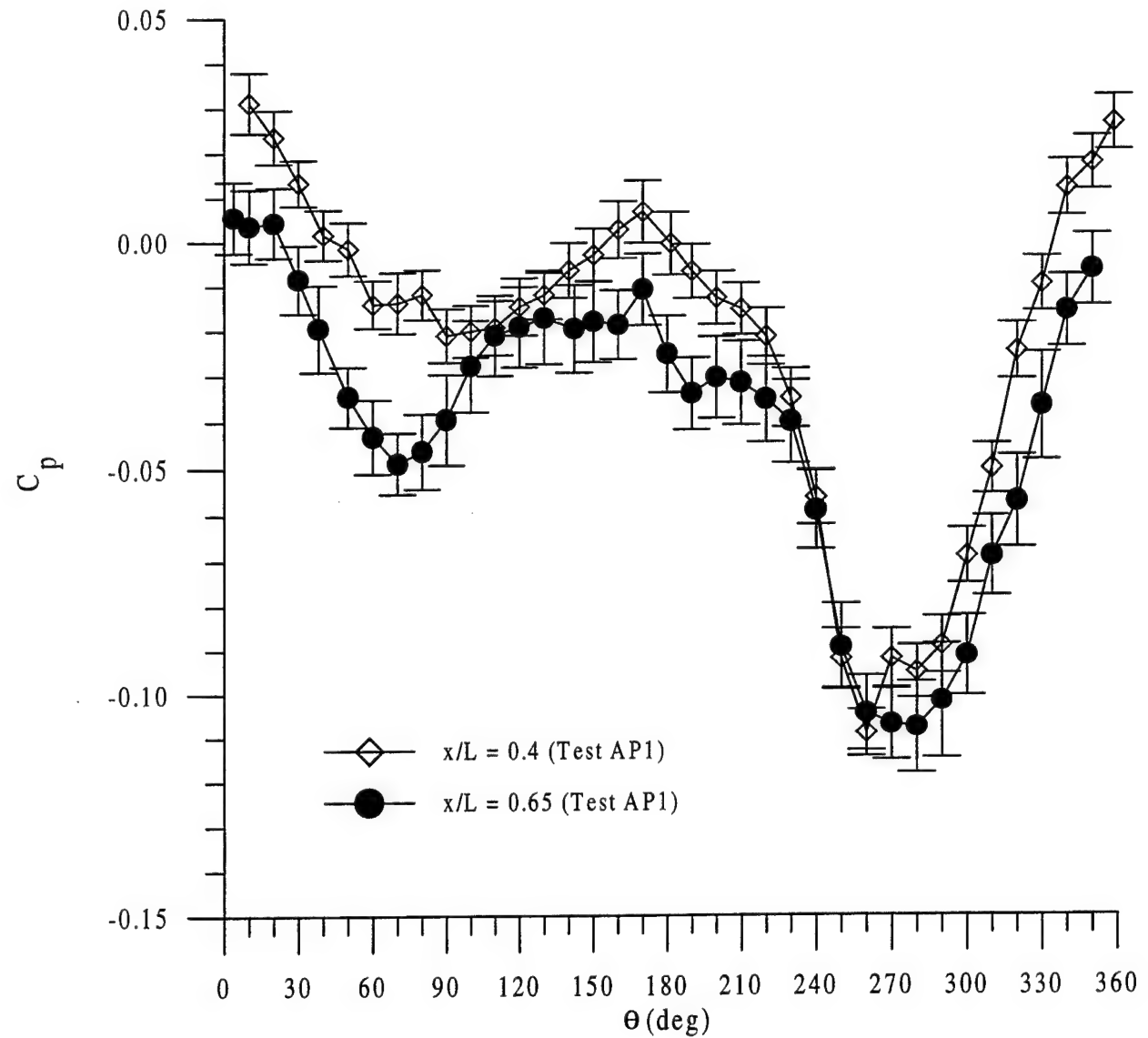
Figure 9 Circumferential pressure distributions: $\beta = 9.5$ deg, $U = 14.8$ m/s, sail on
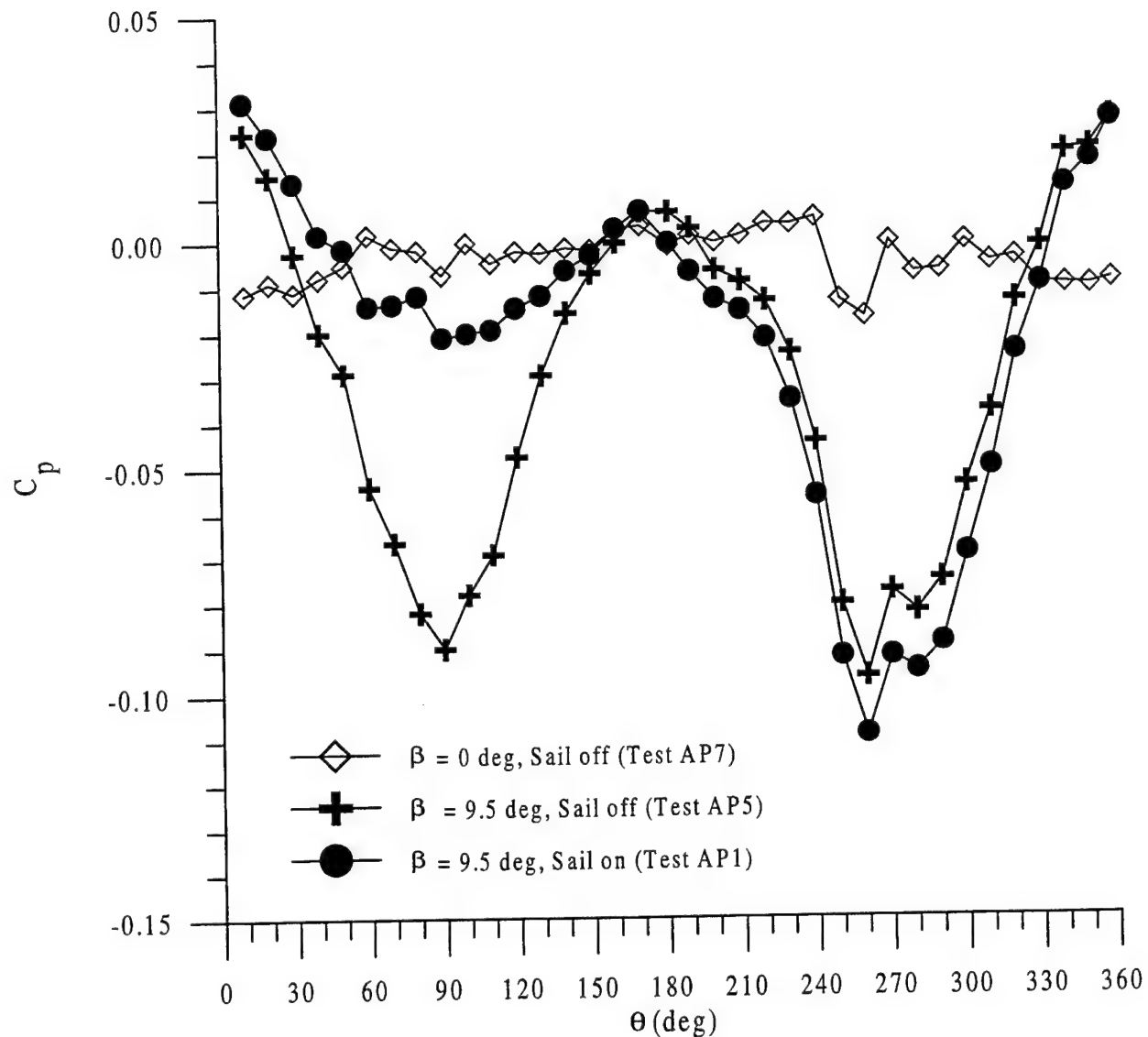
Figure 10 Demonstration of the effect on pressures of adding the sail: $x/L = 0.47$
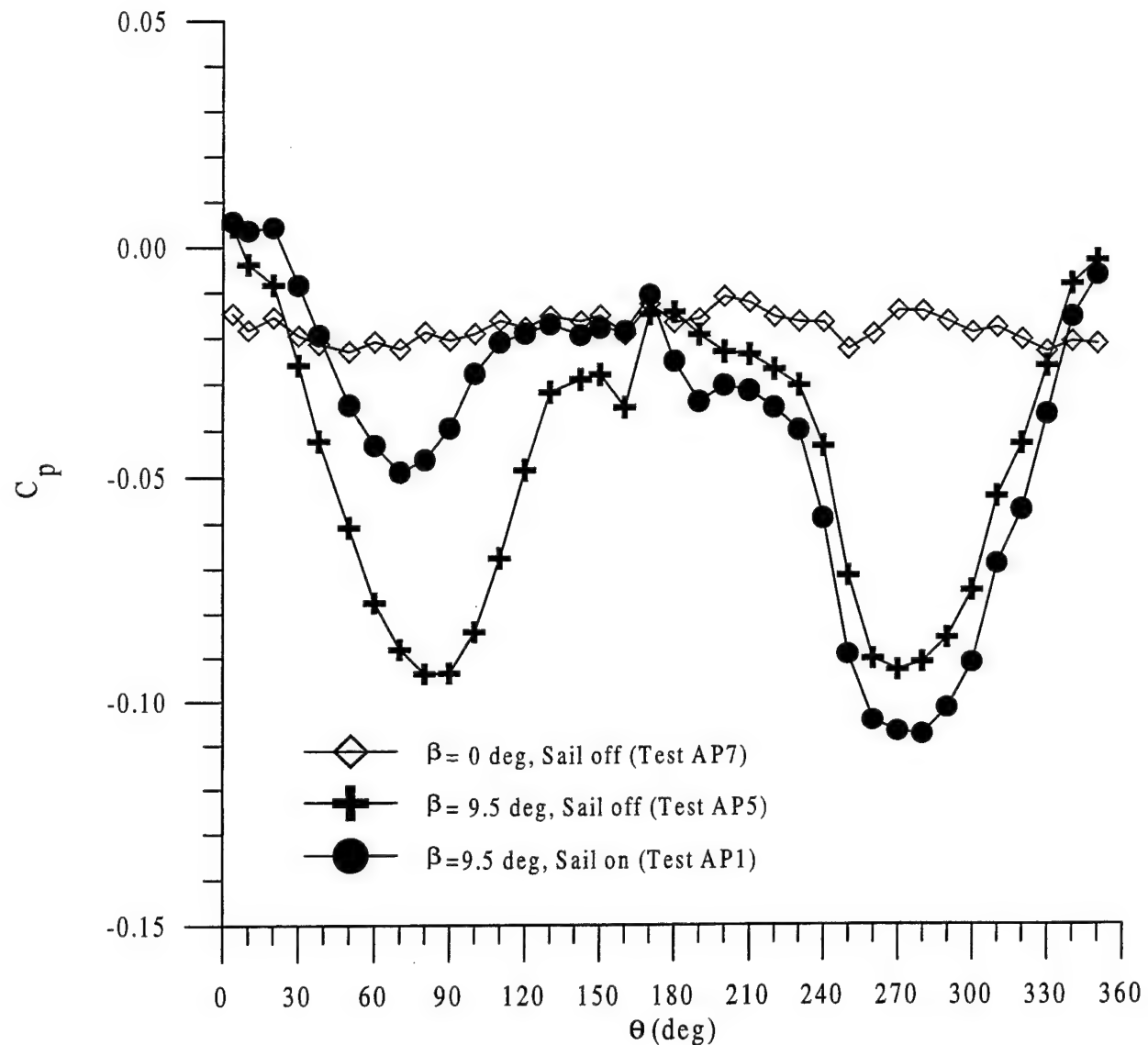
Figure 11 Demonstration of the effect on pressures of adding the sail: $x/L = 0.65$
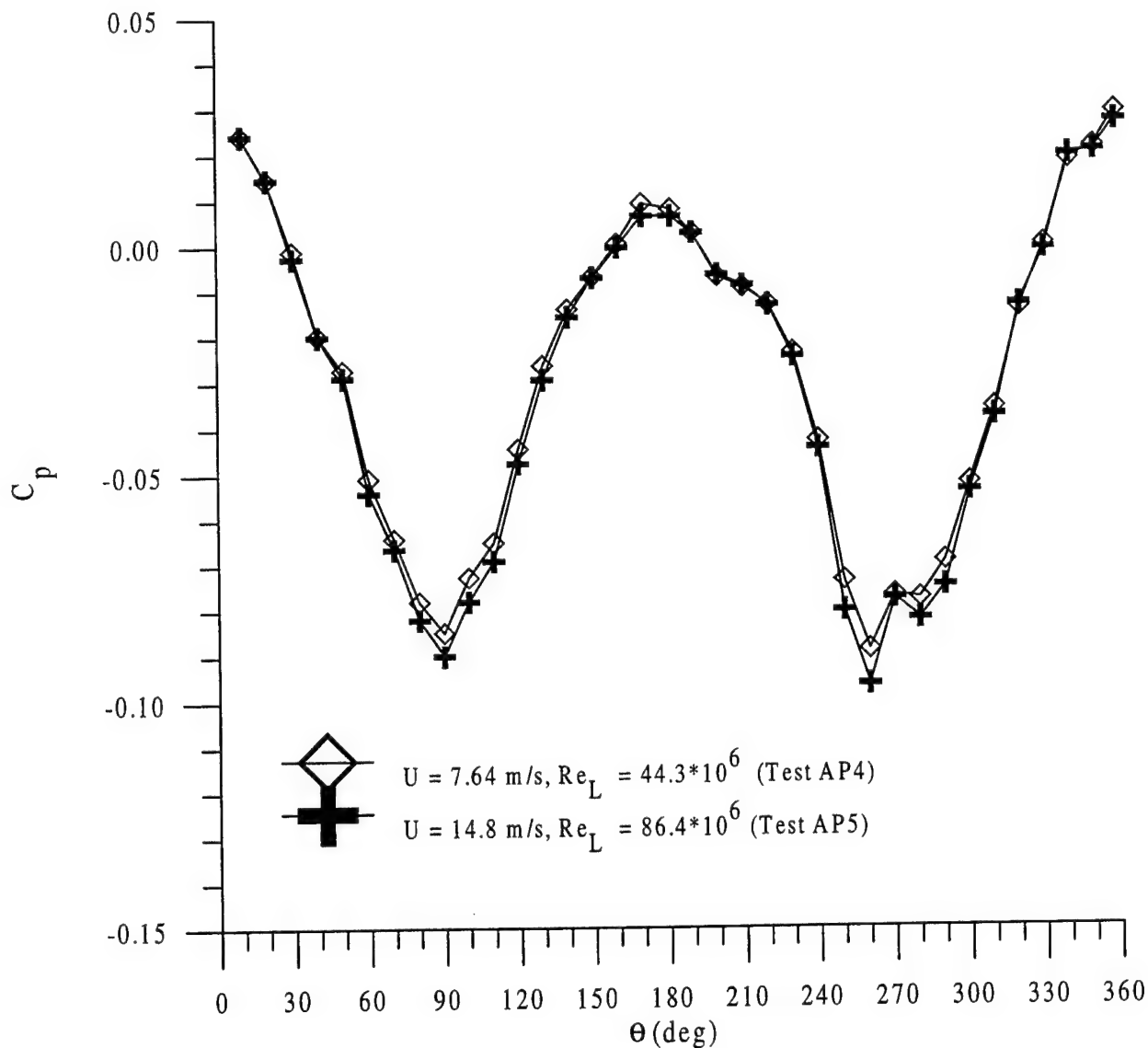
Figure 12 Reynolds number effects: β = 9.5 deg, sail off, *x/L* = 0.47
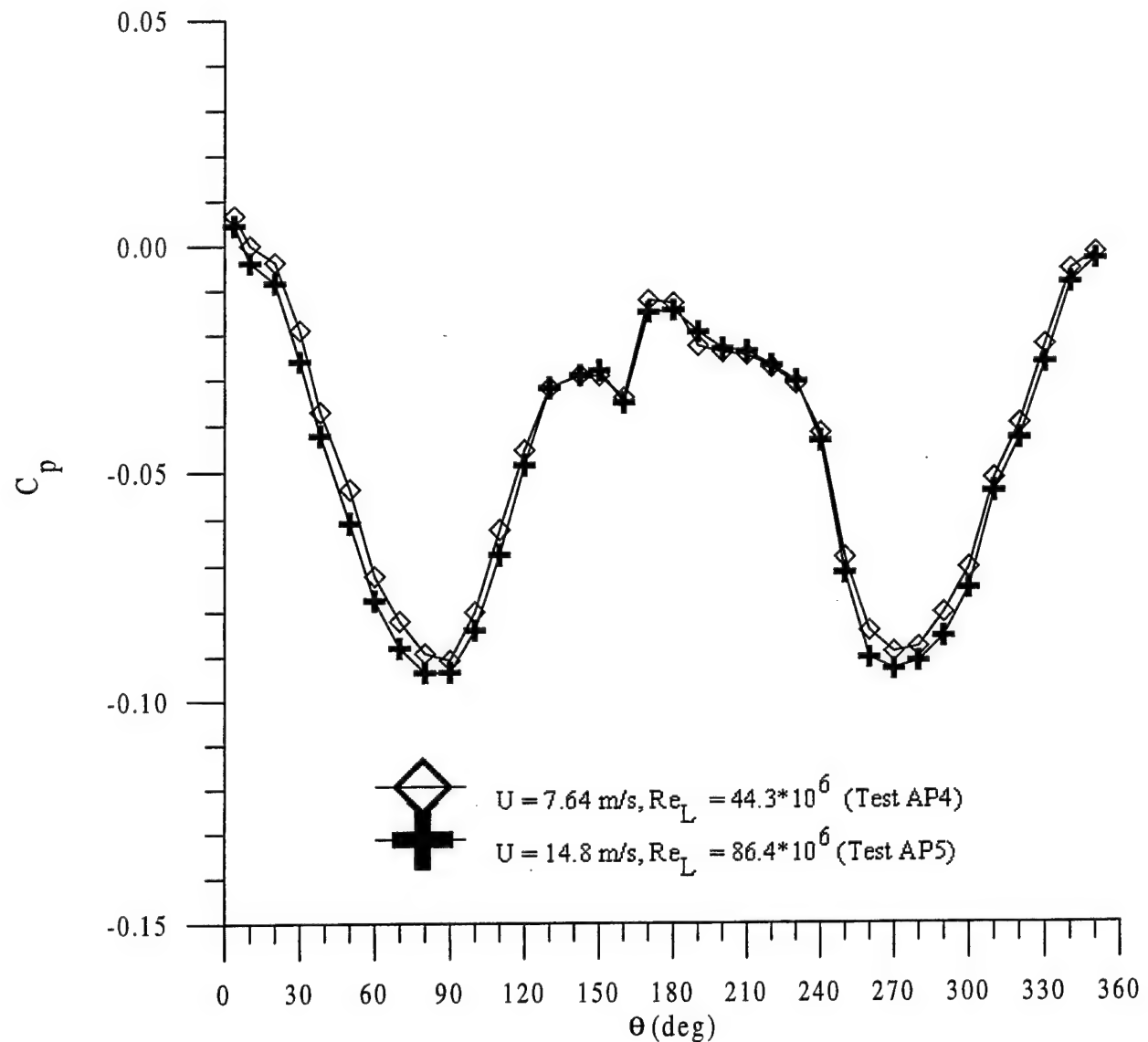
Figure 13 Reynolds number effects: $\beta = 9.5$ deg, sail off, $x/L = 0.65$
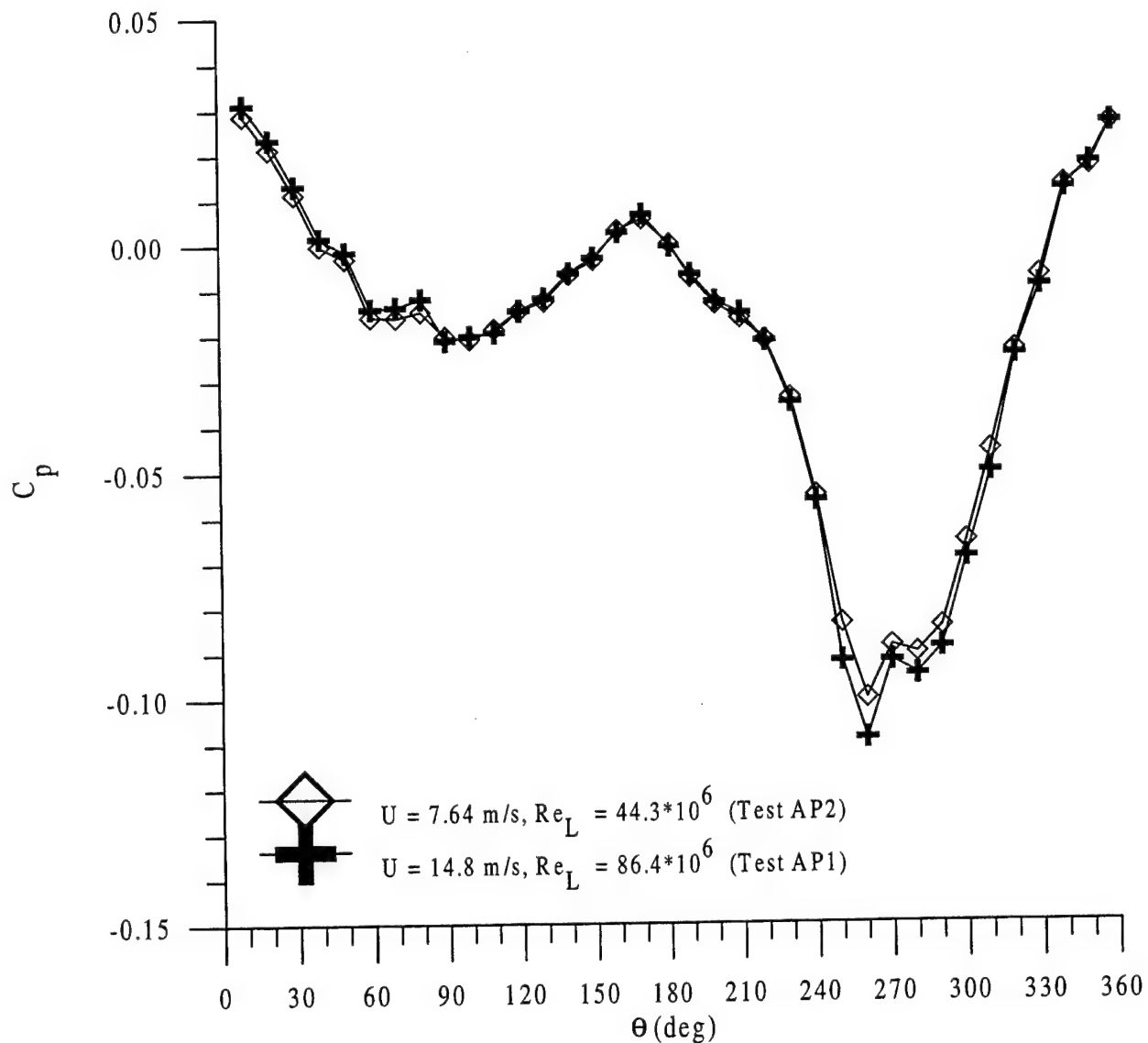
Figure 14 Reynolds number effects: $\beta = 9.5$ deg, sail on, $x/L = 0.47$
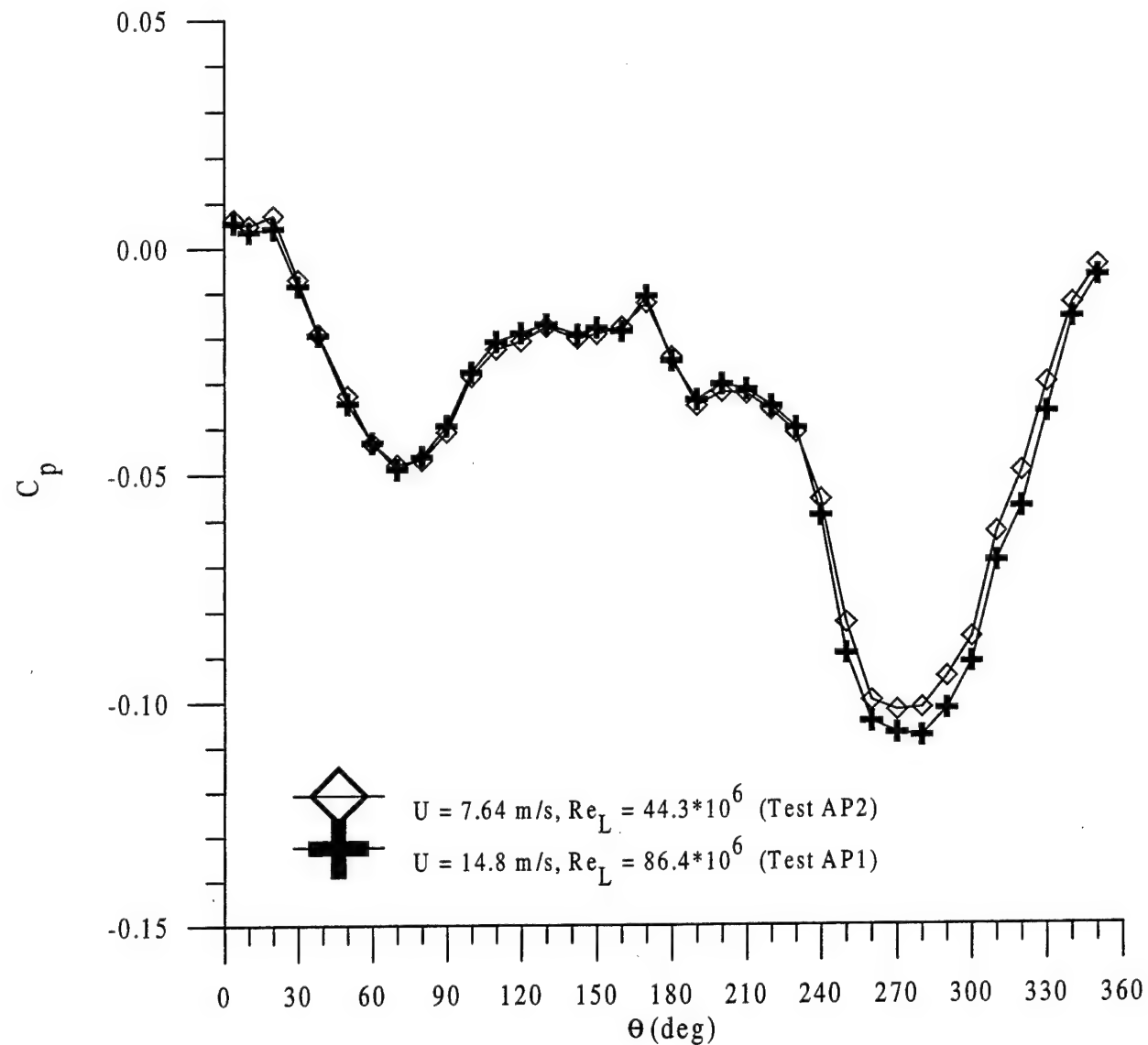
Figure 15 Reynolds number effects: $\beta = 9.5$ deg, sail on, $x/L = 0.65$
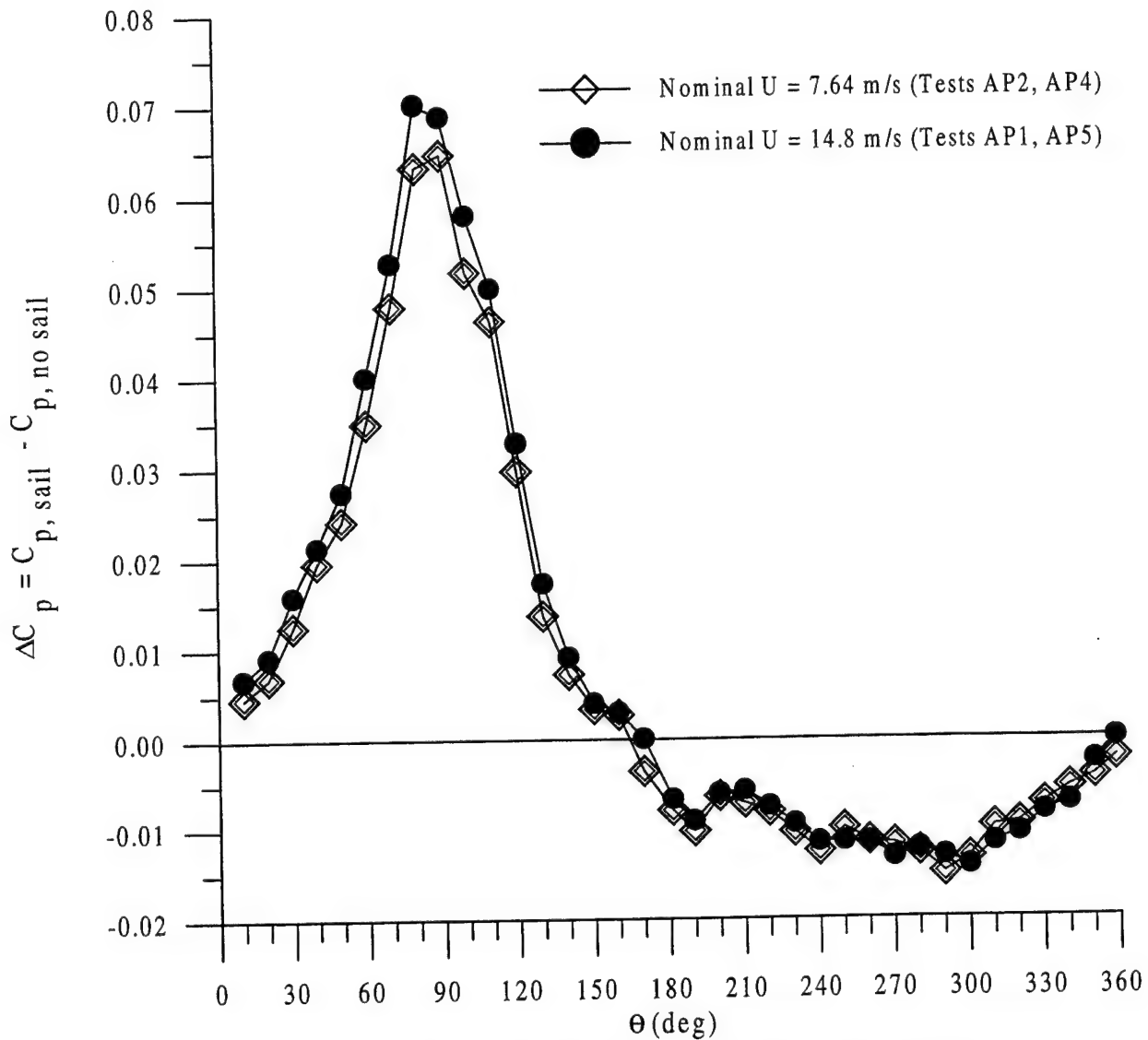
Figure 16 Pressure difference due to addition of sail: $\beta = 9.5$ deg, $x/L = 0.47$
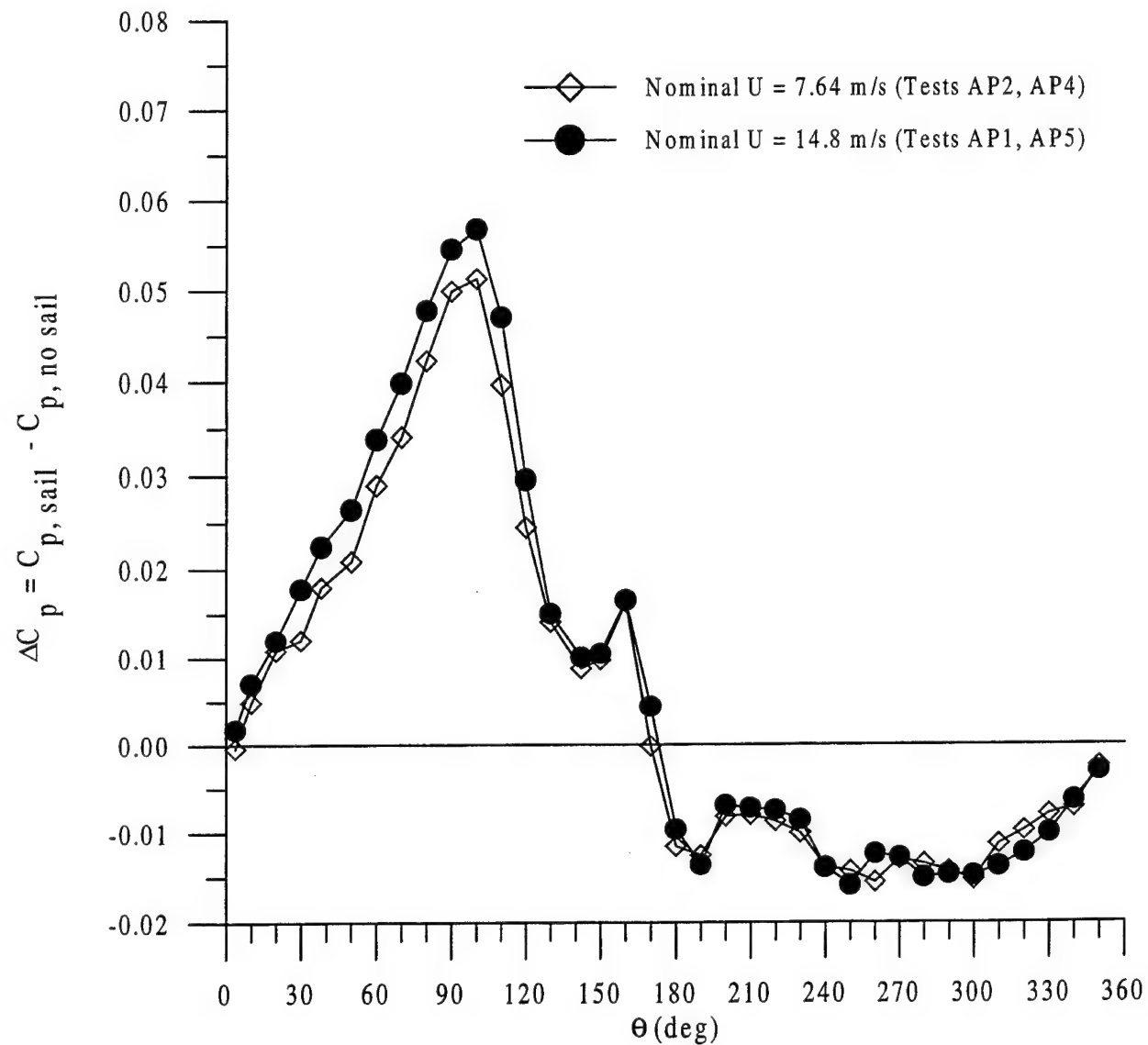
Figure 17 Pressure difference due to addition of sail: $\beta = 9.5$ deg, $x/L = 0.65$
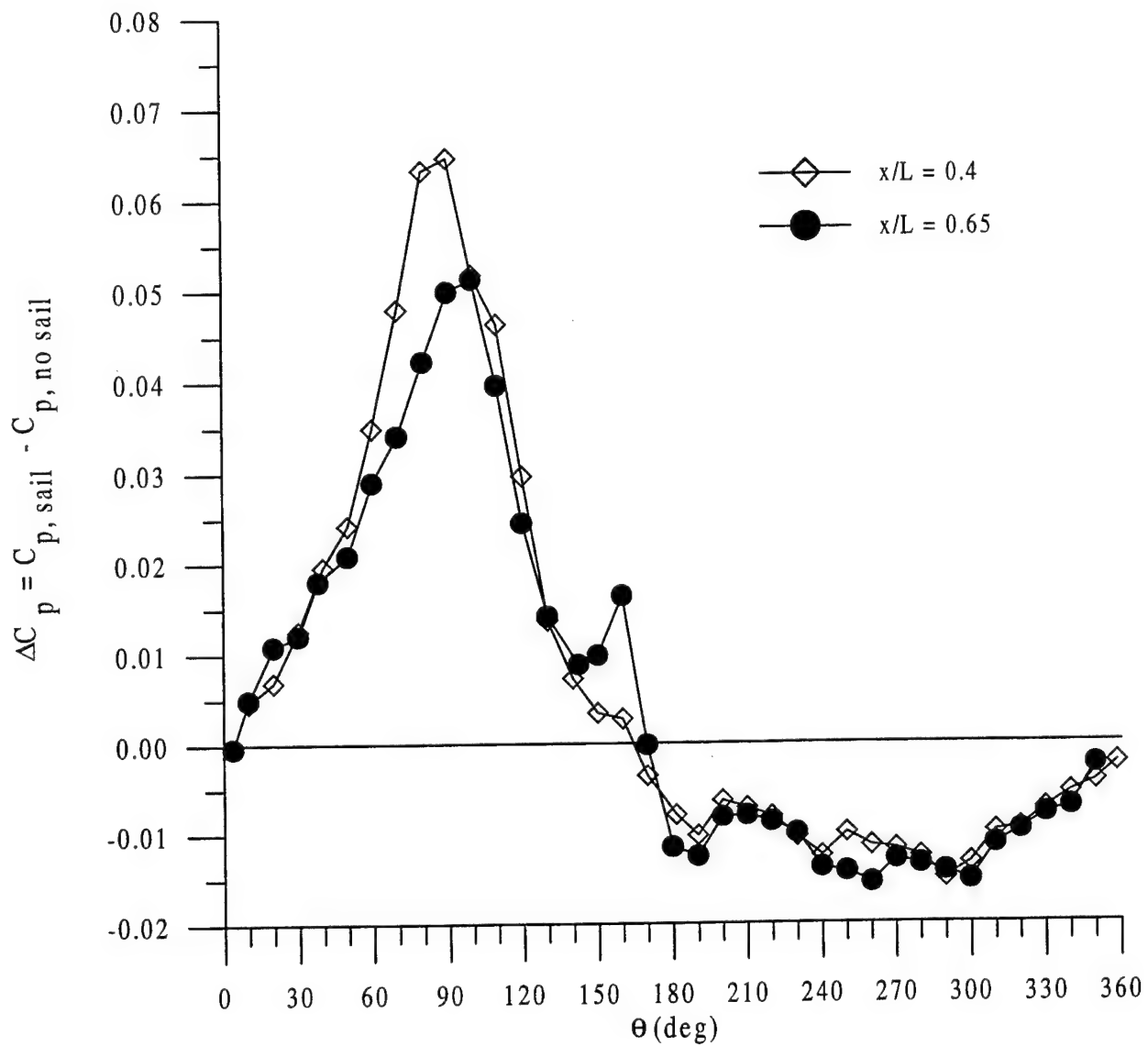
Figure 18 Comparison of sail addition effects on pressure differences: $\beta = 9.5$ deg
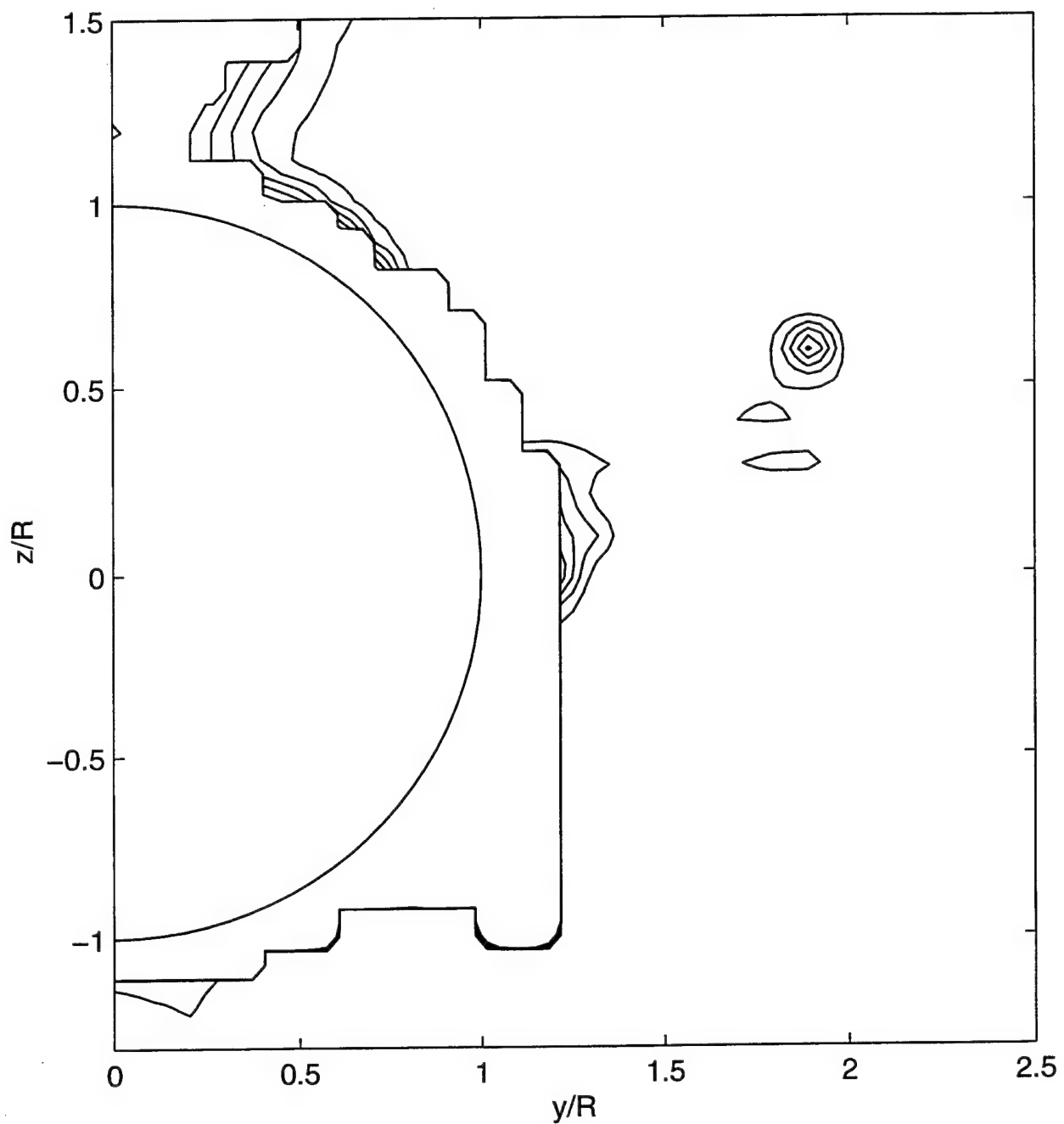
u_{max} = 17.1 m/s, F_V = 0.75, N_{cont} = 10

Figure 19 Streamwise velocity contours: β = 9.5 deg, U = 14.8 m/s, sail on, x/L = 0.47 (Test AV01)
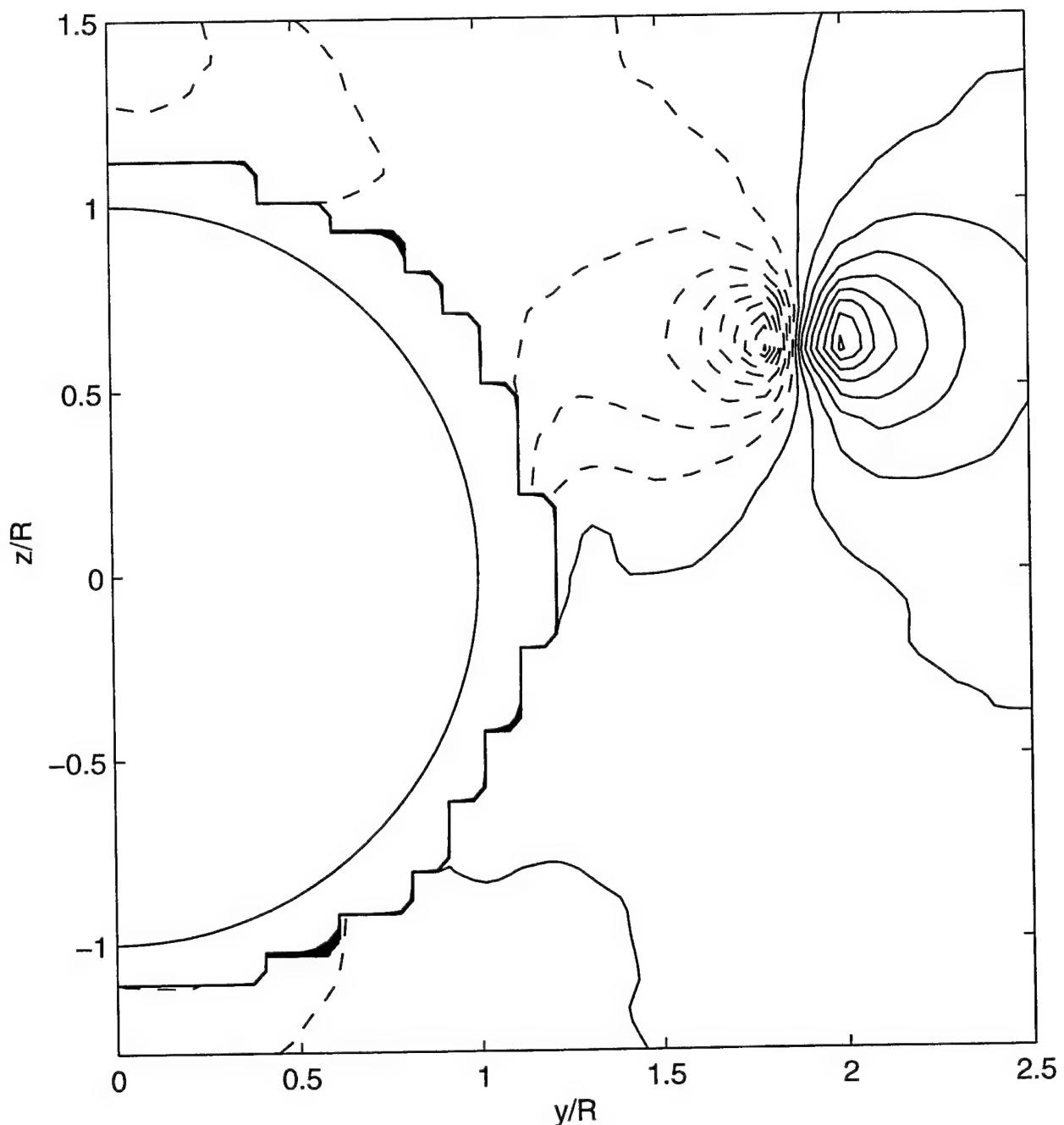
$w_{max} = 7.53$ m/s, $F_V = 0.0$, $N_{cont} = 10$

Figure 20 Transverse velocity contours: $\beta = 9.5$ deg, $U = 14.9$ m/s, sail on, $x/L = 0.47$ (Test AV04)
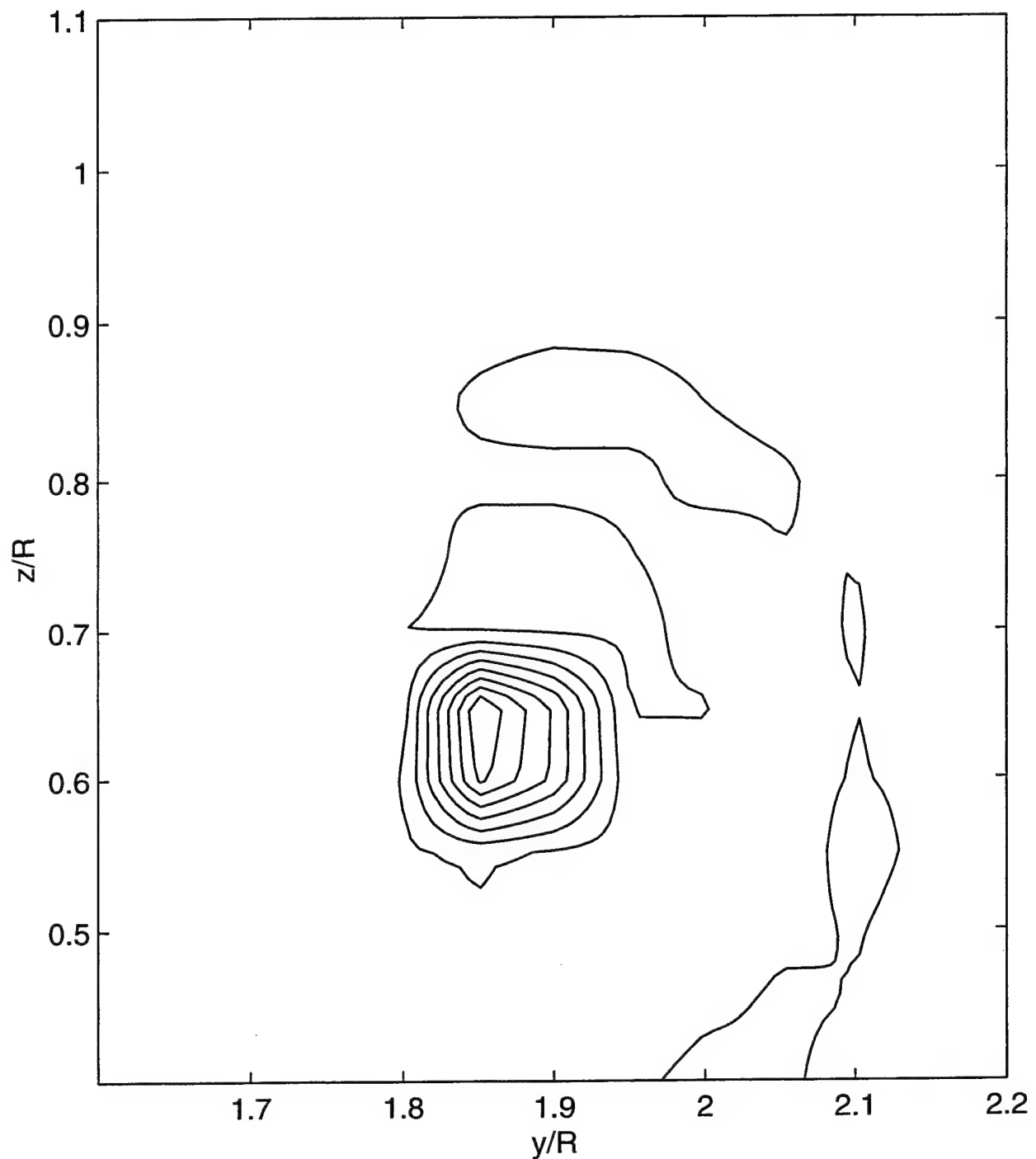
$u_{max} = 17.6$ m/s, $F_V = 0.8$, $N_{cont} = 10$

Figure 21 Streamwise velocity contours (detailed grid): $\beta = 9.5$ deg, $U = 14.9$ m/s, sail on, $x/L = 0.47$ (Test AV06)
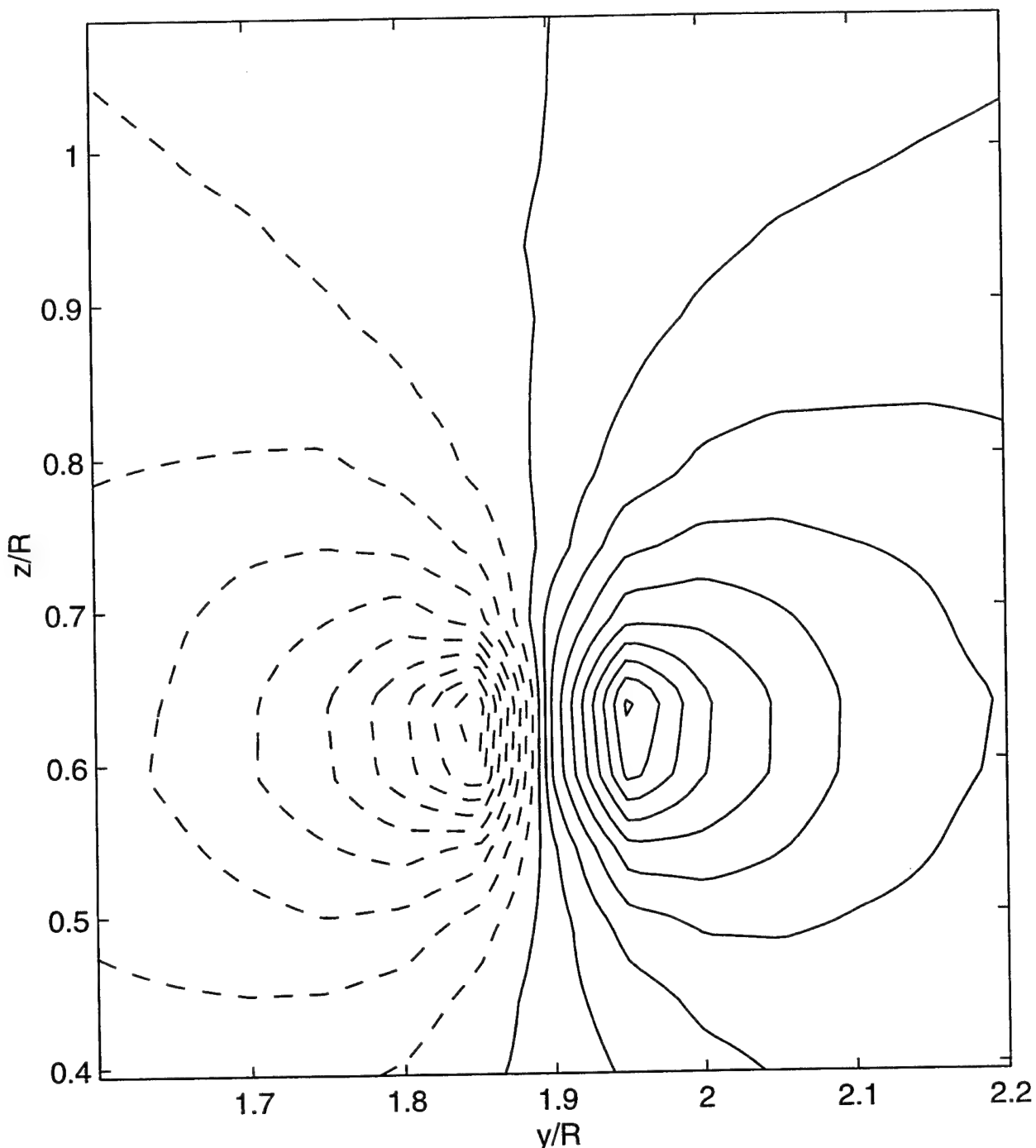
$w_{max} = 11.25$ m/s, $F_v = 0$, $N_{cont} = 10$

Figure 22 Transverse velocity contours (detailed grid): $\beta = 9.5$ deg, $U = 14.9$ m/s, sail on, $x/L = 0.47$ (Test AV05)
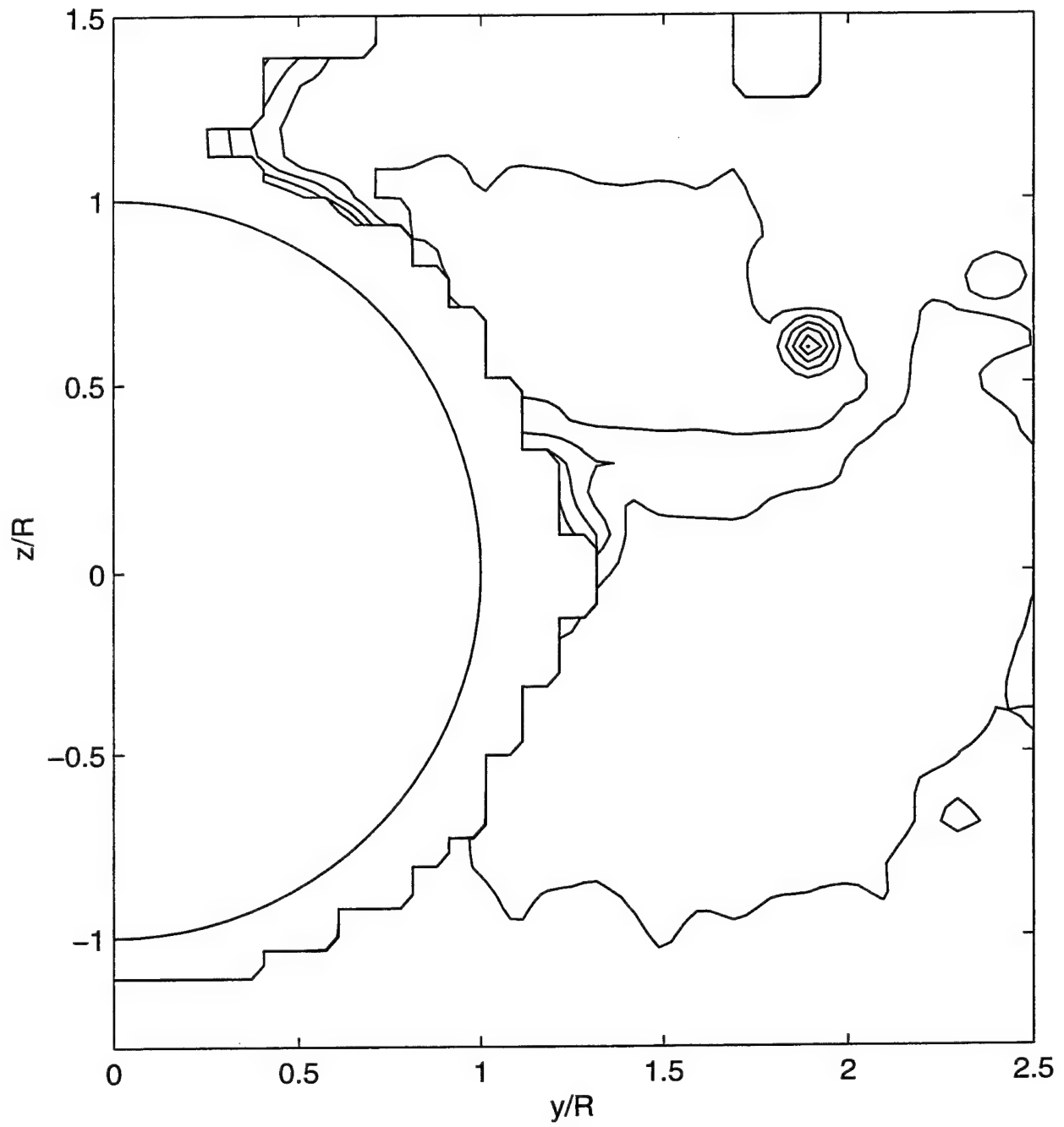
$u_{max} = 9.00$ m/s, $F_v = 0.75$, $N_{cont} = 10$

Figure 23 Streamwise velocity contours: $\beta = 9.5$ deg, $U = 7.64$ m/s, sail on, $x/L = 0.47$ (Test AV02)

$w_{max} = 3.84$ m/s, $F_V = 0$, $N_{cont} = 10$
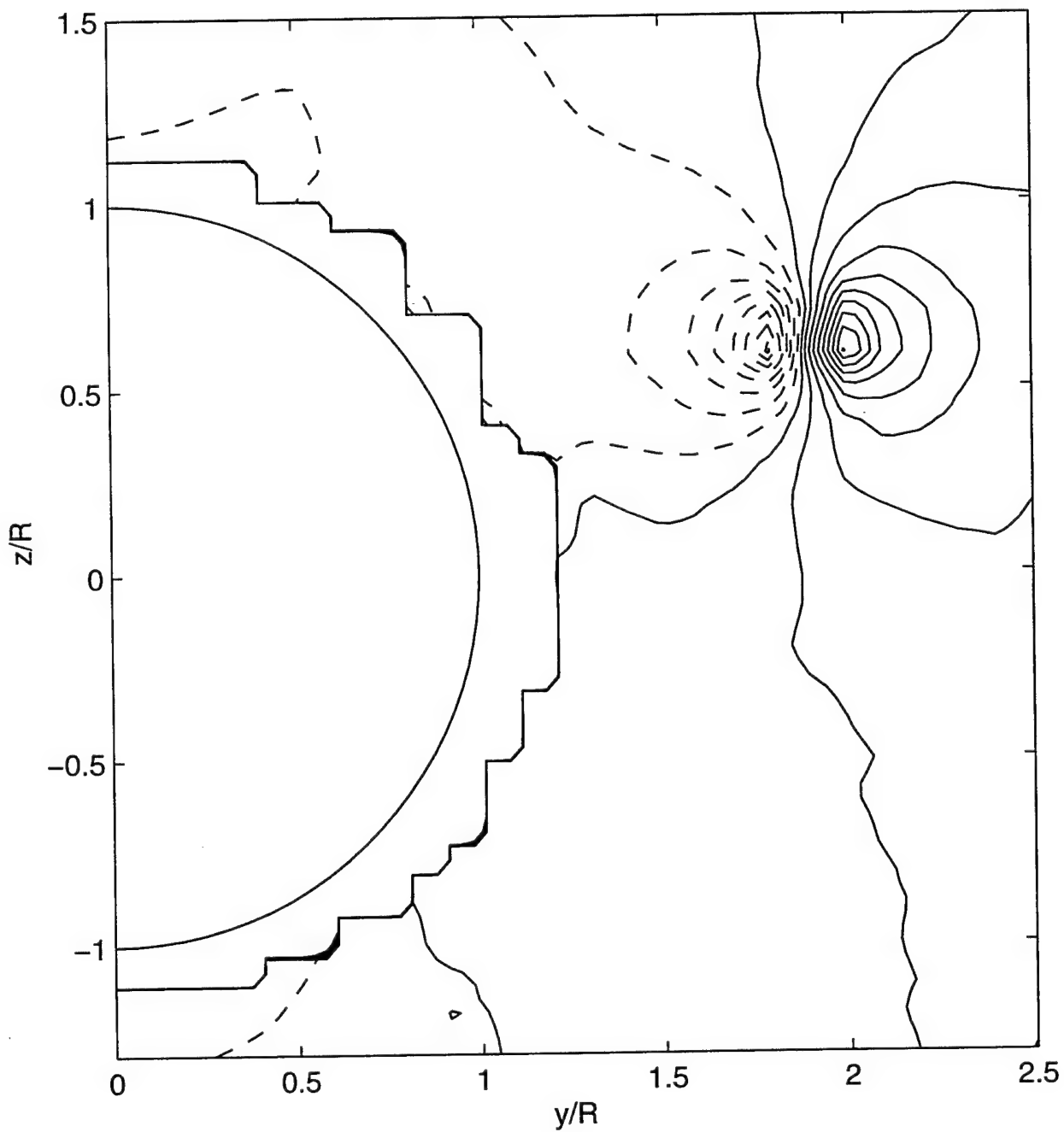
Figure 24 Transverse velocity components: $\beta = 9.5$ deg, $U = 7.64$ m/s, sail on, $x/L = 0.47$ (Test AV03)
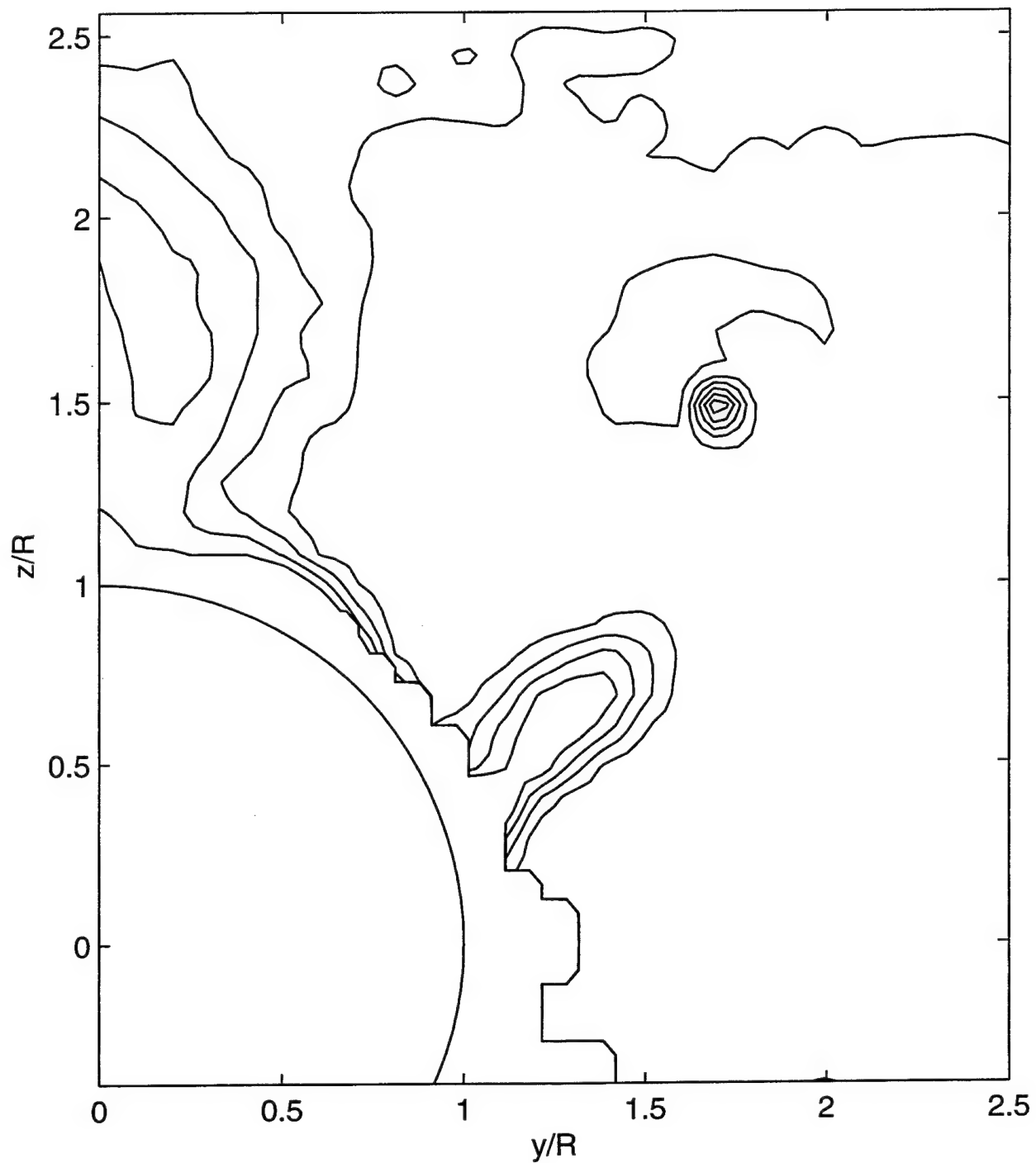
$u_{max} = 17.3$ m/s, $F_V = 0.8$, $N_{cont} = 10$

Figure 25 Streamwise velocity contours: $\beta = 9.5$ deg, $U = 14.9$ m/s, sail on, $x/L = 0.65$ (Test AV07)
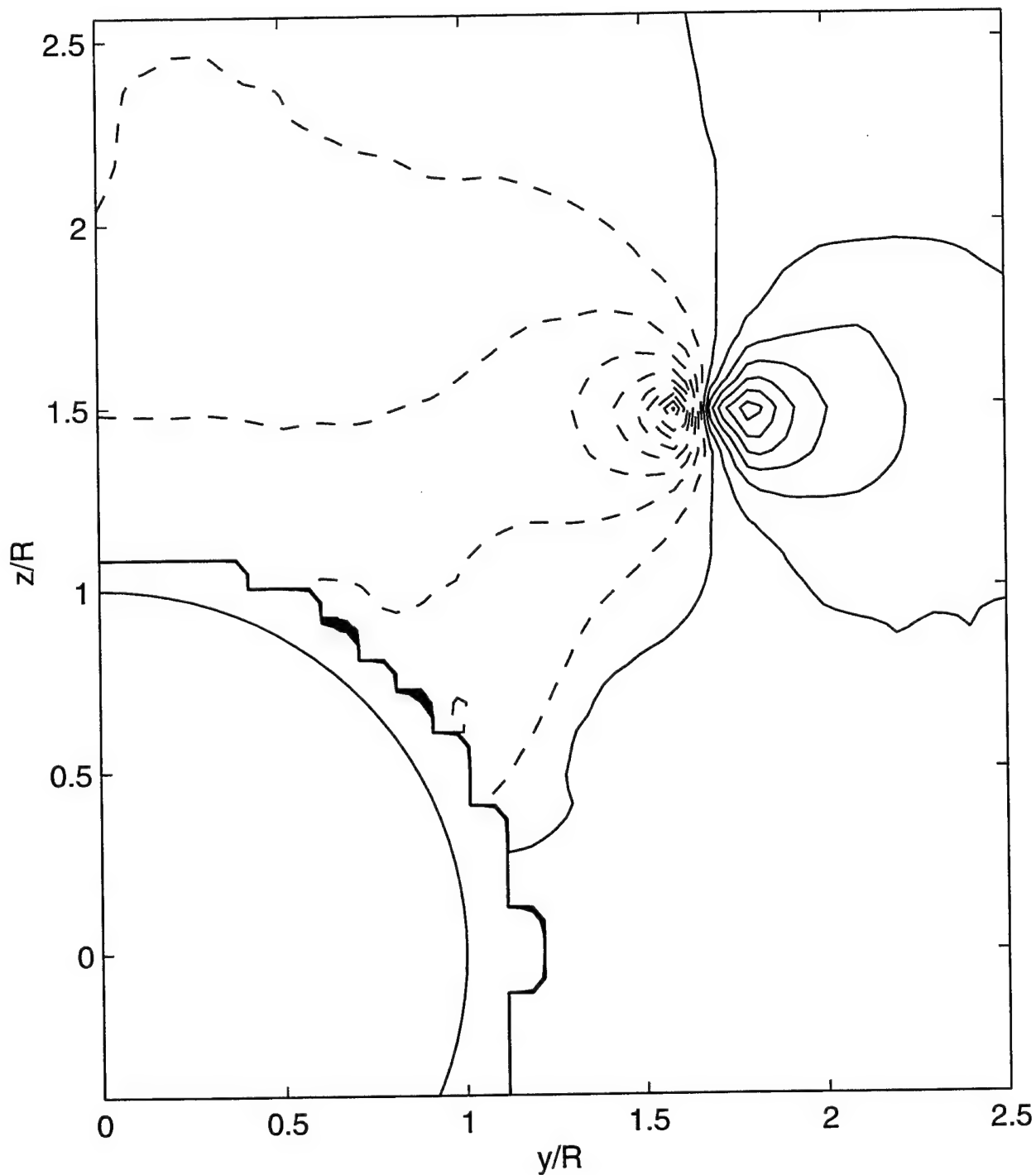
$w_{max} = 9.35$ m/s, $F_V = 0$, $N_{cont} = 10$

Figure 26 Transverse velocity contours: $\beta = 9.5$ deg, $U = 14.9$ m/s, sail on, $x/L = 0.65$ (Test AV08)
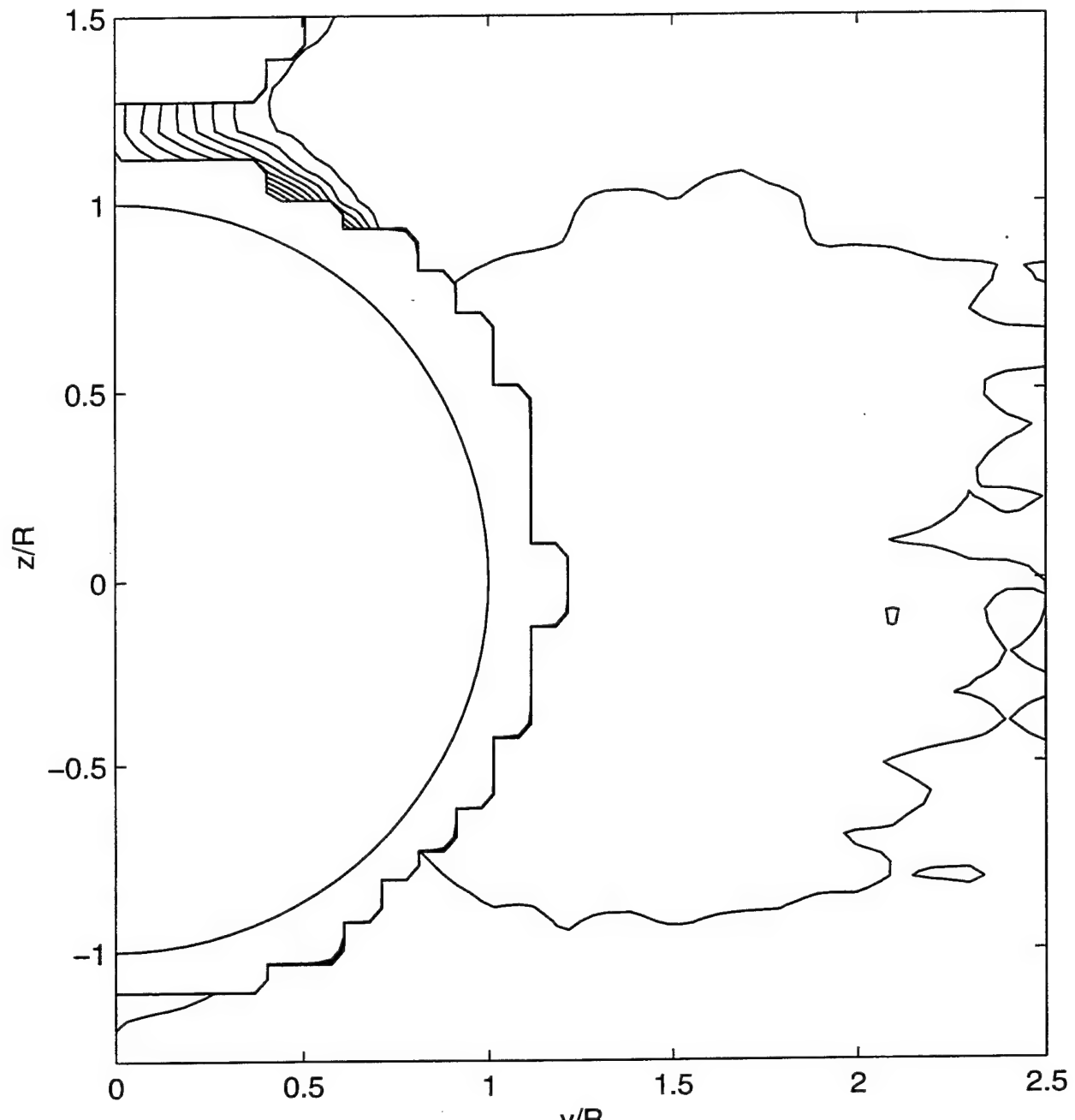
$u_{max} = 15.3$ m/s, $F_V = 0.8$, $N_{cont} = 10$

Figure 27 Streamwise velocity contours: $\beta = 9.5$ deg, $U = 14.9$ m/s, sail off, $x/L = 0.47$ (Test AV14)
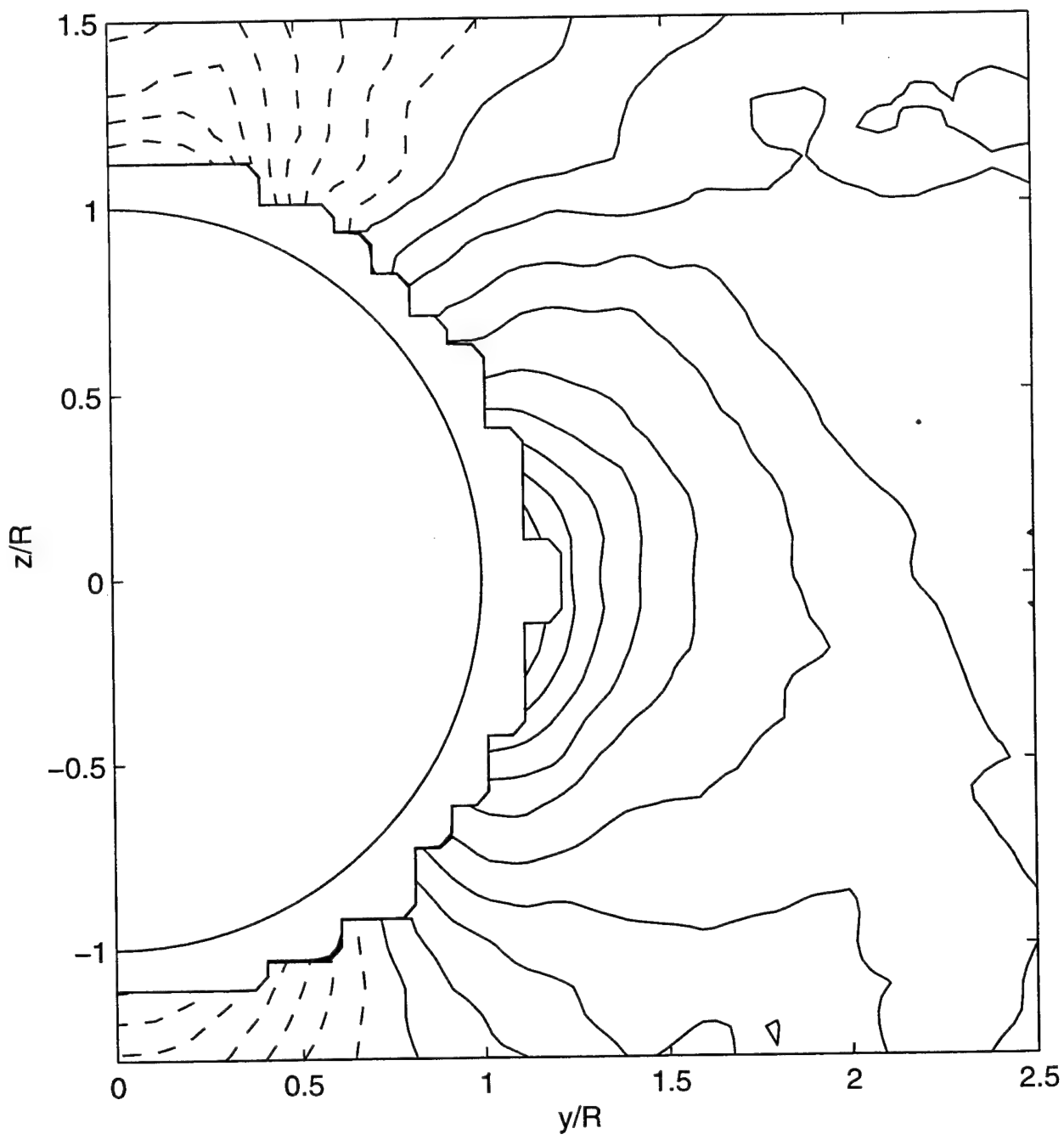
$w_{max} = 2.34$ m/s, $F_V = 0$, $N_{cont} = 10$

Figure 28 Transverse velocity contours: $\beta = 9.5$ deg, $U = 14.9$ m/s, sail off, $x/L = 0.47$ (Test AV12)
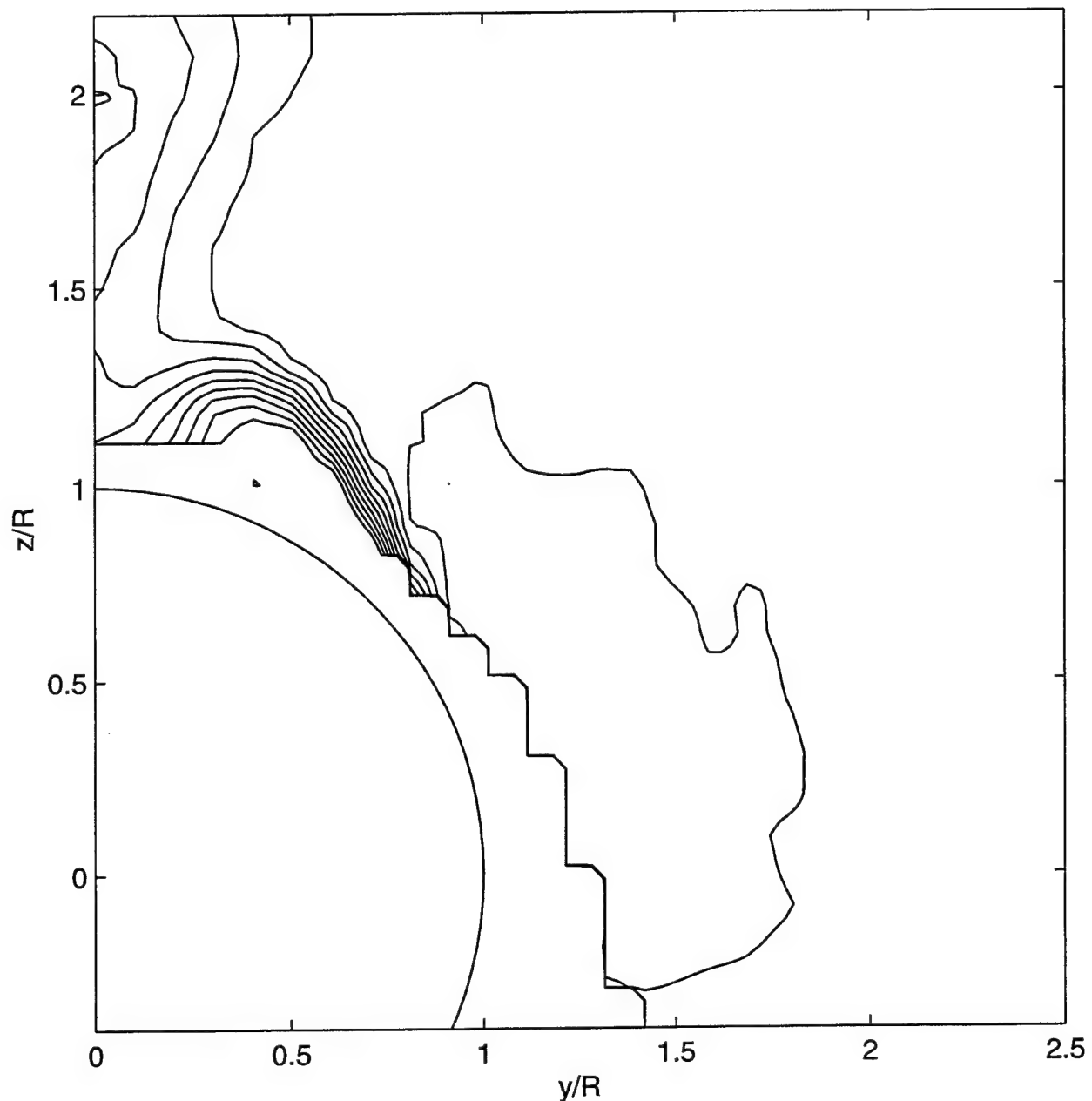
$u_{max} = 15.3$ m/s, $F_V = 0.8$, $N_{cont} = 10$

Figure 29 Streamwise velocity contours: $\beta = 9.5$ deg, $U = 14.9$ m/s, sail off, $x/L = 0.65$ (Test AV09)
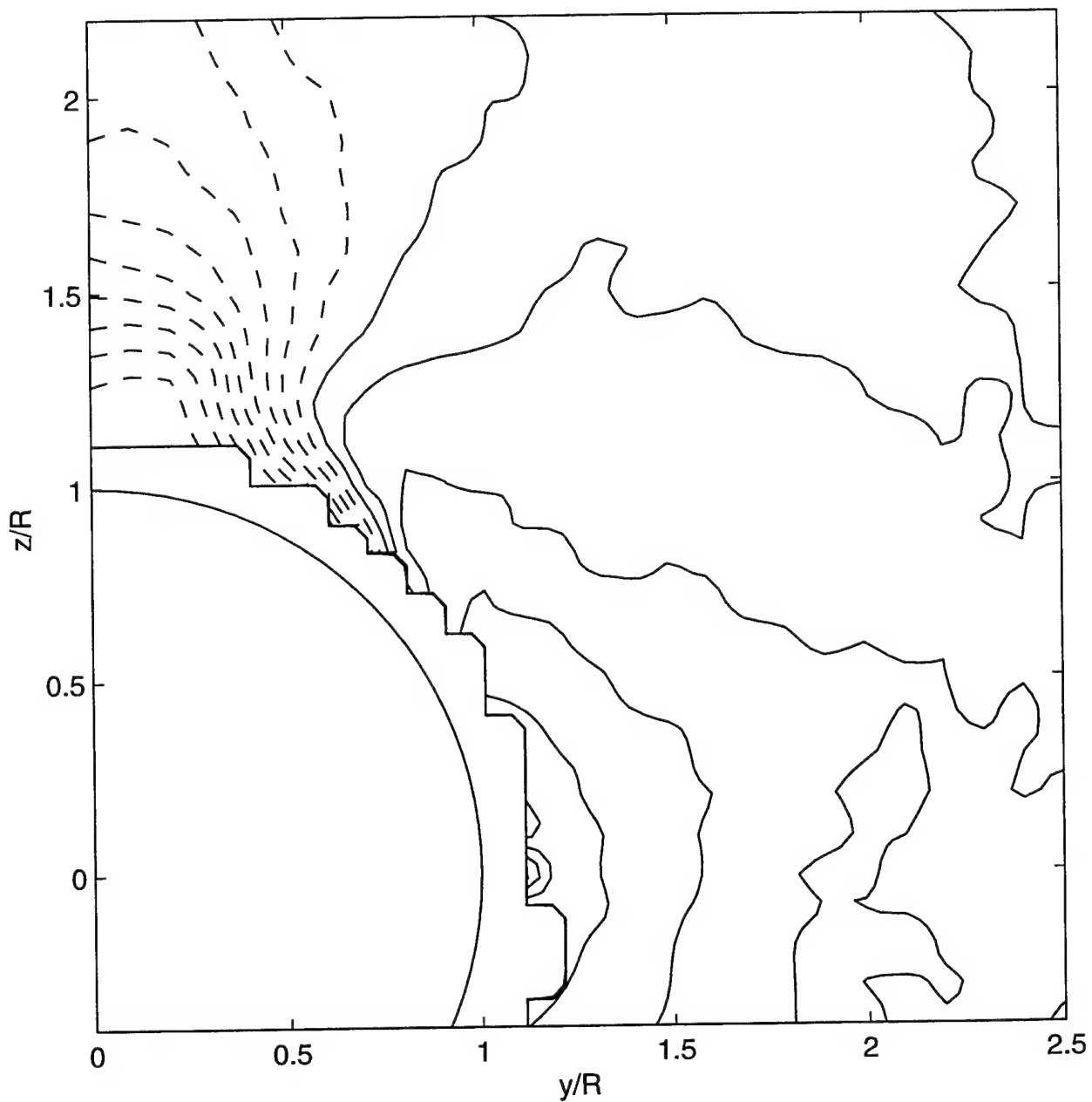
$w_{max} = 3.03$ m/s, $F_V = 0$, $N_{cont} = 10$

Figure 30 Transverse velocity contours: $\beta = 9.5$ deg, $U = 14.9$ m/s, sail off, $x/L = 0.65$ (Test AV10)
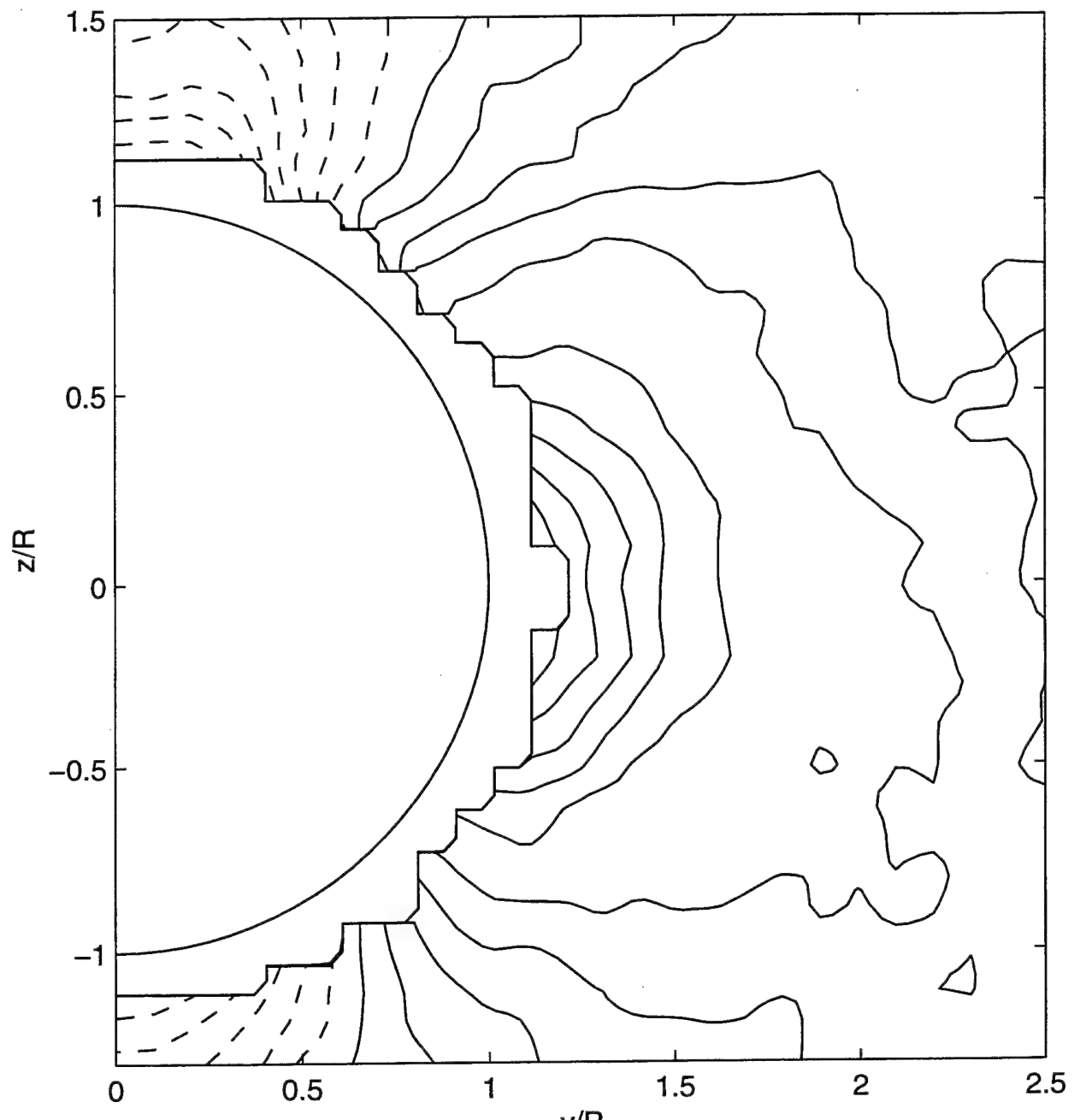
$w_{max} = 1.21$ m/s, $F_v = 0$, $N_{cont} = 10$

Figure 31 Transverse velocity contours: $\beta = 9.5$ deg, $U = 7.60$ m/s, sail off, $x/L = 0.47$ (Test AV11)
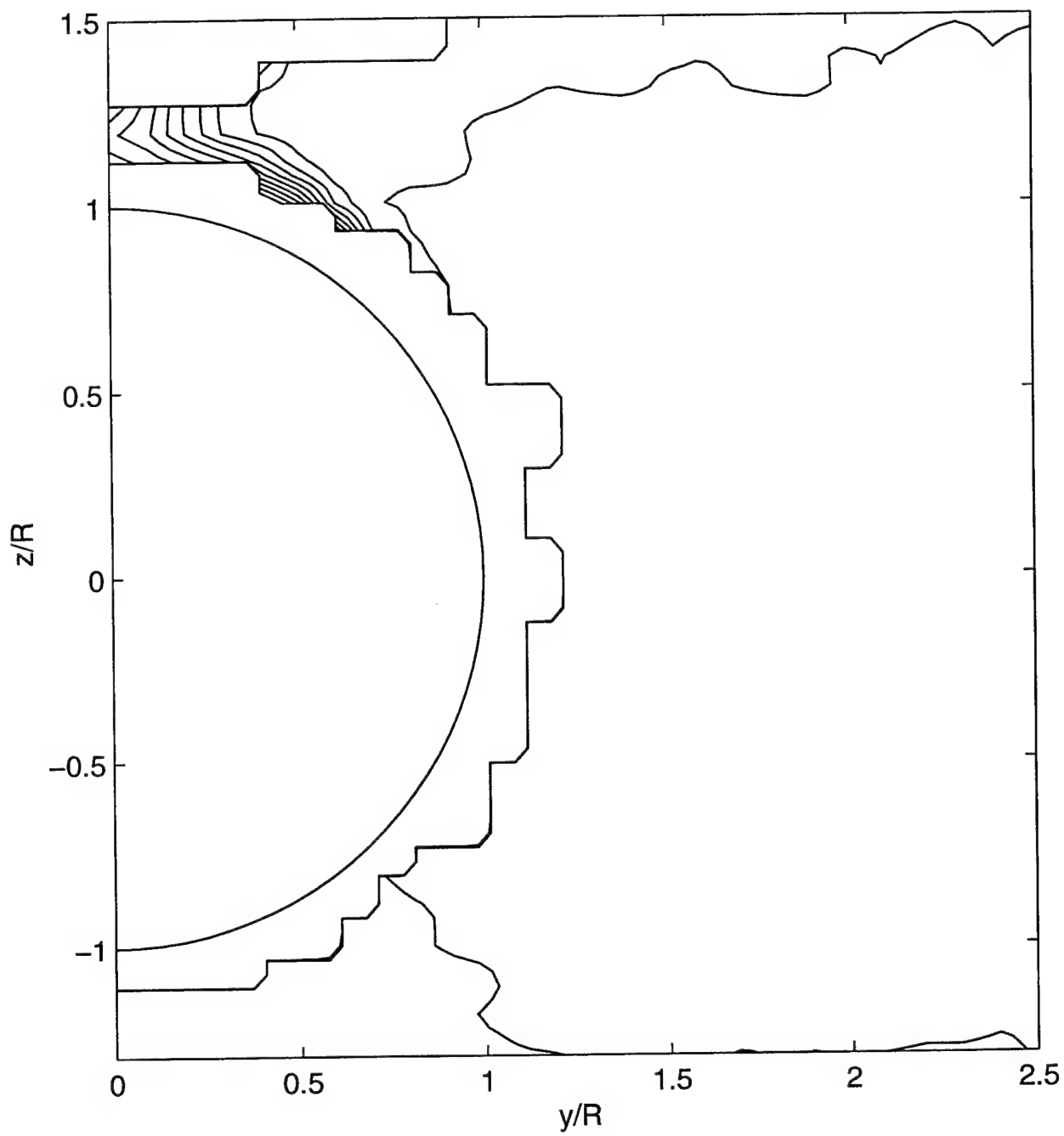
$u_{max} = 7.73$ m/s, $F_v = 0.8$, $N_{cont} = 10$

Figure 32 Streamwise velocity contours: $\beta = 9.5$ deg, $U = 7.60$ m/s, sail off, $x/L = 0.47$ (Test AV13)
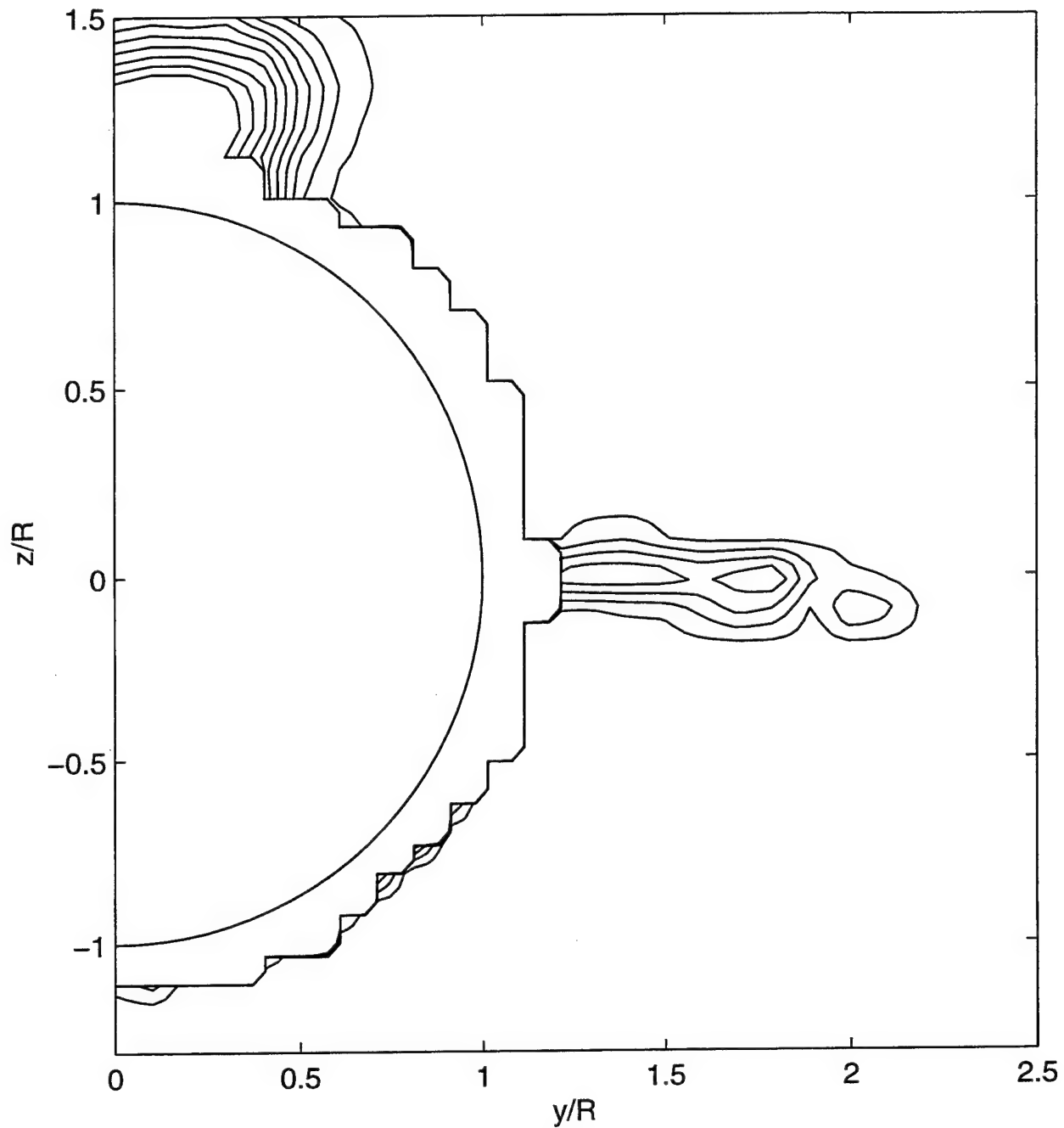
$u_{max} = 15.0$ m/s, $F_V = 0.85$, $N_{cont} = 10$

Figure 33 Streamwise velocity contours: $\beta = 0$ deg, $U = 14.9$ m/s, sail on, $x/L = 0.47$ (Test AV16)
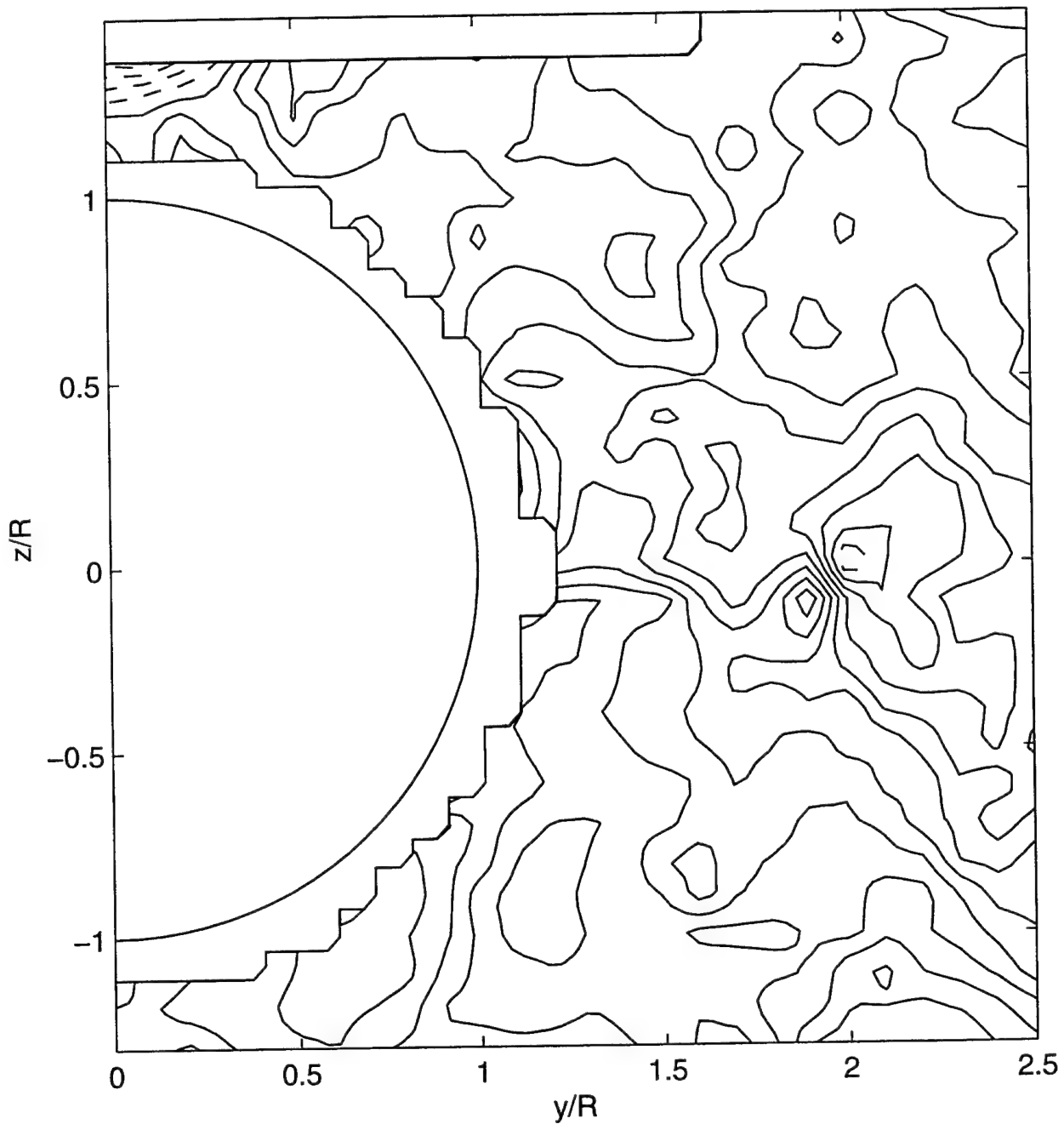
$w_{max} = 0.536$ m/s, $F_V = 0$, $N_{cont} = 10$

Figure 34 Transverse velocity contours: $\beta = 0$ deg, $U = 14.9$ m/s, sail on, $x/L = 0.47$ (Test AV15)
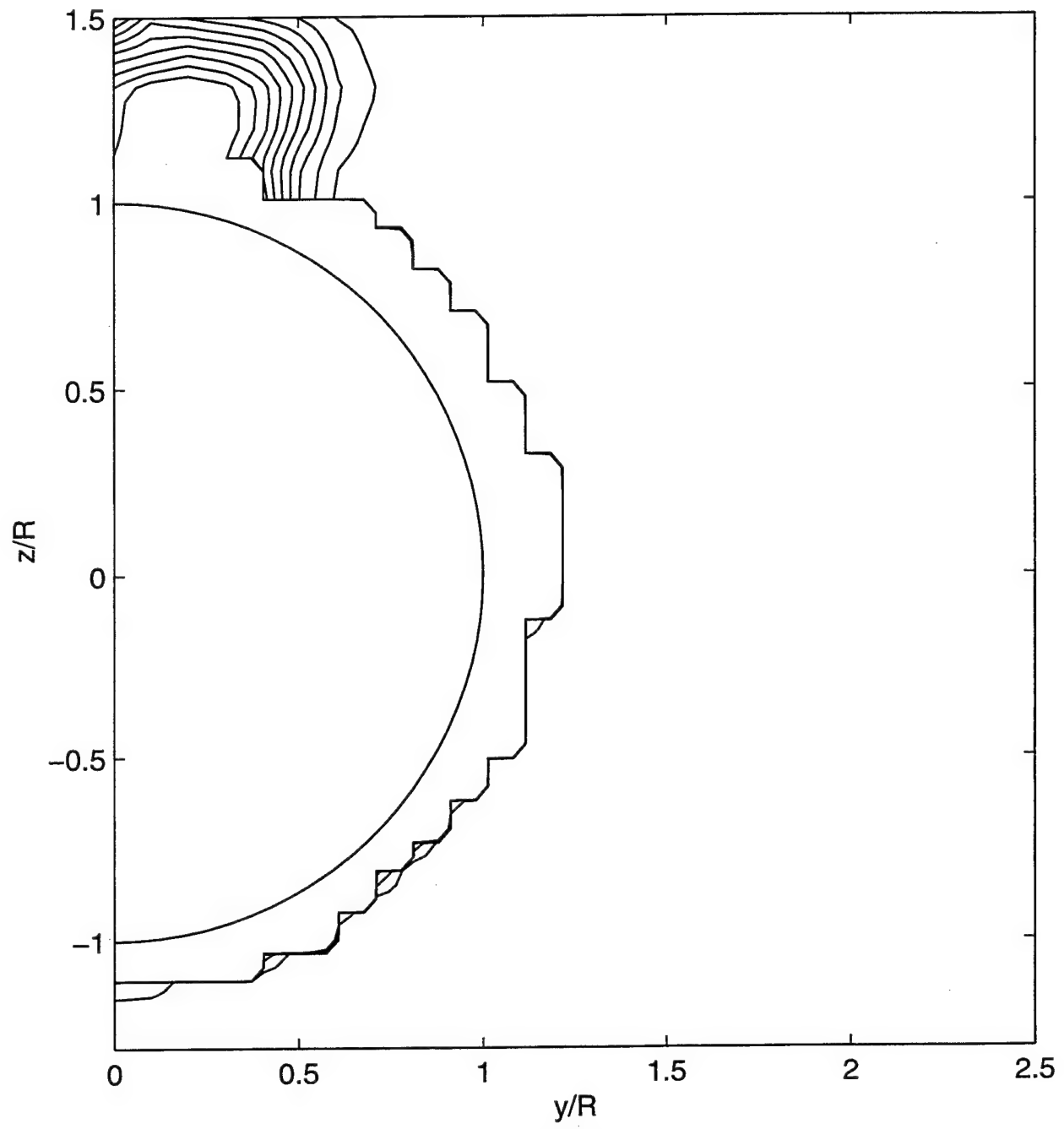
$u_{max} = 15.04$ m/s, $F_V = 0.85$, $N_{cont} = 10$

Figure 35 Streamwise velocity contours: $\beta = 0$ deg, $U = 14.9$ m/s, sail off, $x/L = 0.47$ (Test AV17)
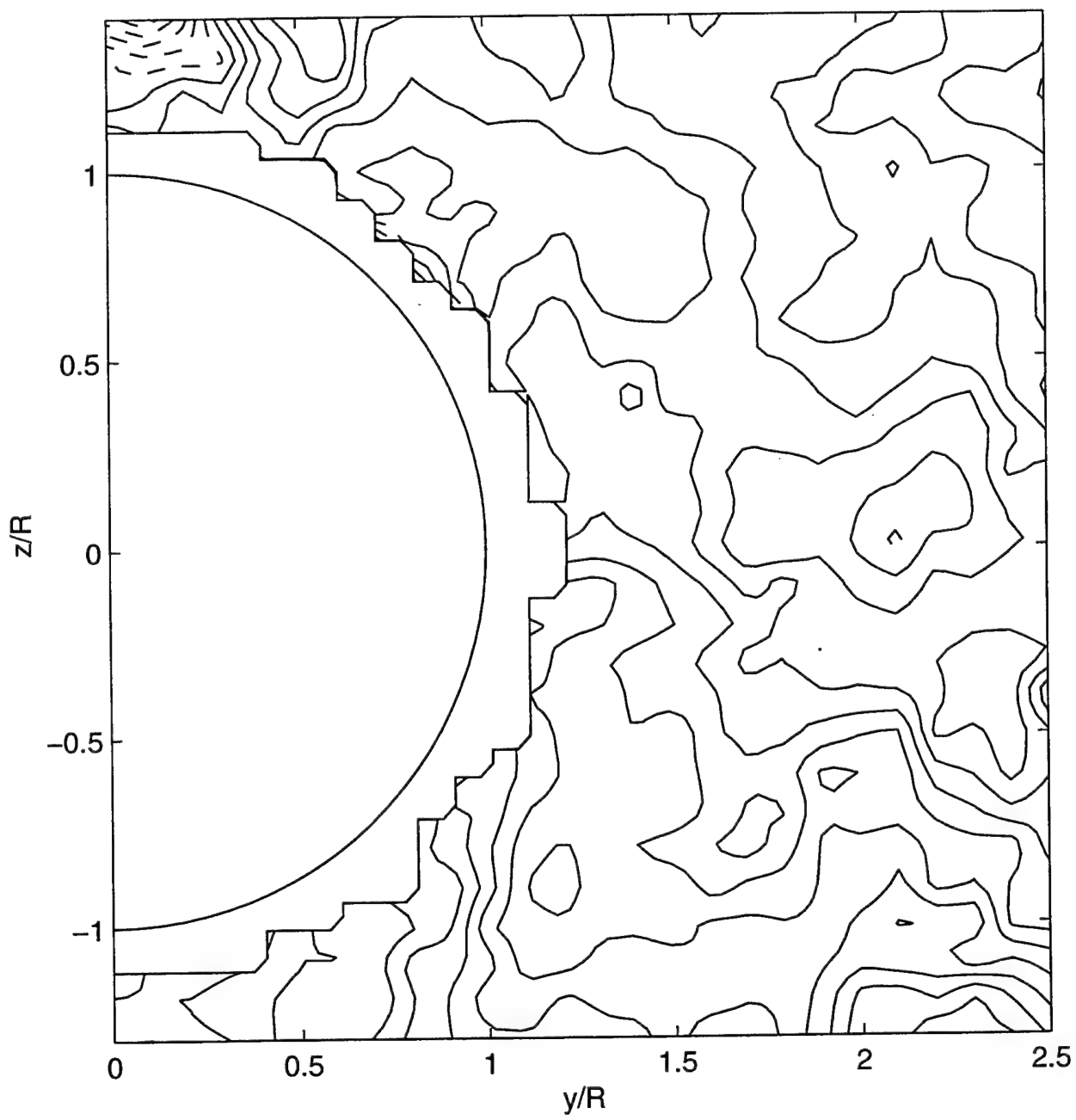
$w_{max} = 0.504$ m/s, $F_v = 0$, $N_{cont} = 10$

Figure 36 Transverse velocity contours: $\beta = 0$ deg, $U = 14.9$ m/s, sail off, $x/L = 0.47$ (Test AV18)
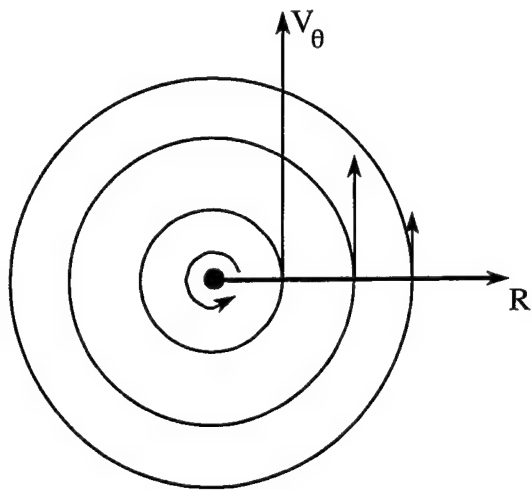
Figure 37 Illustration of tangential velocity component for potential vortex
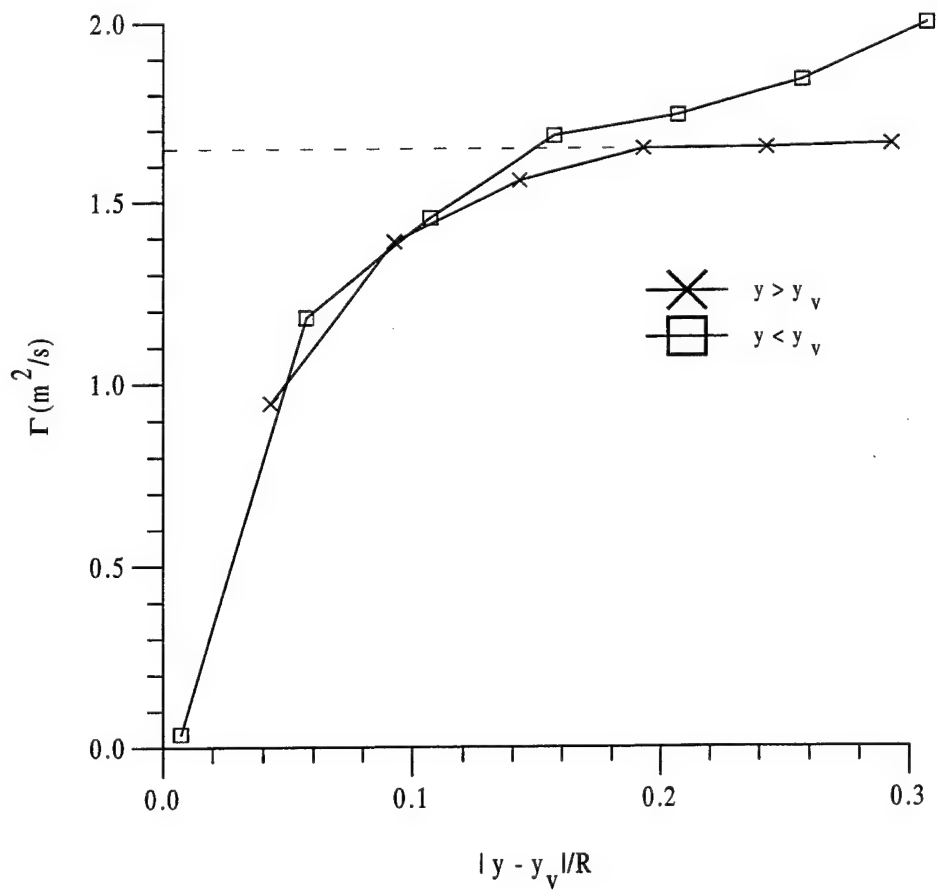
Figure 38 First estimate of vortex circulation using potential vortex: $\beta = 9.5$ deg, $U = 14.9$ m/s, $x/L = 0.47$
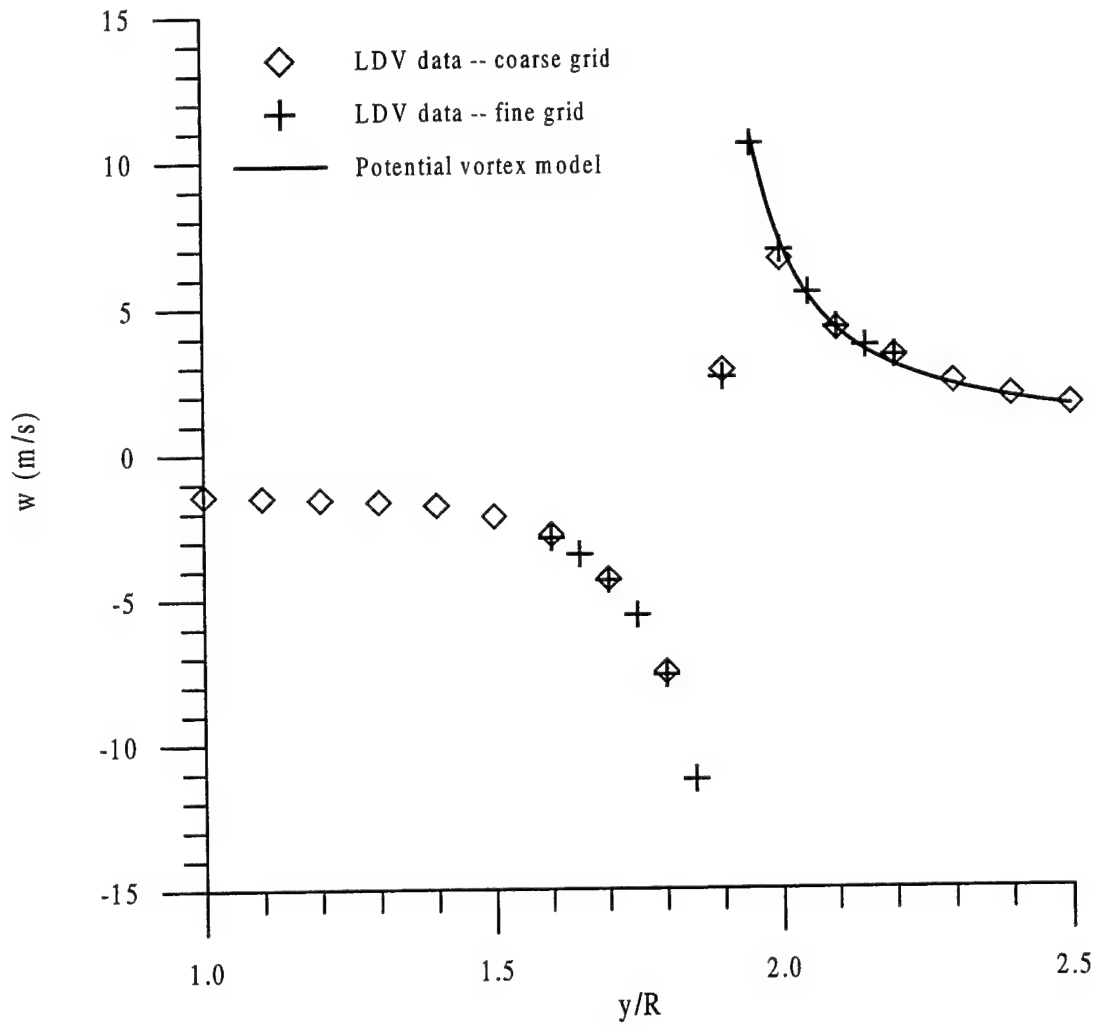
Figure 39 Example of transverse velocities in vicinity of vortex core: $\beta = 9.5$ deg, $U = 14.9$ m/s, $x/L = 0.47$
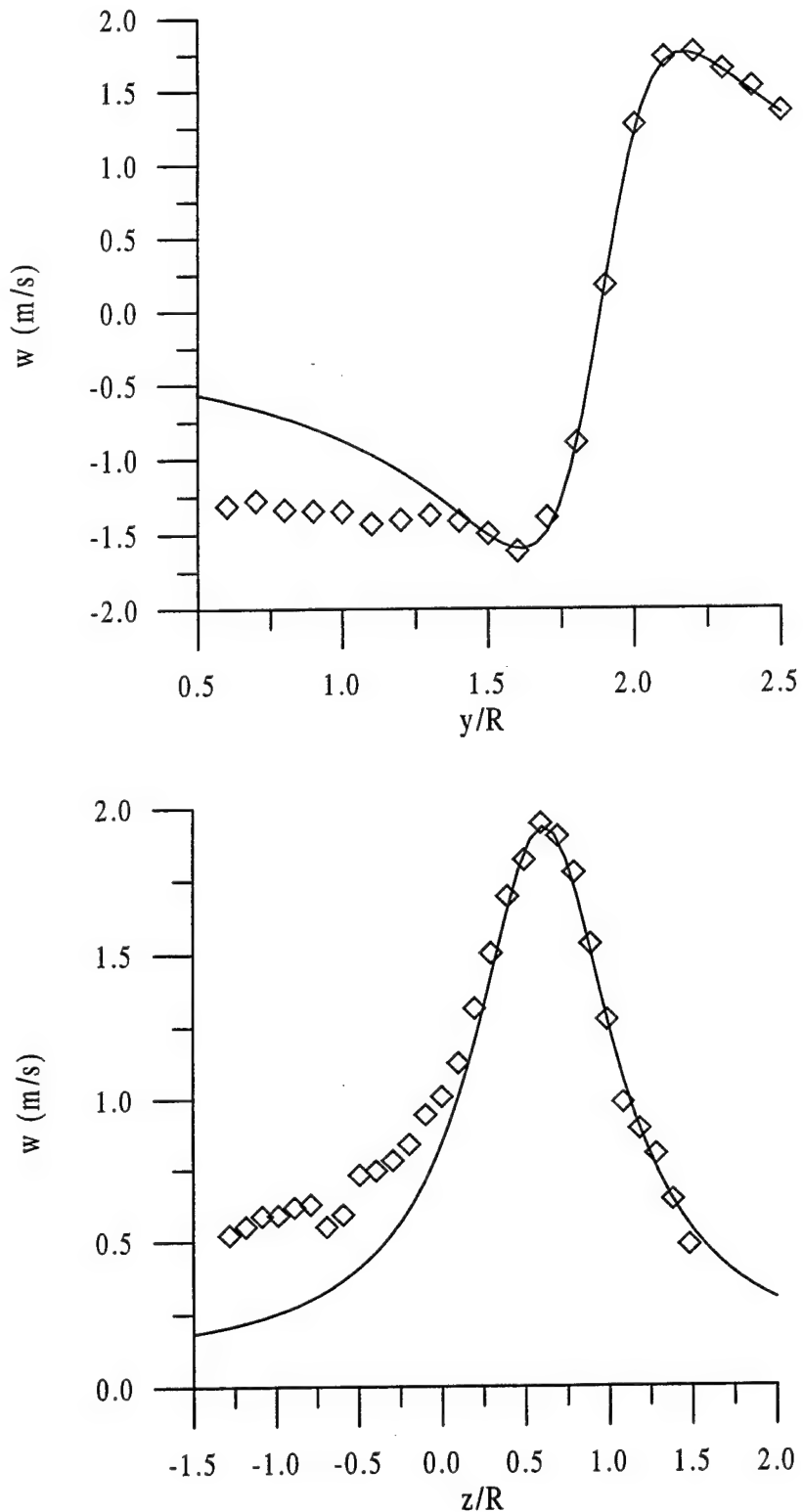
Figure 40 Examples of curve fits to general vortex velocity function: $\beta = 9.5$ deg, $U = 14.9$ m/s, $x/L = 0.47$
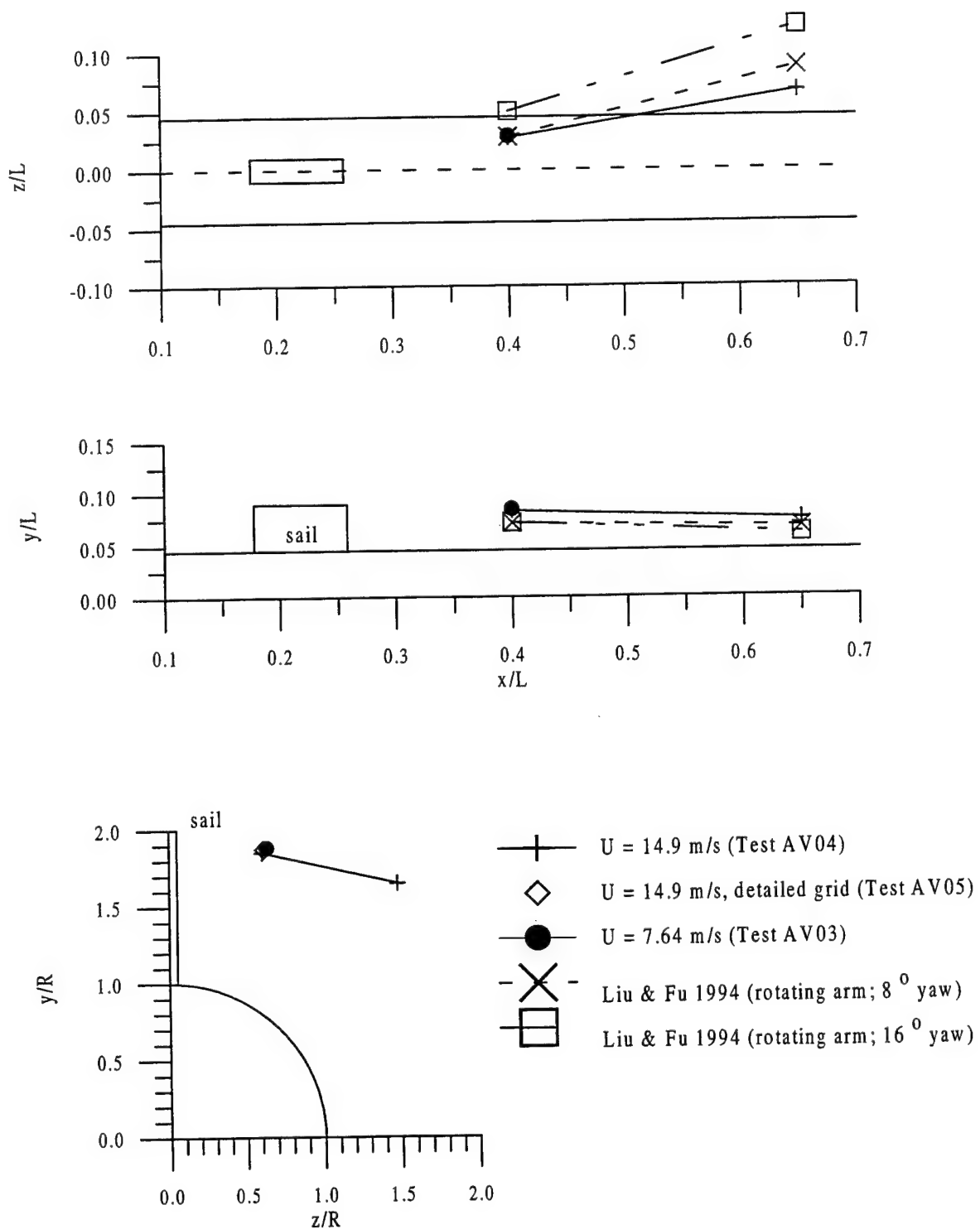
Figure 41 Vortex trajectory data: β = 9.5 deg
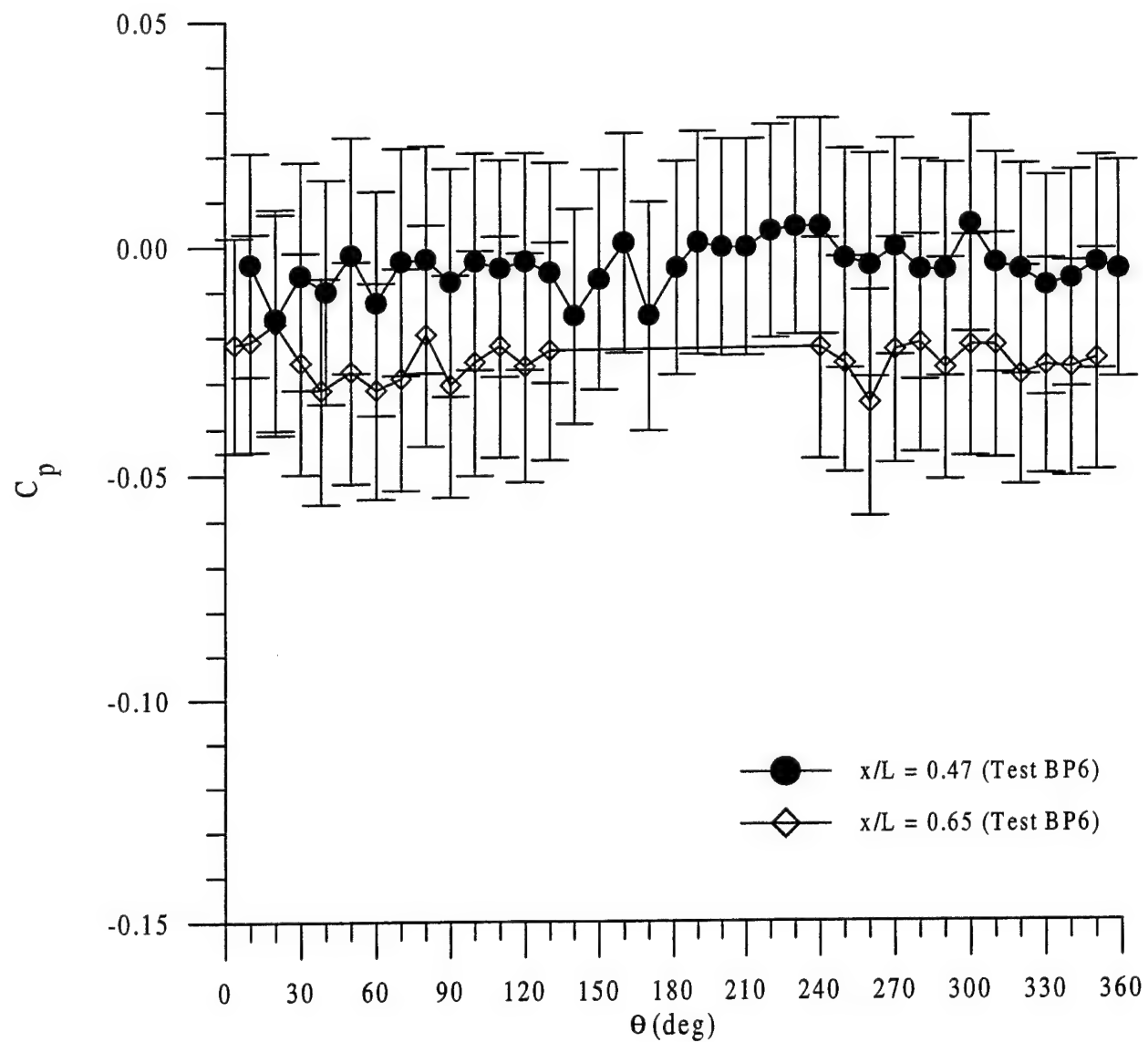
Figure 42 Circumferential pressure distributions: β = 0 deg, U = 5.25 m/s, sail off
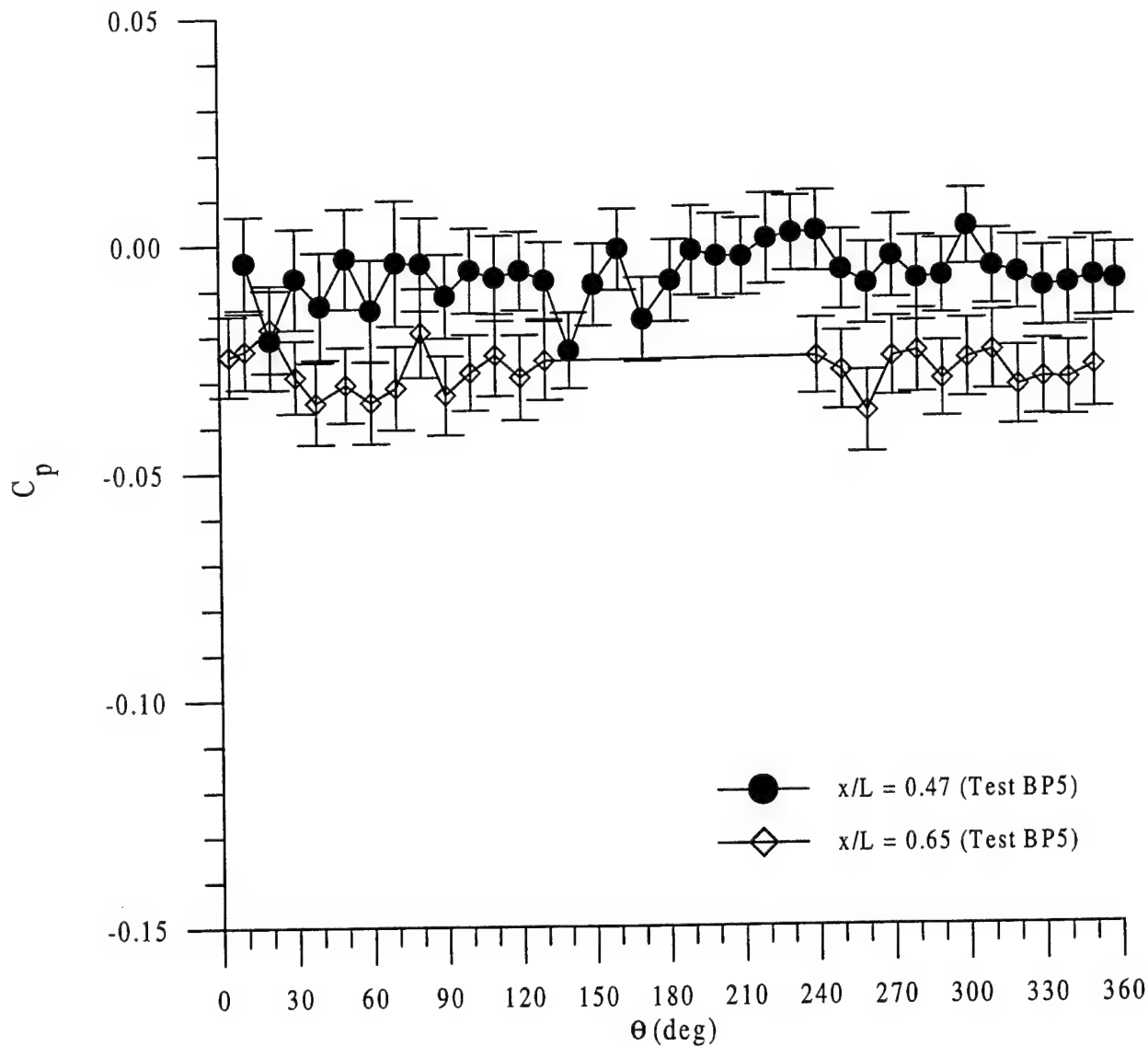
Figure 43 Circumferential pressure distributions: β = 0 deg, U = 10.5 m/s, sail off
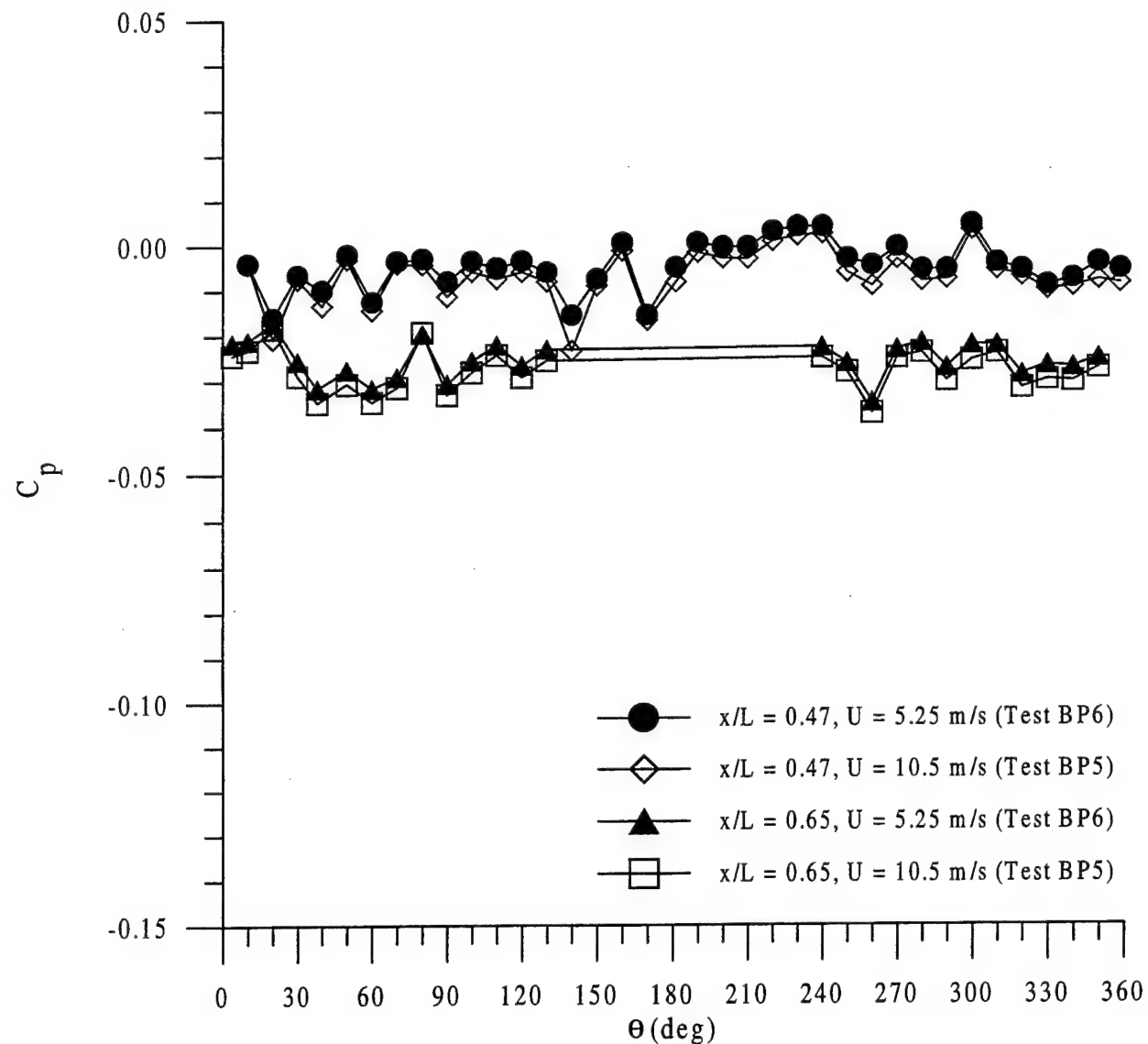
Figure 44 Illustration of Reynolds number effects: β = 0 deg, sail off
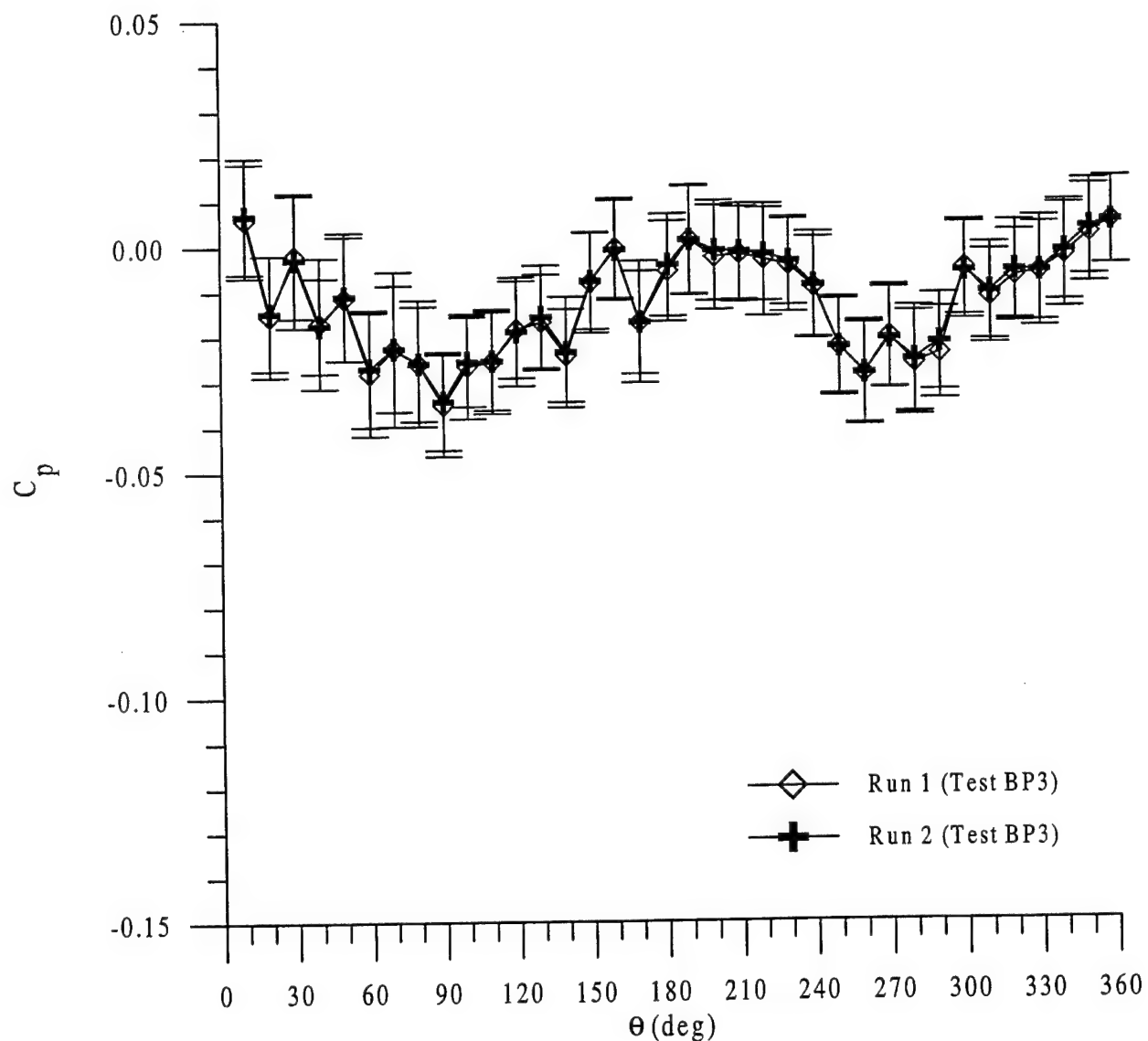
Figure 45 Circumferential pressure distributions: $\beta = 5$ deg, $U = 9.18$ m/s, sail off, $x/L = 0.47$
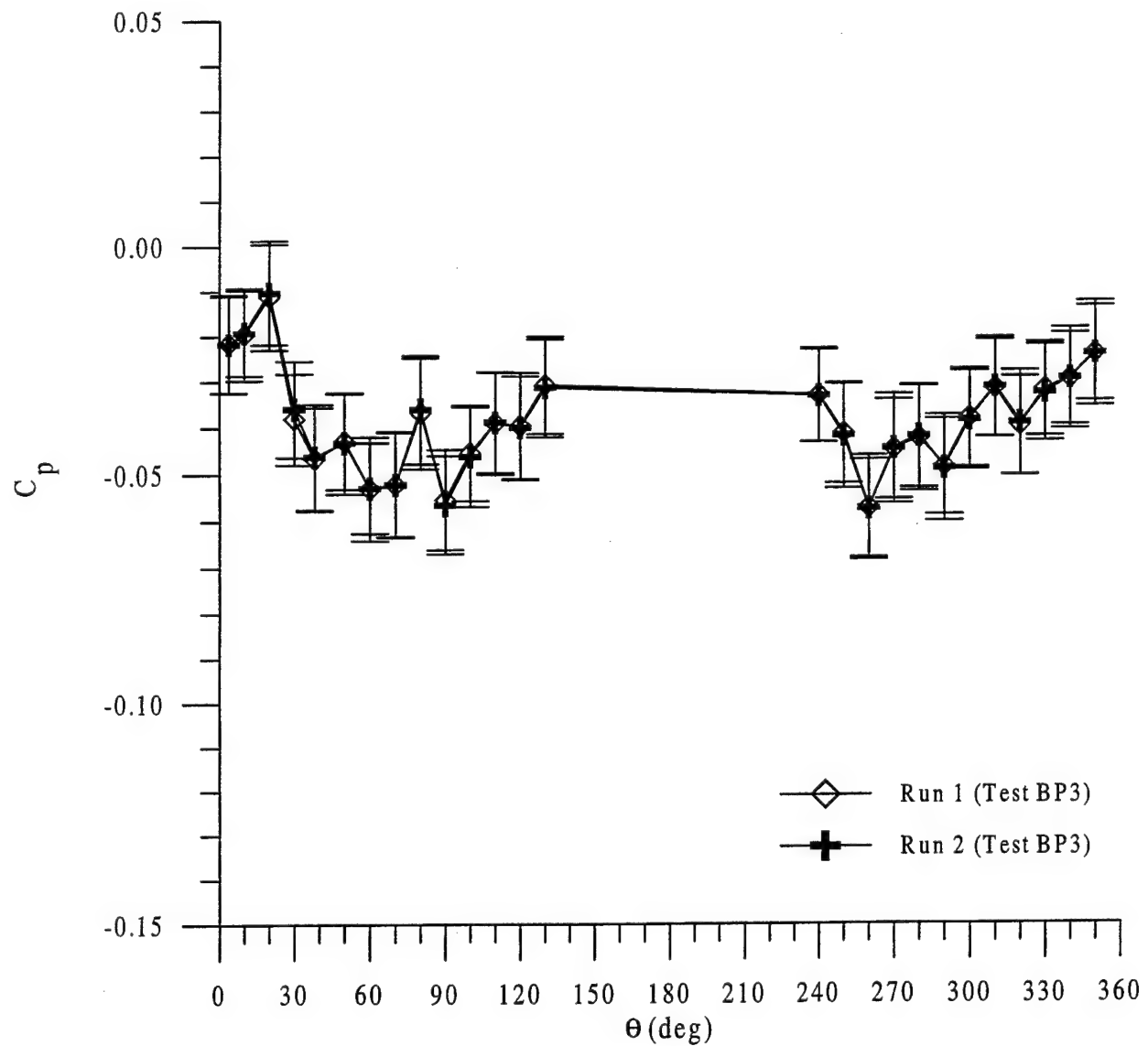
Figure 46 Circumferential pressure distributions: $\beta = 5$ deg, $U = 9.18$ m/s, sail off, $x/L = 0.65$
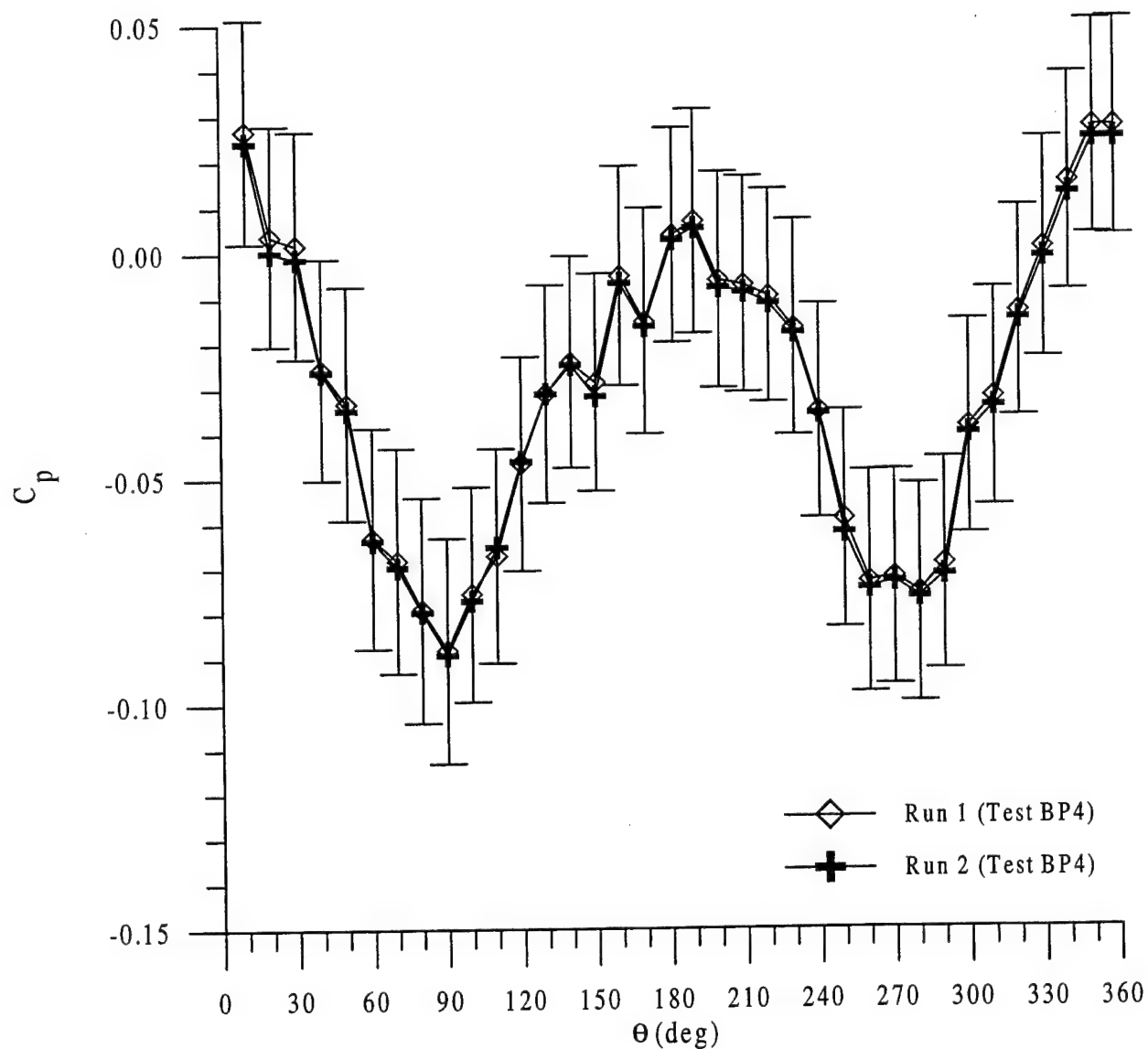
Figure 47 Circumferential pressure distributions: $\beta = 9.5$ deg, $U = 5.15$ m/s, sail off, $x/L = 0.47$
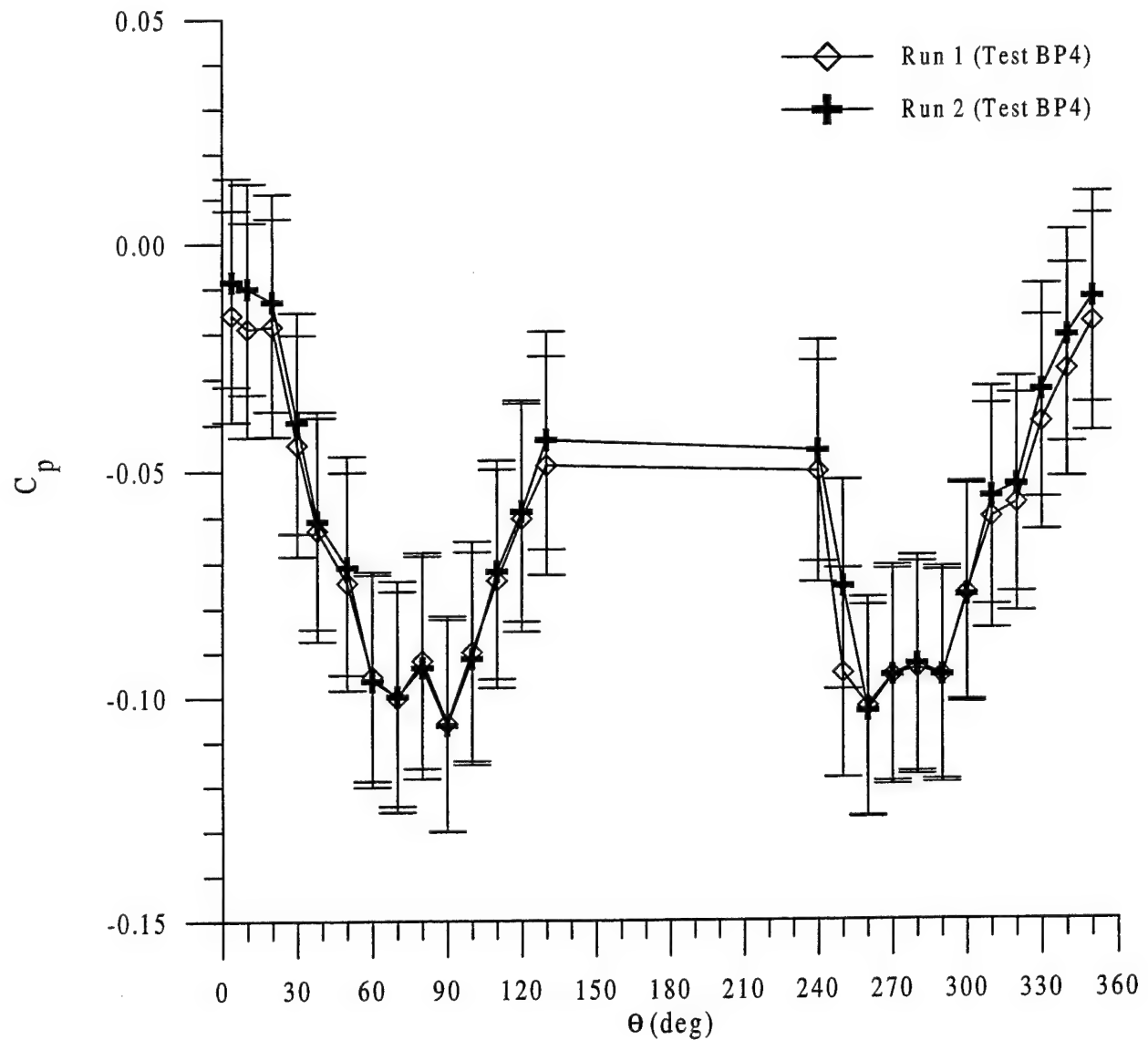
Figure 48 Circumferential pressure distributions: β = 9.5 deg, U = 5.15 m/s, sail off, x/L = 0.65
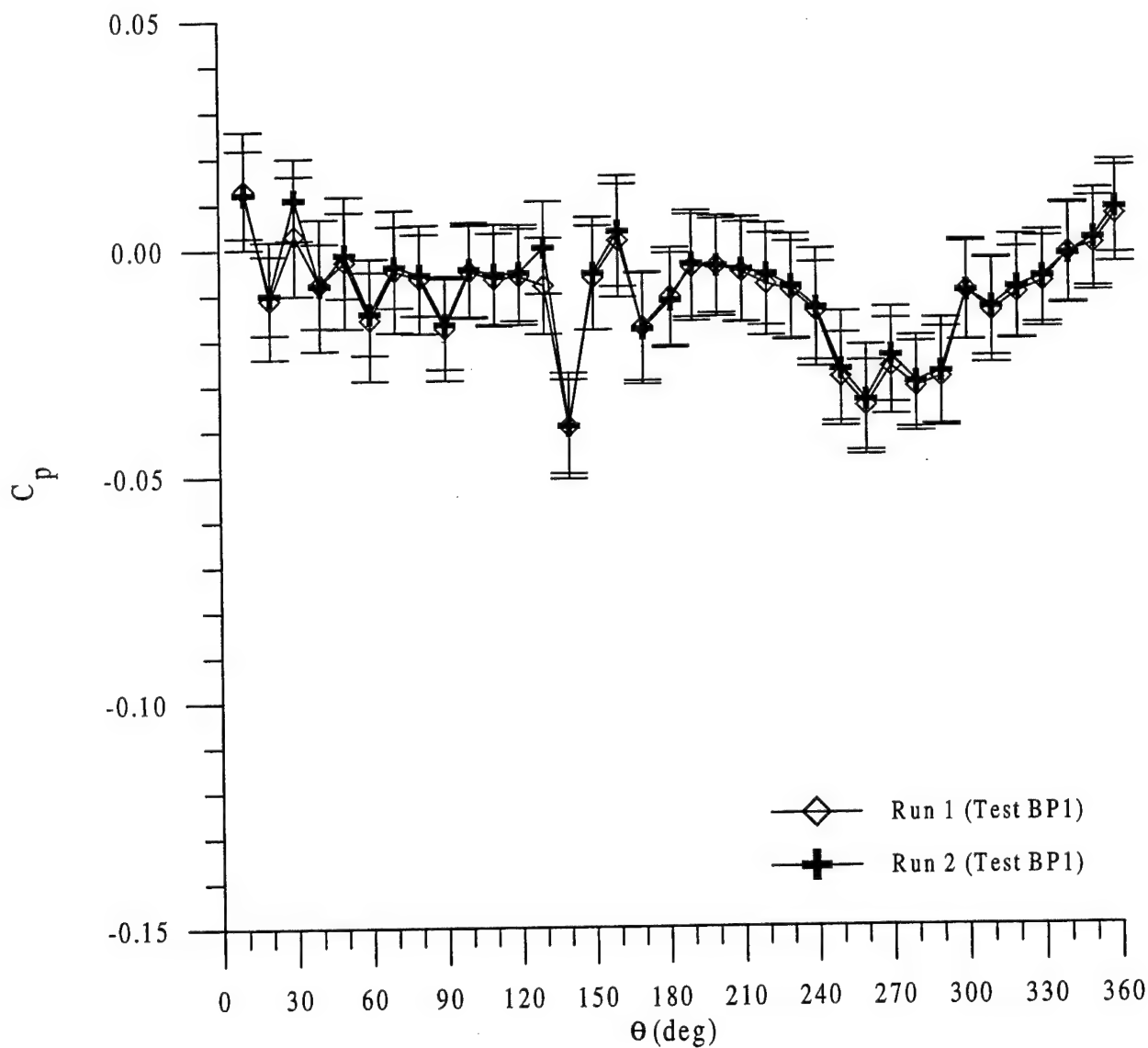
Figure 49 Circumferential pressure distributions: $\beta = 5$ deg, $U = 9.18$ m/s, sail on, $x/L = 0.47$
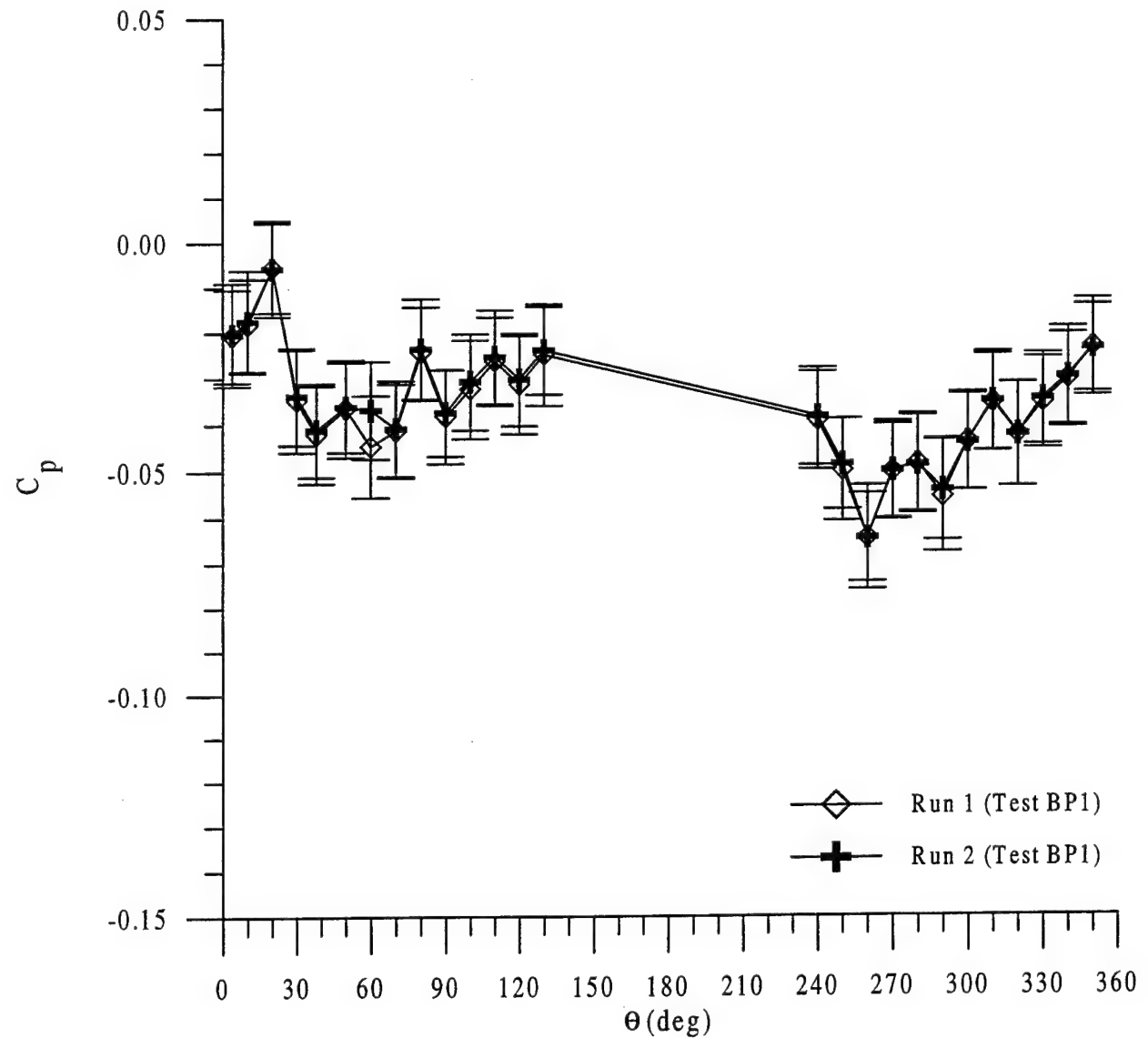
Figure 50 Circumferential pressure distributions: $\beta = 5$ deg, $U = 9.18$ m/s, sail on, $x/L = 0.65$
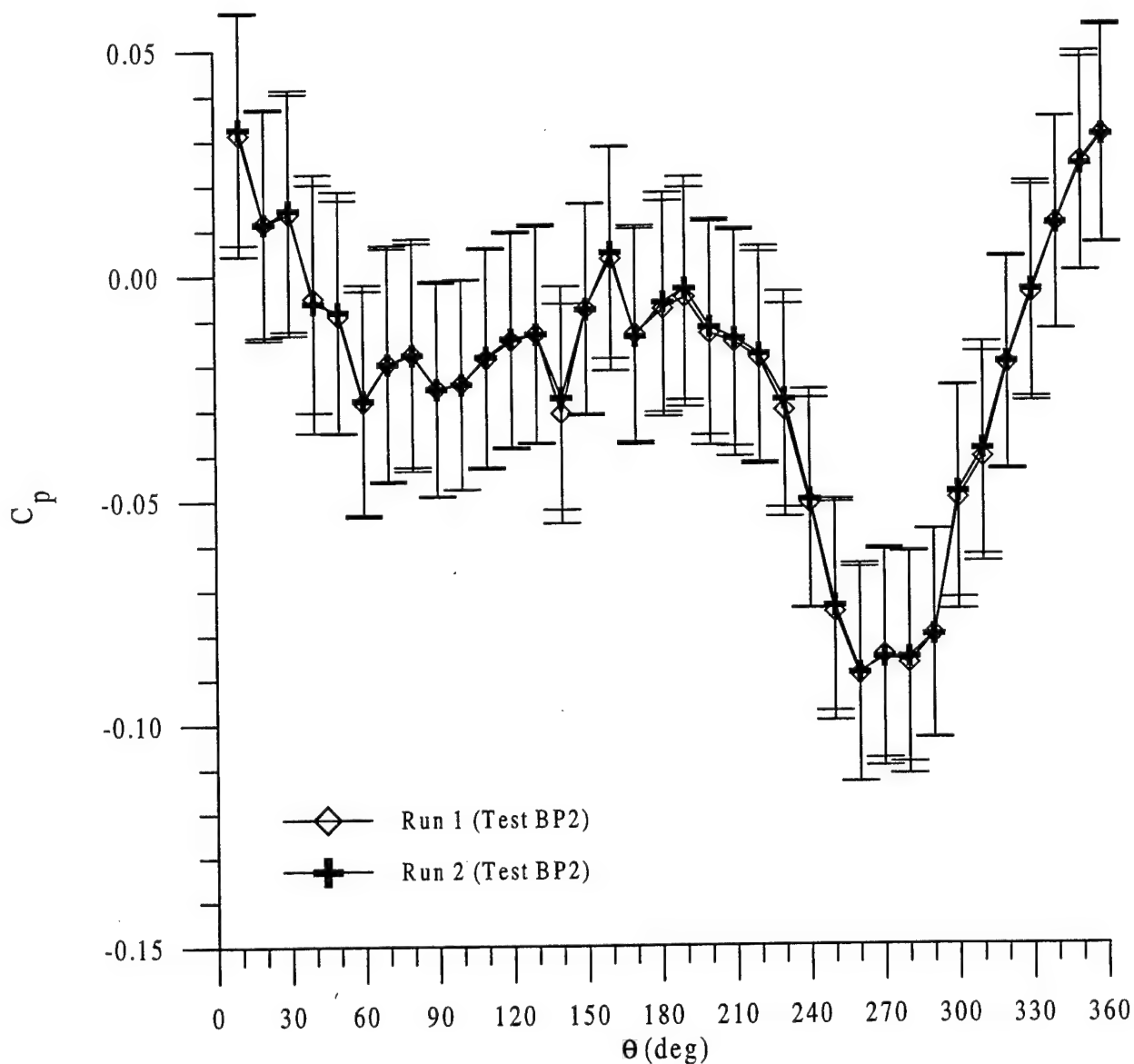
Figure 51 Circumferential pressure distributions: $\beta = 9.5$ deg, $U = 5.14$ m/s, sail on, $x/L = 0.47$
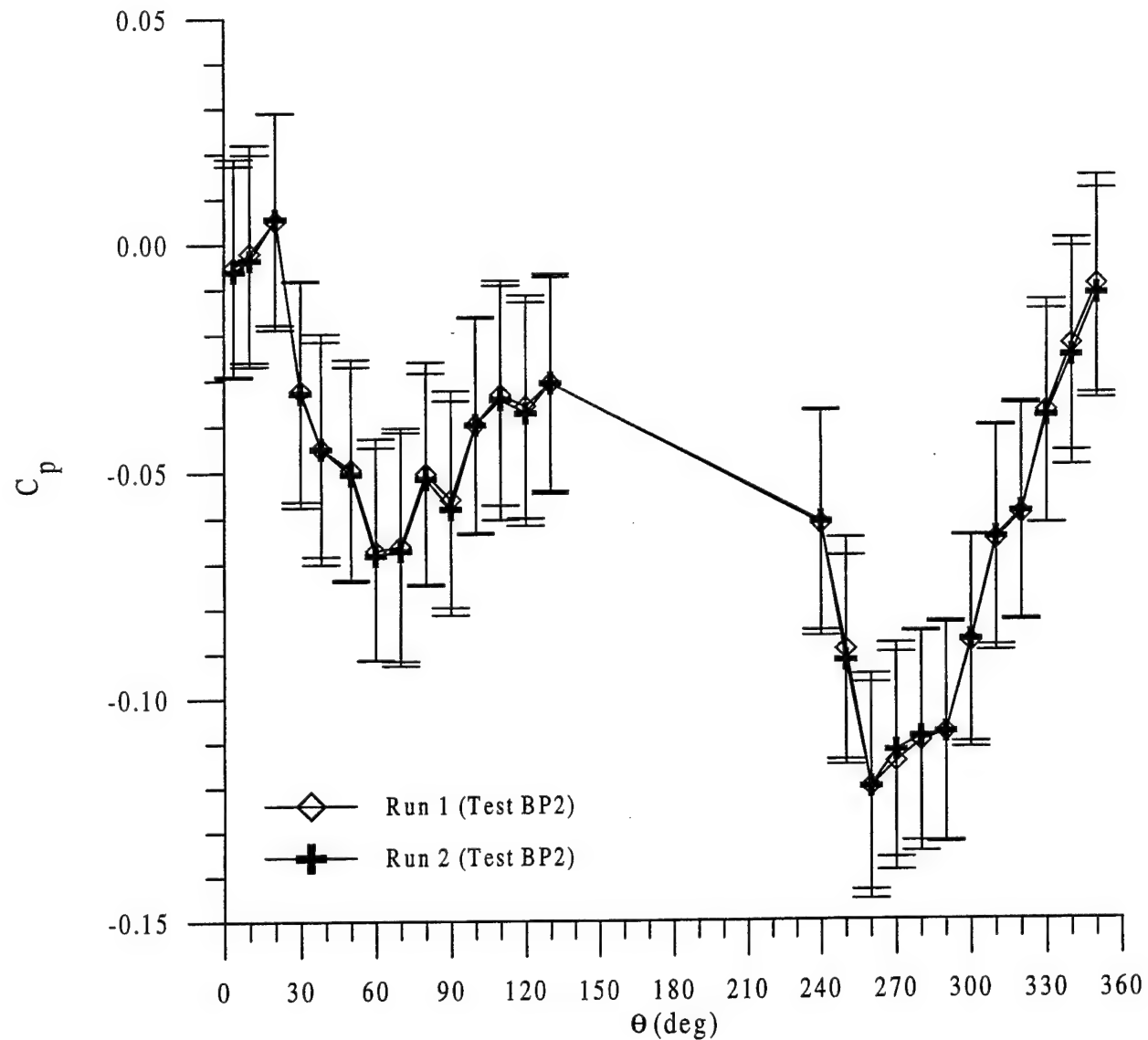
Figure 52 Circumferential pressure distributions: $\beta = 9.5$ deg, $U = 5.14$ m/s, sail on, $x/L = 0.65$
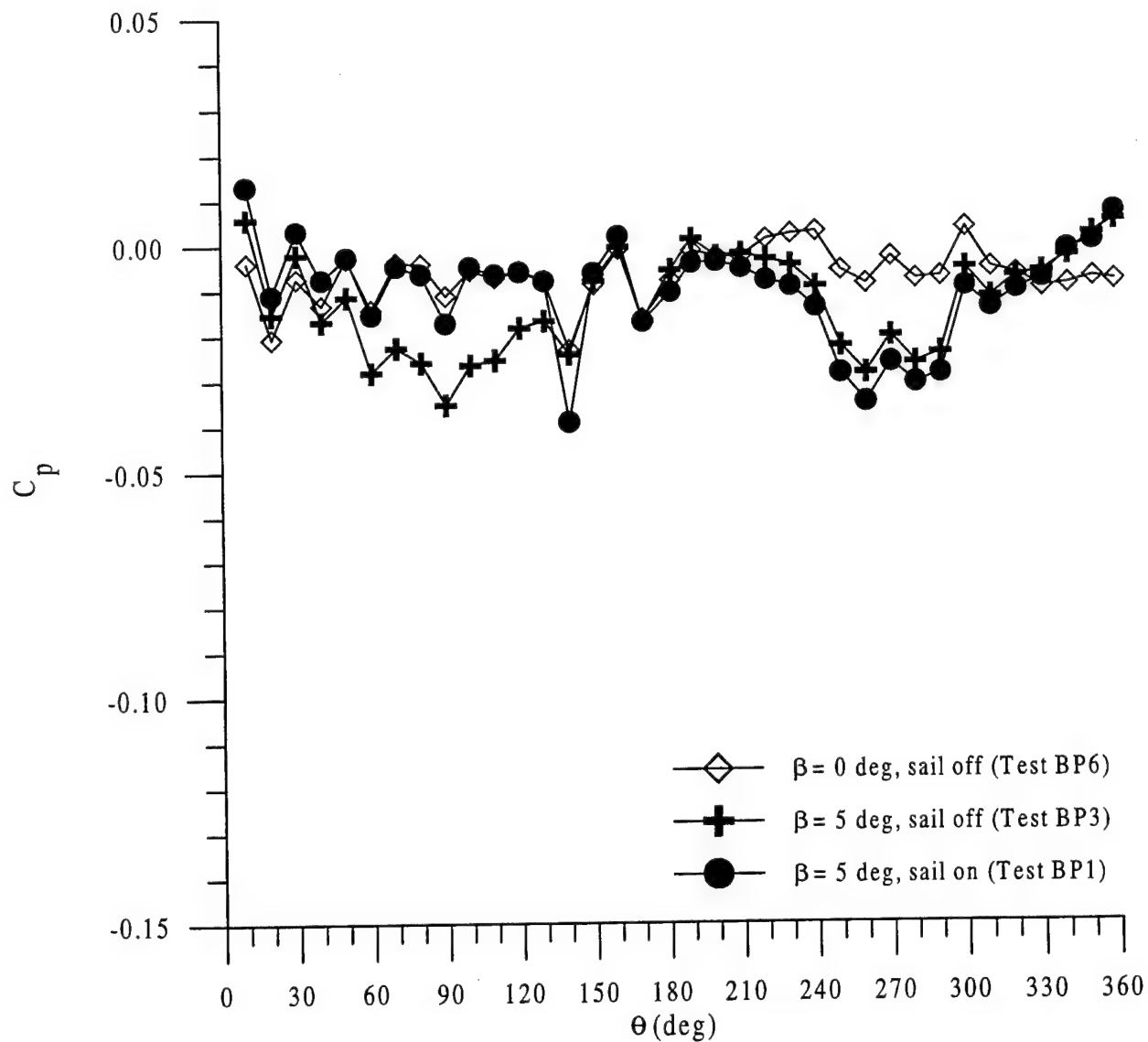
Figure 53 Demonstration of the effect on pressures of adding the sail: $x/L = 0.47$
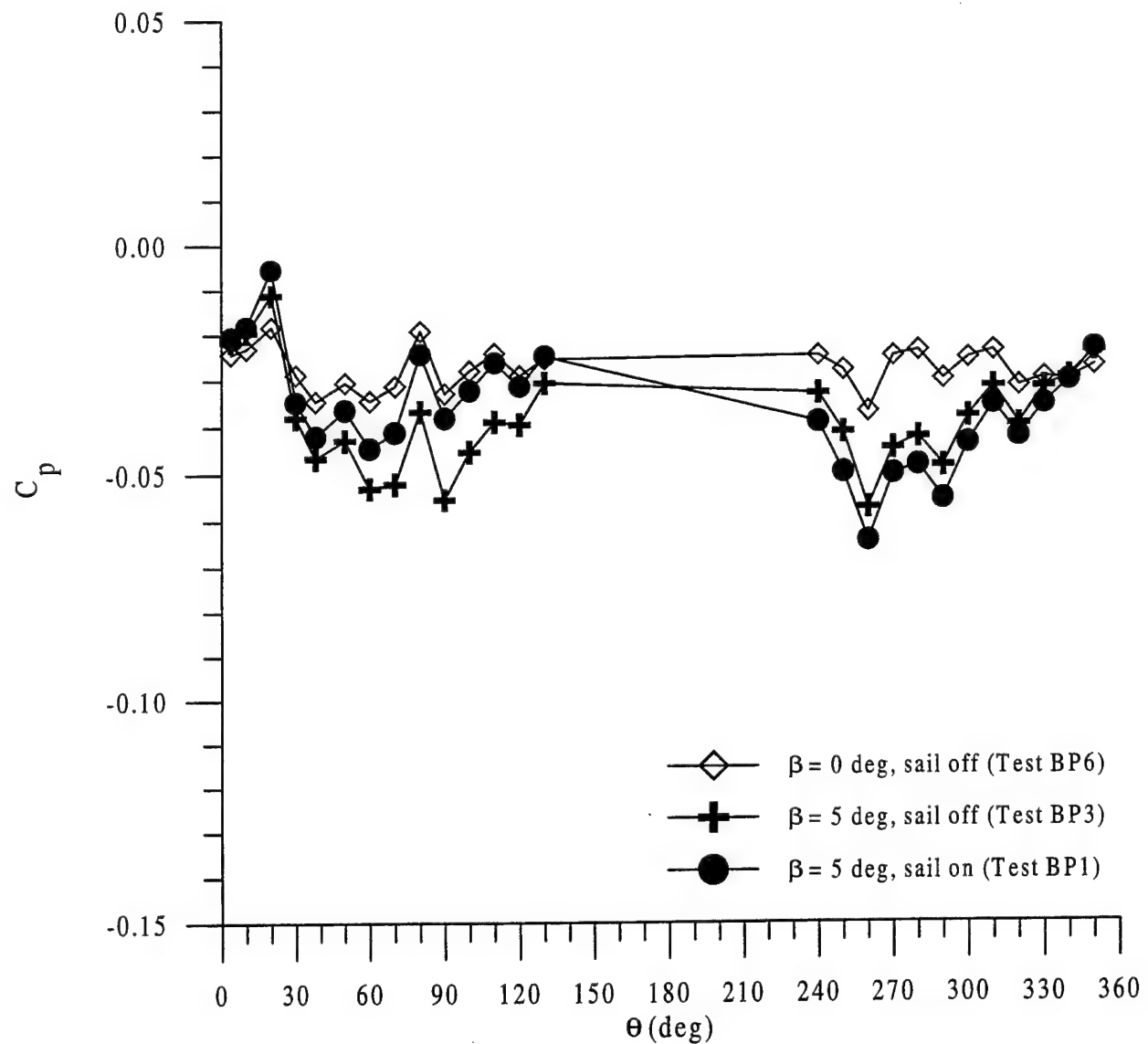
Figure 54 Demonstration of the effect on pressures of adding the sail: $x/L = 0.65$
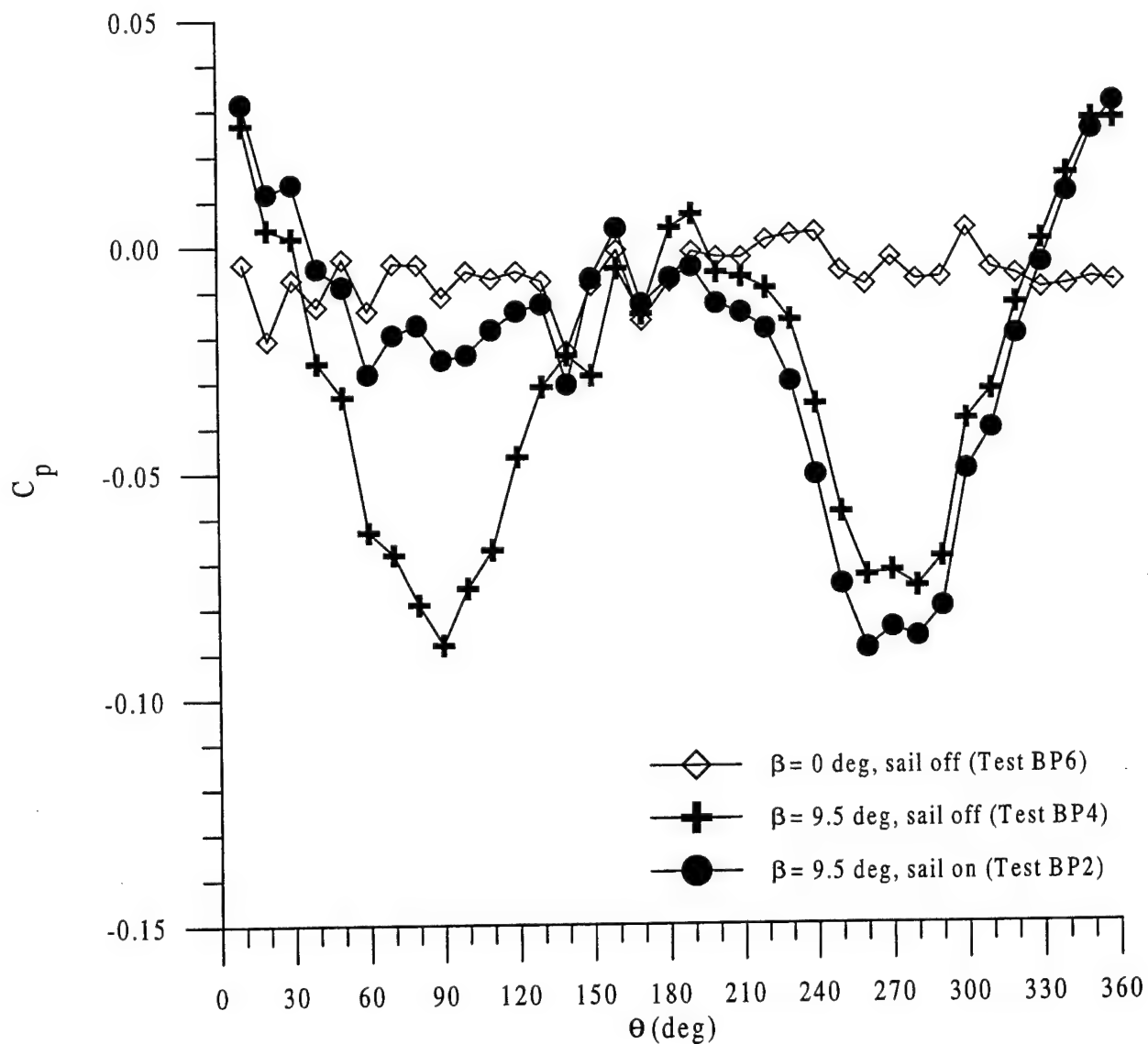
Figure 55 Demonstration of the effect on pressures of adding the sail: $x/L = 0.47$
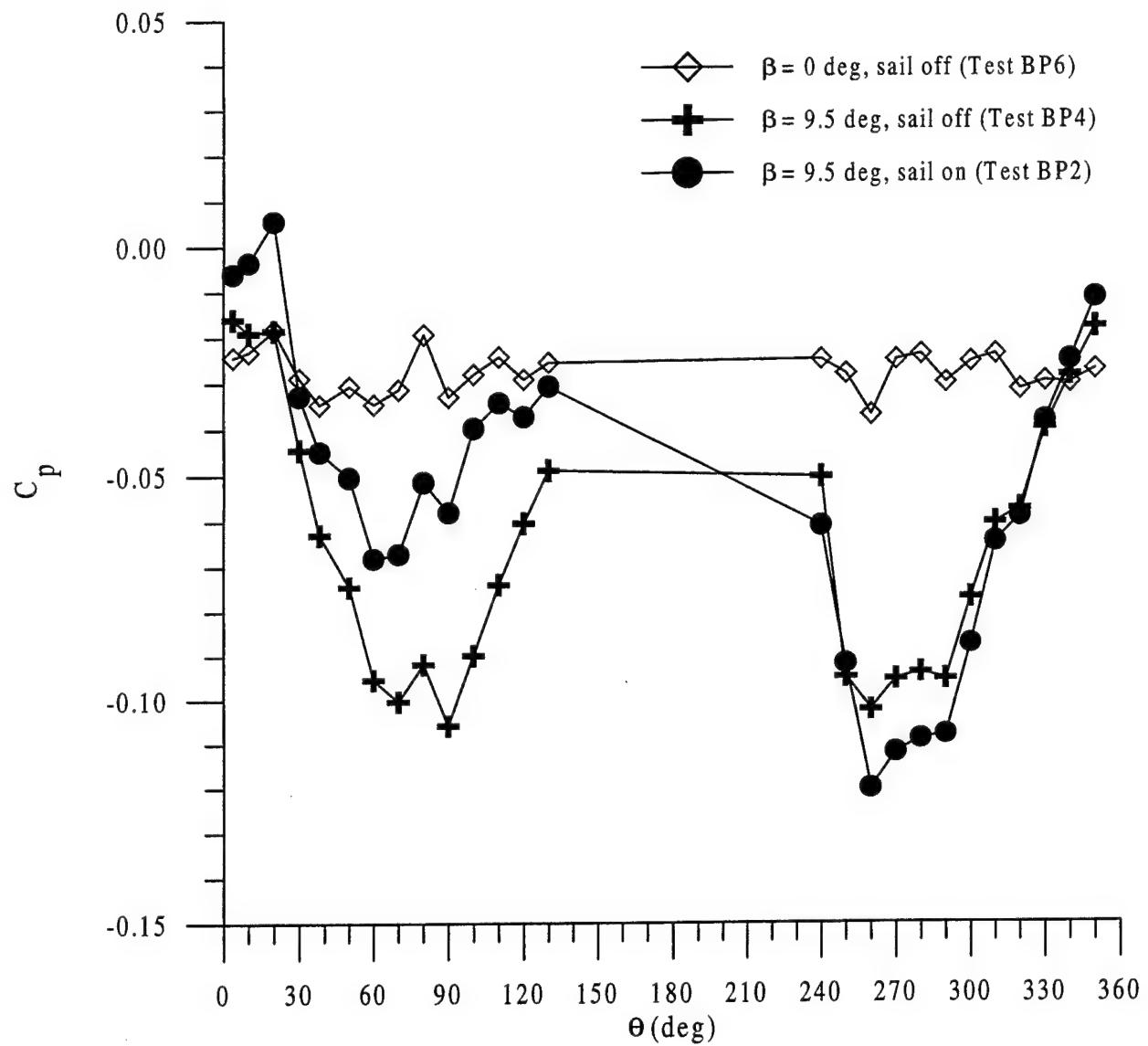
Figure 56 Demonstration of the effect on pressures of adding the sail: $x/L = 0.47$
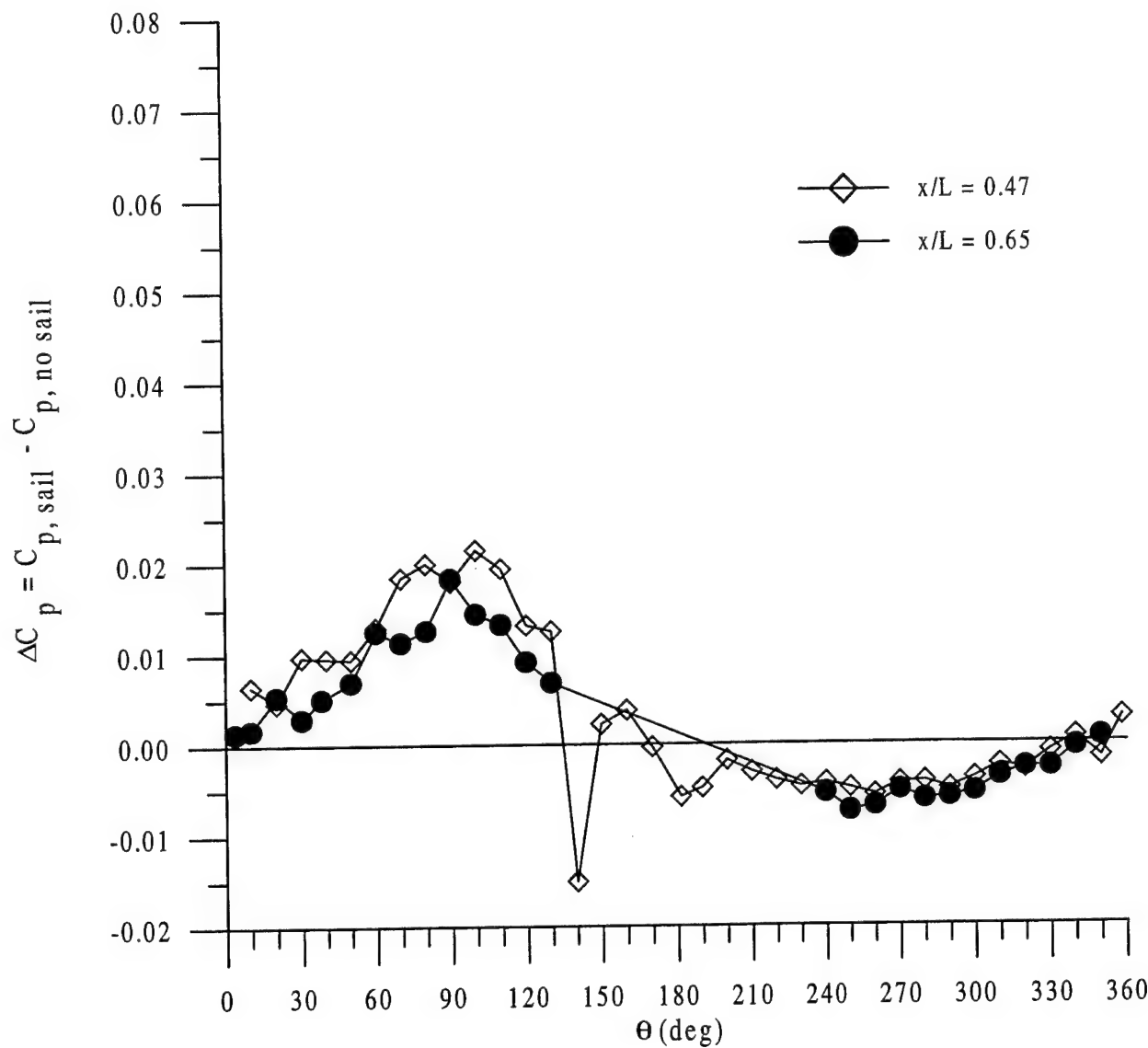
Figure 57 Pressure difference due to addition of sail: $\beta = 5$ deg
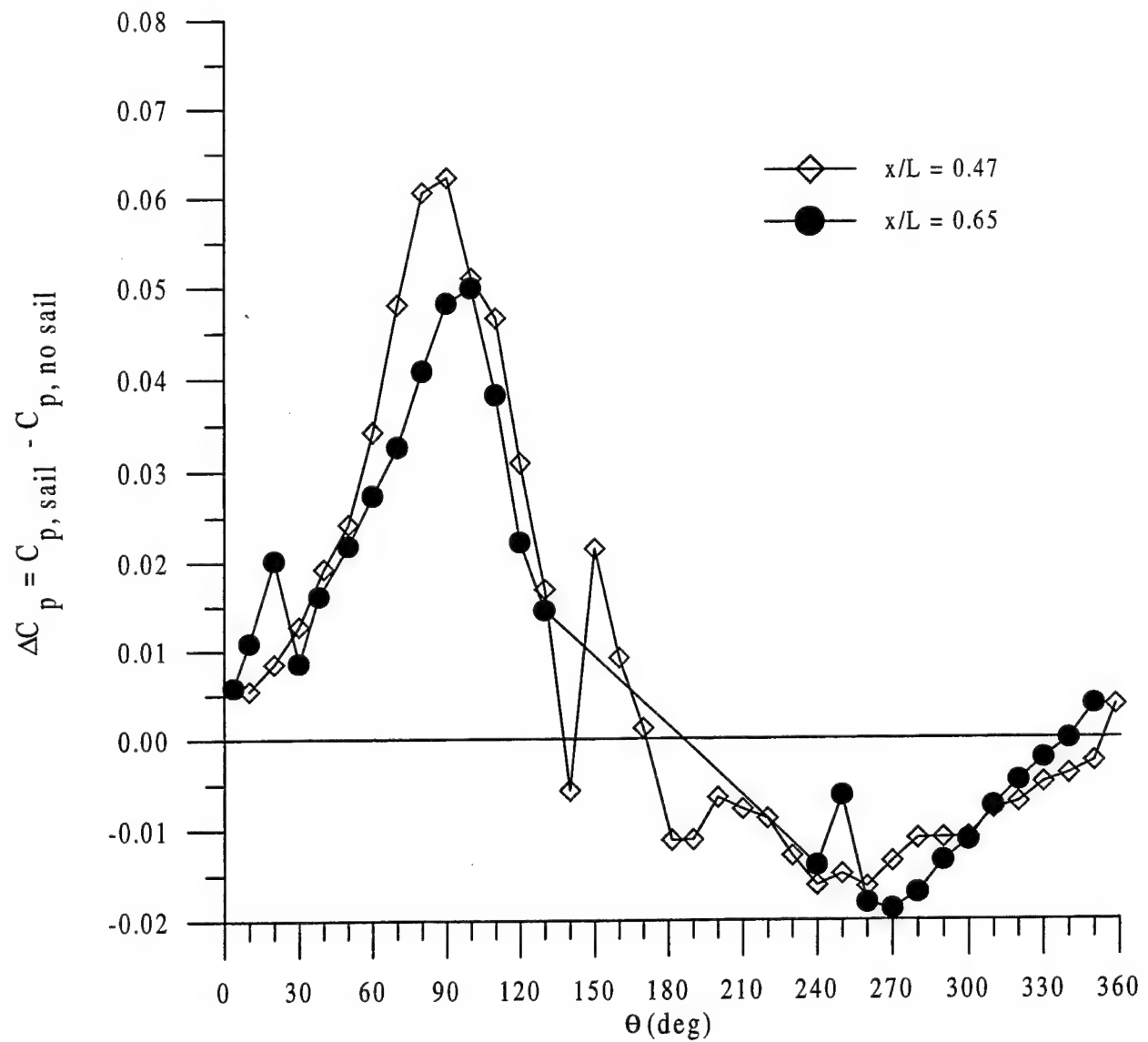
Figure 58 Pressure difference due to addition of sail: $\beta = 9.5$ deg
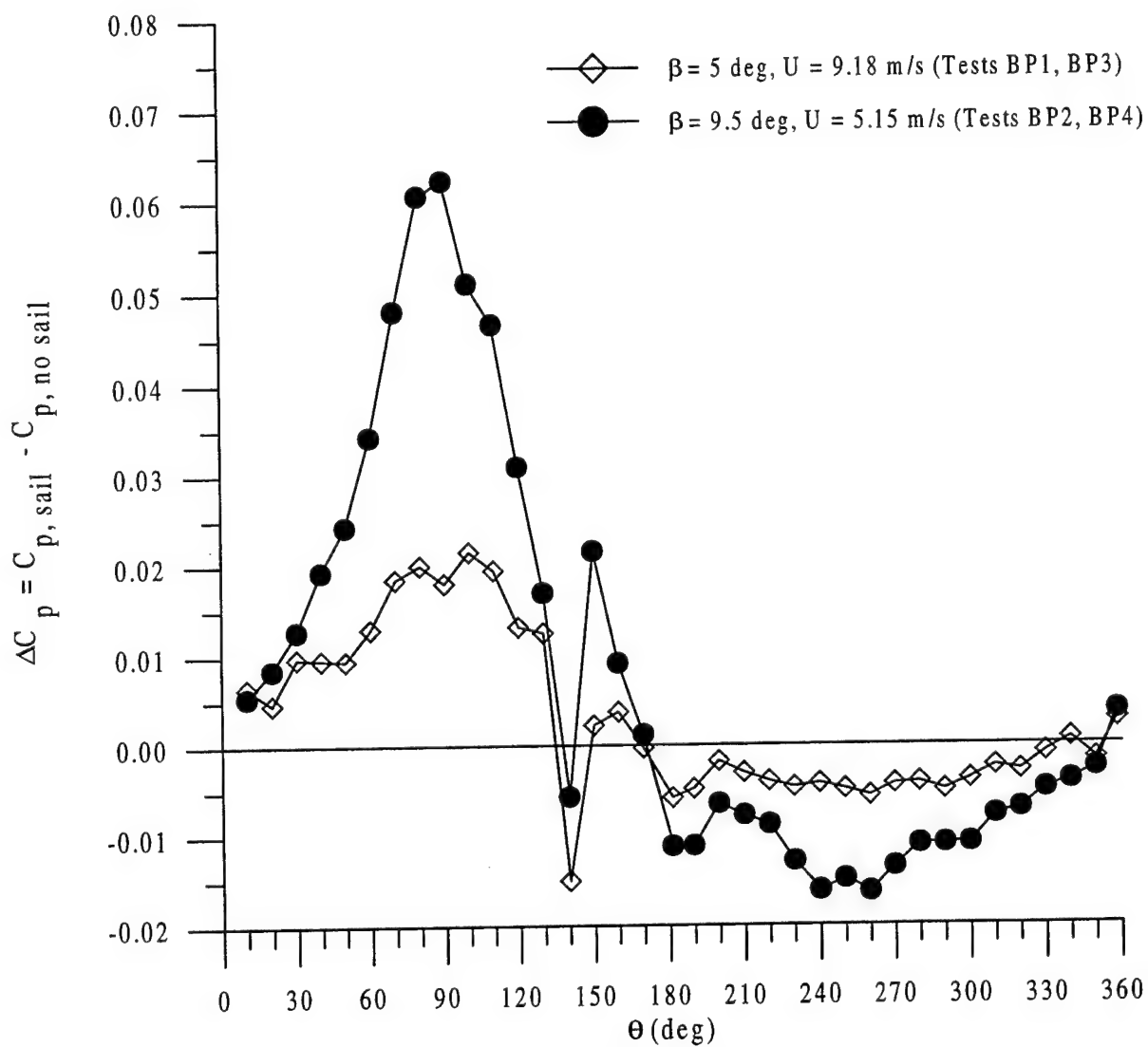
Figure 59 Development of pressure difference with angle of drift: $x/L = 0.47$
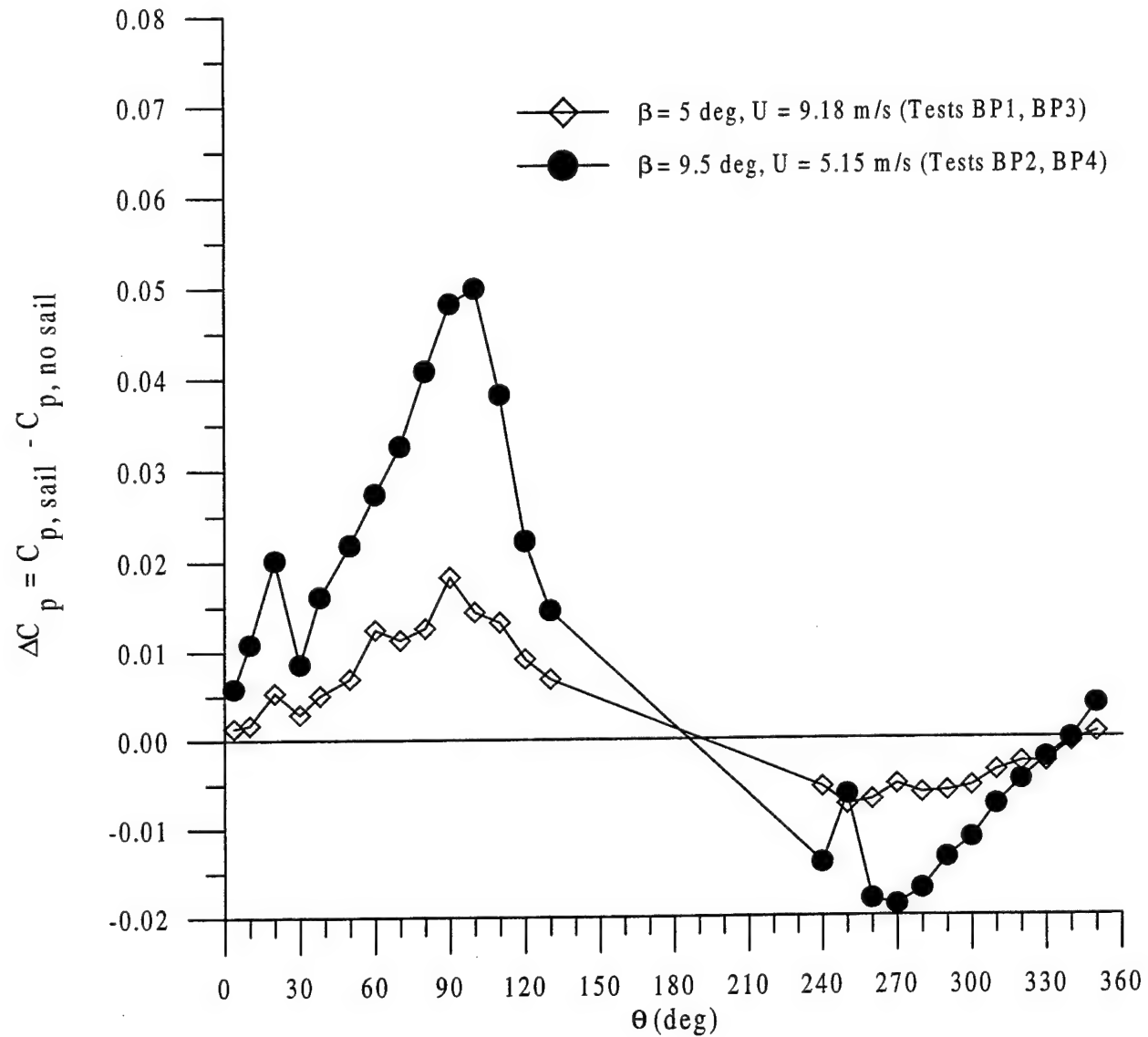
Figure 60 Development of pressure difference with angle of drift: *x/L* = 0.65
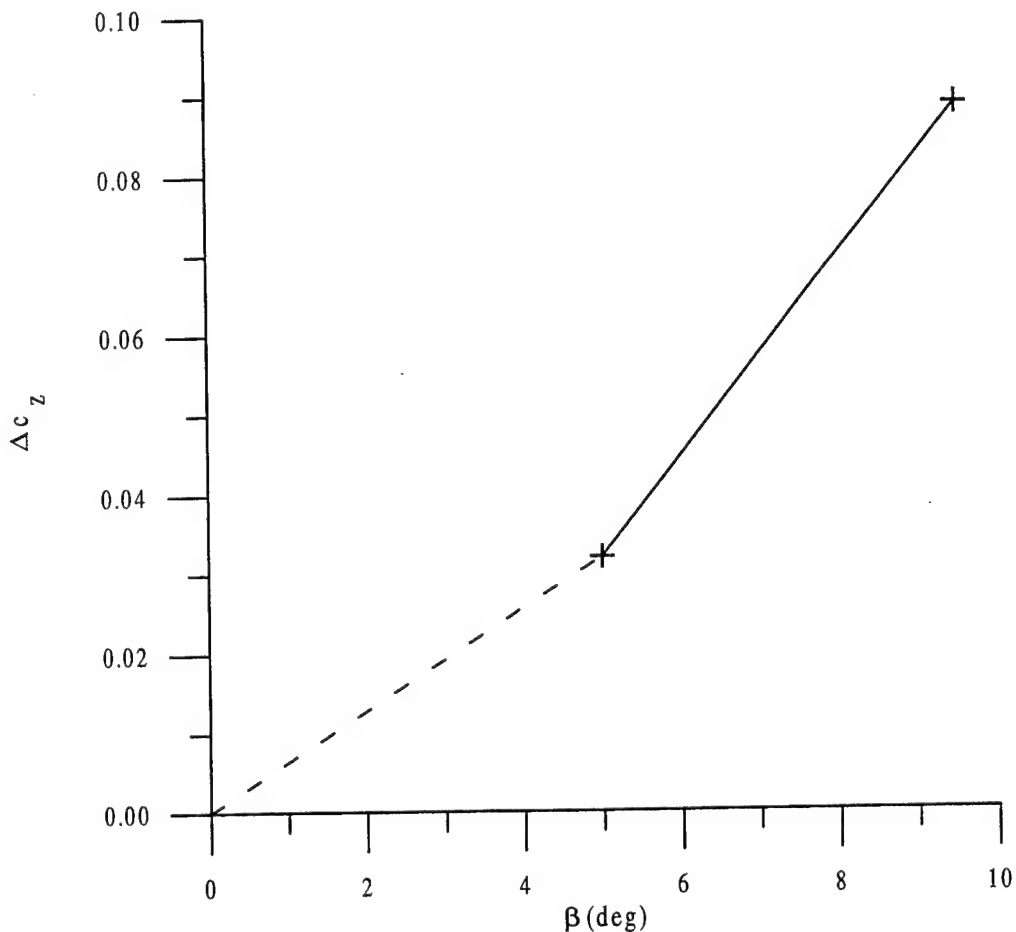
Figure 61 Variation of section vertical force coefficient obtained from pressure coefficient integrations
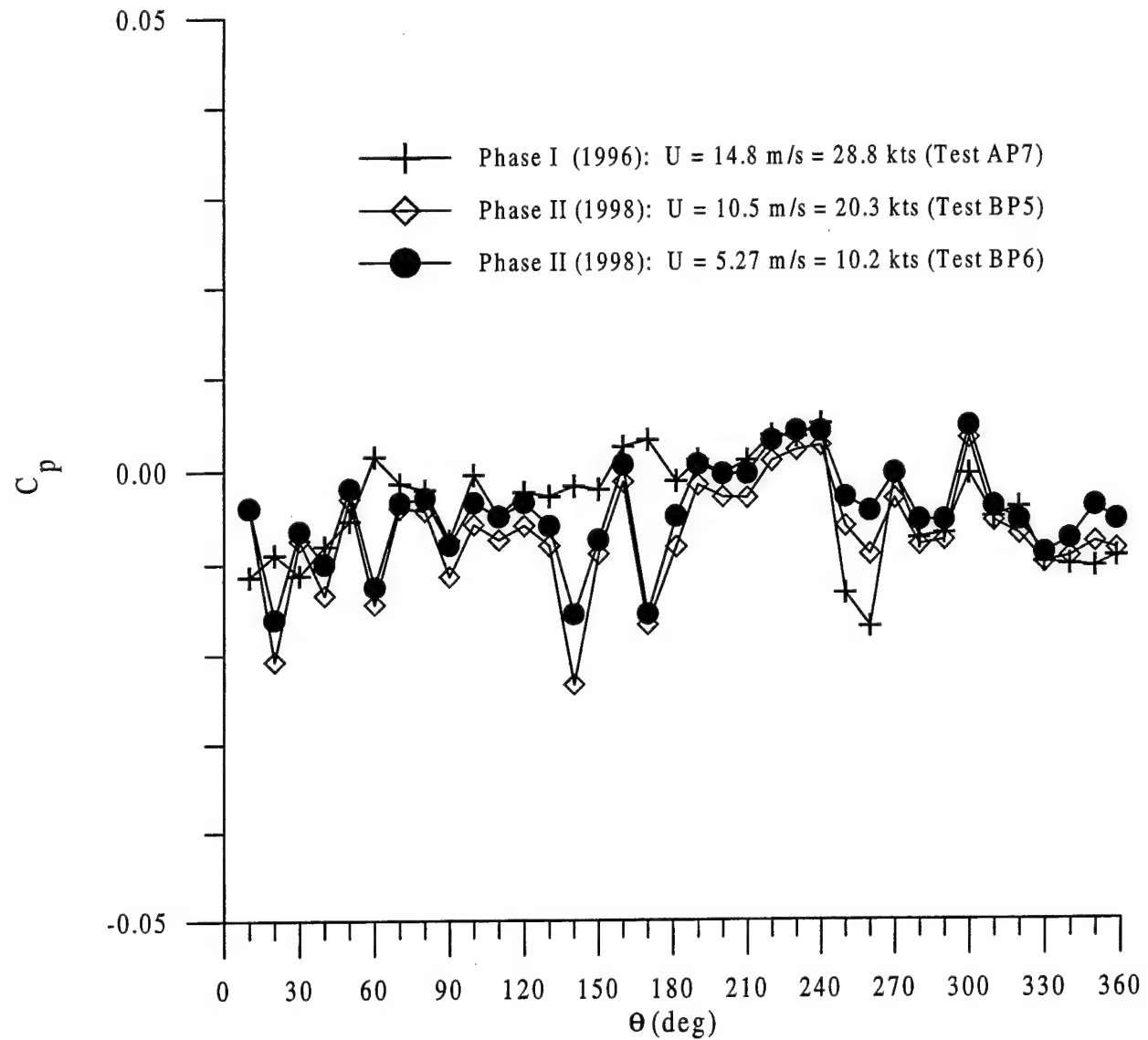
Figure 62 Comparison of Phase I and II pressure distributions: β = 0 deg, sail off, *x/L* = 0.47
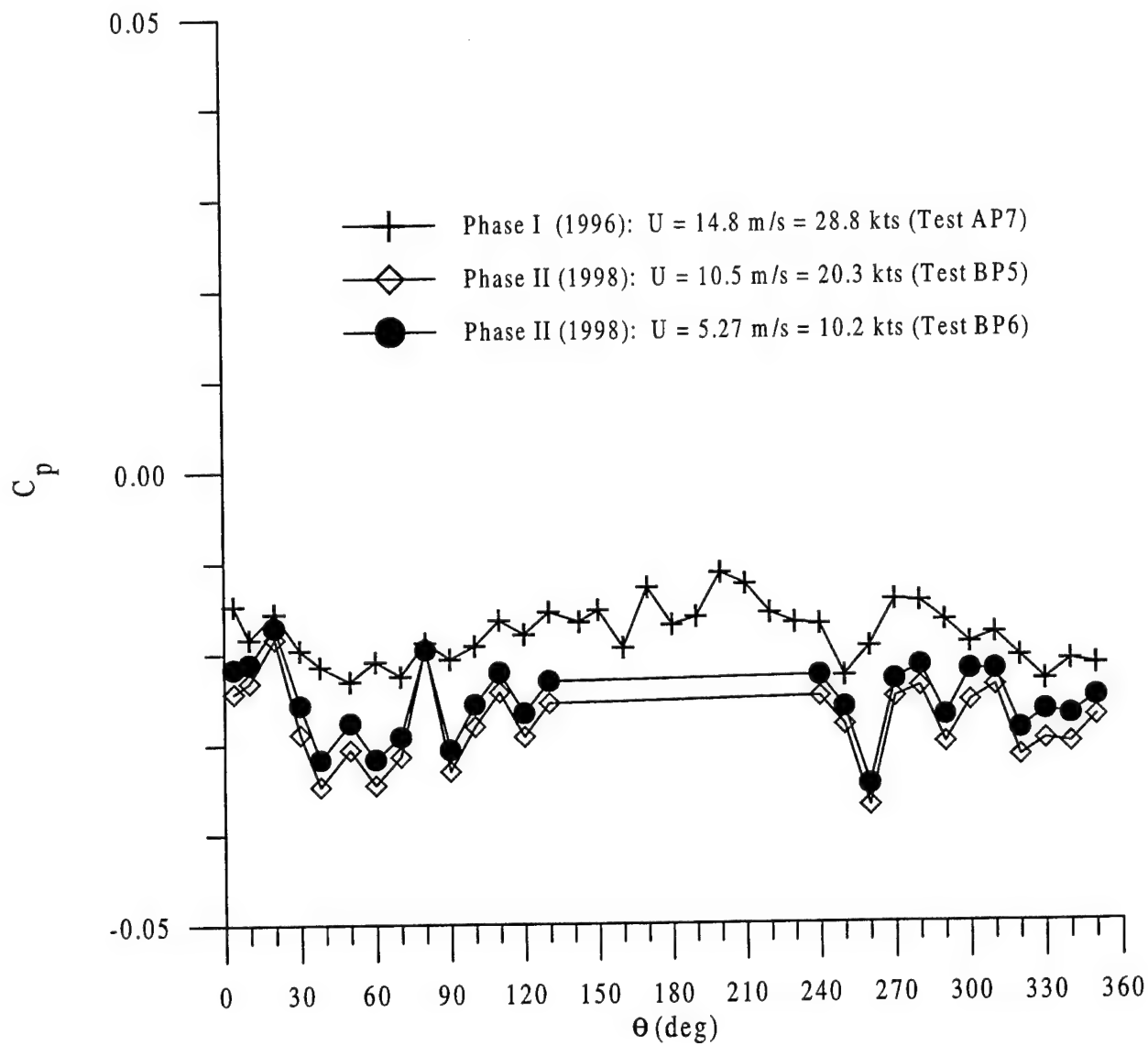
Figure 63 Comparison of Phase I and II pressure distributions: β = 0 deg, sail off, x/L = 0.65
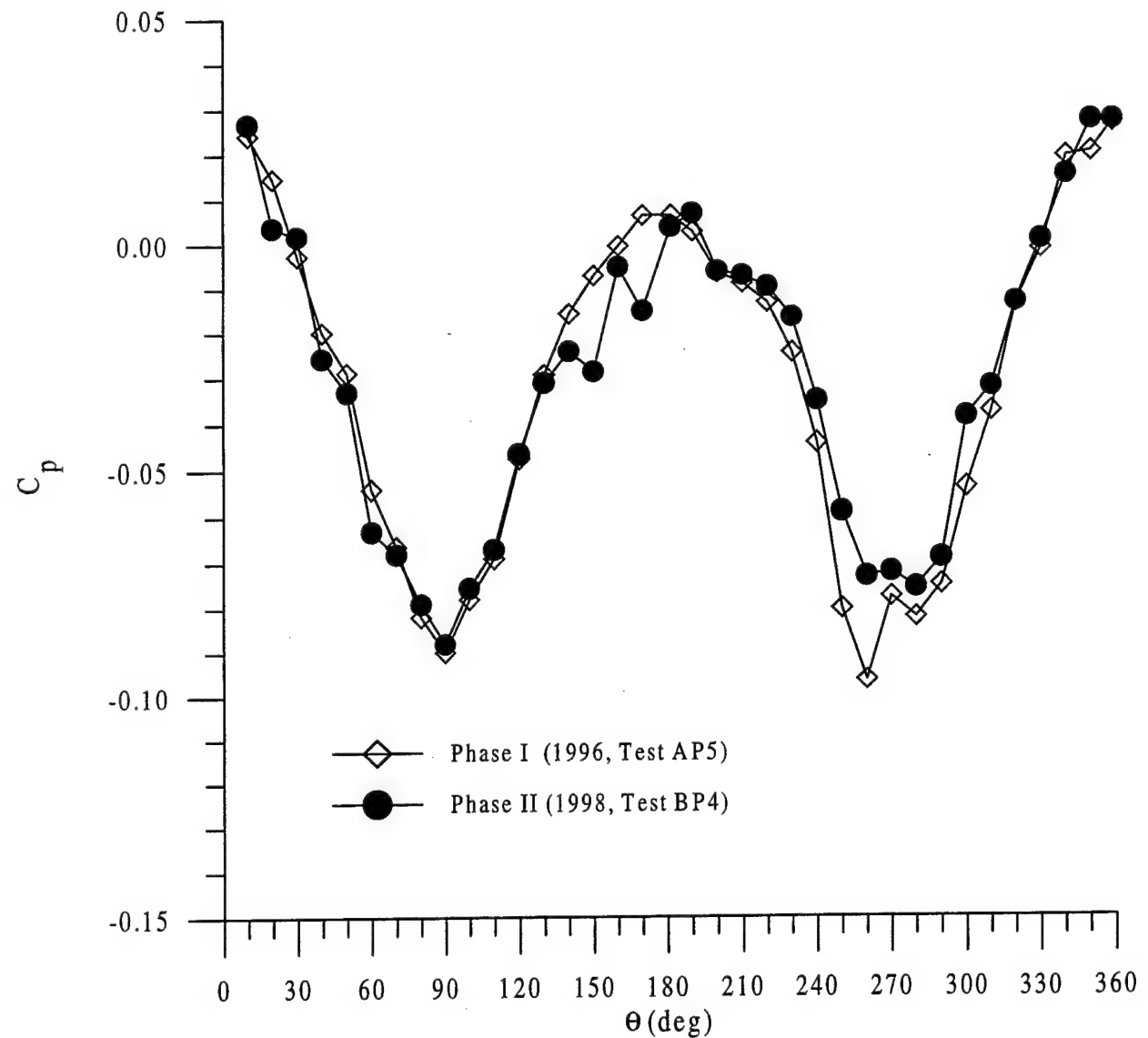
Figure 64 Comparison of Phase I and II pressure distributions: $\beta = 9.5$ deg, sail off, $x/L = 0.47$
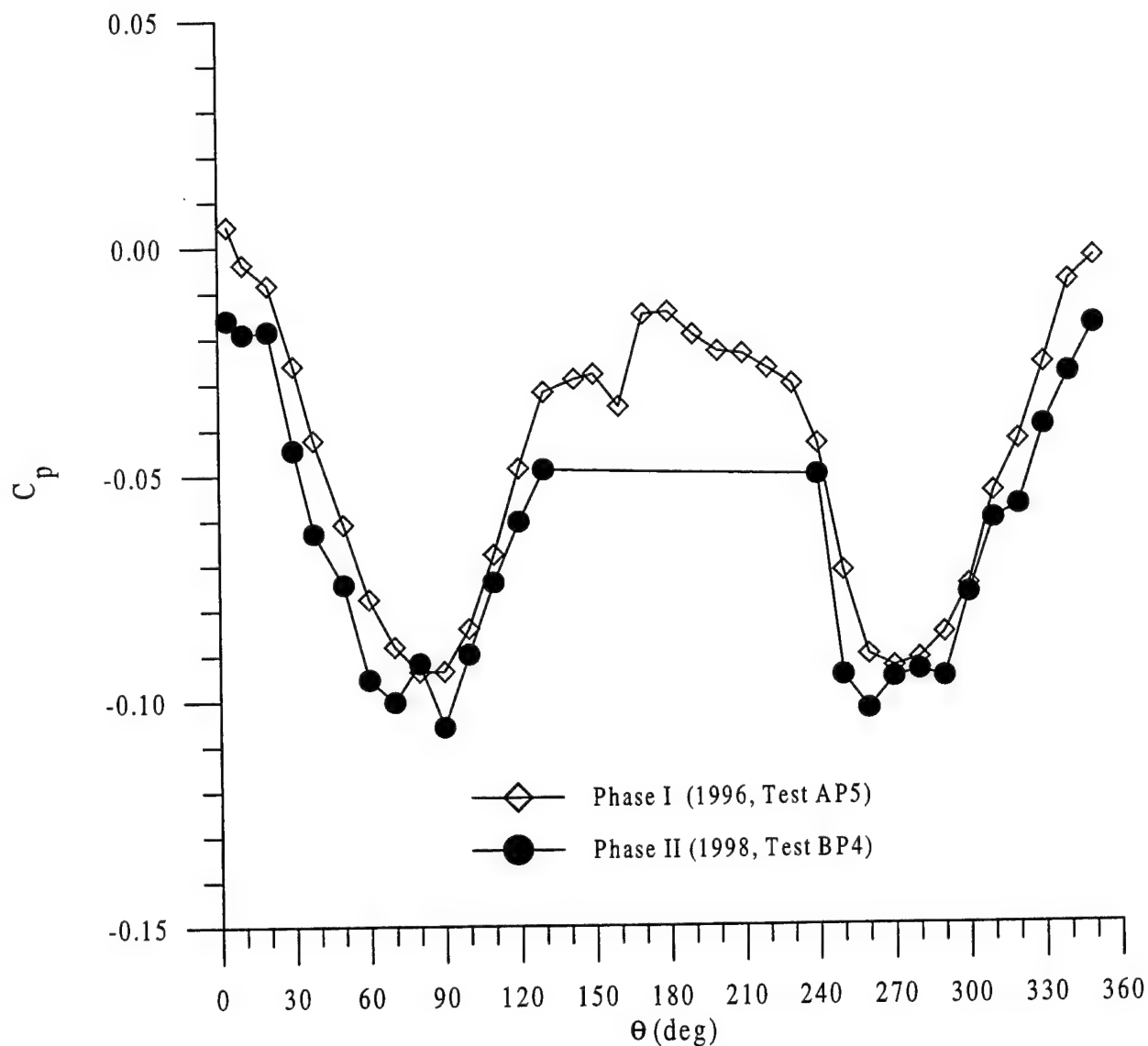
Figure 65 Comparison of Phase I and II pressure distributions: $\beta = 9.5$ deg, sail off, $x/L = 0.65$
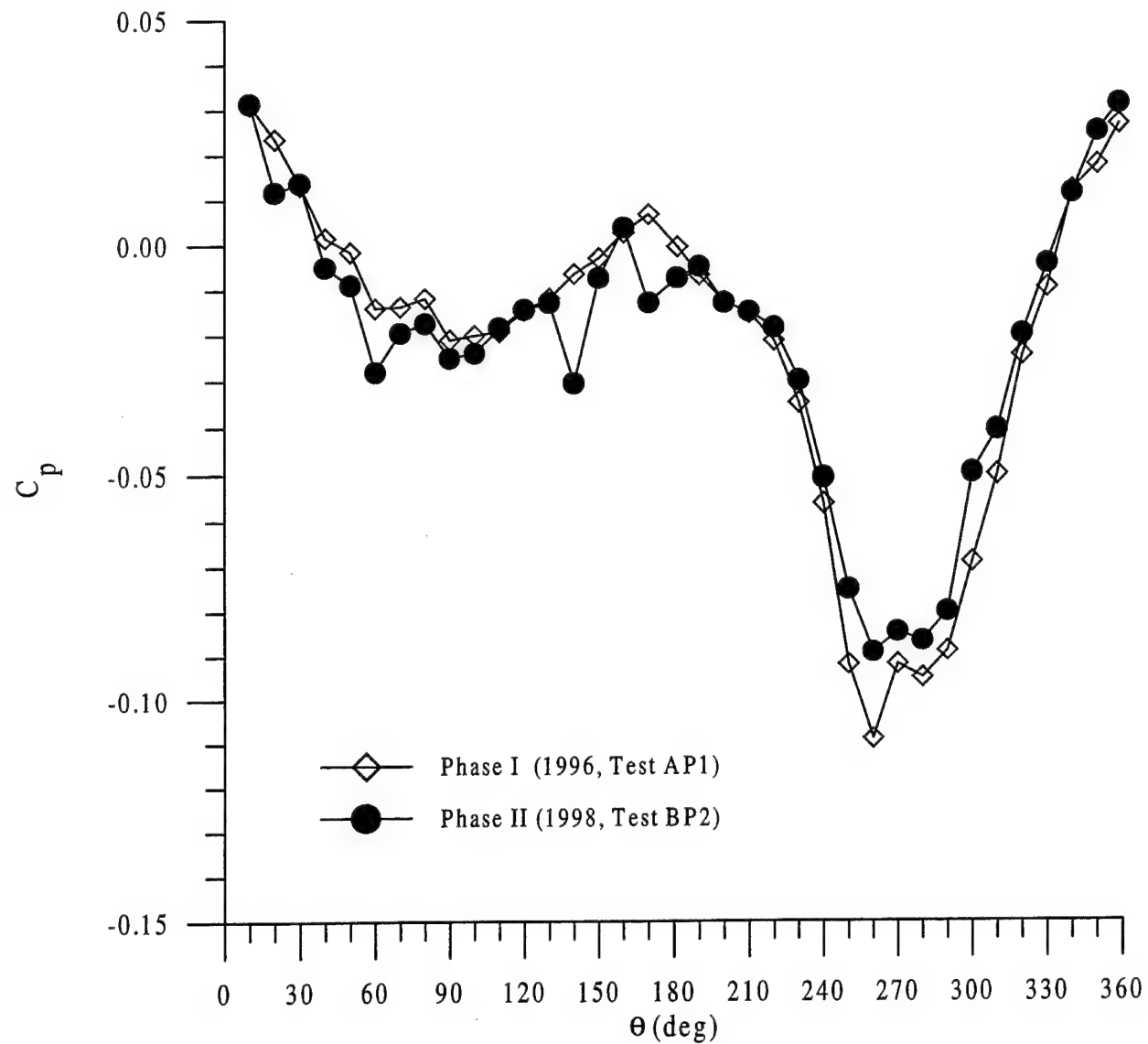
Figure 66 Comparison of Phase I and II pressure distributions: $\beta = 9.5$ deg, sail on, $x/L = 0.47$
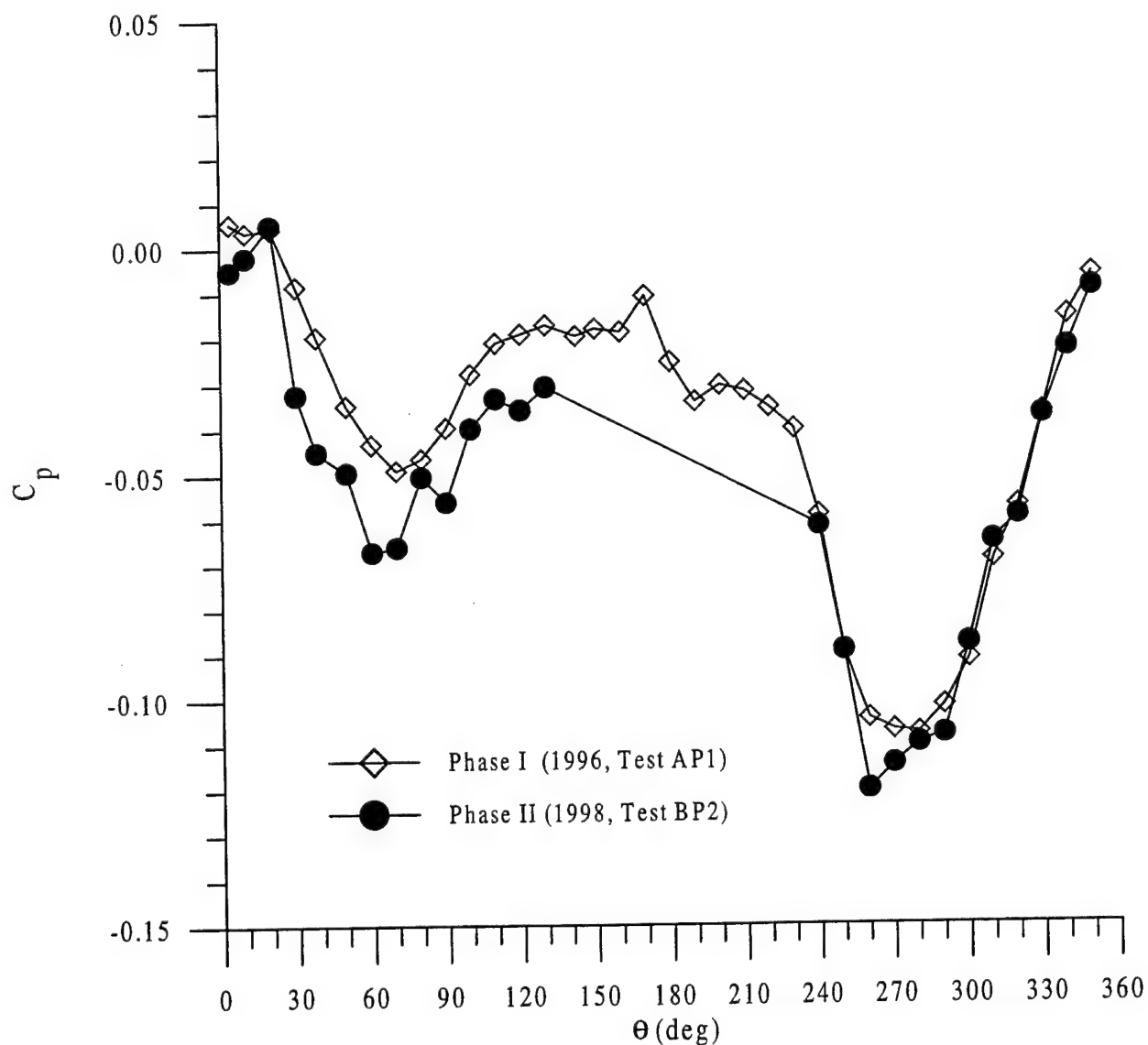
Figure 67 Comparison of Phase I and II pressure distributions: β = 9.5 deg, sail on, *x/L* = 0.65
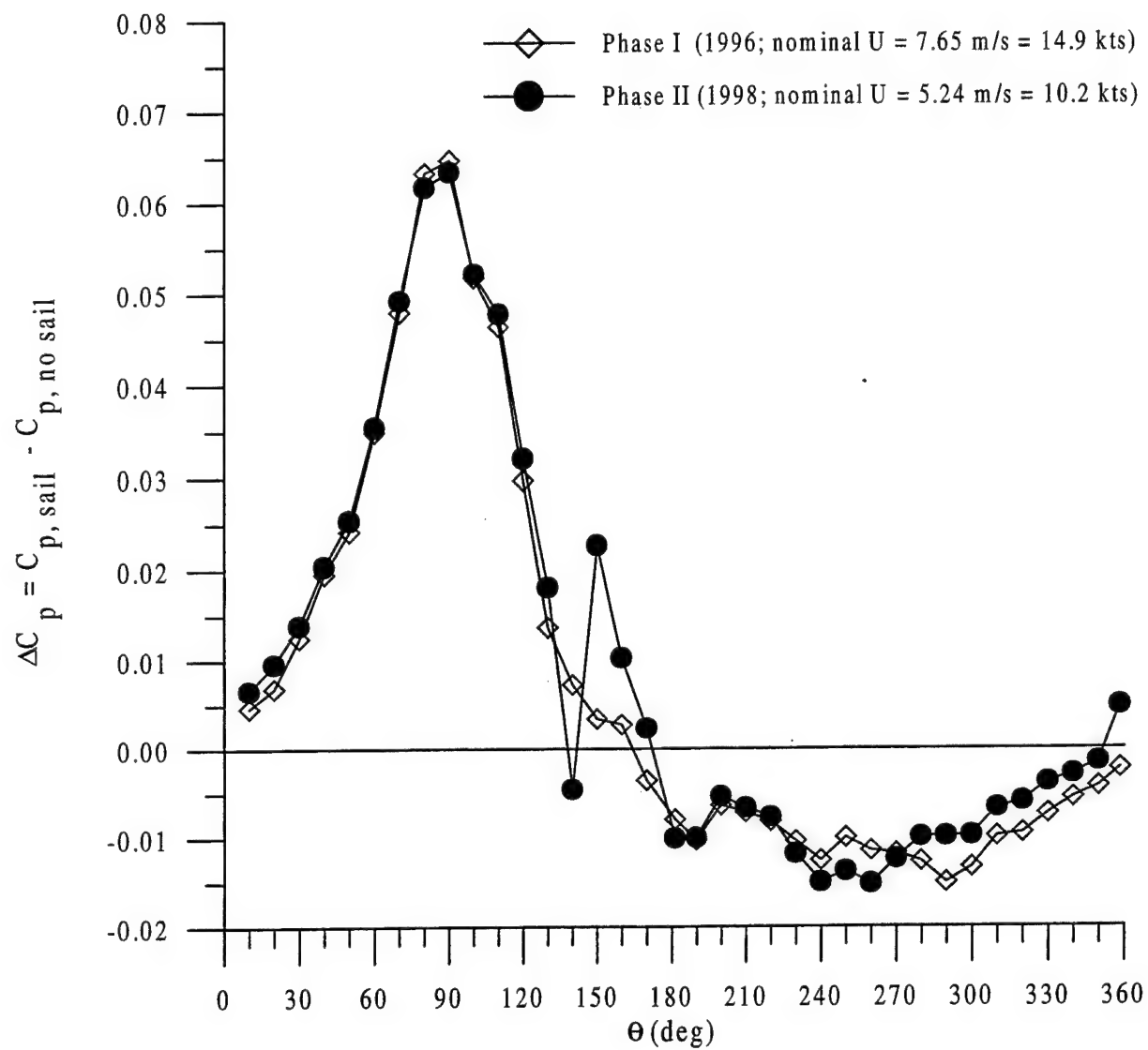
Figure 68 Comparison of Phase I and II pressure differences: $\beta = 9.5$ deg, $x/L = 0.47$
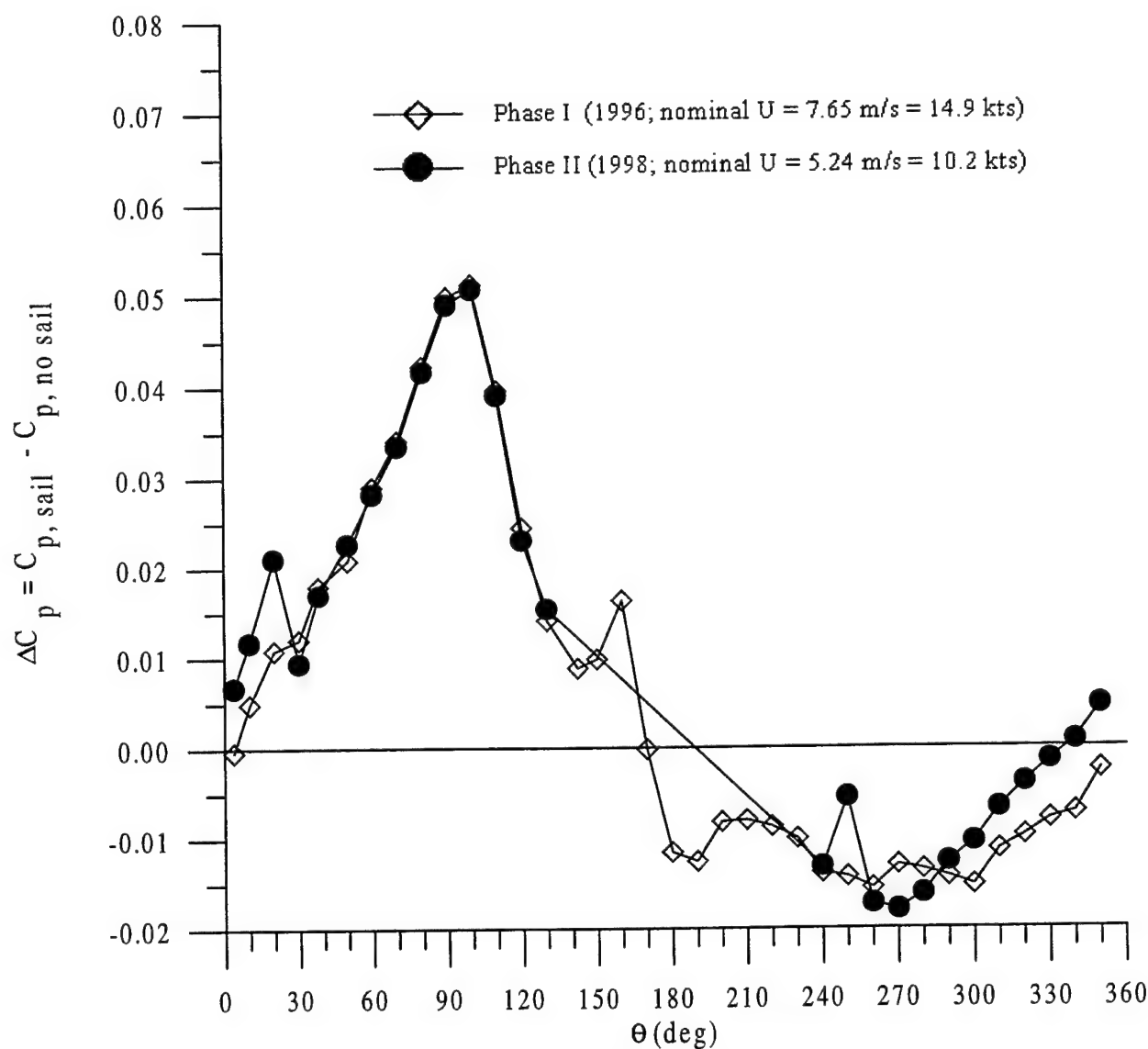
Figure 69 Comparison of Phase I and II pressure differences: $\beta = 9.5$ deg, $x/L = 0.65$
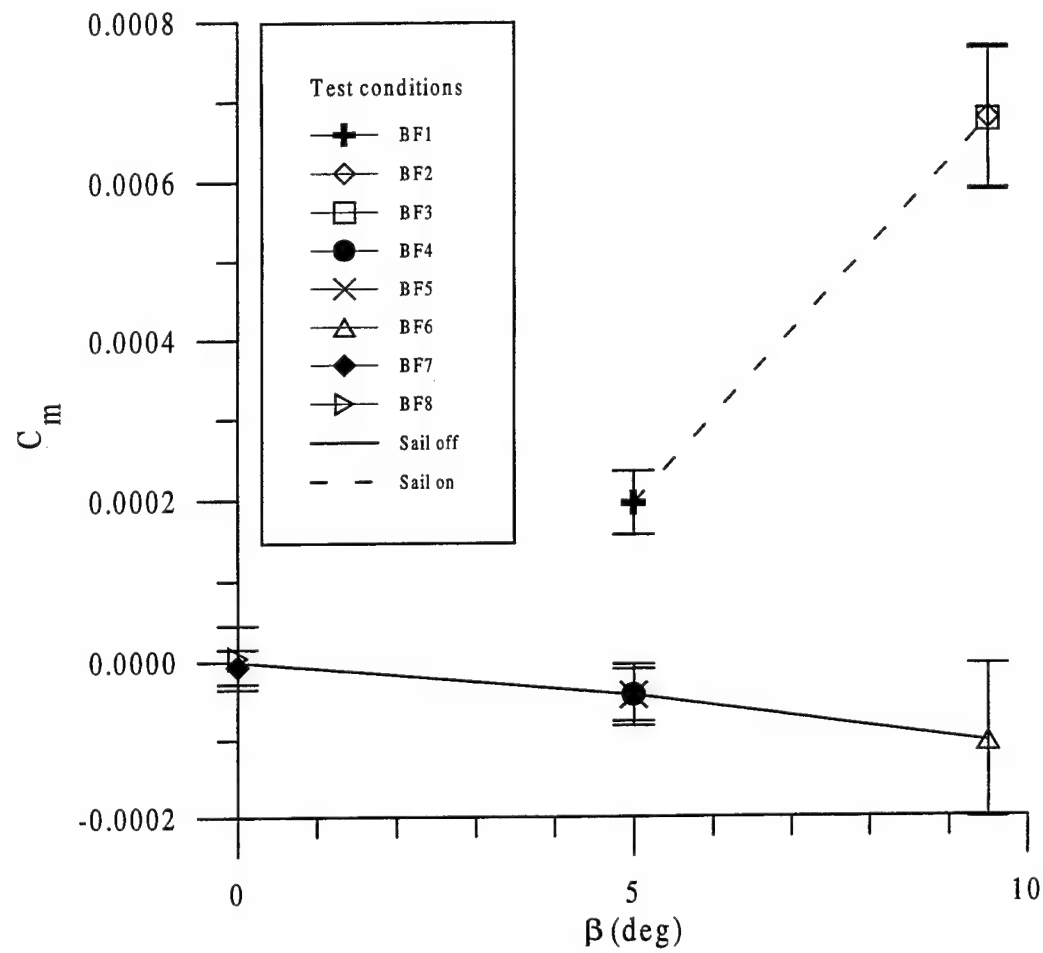
Figure 70 Pitching moment variation with drift angle
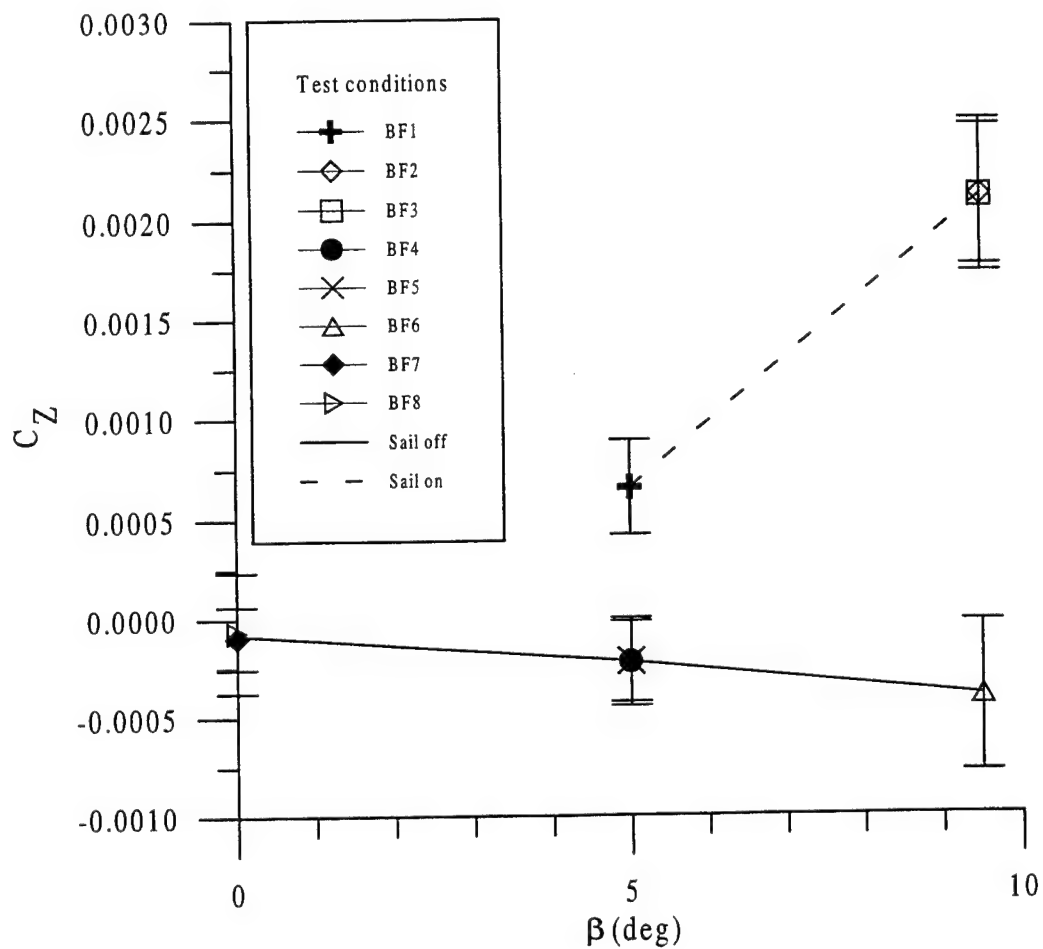
Figure 71 Vertical force variation with drift angle
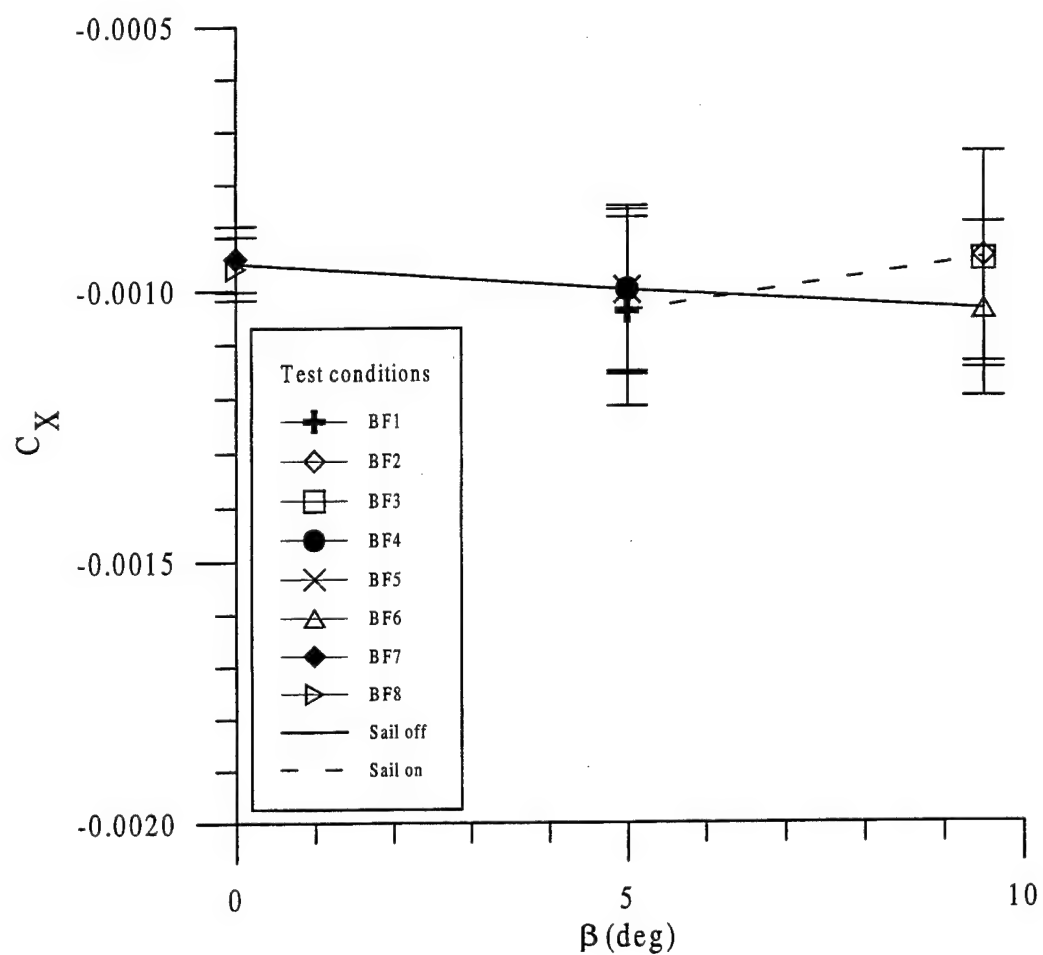
Figure 72 Axial force variation with drift angle
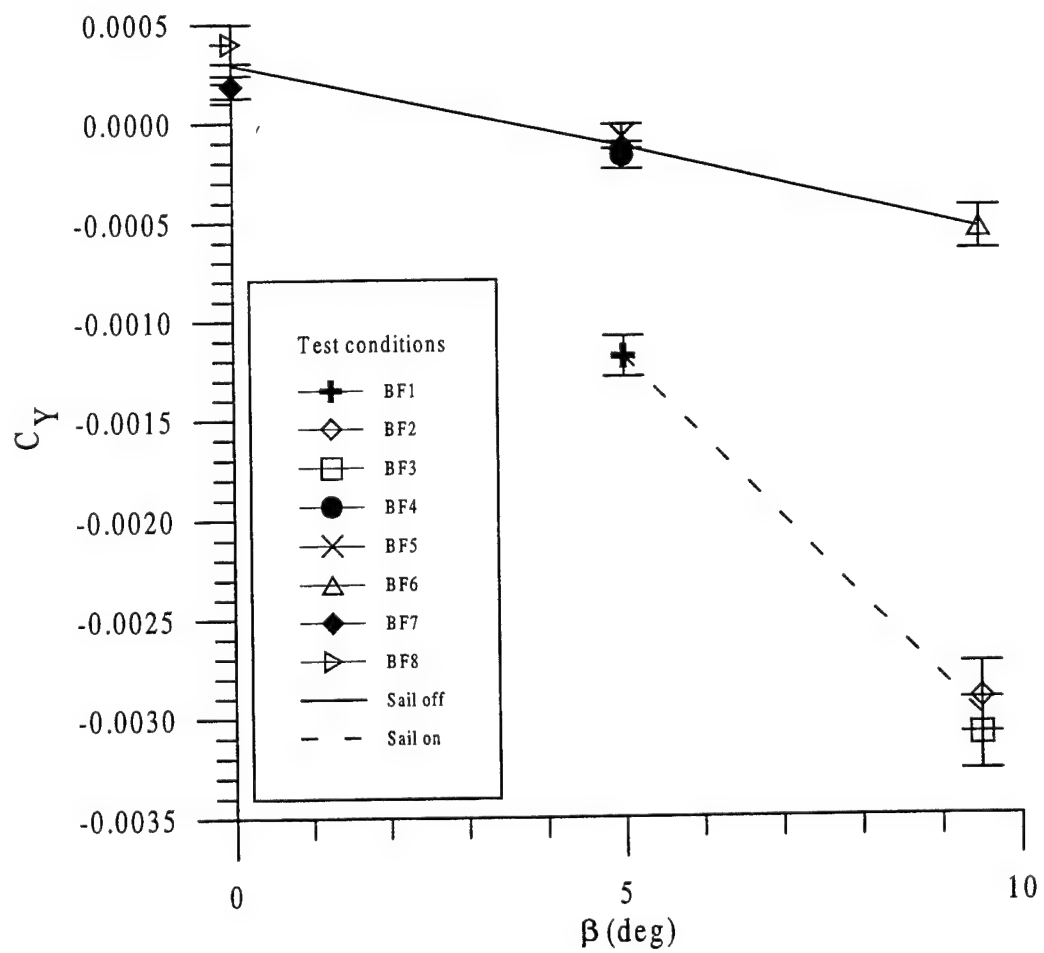
Figure 73 Side force variation with drift angle
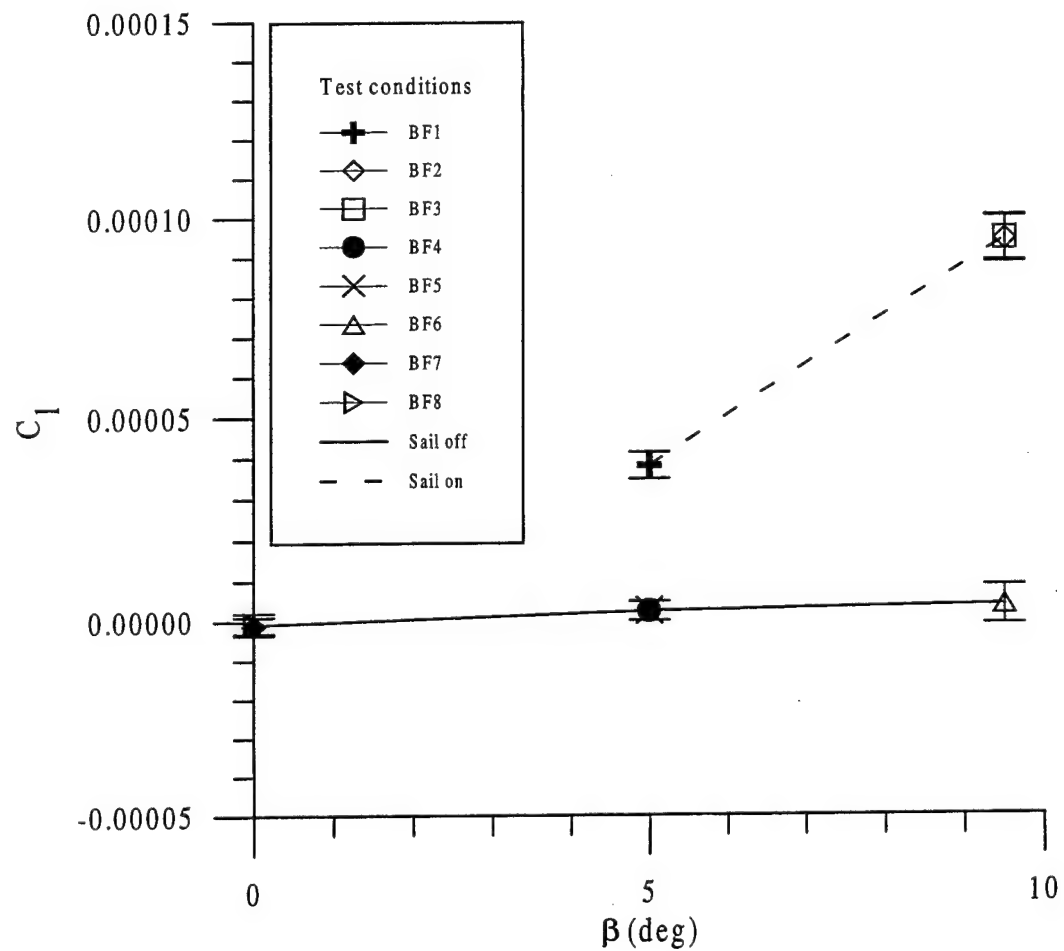
Figure 74 Rolling moment variation with drift angle
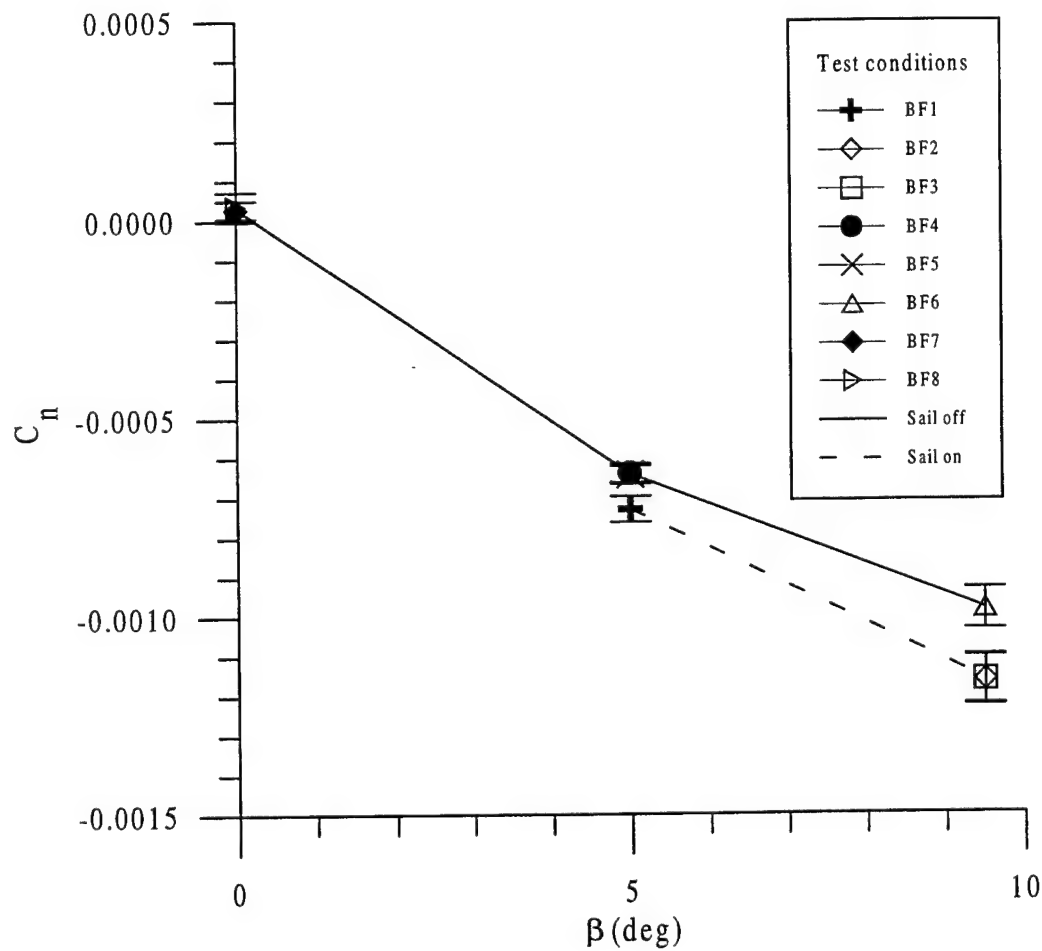
Figure 75 Yawing moment variation with drift angle
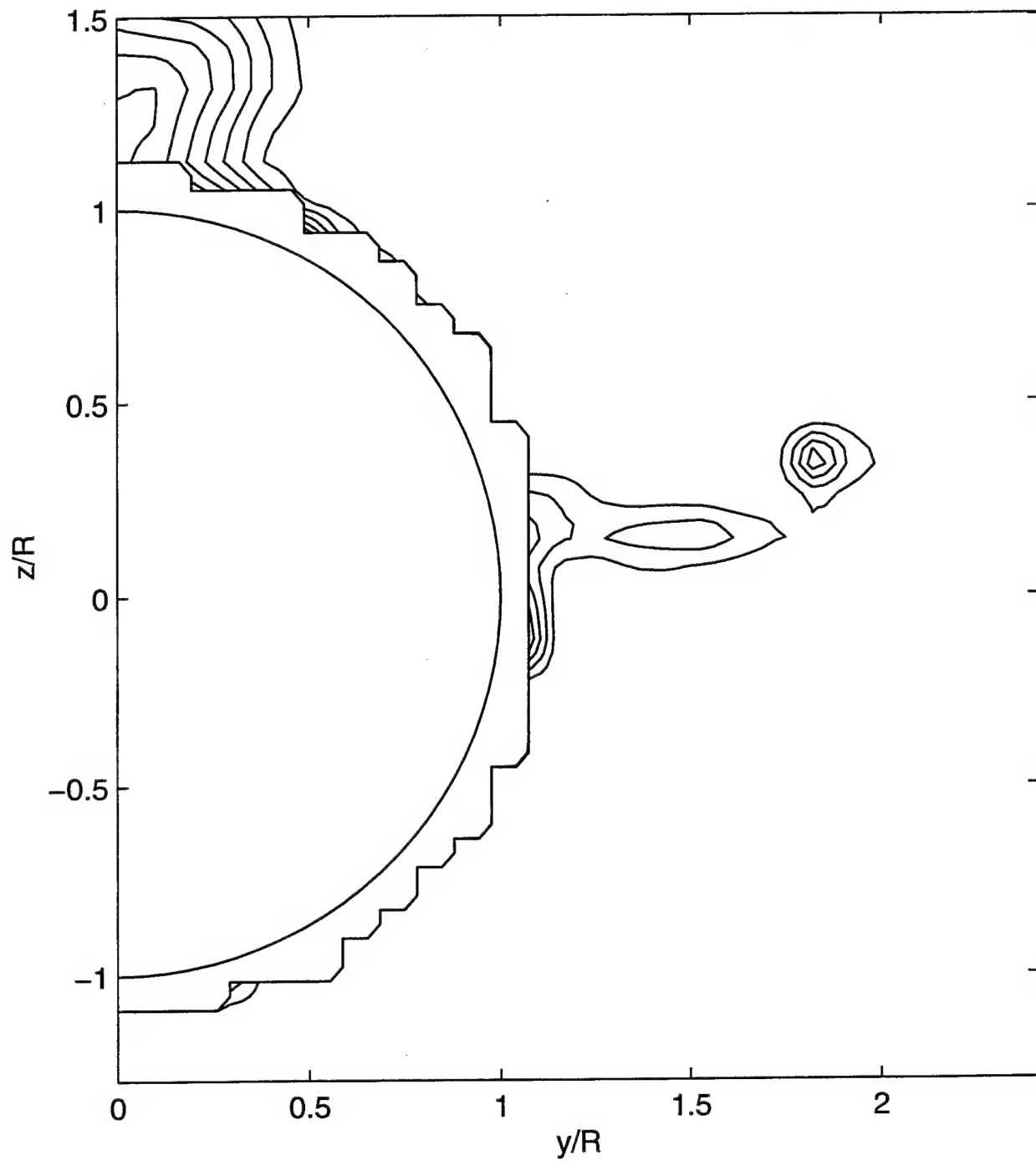
$u_{max} = 9.45$ m/s, $F_V = 0.75$, $N_{cont} = 10$

Figure 76 Streamwise velocity contours: $\beta = 5$ deg, $U = 9.33$ m/s, sail on, $x/L = 0.47$ (Test BV01)
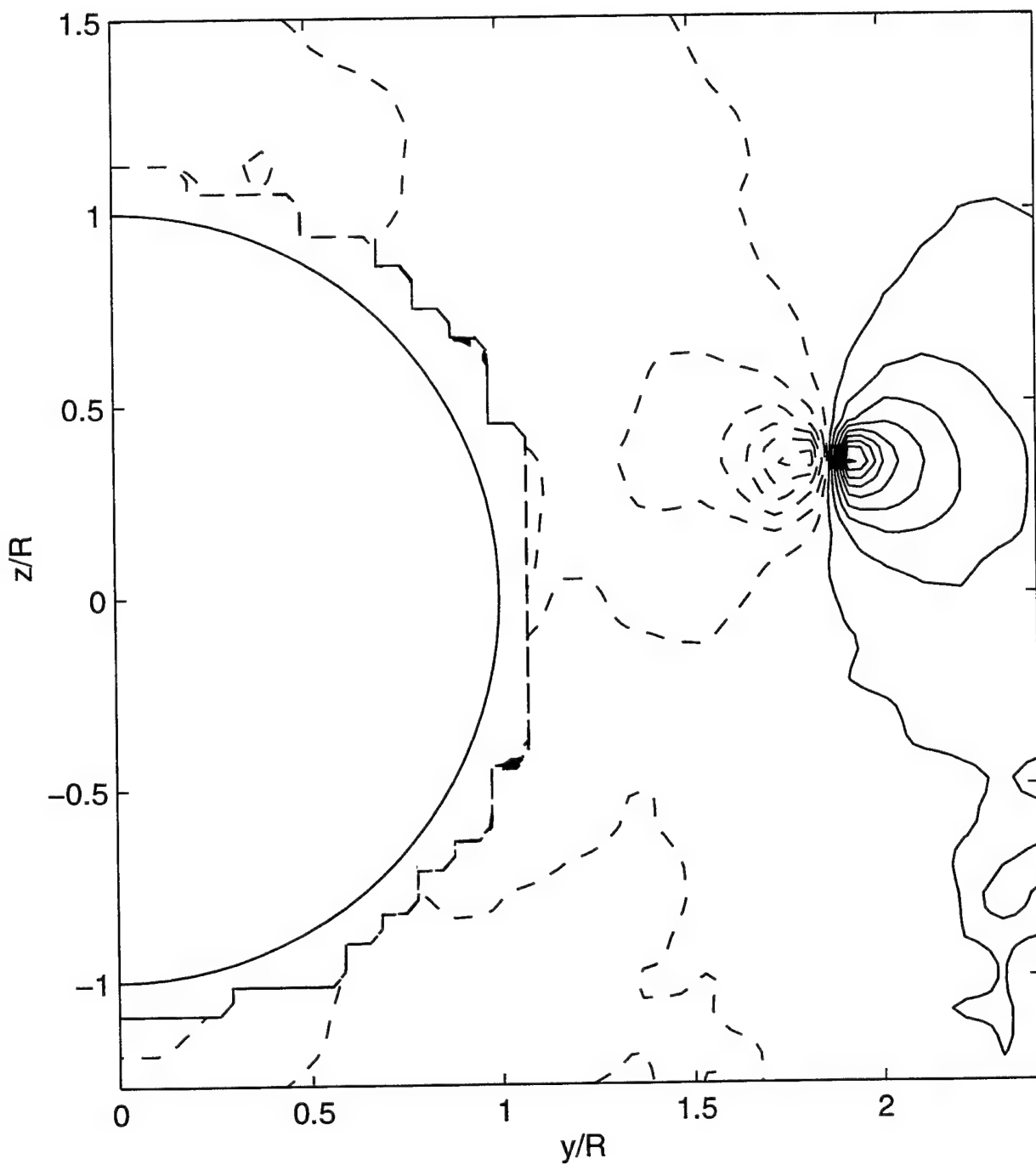
$w_{max} = 2.90$ m/s, $F_V = 0$, $N_{cont} = 10$

**Figure 77** Transverse velocity contours: $\beta = 5$ deg, $U = 9.29$ m/s, sail on, $x/L = 0.47$ (Test BV02)

$u_{max} = 9.44$ m/s, $F_V = 0.8$, $N_{cont} = 10$
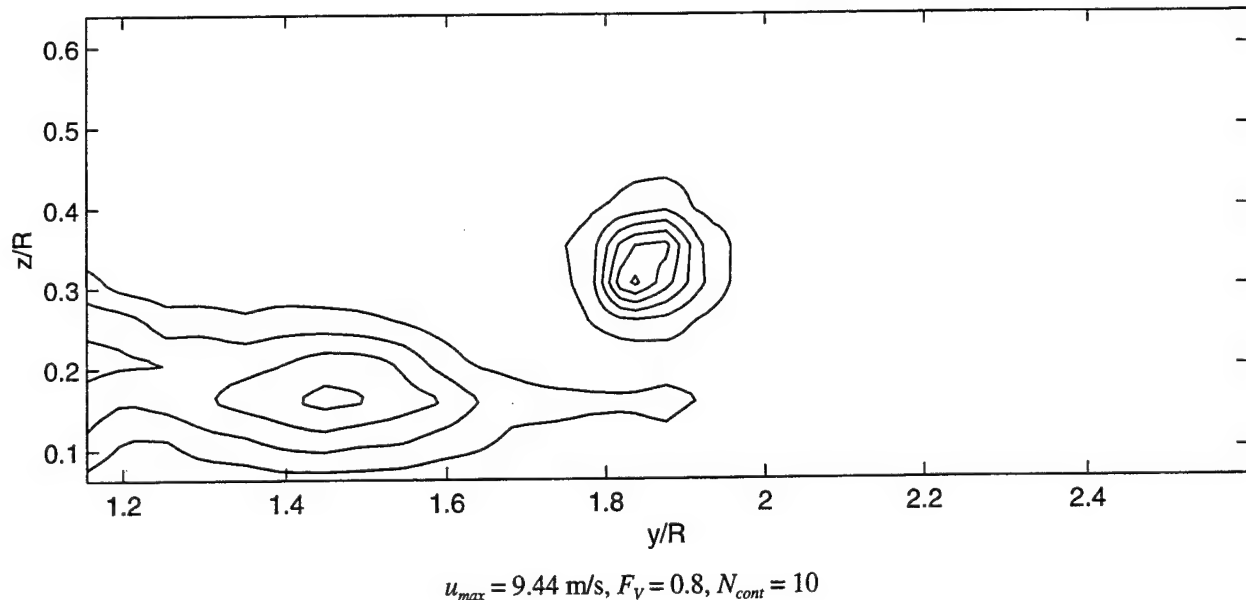
Figure 78 Streamwise velocity contours (detailed grid): $\beta = 5$ deg, $U = 9.36$ m/s, sail on, $x/L = 0.47$ (Test BV03)

$w_{max} = 3.27$ m/s, $F_V = 0.0$, $N_{cont} = 10$
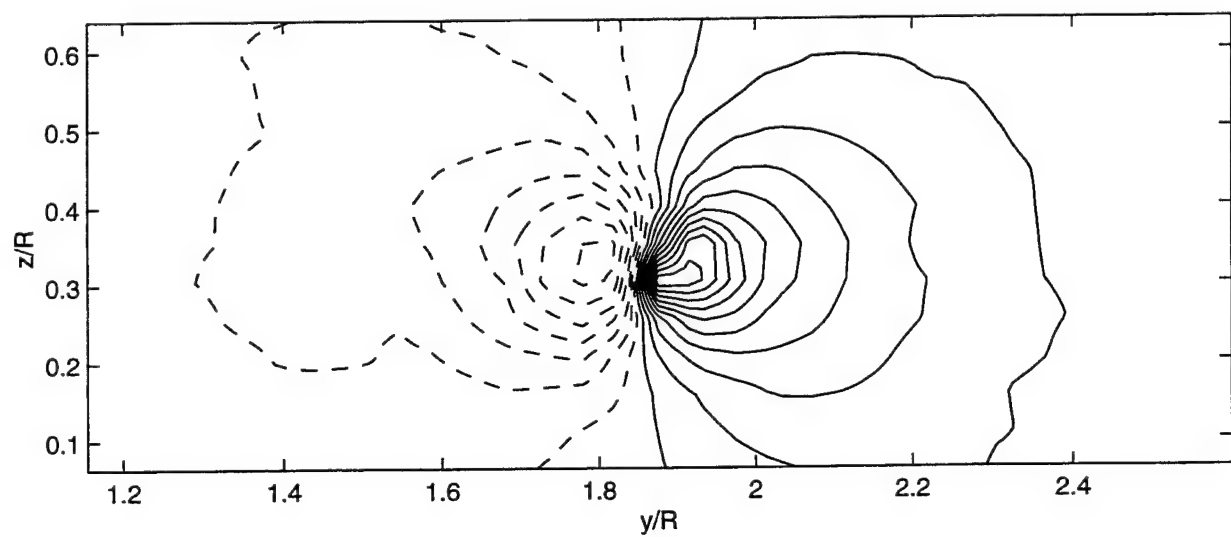
**Figure 79** Transverse velocity contours (detailed grid): $\beta = 5$ deg, $U = 9.39$ m/s, sail on, $x/L = 0.47$ (Test BV04)
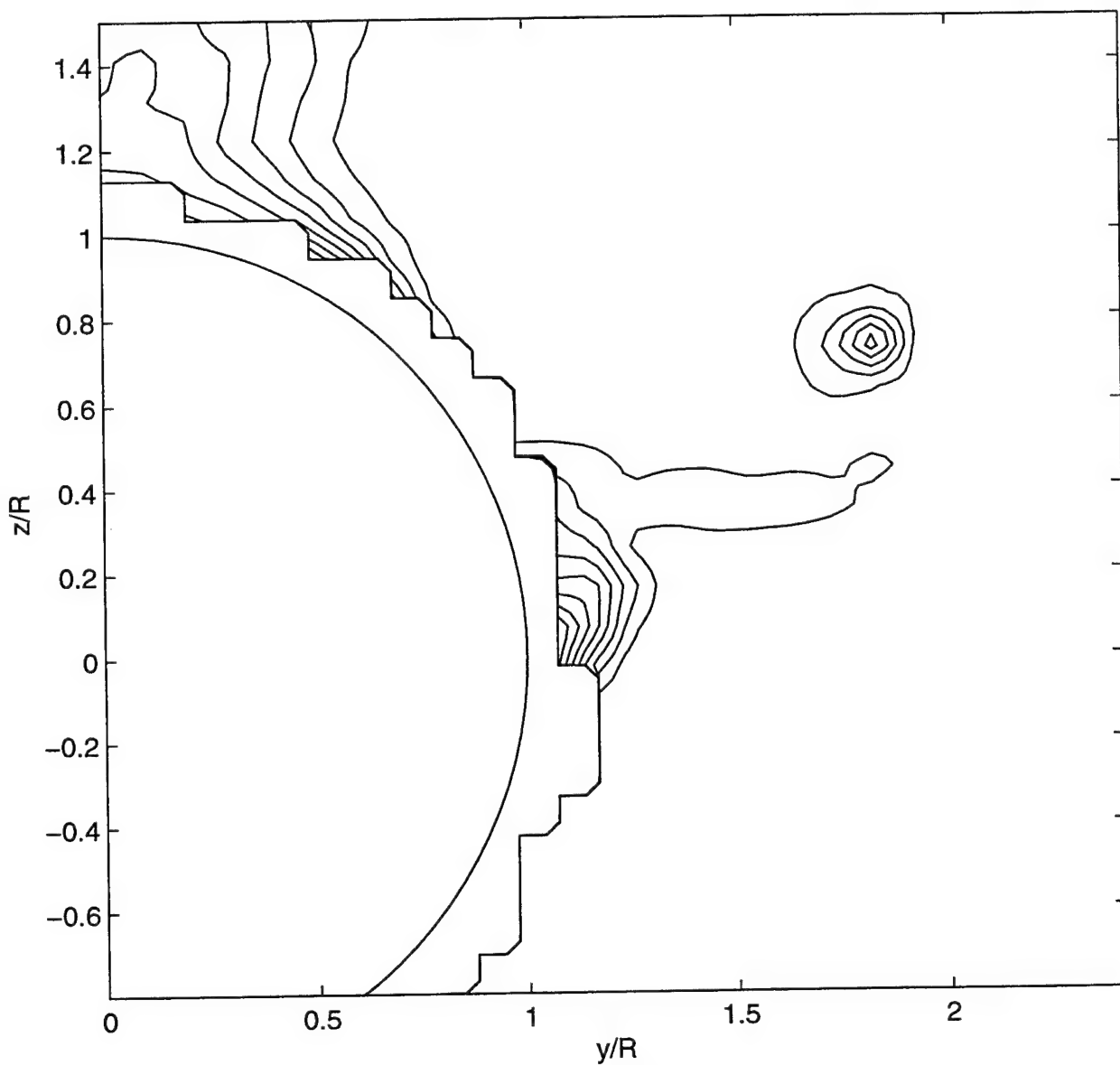
$u_{max} = 9.48$ m/s, $F_V = 0.8$, $N_{cont} = 10$

Figure 80 Streamwise velocity contours: $\beta = 5$ deg, $U = 9.38$ m/s, sail on, $x/L = 0.59$ (Test BV05)
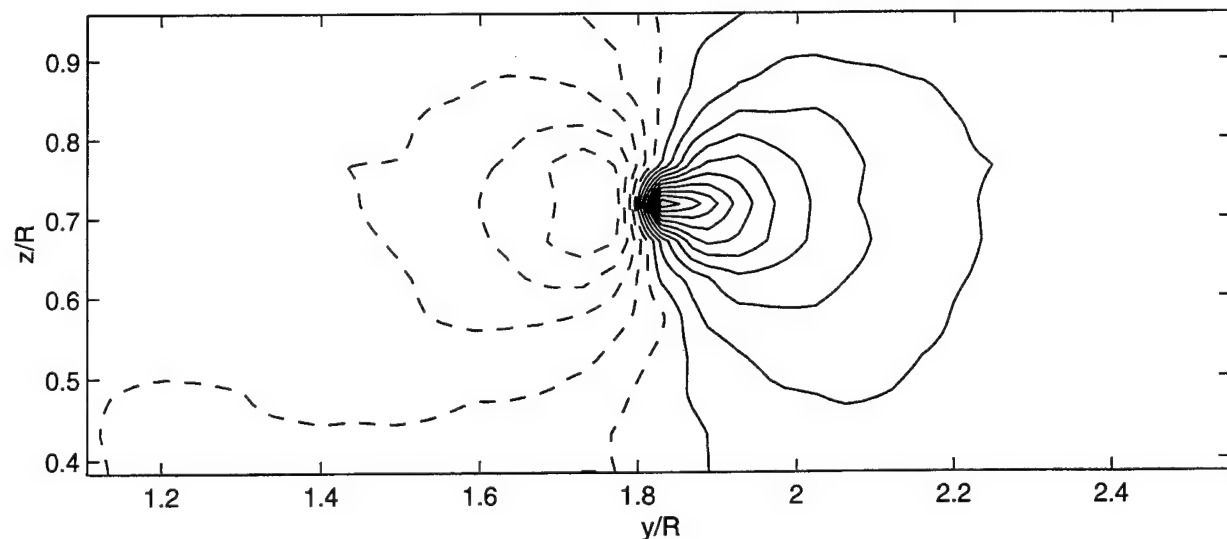
$w_{max} = 3.38$ m/s, $F_v = 0$, $N_{cont} = 10$

Figure 81 Transverse velocity contours (detailed grid): $\beta = 5$ deg, $U = 9.39$ m/s, sail on, $x/L = 0.59$ (Test BV06)

$u_{max} = 5.43$ m/s, $F_v = 0.85$, $N_{cont} = 10$
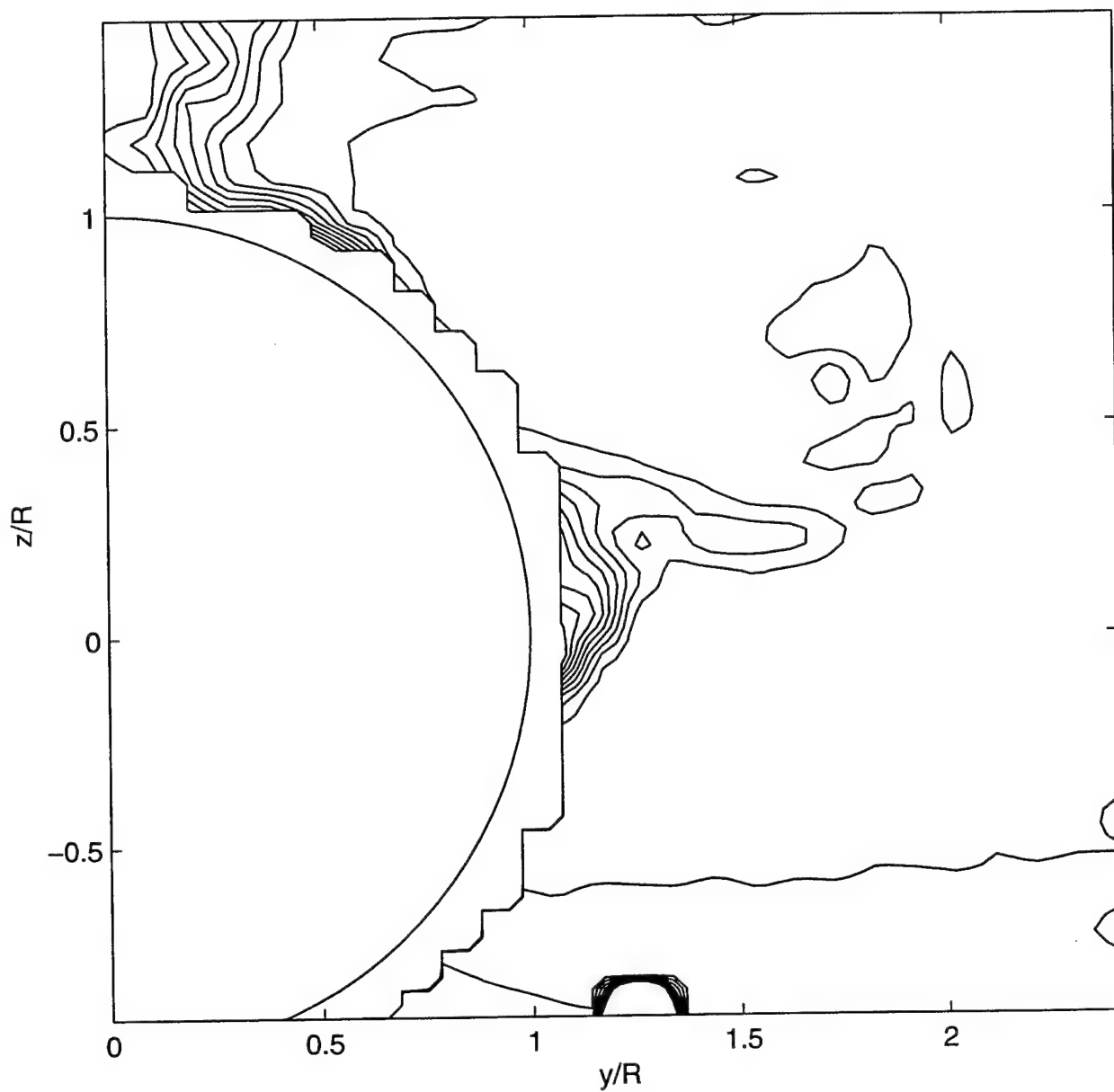
**Figure 82** Streamwise velocity contours: $\beta = 9.5$ deg, $U = 5.24$ m/s, sail on, $x/L = 0.48$ (Test BV07)

$w_{max} = 3.76$ m/s, $F_v = 0$, $N_{cont} = 10$
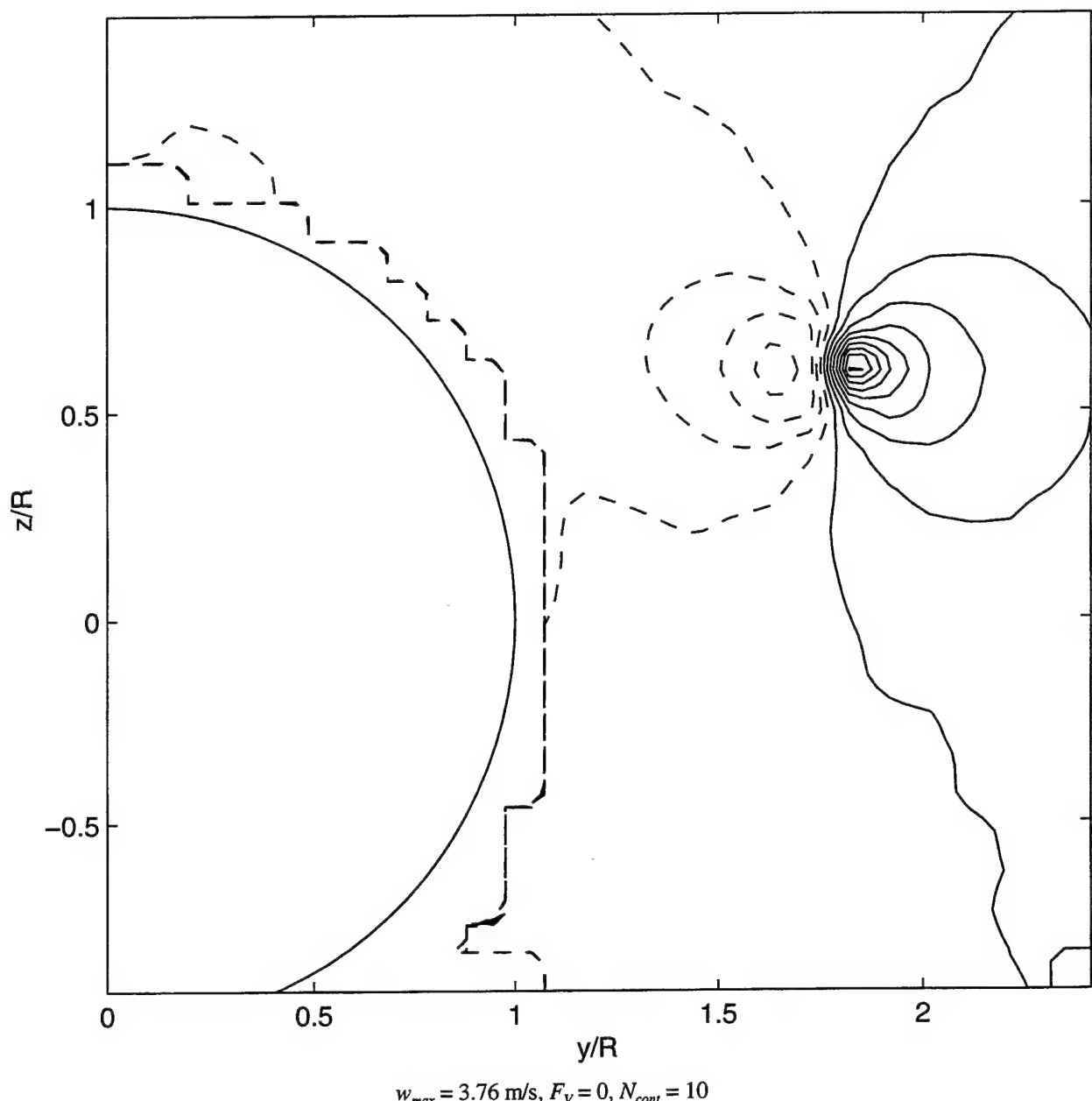
Figure 83 Transverse velocity contours: $\beta = 9.5$ deg, $U = 5.23$ m/s, sail on, $x/L = 0.48$ (Test BV08)
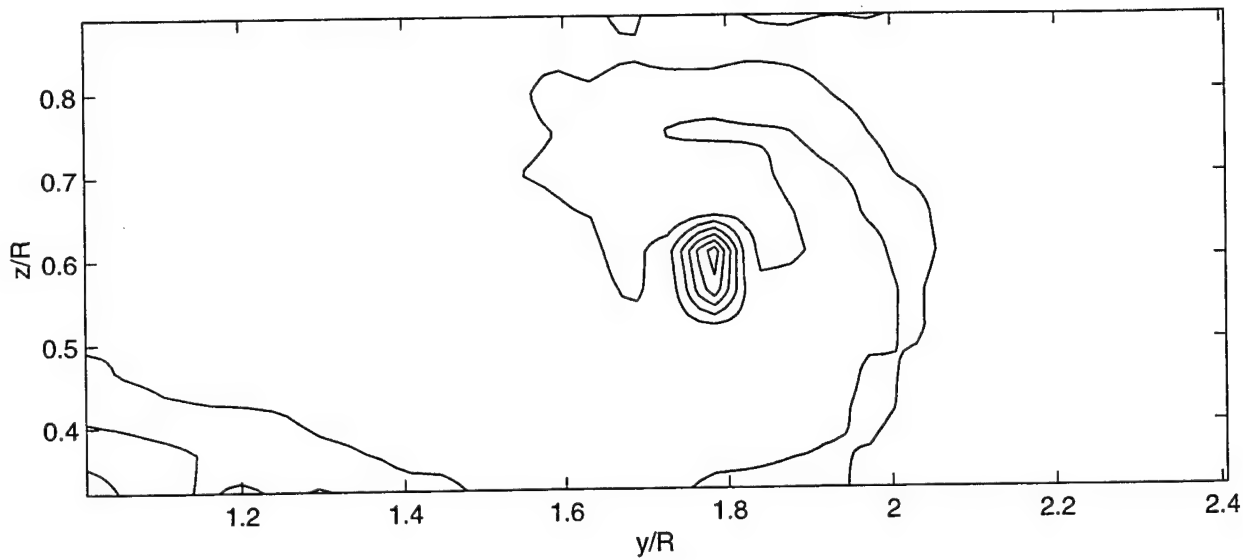
$u_{max} = 6.20$ m/s, $F_V = 0.75$, $N_{cont} = 10$

Figure 84 Streamwise velocity contours (detailed grid): $\beta = 9.5$ deg, $U = 5.25$ m/s, sail on, $x/L = 0.48$ (Test BV09)
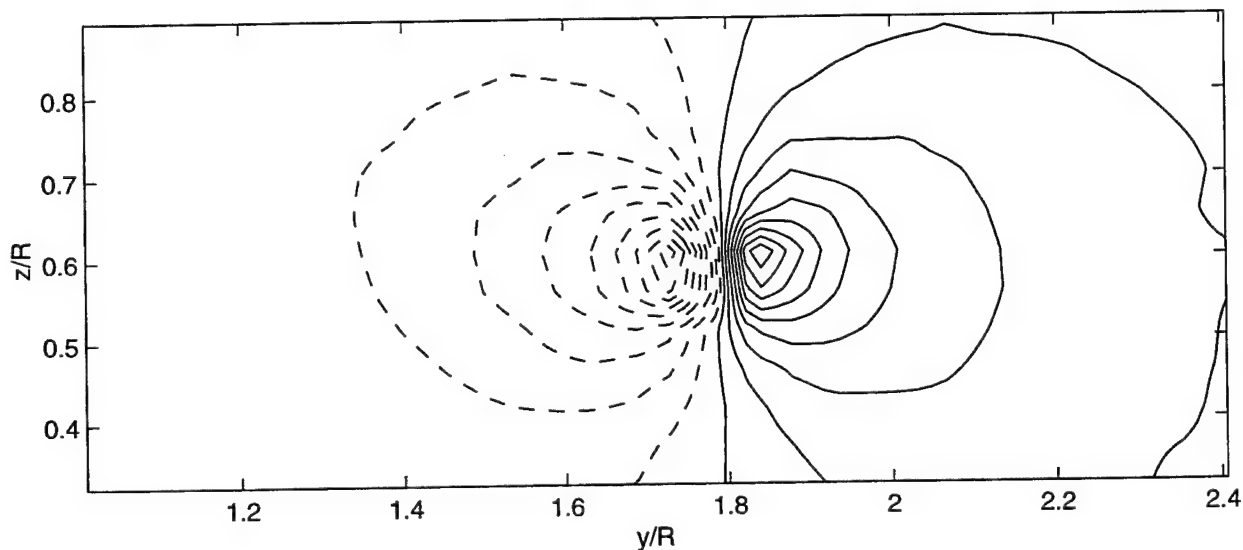
$w_{max} = 4.20$ m/s, $F_V = 0$, $N_{cont} = 10$

Figure 85 Transverse velocity contours (detailed grid): $\beta = 9.5$ deg, $U = 5.24$ m/s, sail on, $x/L = 0.48$ (Test BV10)

128
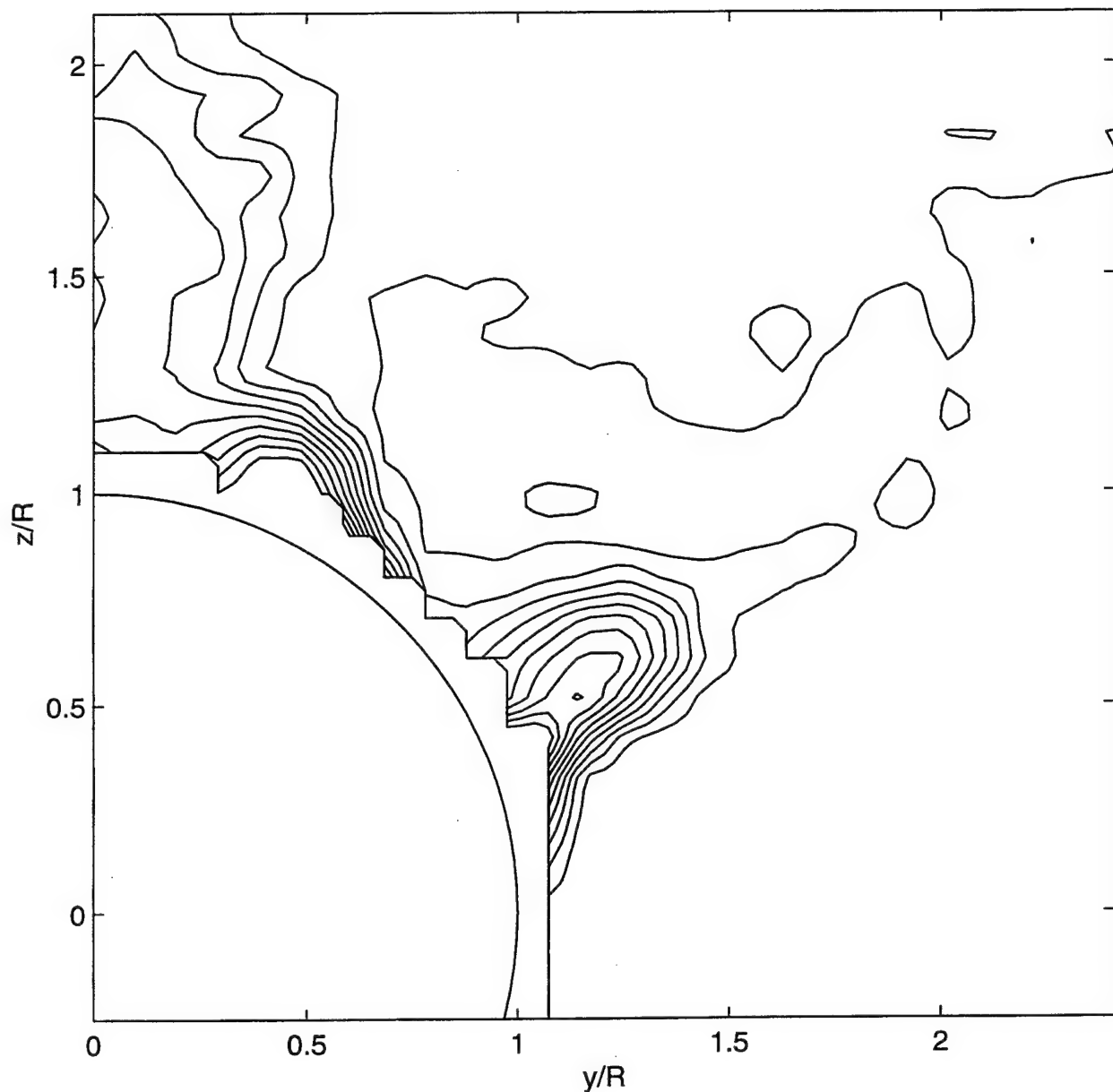
$u_{max} = 5.37$ m/s, $F_v = 0.75$, $N_{cont} = 10$

Figure 86 Streamwise velocity contours: $\beta = 9.5$ deg, $U = 5.29$ m/s, sail on, $x/L = 0.62$ (Test BV13)
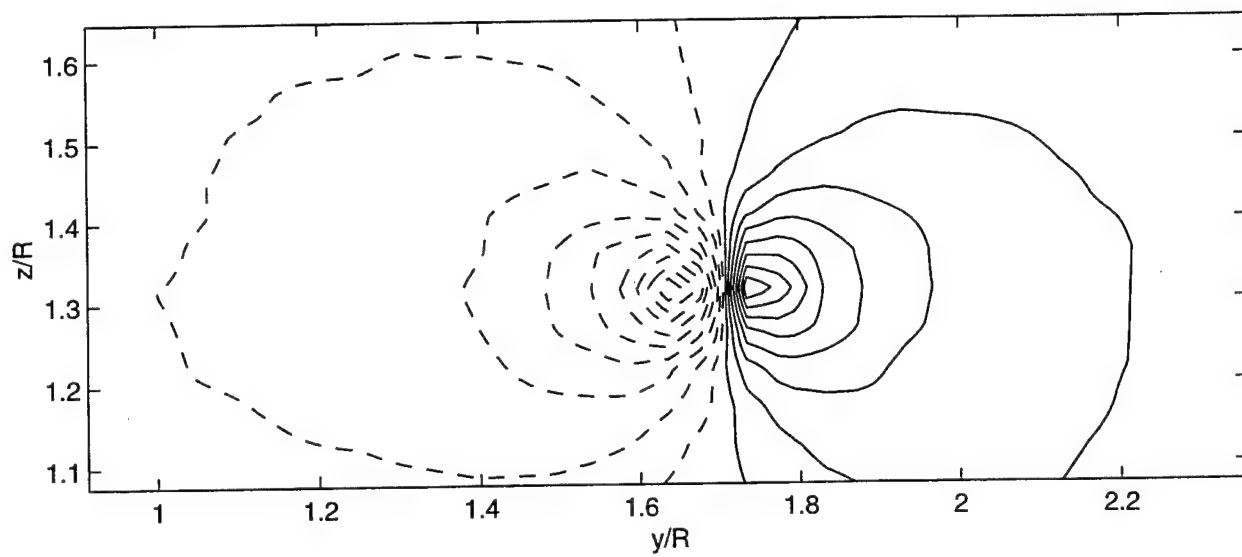
$w_{max} = 4.19$ m/s, $F_v = 0$, $N_{cont} = 10$

**Figure 87** Transverse velocity contours (detailed grid): $\beta = 9.5$ deg, $U = 5.28$ m/s, sail on, $x/L = 0.62$ (Test BV14)
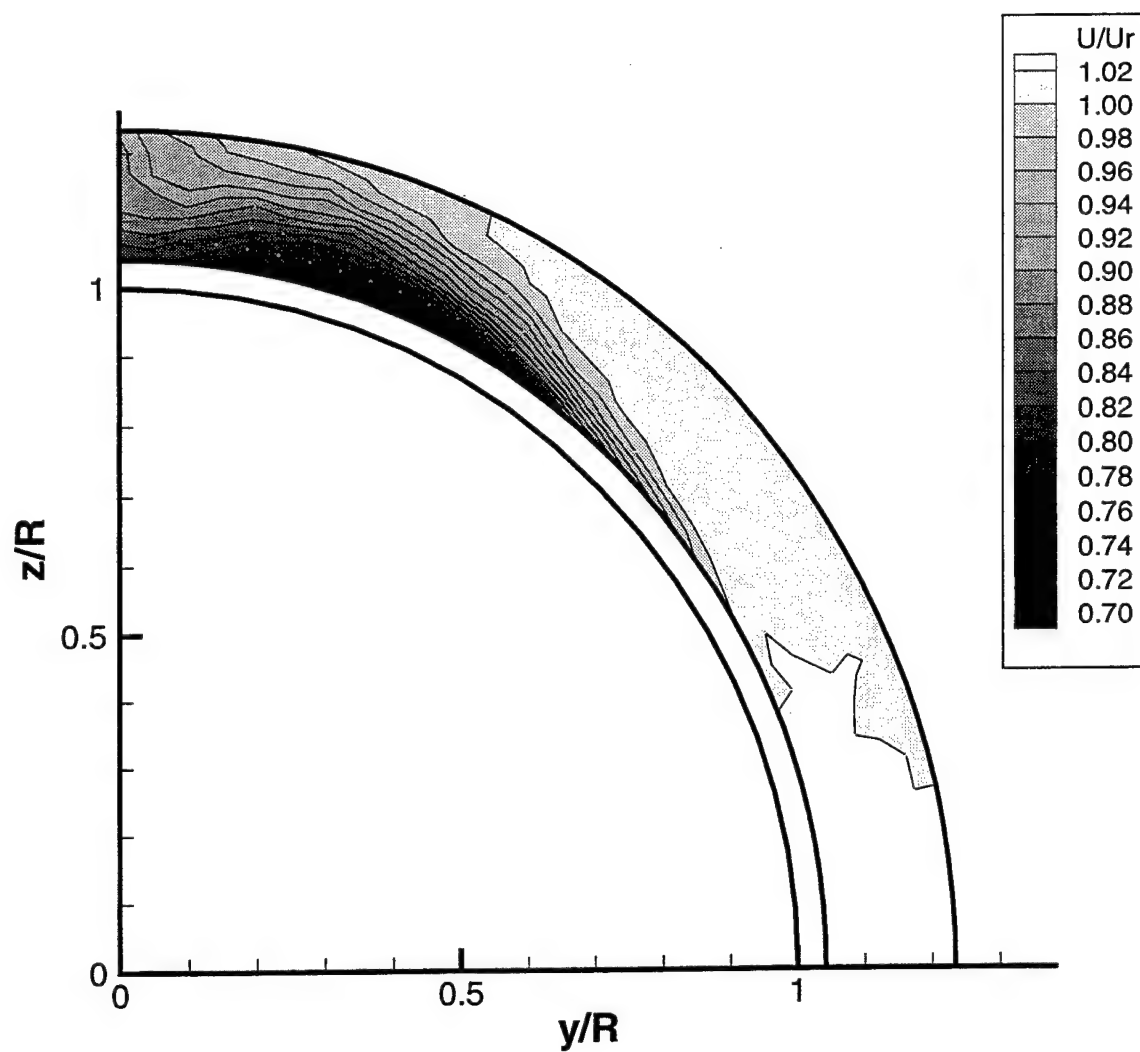
Figure 88 Streamwise velocity contours (boundary layer): $\beta = 5$ deg, $U = 5.27$ m/s, sail off, $x/L = 0.48$ (Test BV19)
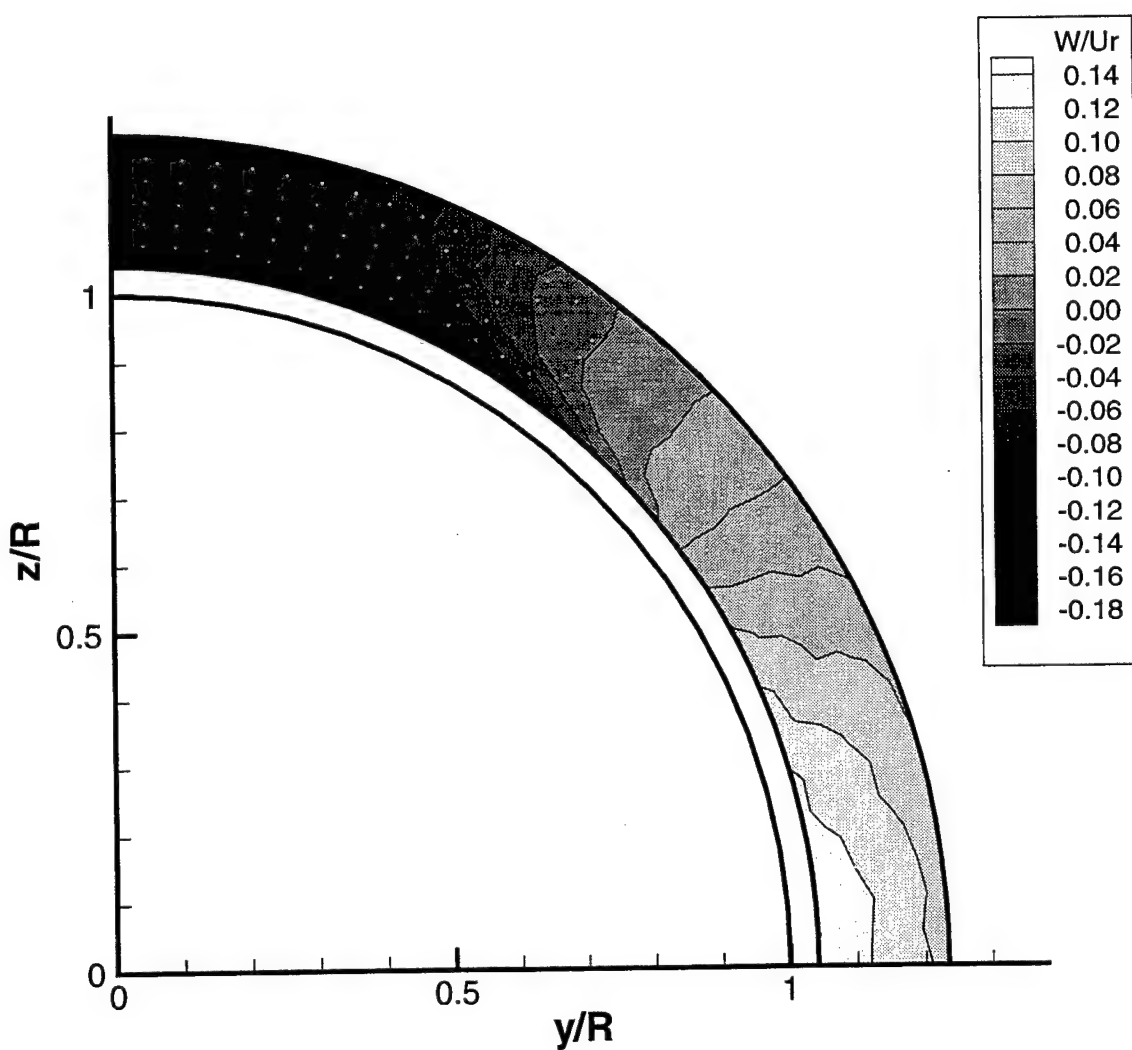
Figure 89 Transverse velocity contours (boundary layer): β = 5 deg, U = 5.27 m/s, sail off, x/L = 0.48 (Test BV20)
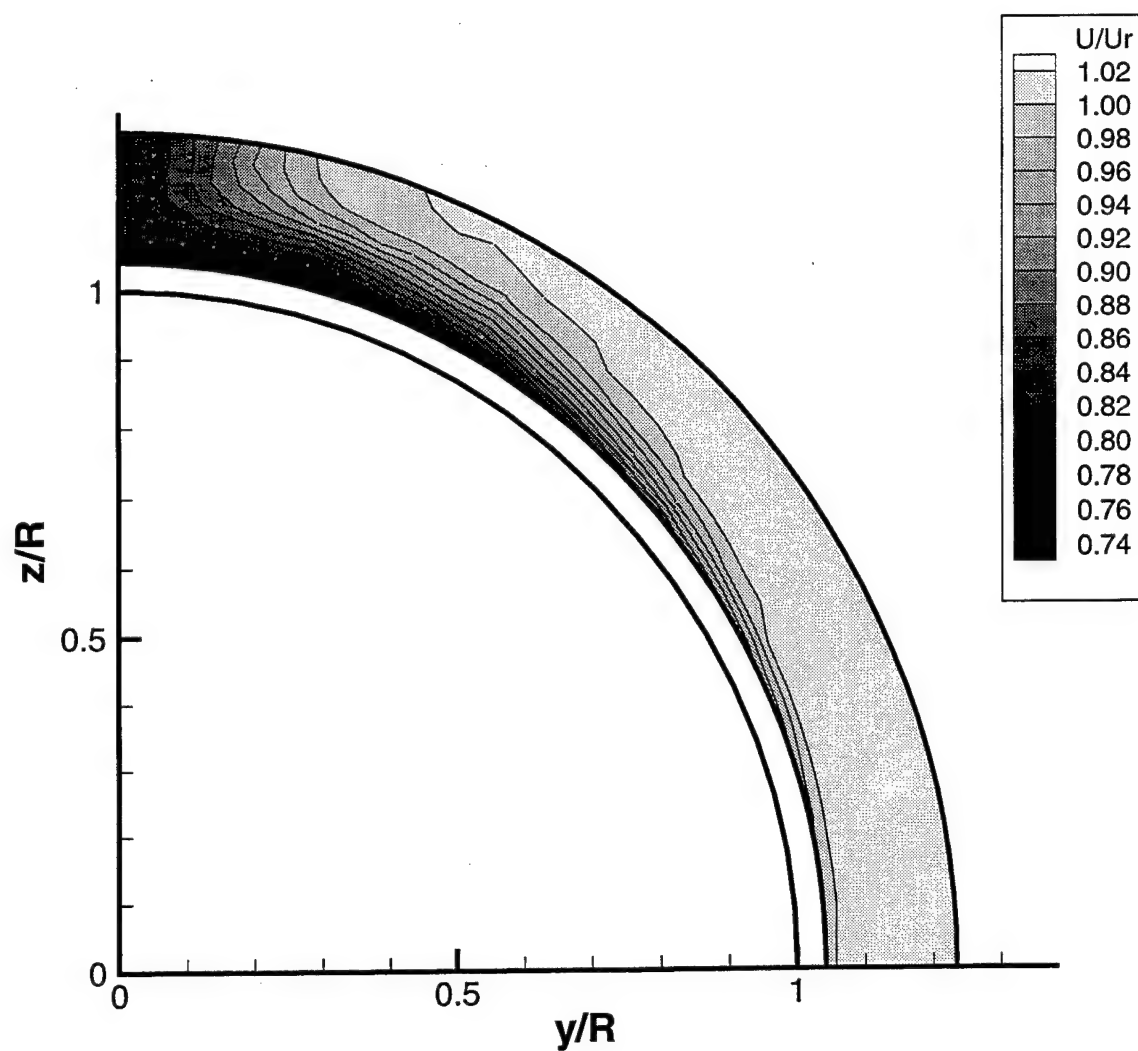
Figure 90 Streamwise velocity contours (boundary layer): $\beta = 5$ deg, $U = 9.42$ m/s, sail off, $x/L = 0.47$ (Test BV17)
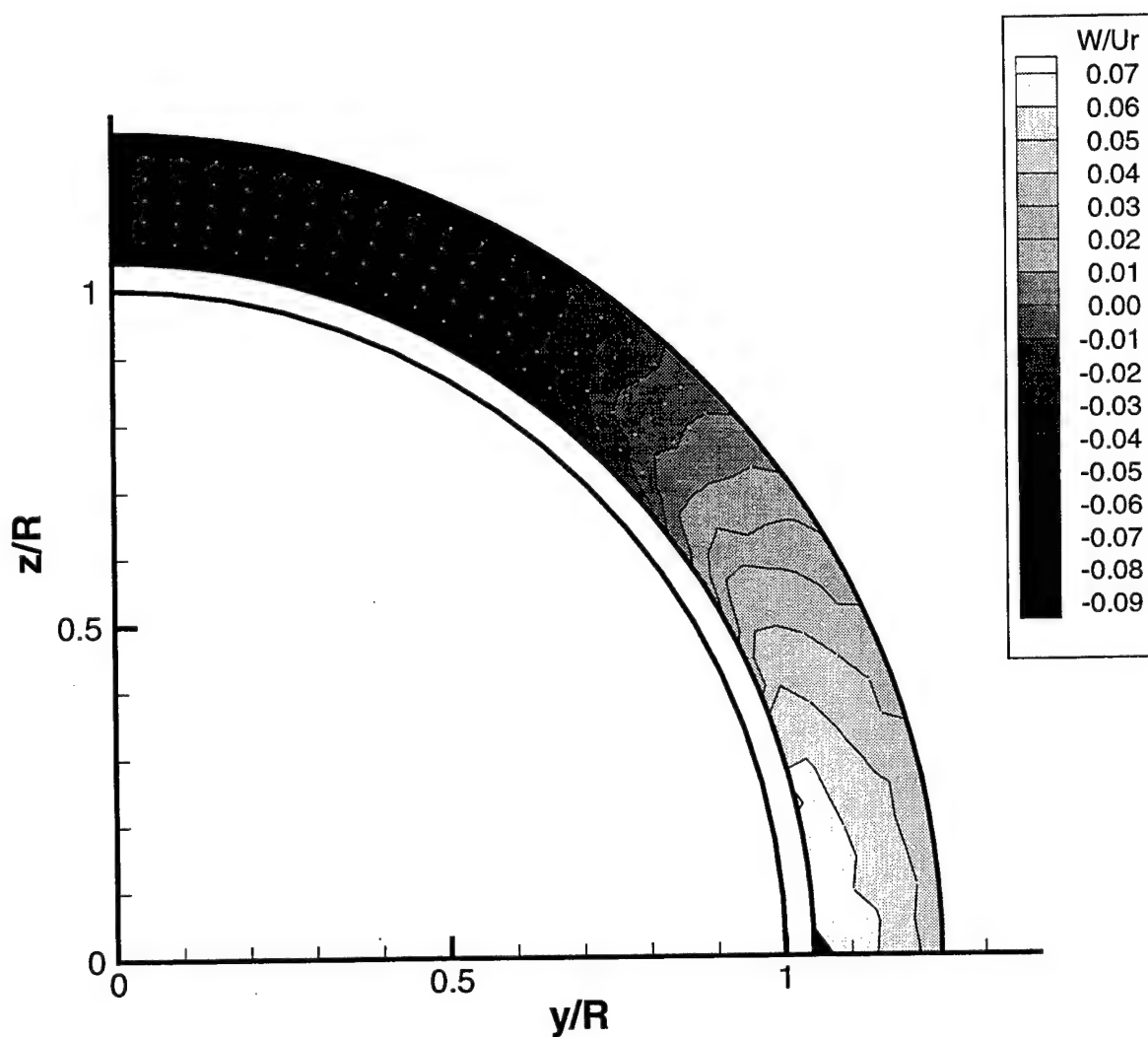
Figure 91 Transverse velocity contours (boundary layer): $\beta = 5$ deg, $U = 9.41$ m/s, sail off, $x/L = 0.47$ (Test BV18)
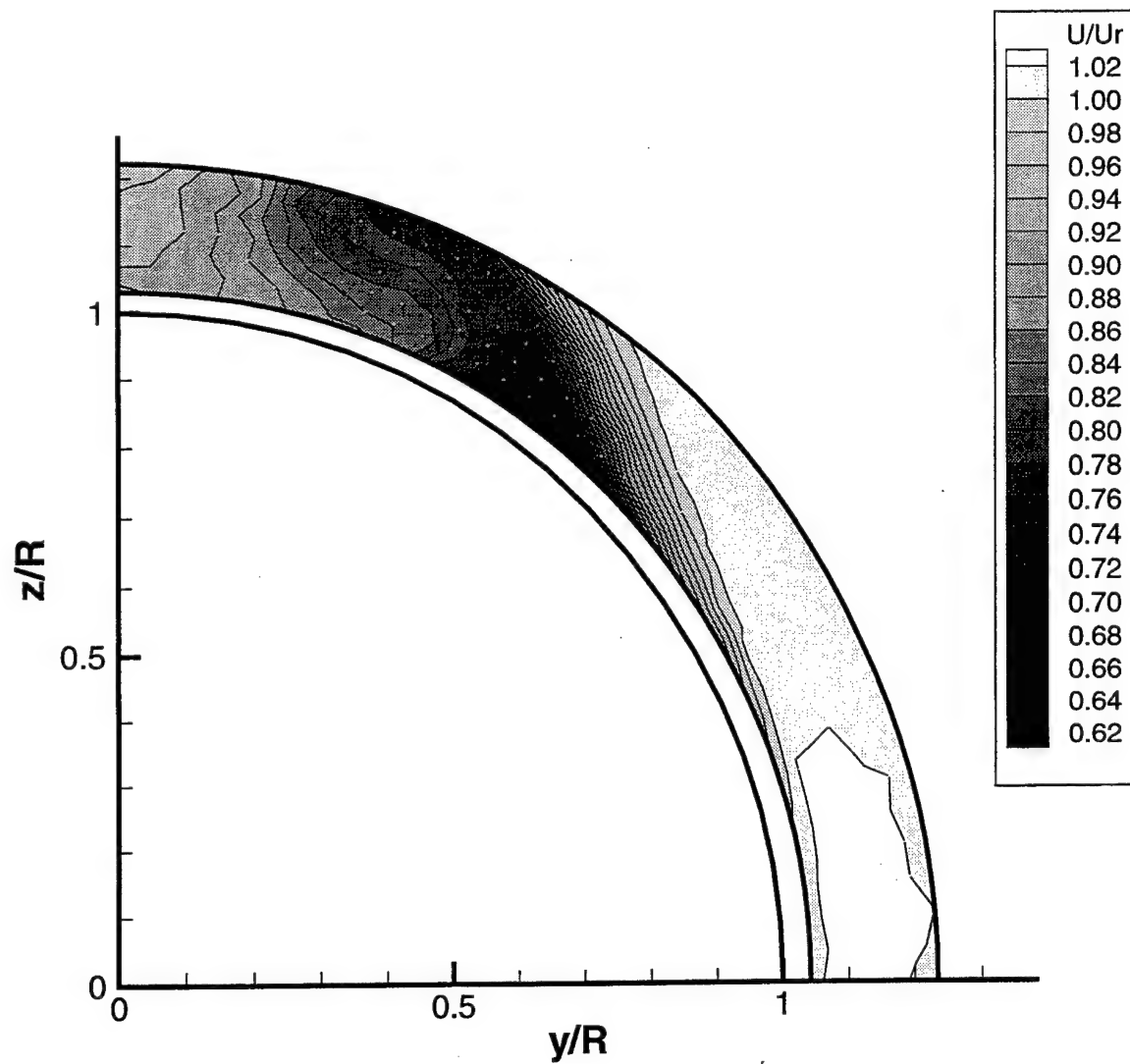
Figure 92 Streamwise velocity contours (boundary layer): $\beta = 5$ deg, $U = 5.31$ m/s, sail off, $x/L = 0.62$ (Test BV21)
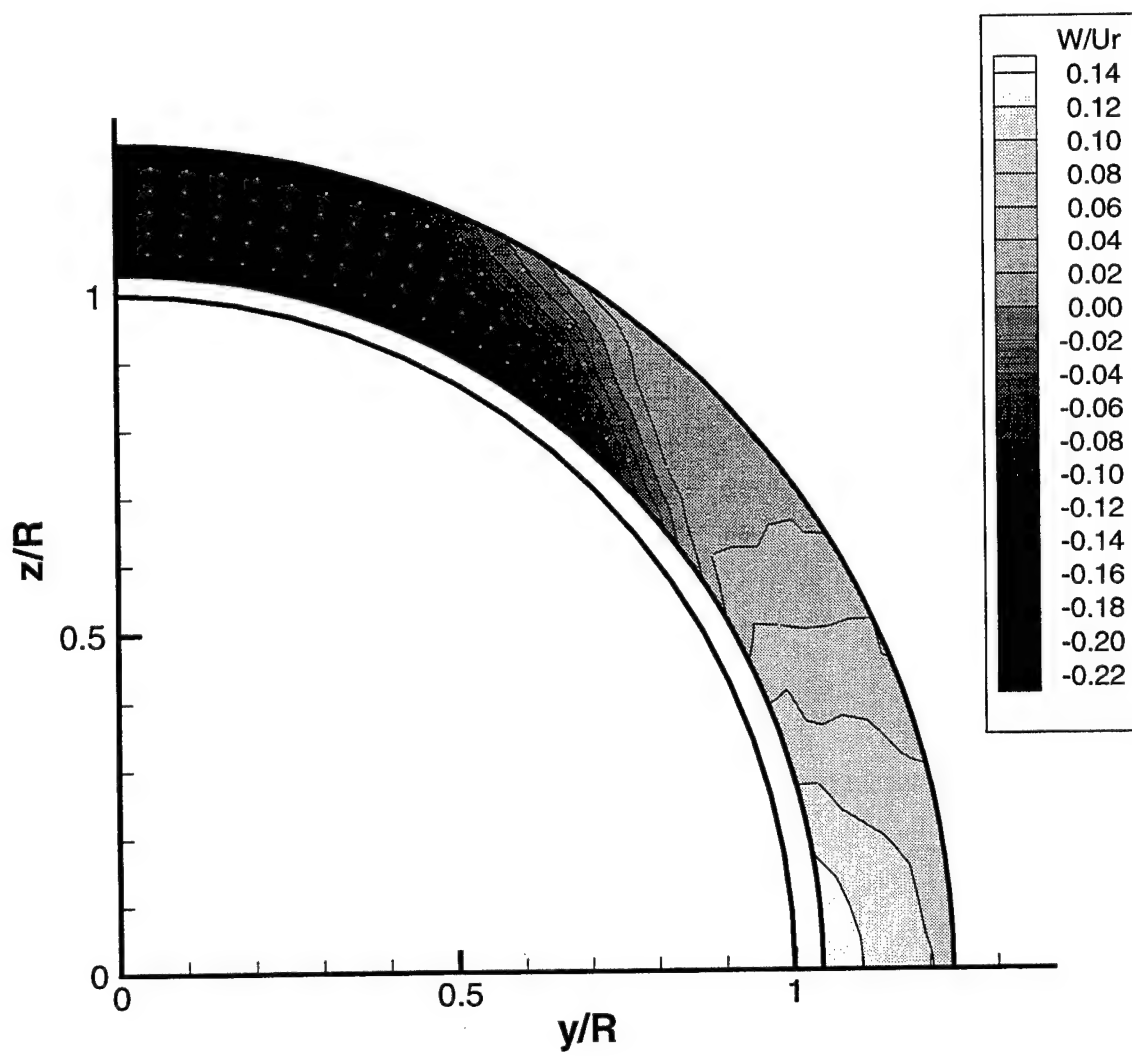
Figure 93 Transverse velocity contours (boundary layer): $\beta = 5$ deg, $U = 5.30$ m/s, sail off, $x/L = 0.62$ (Test BV22)
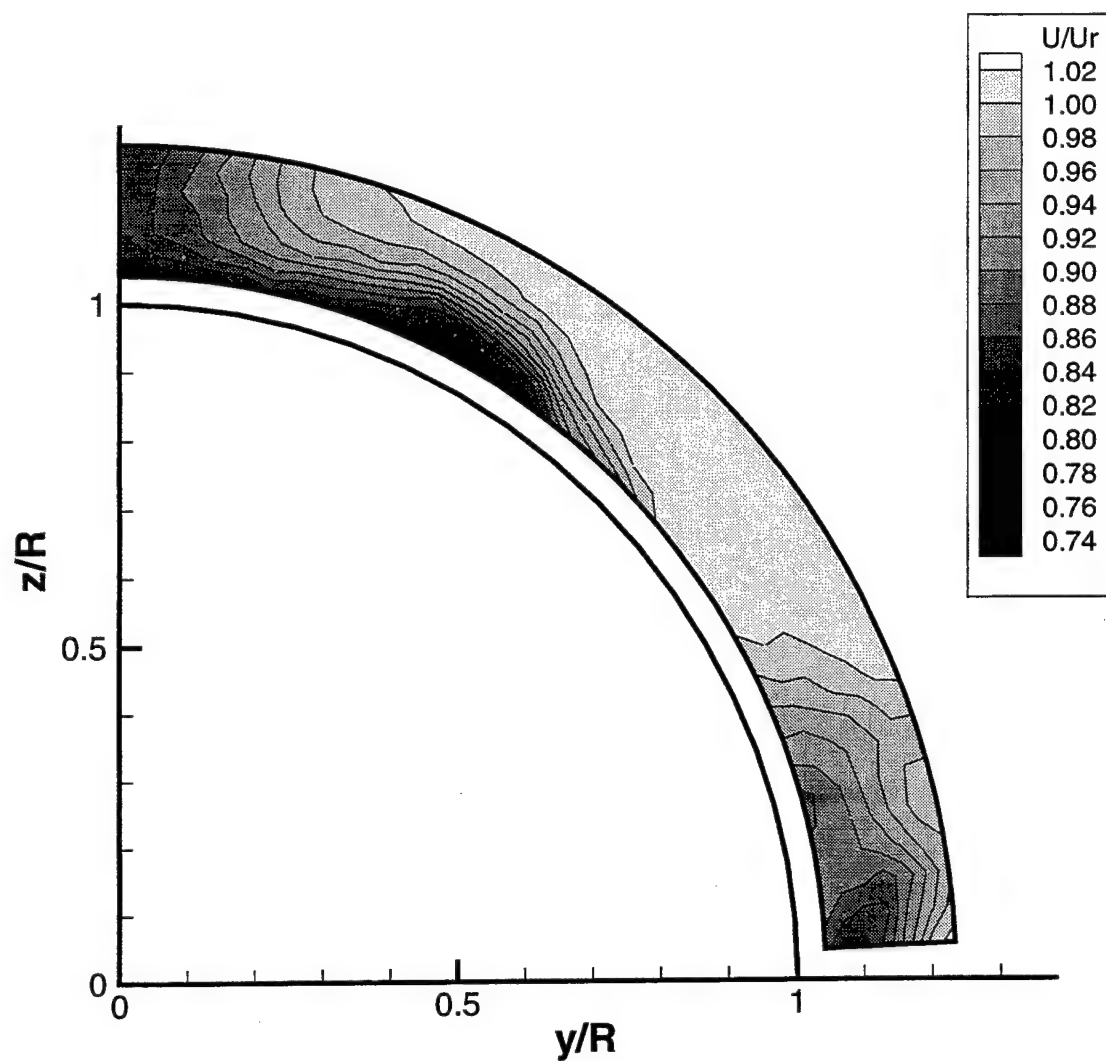
Figure 94 Streamwise velocity contours (bound. layer): β = 9.5 deg, U = 5.24 m/s, sail on, x/L = 0.48 (Test BV11)
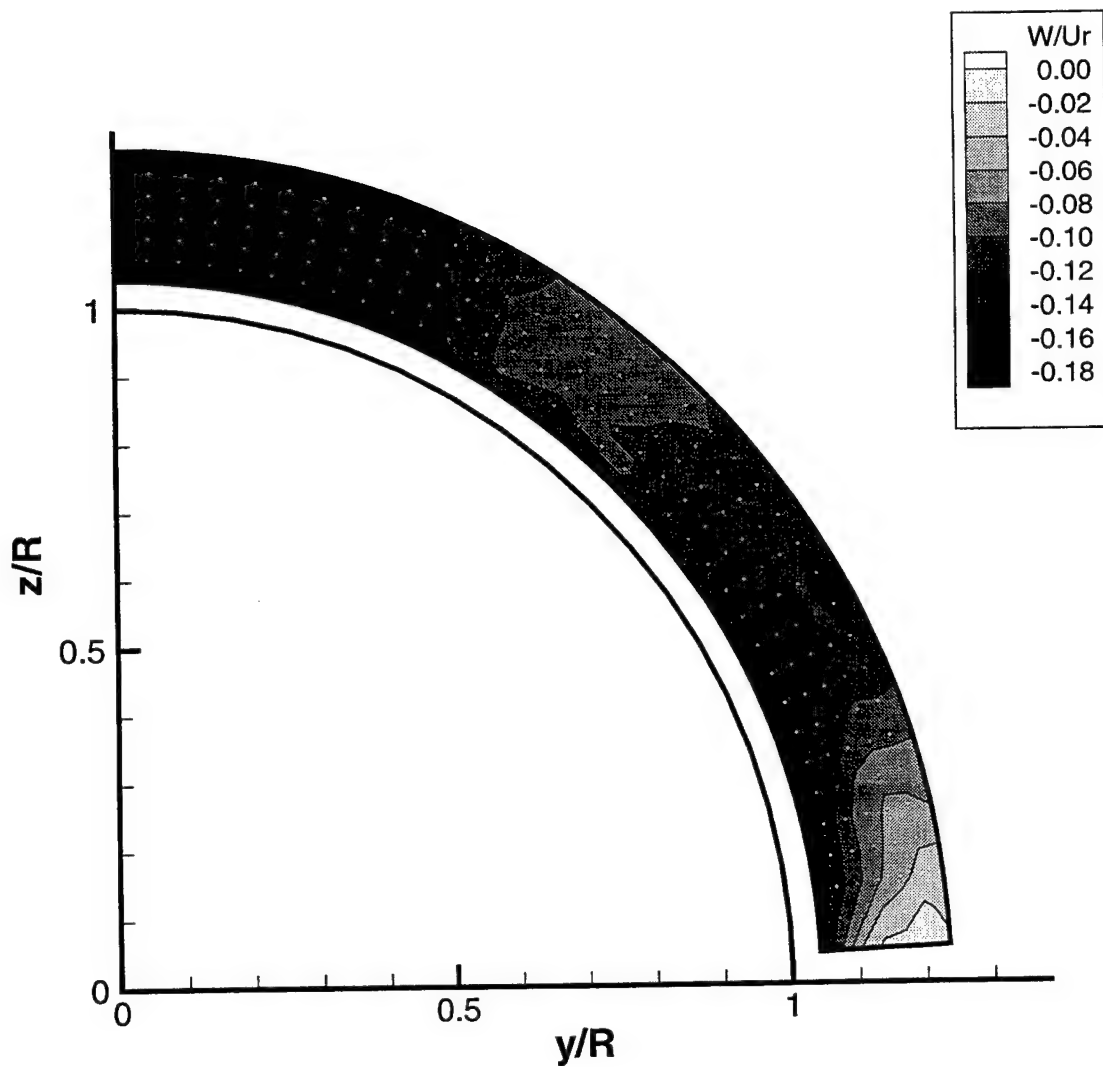
Figure 95 Transverse velocity contours (bound. layer): $\beta = 9.5$ deg, $U = 5.24$ m/s, sail on, $x/L = 0.48$ (Test BV12)

138
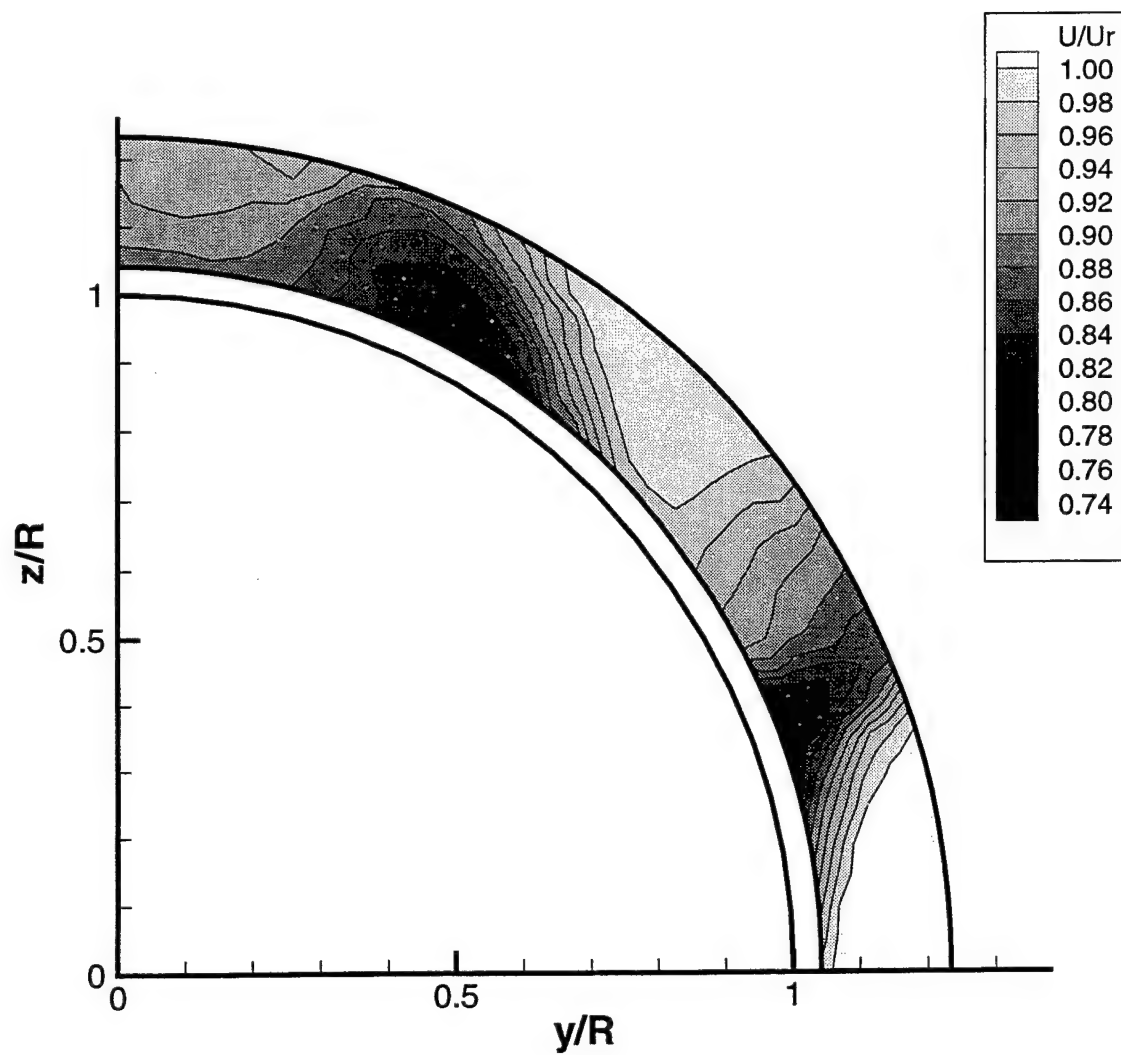
Figure 96 Streamwise velocity contours (bound. layer): $\beta = 9.5$ deg, $U = 5.29$ m/s, sail on, $x/L = 0.62$ (Test BV15)
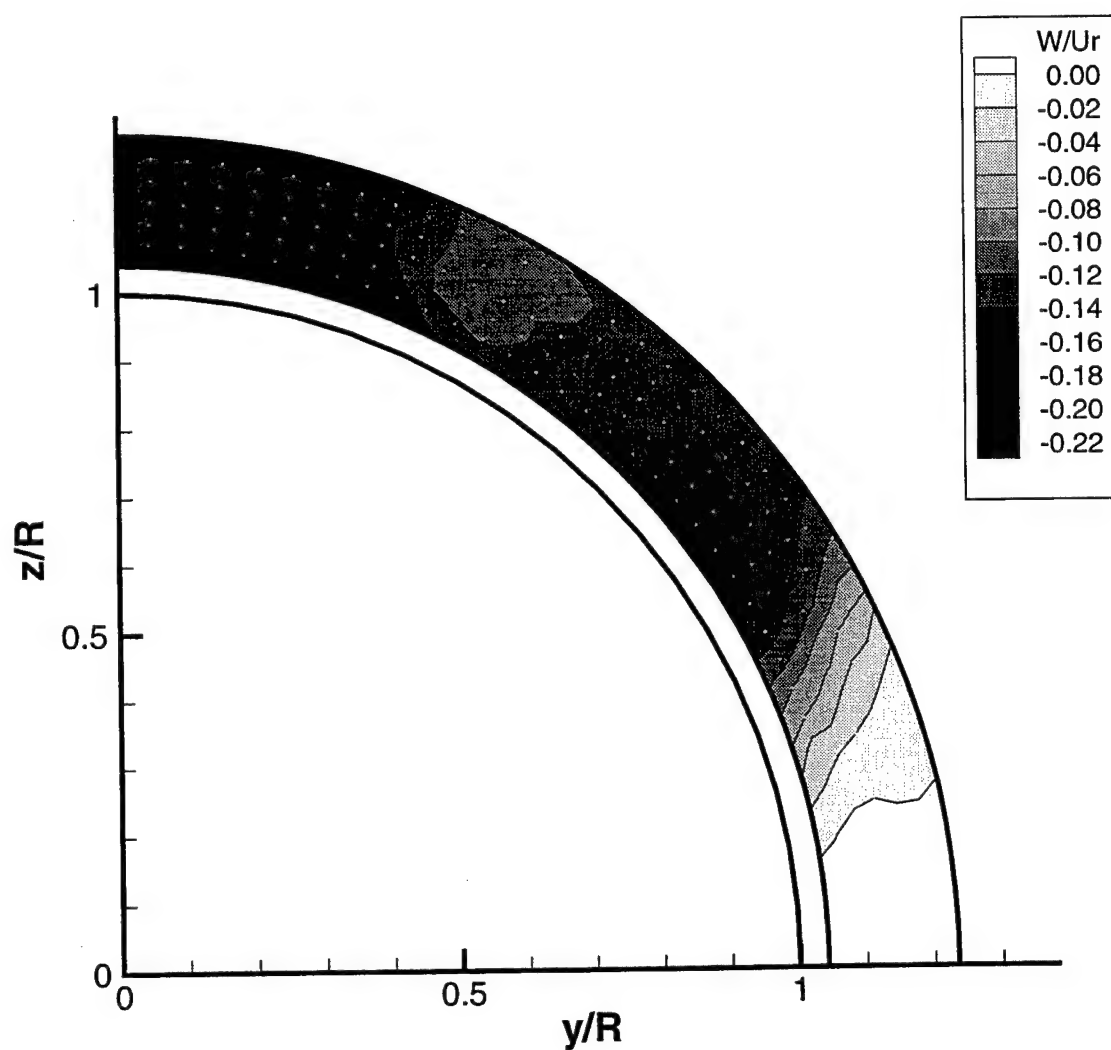
Figure 97 Transverse velocity contours (bound. layer): $\beta = 9.5$ deg, $U = 5.29$ m/s, sail on, $x/L = 0.62$ (Test BV16)
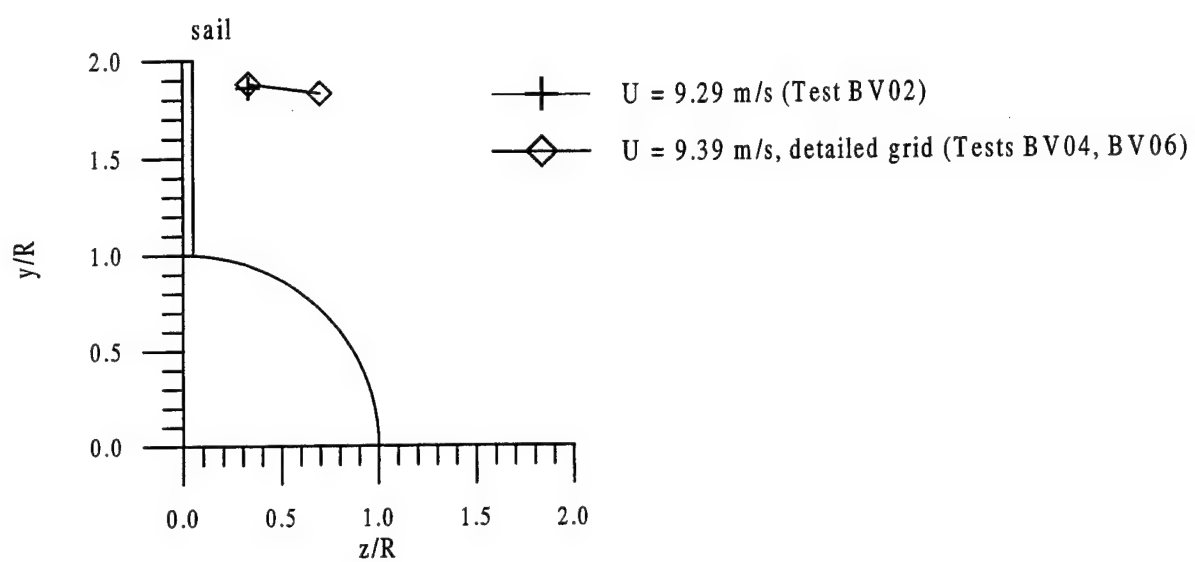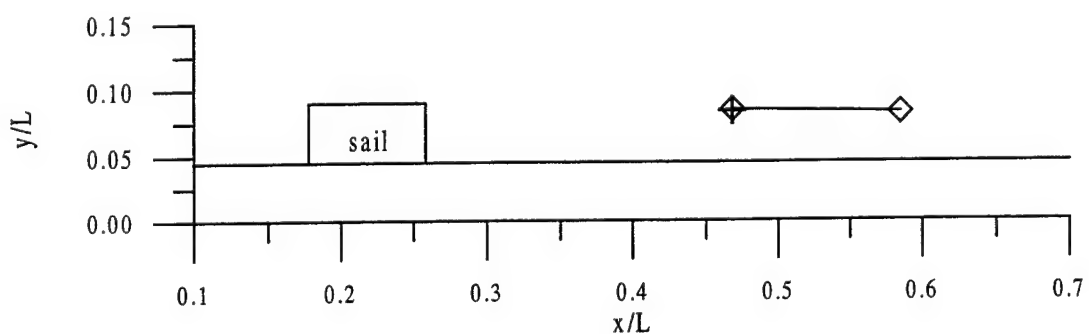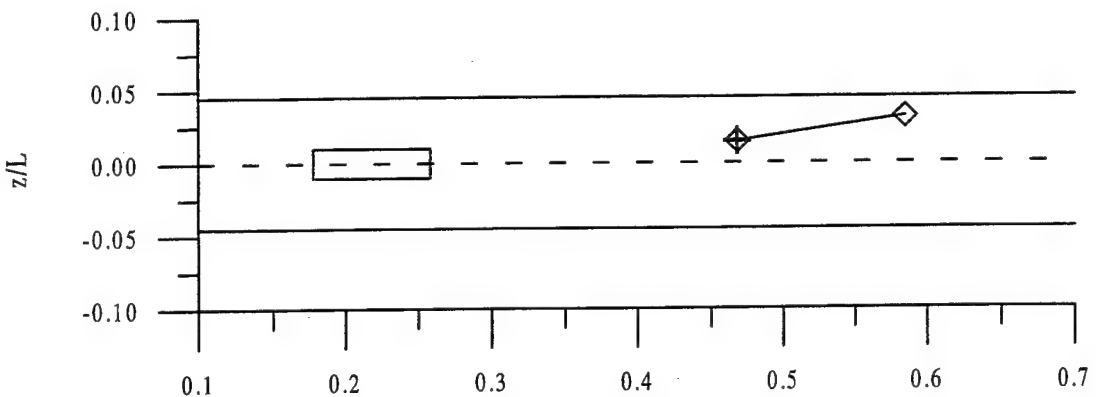
Figure 98 Vortex trajectory data: β = 5 deg
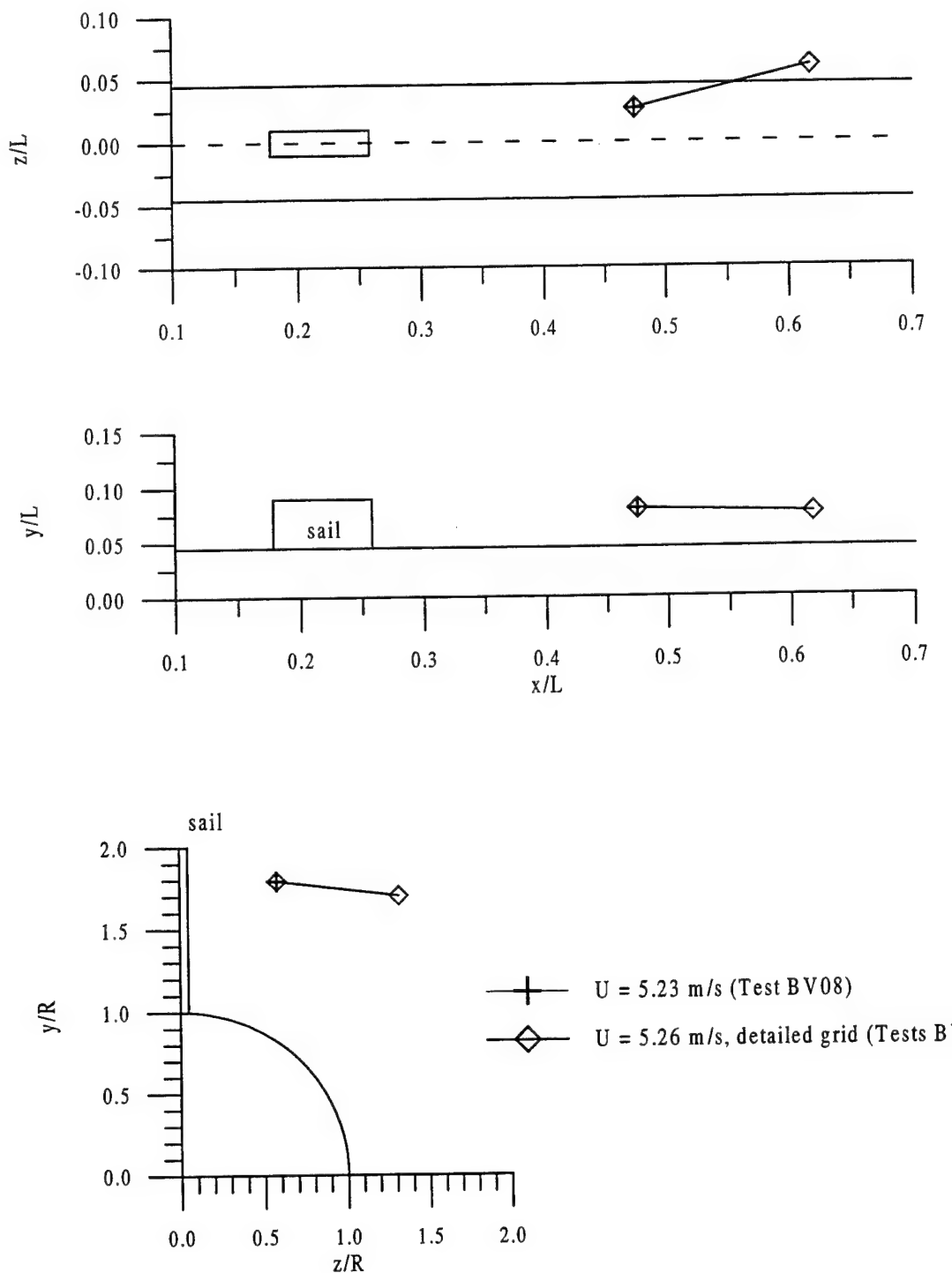
Figure 99 Vortex trajectory data: $\beta = 9.5$ deg
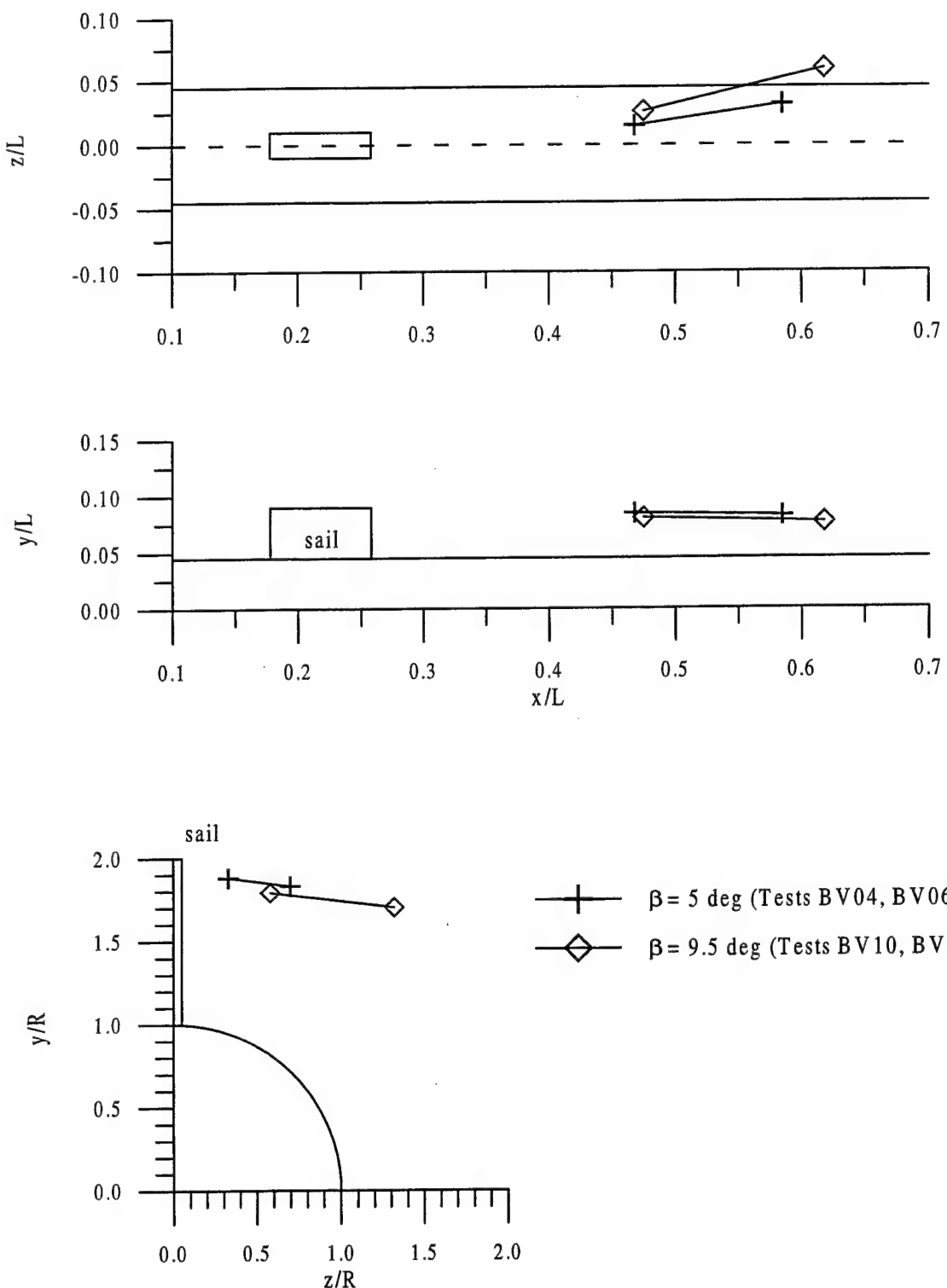
Figure 100 Comparison of vortex trajectory data at two drift angles
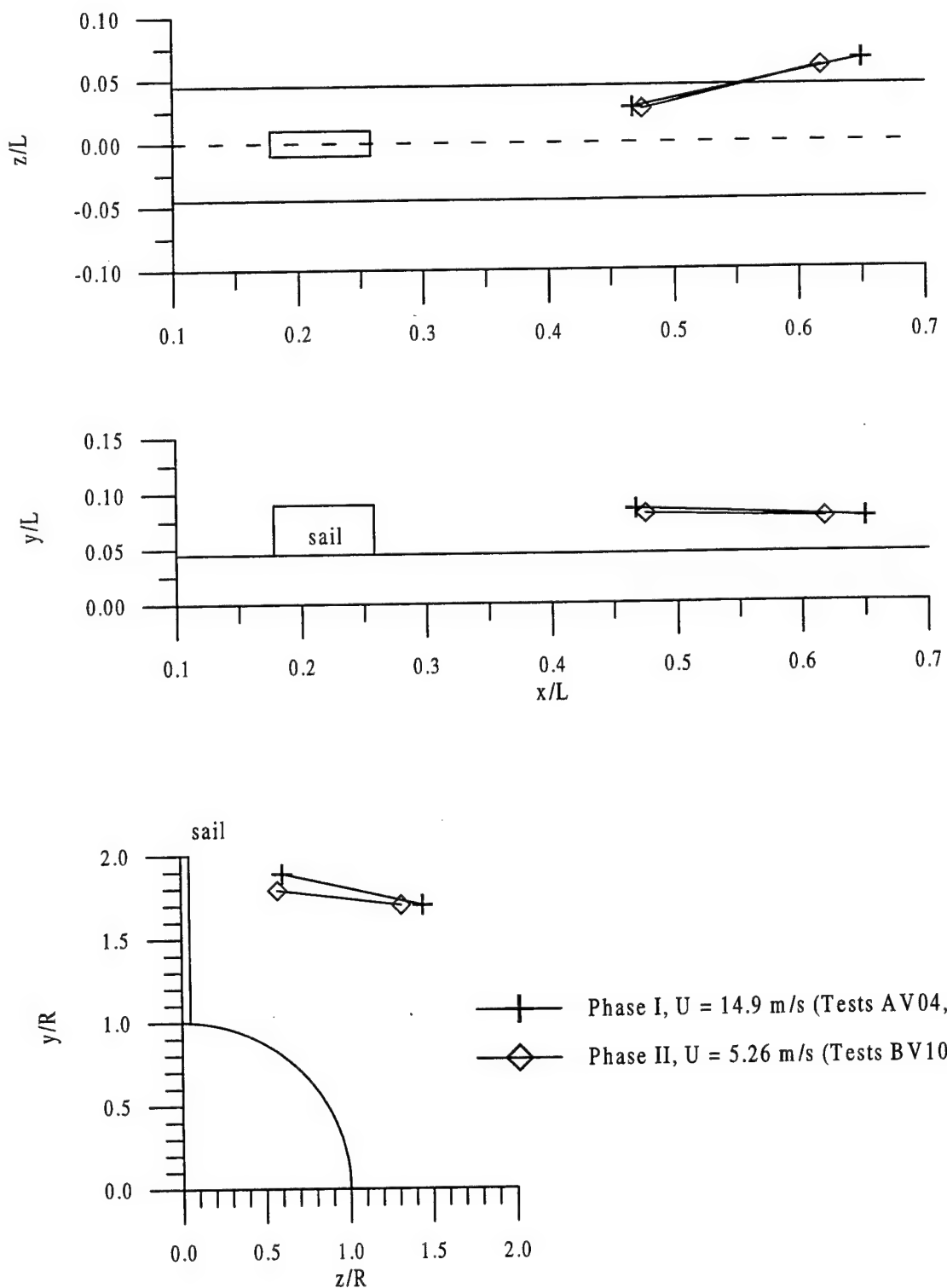
Figure 101 Comparison of Phase I and II vortex trajectory data: $\beta = 9.5$ deg

144
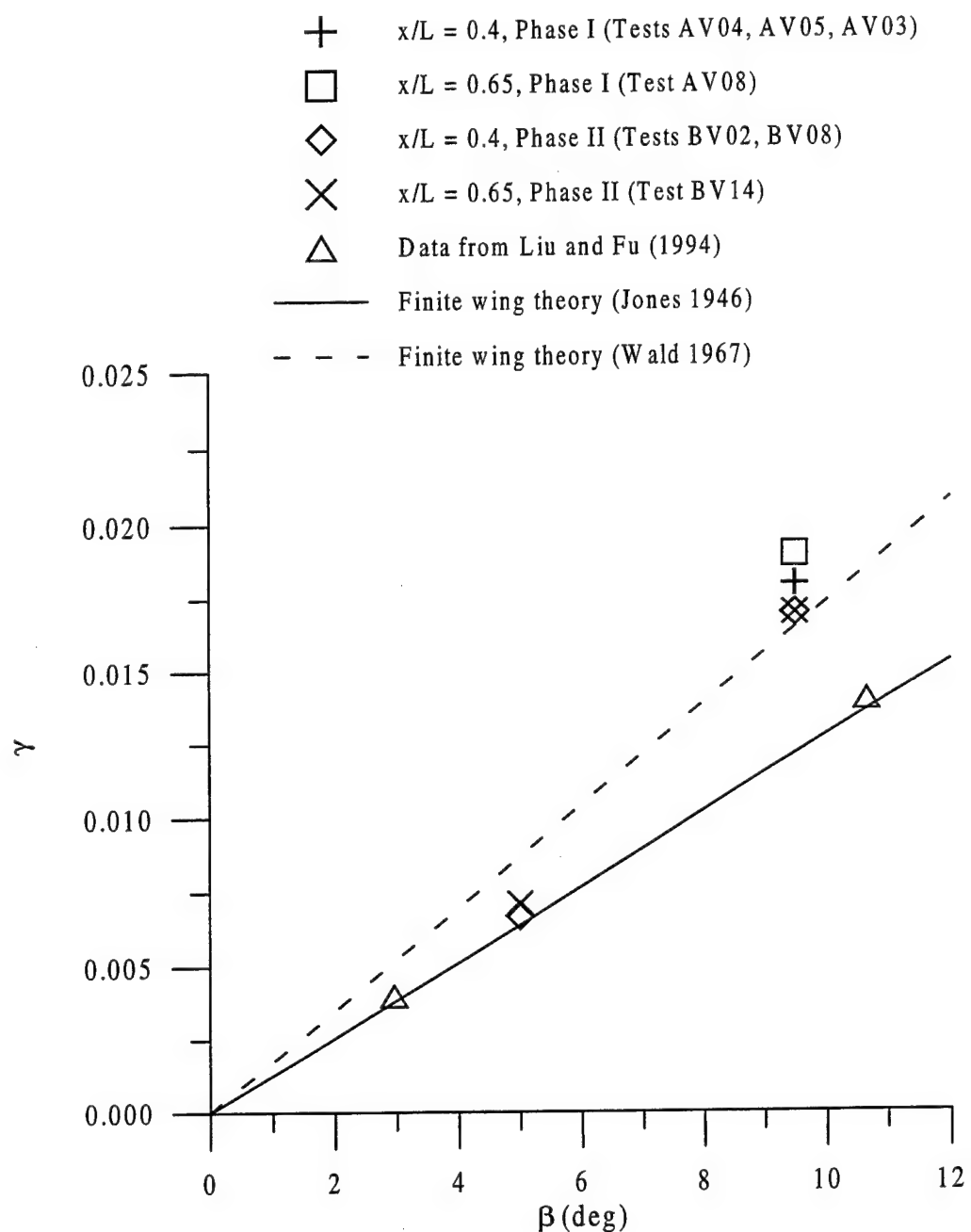
Figure 102 Comparison of estimated circulation values with theories and with other measurements

APPENDIX

RENOVATION AND INITIAL OPERATION OF A

HIGH-SPEED WATER TUNNEL

By

Michael Lamar Lindsey

A Thesis
Submitted to the Faculty of
Mississippi State University
in Partial Fulfillment of the Requirements
for the Degree of Master of Science
in Aerospace Engineering
in the Department of Aerospace Engineering

Mississippi State, Mississippi

December 1998

Name: Michael Lamar Lindsey

Date of Degree: December 18, 1998

Institution: Mississippi State University

Major Field: Aerospace Engineering

Major Professor: Dr. David H. Bridges

Title of Study: RENOVATION AND INITIAL OPERATION OF A
HIGH-SPEED WATER TUNNEL

Pages in Study: 56

Candidate for Degree of Master of Science

The renovation and initial operation of a high-speed water tunnel at Mississippi State University are discussed. A summary of the tunnel design features and method of construction is included. The tunnel was taken apart so that the interior could be recoated with a Duratec® coating. A new test section was purchased and instrumented with static pressure taps. After the tunnel was reassembled, it was tested under static pressure up to 50 psi. It was discovered that propeller speeds greater than about 700 RPM produced cavitation, so the propeller was limited to speeds less than 700 RPM. The calibration, use, and results of a pressure transducer to measure static pressures in the test section are discussed. Suggestions for future work are also presented.

DEDICATION

I would like to dedicate this research to my parents, Fred and Sandra Lindsey. Thank you for all of your support and encouragement.

ACKNOWLEDGEMENTS

TABLE OF CONTENTS

(A-6)

v

LIST OF TABLES

LIST OF FIGURES

LIST OF SYMBOLS

A	area
V	velocity
p	pressure
psi	pounds per square inch
psig	pounds per square inch gauge pressure
Δp	change in pressure
Δp_{cont}	pressure drop across the contraction
V	voltage
q_{ts}	dynamic pressure in the test section
a	slope of calibration curve
b	y-intercept of calibration curve
N	number of samples
SEE	standard error of the estimate
$B_{\Delta p}$	bias of change in pressure
$P_{\Delta p}$	precision of change in pressure
P_V	precision of voltage
$U_{\Delta p}$	total uncertainty of change in pressure
d	diameter of static pressure hole
θ	momentum thickness
ρ	density
ν	kinematic viscosity
Re	Reynolds number
C_f	skin friction coefficient
τ_w	wall shear stress
u_e	velocity at edge of boundary layer

CHAPTER I

INTRODUCTION

In 1961, preliminary design was begun on a water tunnel at Mississippi State University[1]. One of the reasons for its construction was that at the time no sophisticated water tunnels were available for active research in the southeastern part of the United States. Interest was also generated by the construction of submarines on the Gulf Coast in the state of Mississippi.

According to Wells[1], between 1955 and 1960, a great deal of research was performed to determine the aerodynamic forces which acted on airship hulls and related bluff bodies. Because of the similarity between these bodies and submarines, it was decided that a water tunnel should be constructed to perform hydrodynamic research on submarines.

This water tunnel was successfully completed and was used to perform experiments. One experiment which was performed was the calibration of electro-magnetic flow sensors for National Space Technology Laboratories. There was a period during which the water tunnel was not used. During this period, the tunnel was not maintained in operable status.

Recently, it was decided to renovate the water tunnel at Mississippi State so that additional research could be performed, possibly in support of the Large Cavitation Channel in Memphis. The Large Cavitation Channel is used to conduct tests for the United States Navy. Scale models of submarines are placed in the test section, and the forces acting on it are determined. Because the models are not full scale, Reynolds number correction factors must be used. One direction of possible future research for the water tunnel at Mississippi State is verification and possible improvement of these Reynolds number correction factors.

The first step in renovating the water tunnel was to completely disassemble it so that the interior could be cleaned and sanded. Next the interior was coated with Duratec® to make it water proof. A new Plexiglas® test section was purchased. Holes were drilled in the test section to allow measurements of the static pressure to be made. Five pressure taps were equally spaced on one side of the test section to measure the pressure drop along the test section. On the other side of the test section, two pressure taps were drilled. These two pressure taps were located directly opposite the first and last pressure taps on the other side. The most upstream of the two pressure taps was used to provide a reference pressure to a 2-psi differential pressure transducer. The downstream pressure tap will later be used to study errors in the measurement of

2

static pressure caused by the size of the static pressure hole.

An electric motor was purchased to provide power to circulate the water. It was decided that the motor should turn the propeller shaft directly instead of using belts as the original drive system used. To accomplish this, a flexible coupling was purchased that could compensate for some error in the positioning of the electric motor. Before the motor and propeller shaft were installed, the original bearings and seals were replaced with new ones.

After the tunnel renovation was completed, tests were conducted at various RPM settings which corresponded to various test section velocities. The pressure drop across the contraction was measured using a 25-psi differential pressure gauge. The velocity in the test section was computed using this pressure drop and the area ratio of the contraction. The pressure differences between the reference pressure tap and the other six pressure taps were also recorded. This was accomplished using a 2-psi differential pressure transducer and a 16-bit high resolution analog-to-digital converter attached to a computer.

CHAPTER II

BACKGROUND

Description of Facility

In 1961, when preliminary design was begun on the water tunnel, the highest speed of existing water tunnels was 80 to 100 ft/s[1]. The design point of the tunnel was set as 75 ft/s with a test section pressure range from 16 psig to 60 psig. A diagram of the resulting design is shown in Figure 18.

It was determined that 2-in diameter models were the smallest which could be made accurately. The ratio of test section diameter to model diameter was desired to be six or greater. This ratio was deemed large enough to reduce the effects of blockage to an acceptable amount. This gave a test section diameter of 12 in.

Another factor which affected test section diameter was contraction ratio. The shop facilities at the time could only turn forms having diameters less than 41 in. Because of this, the largest diameter of the water tunnel, including the section before the contraction, was set to 40 in. For a 12-in diameter test section, the resulting contraction ratio was about 11:1. If an 11-in diameter test section were

4

used, the contraction ratio would be about 13:1. Because low levels of turbulence were desired, it was decided that the test section should be 11 in in diameter.

According to Wells[1], the contraction is the most powerful means of reducing flow disturbances before they reach the test section. The velocity fluctuations in the direction of the flow are divided by the contraction ratio as the water flows through the contraction. Also, the mean velocity of the flow is multiplied by the contraction ratio as it passes through the contraction. This means that the velocity fluctuations relative to the local mean flow velocity are divided by the contraction ratio squared. However, the transverse velocity fluctuations relative to the local mean flow are only divided by the square root of the contraction ratio. This unequal reduction in relative velocity fluctuations was not considered a problem. It was expected that some level of isotropic turbulence would exist which would contribute to the velocity fluctuations in all three directions. In the axial direction, velocity fluctuations would also be caused by boundary layer effects, residual impeller whirl, and over- or under-turning of the flow at the fourth corner. It was thought that these sources could cause velocity fluctuations which were an order of magnitude larger than those caused by turbulence.

The contraction was designed to be short to minimize boundary layer development and the losses associated with

it. However, it had to be long enough so that adverse pressure gradients were not created in the entrance or exit to the contraction. Most studies of contraction design recommended that approximately two-thirds of the contraction be devoted to the exit, or convex, portion of the contraction[1]. These studies said that the threat of an adverse pressure gradient in the entrance region was less because of the slower velocities. Because of these studies, the exit length was set to twice the entrance length. The overall contraction length was chosen as 60 in. The method described by Cohen and Ritchie[2] was used to design the contraction. This method was based on prior work done by Szezeniowski[3] and Tsien[4]. Using this method and a computer operated by the University Computing Center, a contraction was designed which had virtually no adverse wall pressure gradient and, in theory, an almost uniform exit velocity. The results of this method are shown in Figure 1 and Table 1.
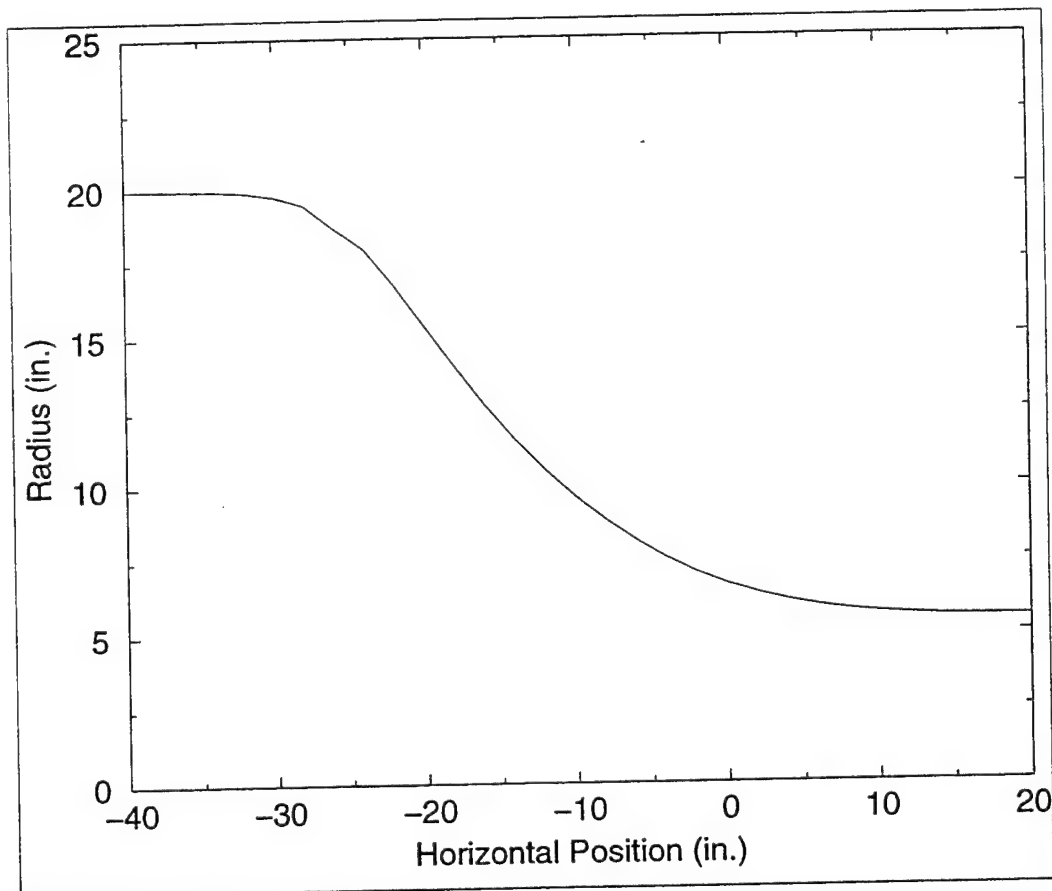
Figure 1 Contraction Geometry.

A fine-grained honeycomb was to be added between the
fourth corner and the contraction. Because the flow
conditions after the fourth corner could not be determined,
the fineness ratio of the honeycomb was arbitrarily set to
20:1. Higher fineness ratios would improve the flow, but
would also require more power because of the added drag.
The fineness ratio is the ratio of the length of the
honeycomb in the flow direction to the cell size. The
honeycomb would be made of 0.25-in cells which were 5 in

7

long. Although this honeycomb was planned for the water tunnel, it was never added.

The diffuser is another section of the tunnel which was carefully designed. A cycloidal curve was chosen to be used as the transition to the diffuser. This was to allow continuous first and second derivatives of the wall profile. According to Wells[1], any discontinuity in the second derivative would cause a sudden step decrease in the wall pressure. This was to be avoided because it might cause cavitation. The diffuser has a total included angle of 5.73 degrees. This angle is smaller than average which makes the diffuser longer. This also raised the power requirement, but it was thought that the improvement in the flow was more important. The resulting diffuser transition design is shown in Figure 2 and Table 2.
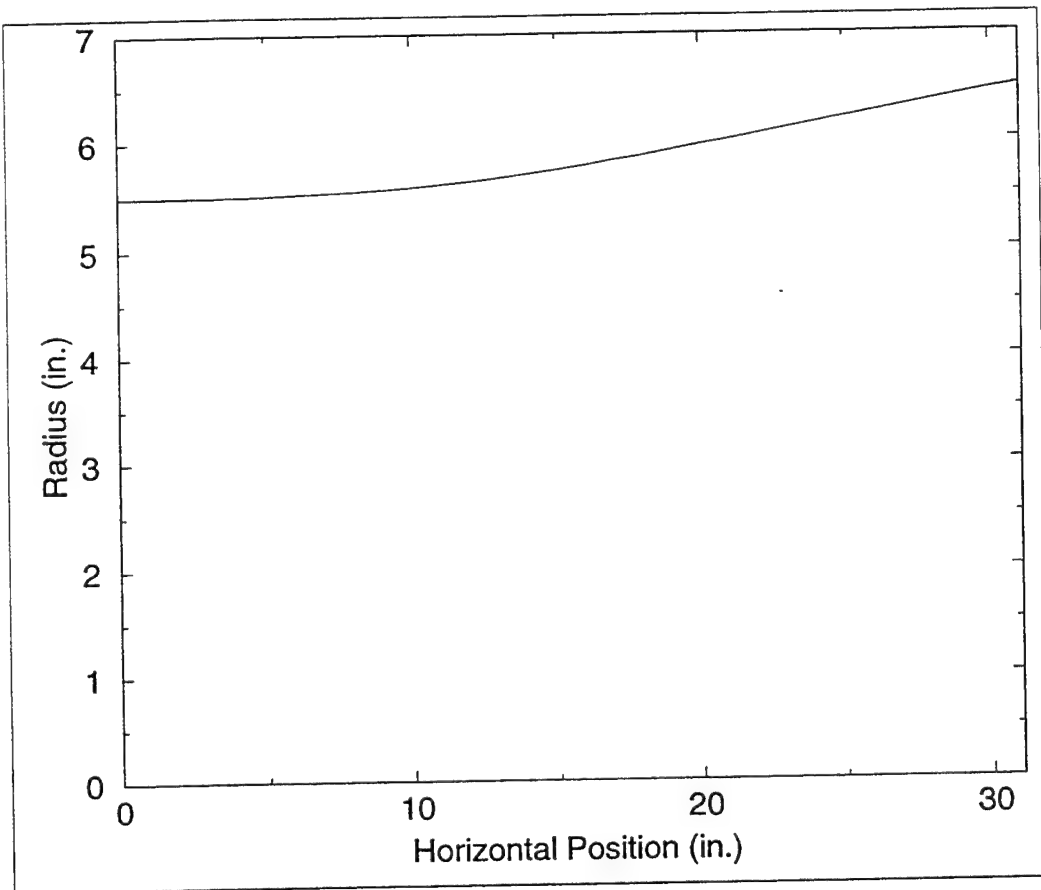
Figure 2 Diffuser Transition Geometry.

Each corner has a set of turning vanes. The turning vanes are similar to the profiles developed from circular arcs. The turning vanes were designed and arranged so that the gap between consecutive vanes was approximately constant. This meant that the velocity remained constant through the turning vanes. The gap-to-chord ratio for the first two corners was 0.375:1. Based on previous research, this ratio would provide minimum losses. For the third and fourth corner, the trailing edges of the turning vanes were lengthened to improve the turning effect. Because of this, the gap to chord ratio for corners three and four was only

9

0.33:1. The vanes were chosen to be as small as possible to minimize friction losses, but large enough to carry the applied loads structurally. For the structural analysis, the vanes were treated as beams with fixed ends and a uniformly applied load. Using a gap of 1 in, the maximum deflection was predicted as 0.1 in for a velocity of 75 ft/s in the test section. This was considered the maximum allowable, so a gap of 1 in was selected. The turning vanes in the 40-in elbows were also reinforced with a strut of aluminum near the centerline. This was added to strengthen the vanes in torsion about their longitudinal axis to reduce the risk of flutter. The strut was mounted 0.75 in from the centerline of the vanes. It was thought that this would suppress any other vibrations.

According to Wells[1], based on a test section speed of 75 ft/s, a head loss of 24 ft was predicted. An approximation of the specific speed showed that an axial flow pump should be used. Assuming a pump efficiency of 80%, a motor with a minimum of 175 horsepower would be required. The cavitation index of typical three-bladed, axial flow pumps was used to determine the minimum height of 13 ft, 2 in between the pump centerline and the test section centerline. This height ensured that the pump would not cavitate provided that the pressure in the test section was kept high enough to prevent cavitation from occurring in the diffuser.

An automotive engine was chosen to provide power to turn the pump. The engine would turn the propeller shaft using a V-belt drive. This would prevent most of the engine vibrations from being transmitted to the tunnel.

Construction Method

The tunnel was made almost entirely of fiberglass which is extremely strong for its weight. Metal reinforcements were used for the bolt holes between tunnel sections. The test section is industrial Plexiglas® tubing. It is attached at both ends by a machined aluminum flange which can be tightened around the test section. Also, an aluminum strut is used in the larger elbows to support the turning vanes. The turning vanes were made out of unidirectional fiberglass.

New Operating Point

When the renovation of this tunnel was begun in 1996, the new design speed for the tunnel was set at 50 ft/s in the test section. Because drag is proportional to the velocity squared and power is drag times velocity, the power varies with the velocity cubed. Using this analysis, it was determined that only 50 horsepower would be required to provide a test section velocity of 50 ft/s. Because of this change in required power, a 50-horsepower electric motor and a motor controller were purchased. The motor controller

11

allows precise control of the motor speed and also allows for programmable acceleration and deceleration. The operating pressure had to be reduced, because the pressure could only be taken up to about 50 psig using the campus water lines.

CHAPTER III

DESCRIPTION OF RENOVATION

Problems of Existing Tunnel
and Recoating Process

When the tunnel was first disassembled, chips and bubbles were found in the original coating. There was also potential for cracks in the coating that could cause leaks. Because of these problems, it was decided to recoat the interior of the tunnel.

The old coating which contained bubbles or chips was sanded off using an electric sander before the recoating process began. These areas were then painted with Duratec® to replace the thickness which had been sanded off. The entire interior of the tunnel was then recoated with the Duratec® coating. This is the same type of coating which is used on fiberglass ship hulls below the water line. It is a type of vinyl ester. The minimum recommended thickness is 0.020 in. This coating was sprayed onto most of the tunnel. On some parts of the turning vanes, it was applied by brush. Using test pieces it was discovered that each coat sprayed on added slightly over 0.006 in of Duratec®. Because of this, four coats were applied to the interior of the tunnel. This made the Duratec® thicker than the recommended minimum

13

thickness. This extra thickness allowed the coating to be sanded to a smooth finish.

It was discovered during the reassembly of the tunnel that in the recoating process, the o-ring grooves were partially filled with the coating. A router had to be used to make the o-ring grooves the correct dimensions again. It was also discovered after reassembling and pressurizing the tunnel that the tunnel wall leaked in several places. A grinder was used to grind off the layers of fiberglass which were improperly bonded to the rest of the tunnel. New fiberglass was then applied to these areas. A few more leaks in other places have started and then been repaired since the initial operation. The new leaks may indicate structural problems.

During initial runs at high speeds, a knocking sound in the vicinity of the propeller was heard. The tunnel was drained so that it could be inspected. The trailing edges of the four bearing support struts upstream of the propeller were found to be chipped. It is believed that this damage was caused by cavitation forming on the trailing edges of these struts. The trailing edges of these struts were sanded down to remove the damage and then coated with a thin epoxy to water-proof them. It was also discovered that some of the coating was beginning to flake off of the turning vanes in at least one corner. These will have to be recoated.

Drive System

The propeller shaft is supported by three Cutless rubber bearings. These bearings use water as a lubricant and a coolant. One Cutless bearing is contained in a water jacket housing near the propeller. This is the bearing closest to the propeller. Water is supplied to this bearing by piping from a downstream section of the tunnel. The downstream source is a 40-in diameter section. The section of the tunnel containing the cutlass bearing is only 21.5 in in diameter. While water is circulating in the tunnel, the static pressure at the downstream section is higher because of its lower velocity. This pressure difference is increased by the blockage of the tunnel caused by the struts and the shroud around the Cutless bearing. Because of this pressure difference, water is forced from the downstream section to the Cutless bearing. This water is used to cool and lubricate the bearing. Another Cutless bearing is contained in the elbow through which the propeller shaft passes. This bearing depends on the water surrounding it for cooling and lubrication. The third Cutless bearing is contained in a water jacket housing on the outside of the tunnel. Water for this bearing is provided by a tank on the second floor which is kept full by the University water supply. After the water goes through the Cutless bearing, it goes out to the drain.

The outer water jacket housing contains two rotating seals. The inner seal prevents water from the water tunnel from going through the Cutless bearing and then out the drain. If this seal leaked, the pressure in the water tunnel would drop over time. The outer seal keeps water from around the Cutless bearing from leaking out.

A drawing of the outer bearing assembly is shown below in Figure 3. To hold the inner seal in place, a collar is placed on the drive shaft about 2 in outside the tunnel. This collar is held in place by two set screws. A spring-loaded rotating seal goes on the shaft and against this collar. Next a water jacket housing containing a Cutless bearing and the non-rotating seal is bolted onto the tunnel over the shaft. There is an o-ring to make a seal between the outer water jacket housing and the tunnel. The collar mentioned earlier must be positioned close enough to the tunnel so that the o-ring makes a good seal but far enough away from the tunnel to ensure that the rotating seal is properly compressed. Next, an impeller goes onto the drive shaft and is secured with two set screws. This is followed by another spring loaded rotating seal, a non-rotating seal, and a flange with an o-ring. As with the collar, the impeller must be mounted far enough away from the tunnel to compress the rotating seal properly, but close enough to the tunnel to let the o-ring make a good seal. The purpose of the impeller is to circulate water around the outer Cutless

16

bearing. There is a thin metal skin which goes around the outer water jacket housing. By touching this skin, the approximate temperature of the outer cutlass bearing can be determined. This is used to make sure that the outer Cutless bearing does not overheat.
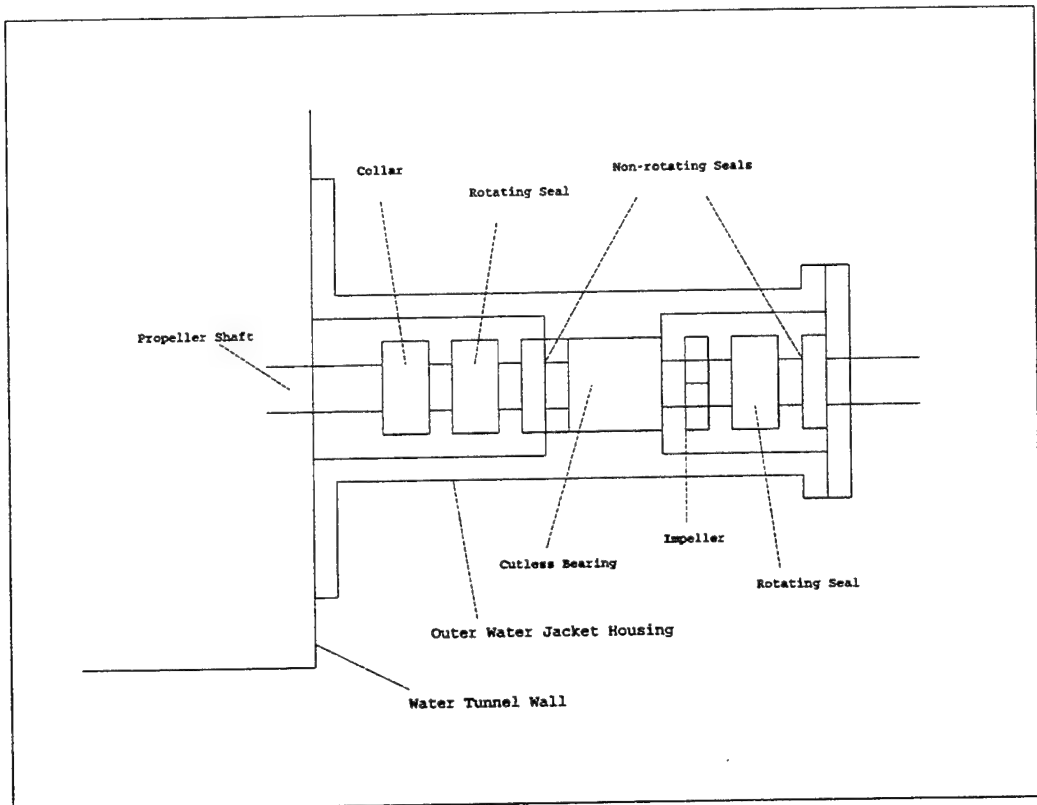
Figure 3 Outer Water Jacket Housing.

A 50-horsepower electric motor is used to turn the propeller. This motor is controlled by a MagneTek® GPD 515 motor controller. This controller allows the motor to be run at a wide range of speeds. It also allows for programmable acceleration and deceleration times. The

17

controller also protects the motor from overheating by cutting off power if necessary.

A Para-Flex® model PX90 flexible cushion coupling was purchased to connect the motor to the propeller shaft. This type of connection allows for a slight misalignment of the two shafts. A stand was made for the motor to raise it to the approximate height required. This stand was made from "I"-beams which were welded together. Bolts were screwed through this stand to raise the motor to the correct height and level it. Horizontal screw jacks were made and attached to the floor. Two were placed on each side of the motor, and one was placed in front. These jacks were used to make final corrections to the positioning of the motor before it was bolted to the floor.

Test Section

A new piece of Plexiglas® acrylic tubing was purchased for the test section. The dimensions of this Plexiglas® tubing are the same as the original test section. The inner diameter is 11 in, and the wall thickness is 0.5 in. The outer diameter of the test section was machined down 0.5 in for a distance of 0.5 in from each end. An aluminum flange is attached to each end of the test section. Each flange has been cut through the top and held together by two bolts. By loosening these two bolts, the flange can be expanded so that it can slide over the end of the test section. The

test section is then temporarily put into place using a few
bolts in each flange to position them correctly. Once the
test section is in place, the two bolts at the top of each
flange are tightened. This securely fastens the flange to
the test section. Having the flanges attached to the tunnel
ensures that they are oriented properly. The test section
is then removed and Permatex® sensor-safe blue RTV silicone
gasket maker is used to make a gasket for each end. The RTV
is applied between the reduced diameter of the test section
at each end and the metal flange. Enough RTV is applied so
that some of it comes out from this groove. The RTV makes a
seal between the flange and the test section and between the
flange and the tunnel.

Seven static pressure taps were located in the test
section. These taps have an inner diameter of 0.0625 in.
Five pressure taps were drilled in one side of the tunnel,
and two pressure taps were drilled in the other side. The
outermost pressure taps were located 3.5 in from each end of
the test section. The remaining three pressure taps were
equally spaced in the 41 in between the outermost taps.

The taps were made by first drilling a 0.0625-in hole
all the way through the test section wall at the desired
locations. Next, brass tubing with this inner diameter was
found, and a hole matching its outer diameter was drilled
halfway through the outer tunnel wall at the same locations.
Two inch long brass tubes were then pushed into these holes

and epoxied in place. This gives the static pressure hole a constant 0.0625-in diameter hole over 2 in into the tap. According to Shaw[5], this is more than sufficient length to prevent any geometry changes in the tubing following it to have any effect on the measured pressure.

CHAPTER IV

INITIAL OPERATION

Static Pressure Tests

It was discovered that a pressure of about 50 psig could be obtained using the water pressure in the University water system. At this pressure, several leaks were discovered. Some of the leaks were pin-hole leaks, but others were cracks or delaminations in the fiberglass. The pin-hole leaks were repaired with fiberglass resin or epoxy. This repair method was unsuccessful for repairing the cracks and delaminations. These leaks were stopped by grinding down the outer layers of fiberglass until a solid layer was reached. Several new layers of fiberglass were then added to the area which had been ground down.

Initial Runs

During the initial runs, the speed of the motor was brought up to 800 RPM. The static pressure of the 40-in diameter section immediately upstream of the contraction was maintained between 45 and 50 psig. At this tunnel pressure and motor speed, a knocking noise was heard in the vicinity of the propeller. The tunnel was drained so that it could

be inspected. Upon inspection, it was discovered that the trailing edges of the struts approximately 1.5 in upstream of the propeller had been chipped. After this discovery, it was conjectured that cavitation pockets formed and collapsed on the trailing edges of these struts as each propeller blade passed. Because of this cavitation and because of the fact that at the present time the tunnel pressure can not be raised above 50 psig, the speed of the motor has been limited to 700 RPM. If the pressure in the tunnel could be raised, this RPM limit could also be raised.

Calculating Test Section Velocity

The test section velocity is calculated using the continuity equation for incompressible flow and Bernoulli's equation:

$$V_1 * A_1 = V_2 * A_2 \tag{1}$$

$$p_1 + (1/2) \rho V_1^2 = p_2 + (1/2) \rho V_2^2 \tag{2}$$

$$\Rightarrow V_2 = \sqrt{\frac{2*(p_1 - p_2)}{\rho * [1 - (A_2/A_1)^2]}} \tag{3}$$

Station 1 is immediately before the contraction, and station 2 is immediately after the contraction. Note that this can also be written as:

$$q_{ts} = \frac{1}{2} * \rho * V_2^2 = \frac{\Delta p_{cont}}{1 - (A_2/A_1)^2} \tag{4}$$

22

In other words, for a large contraction ratio, the dynamic pressure in the test section is almost equal to the pressure drop across the contraction. It should be pointed out that the use of Bernoulli's equation will introduce some error. The reason for this inaccuracy is that Bernoulli's equation applies to inviscid flow only. However, while there are viscous effects in the flow, they are considered to be confined to the boundary layer, which is a very small portion of the flow. It is therefore believed that the calculated test section velocity will be close to the actual velocity. The pressure difference $(p_1-p_2)=\Delta p_{cont}$ was measured using a differential pressure gauge. The areas are known from the contraction geometry, and the properties of water at 70°F were obtained from Munson, et al.[6].

A plot showing velocity in the test section versus propeller speed in RPM is shown in Figure 4. Error bars are included in the plot. The differential pressure gauge used to measure the pressure drop across the contraction did not have a high resolution, and so the error bars on this curve are relatively large.
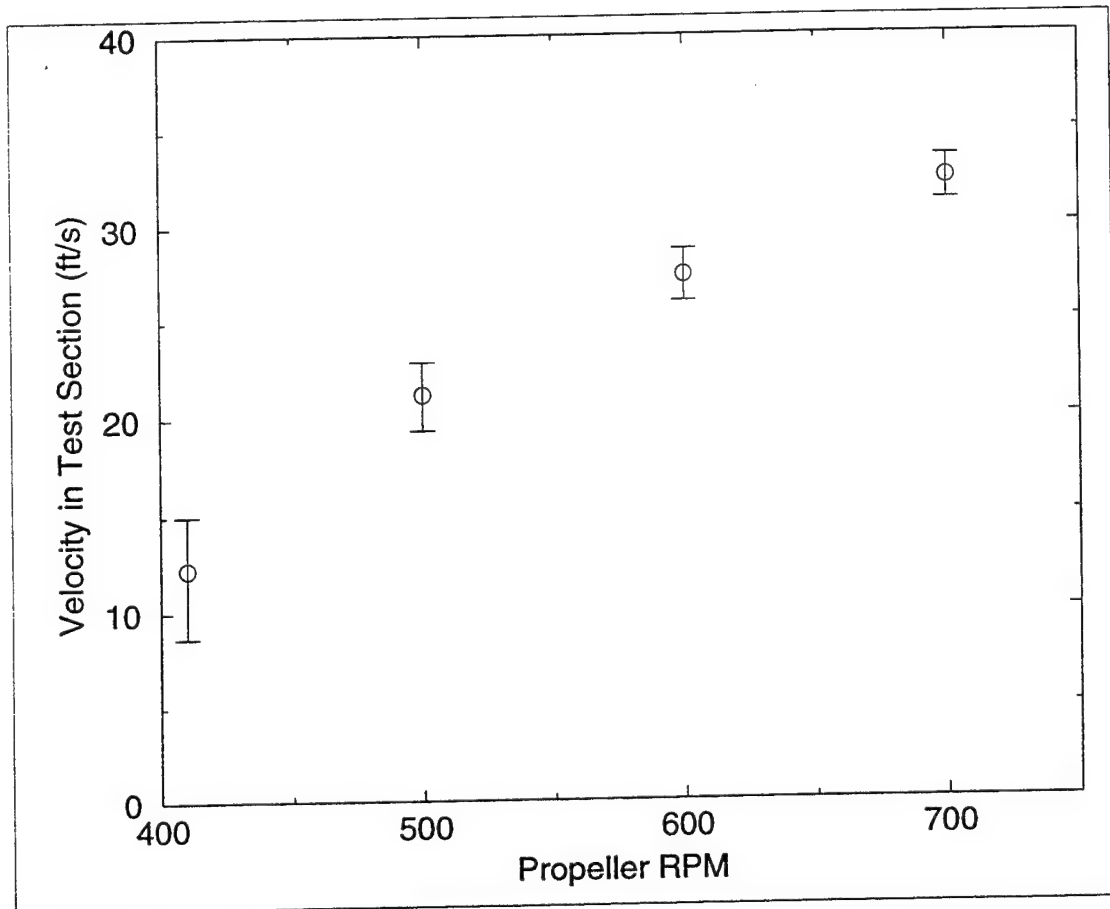
Figure 4 Test Section Velocity vs Propeller RPM.

Start-up Procedure

Several things must be done before each run. The water
must be turned on to a tank upstairs which provides water to
the outermost Cutless bearing. A float is used to limit or
turn off the water if the water level in the tank gets too
high. If water is flowing to the Cutless bearing, the float
will never completely turn off the water to the tank
upstairs. Once the flow of water to the Cutless bearing is
checked, the tunnel should be pressurized to the desired
pressure. Next, the breaker is turned on to the motor

controller.   The desired motor speed can then be entered,
and the motor started.   A complete description of the motor
controller's operation is included in the Appendix.   The
motor should not be run above 700 RPM for tunnel pressures
of only 45 to 50 psig due to problems with cavitation.   If a
lower tunnel pressure is desired, the motor should be
limited to an even lower speed.

CHAPTER V

PRESSURE MEASUREMENTS

Hole Size

Static pressure measurements are used on aircraft to obtain altitude and airspeed. They are also used in a wide variety of laboratory experiments. It is known that errors in static pressure measurements can be introduced by the geometry of the hole which is used to measure the pressure. Research has been done on this problem in the past. One purpose for the water tunnel to be used following its renovation was to investigate this issue at speed and pressure conditions matching those of the Large Cavitation Channel. One method of measuring static pressure is to drill a small hole in the surface over which the flow passes. A tube is then connected between this hole and a pressure gauge. However, the presence of the hole disturbs the flow, and this causes the pressure in the tube to be different from the true static pressure.

To determine the magnitude of the pressure error to be expected, the results of two previous studies were used. These expected pressure errors determine the required accuracy of the pressure measurements.

The hole Reynolds number is needed to use the results of Shaw[5]. To calculate the hole Reynolds number, the wall shear stress must be obtained. Also, the momentum thickness is needed in order to use the results of Ducruet and Dyment[7] because their results are based on the ratio of the static pressure hole diameter to the momentum thickness of the flow. A FORTRAN program called BLACOMP[8] was used to determine these boundary layer properties for the highest tunnel velocity. The calculated skin friction factor from BLACOMP was used to determine the wall shear stress. The continuity equation, Bernoulli's equation, and the pressure drop across the contraction were used in conjunction with the contraction geometry to determine the flow velocity at each station in the contraction. The velocity was assumed to be constant through the test section. The results are shown below.
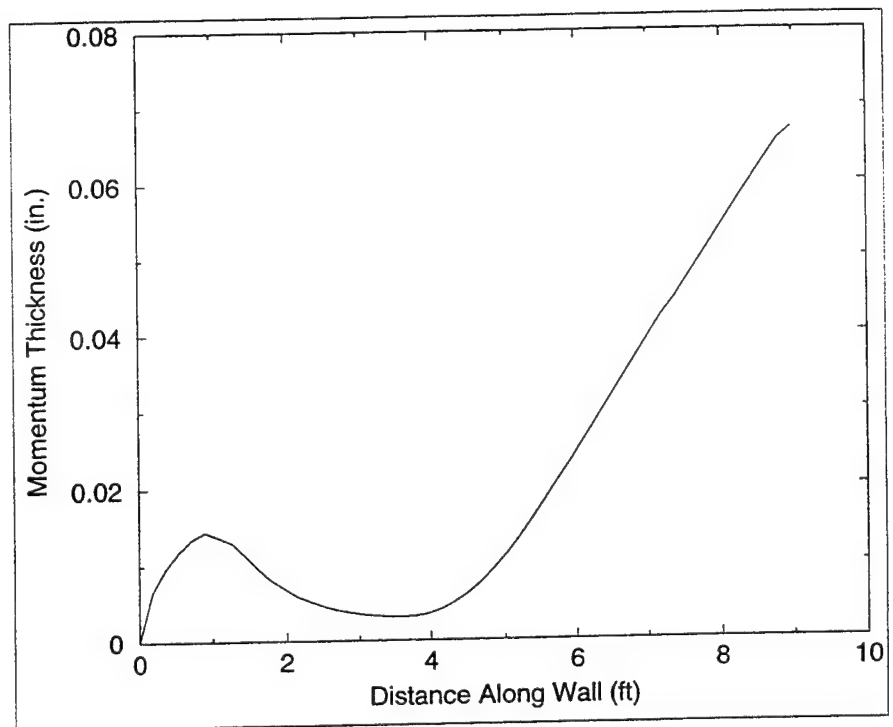
Figure 5 Momentum Thickness.
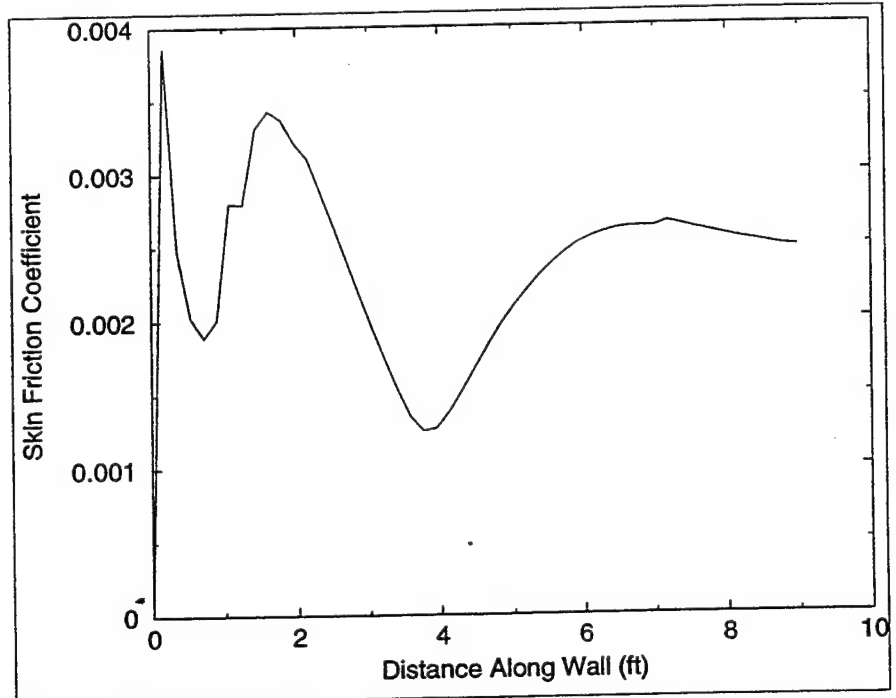
Figure 6 Skin Friction Coefficient.

The equation used to obtain the wall shear stress is shown below.

$$C_f = \frac{2 * \tau_w}{\rho * u_e^2}$$

(5)

With C_f=0.00248, ρ=1.936 slugs/ft^3, and u_e=32 ft/s, the wall shear stress, τ_w, is 2.458 lb/ft^2 or 0.01707 psig at the last pressure taps.

Uncertainty Analysis

Because of the relatively small magnitude of the expected pressure error, an uncertainty analysis is required to determine the accuracy of the pressure measurements. It should be noted that the uncertainty analysis does not include the static pressure hole error. It only provides an estimate of the difference between the actual pressure in the tube and the pressure obtained using the pressure transducer. The confidence level was set at 95%.

In order to obtain useful test results pertaining to static pressure hole error, the uncertainty of the results must be much less than the expected pressure error. To determine the expected static pressure hole error, two previous studies were used. The first study based the static pressure error on the hole Reynolds number. Using the wall shear stress which was calculated from BLACOMP, the hole Reynolds number can be calculated from equation (6).

$$Re=(d/v)*\sqrt{\tau_w/\rho} \qquad\qquad (6)$$

The hole Reynolds number is calculated using d=0.0625 in, v=1.052*10^{-5} ft^2/s, τ_w=2.458 lb/ft^2, and ρ=1.936 slugs/ft^3. The value obtained is 558. Based on this Reynolds number, Shaw[5] predicts a pressure error of about 0.044 psig. The second study based the static pressure error on the ratio of the hole diameter to the momentum thickness. Using the momentum thickness of 0.0668 in obtained from BLACOMP, the ratio is calculated as d/θ=0.94. Based on this ratio and the velocity of the test section at the highest RPM setting, Ducruet and Dyment[7] predict a static pressure hole error of about 0.034 psig. These errors increase with velocity and hole size. To have useful data to contribute to the field of knowledge concerning static pressure hole error, the uncertainty should be considerably less than these values.

A Validyne model DP15 pressure transducer was chosen for the measurement of pressure. It is described in detail in the next section.

The uncertainty analysis must first be applied to the transducer calibration curve. A linear least-squares curvefit was used to obtain the calibration curve. The voltage output for this pressure transducer is linear with respect to pressure difference. Because of this, only a slope *a* and intercept *b* must be obtained. Once these values have been calculated, the standard error of the estimate can be computed from Coleman and Steele[9].

$$SEE = \left(\frac{\Sigma \left(\Delta p_i - (a * V_i + b) \right)^2}{(N-2)} \right)^{\frac{1}{2}} \qquad (7)$$

The values for a and b were obtained from the least-squares curvefit as 0.199 and -0.0081 respectively. The 95% confidence interval is twice the standard error of the estimate. This gives a 95% confidence interval of 0.0212 psig which is the uncertainty of the curvefit and which becomes a fossilized bias, $B_{\Delta p}$, of the pressure difference. All other contributions to the bias, or systematic error, are negligible. The pressure difference is computed using the following equation:

$$\Delta p = a * V + b \qquad (8)$$

The precision of the pressure difference can then be obtained using equation (9).

$$P_{\Delta p}^2 = \left(\frac{\delta \Delta p}{\delta V} * P_v \right)^2 \qquad (9)$$

This gives the precision of the pressure difference as simply 0.199 times the precision of the voltage. The largest precision of the voltage obtained was 0.0077 volts which gives a precision of the pressure difference of 0.0015 psig. The total uncertainty in the pressure difference can now be obtained from the following formula:

$$U_{\Delta p}^2 = P_{\Delta p}^2 + B_{\Delta p}^2 \qquad (10)$$

The total uncertainty, $U_{\Delta p}$, in the pressure difference is therefore 0.0213 psig. This uncertainty is large compared

31

to the expected pressure hole error for a 0.0625-in diameter hole with a velocity of 32 ft/s in the test section. However, if the velocity or the hole diameter was increased, the error would be large enough to measure.

Pressure Transducer Operation

A Validyne DP15 variable reluctance differential pressure transducer was used with a CD15 sine wave carrier demodulator to take the pressure measurements along the test section. The diaphragm of the pressure transducer is magnetically permeable stainless steel. An inductance coil is located on each side of the diaphragm. When a differential pressure is applied to the pressure transducer, the diaphragm is shifted toward one coil and away from the other. This raises the inductance of one coil and lowers the inductance of the other coil. The carrier demodulator generates a DC voltage based on the difference of the inductances of the two coils.

The pressure transducer was connected to the pressure taps through a pressure manifold. This manifold is illustrated in Figure 7 and described in detail in the next section.
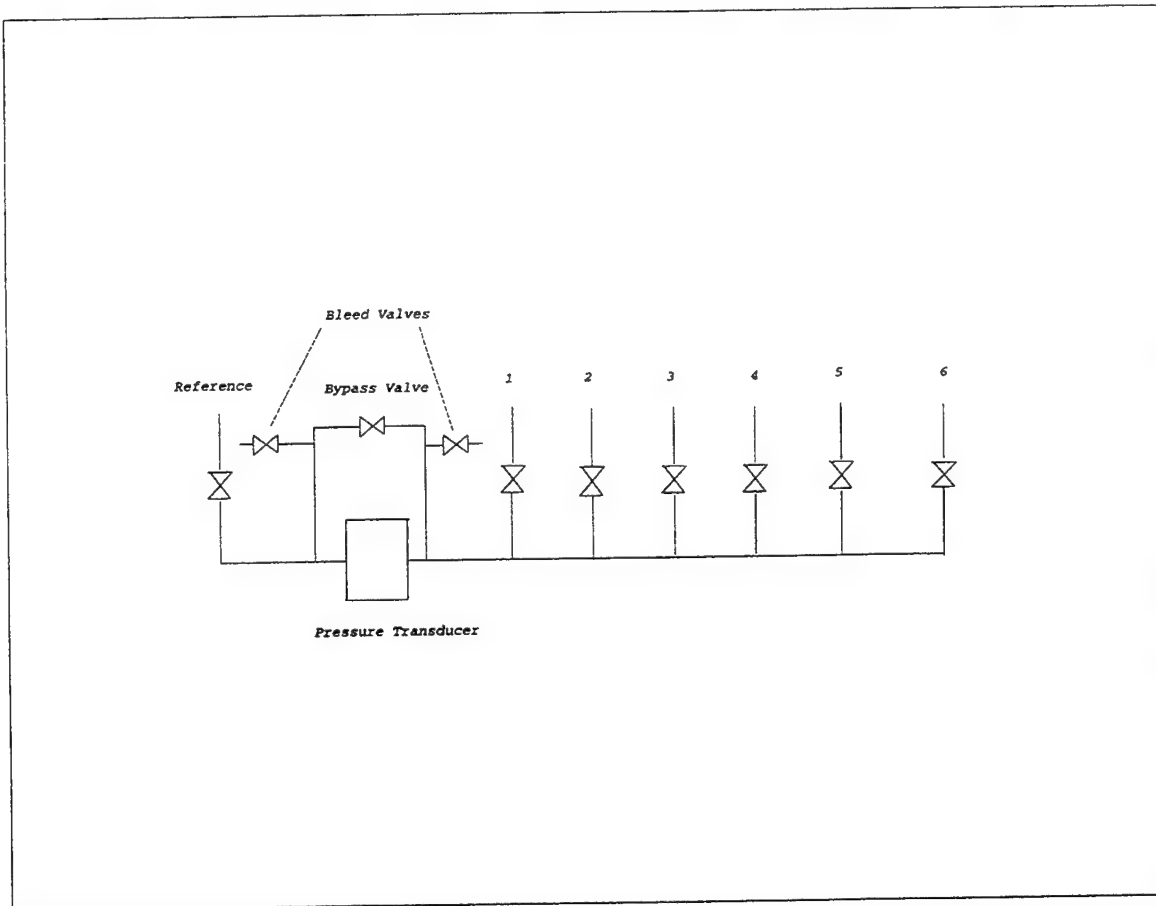
Figure 7 Pressure Manifold.

Before pressures could be obtained from the 2-psig
differential pressure transducer, it had to be calibrated.
The pressure difference of 2 psig which corresponds to 55 in
of water was more than any equipment available could measure
accurately. Because of this, it was decided to construct a
simple apparatus which used columns of water to supply and
measure the pressure difference being applied to the
pressure transducer. This apparatus was constructed of a
board which was mounted vertically on a base. The base has
a bolt on all four corners. By adjusting these four bolts,

33

the board can be leveled. A measuring tape was attached to
the board with 0" at the top and 92" at the bottom. Tubing
was then attached to the board on the left and right of the
measuring tape. With all of the pressure tap valves on the
pressure manifold closed, the tunnel was brought up to a
pressure of about 15 psig. Then the transducer bypass valve
and the two bleed valves, which were connected to the two
tubes mounted on the board, were opened. Next, one of the
pressure tap valves was opened slightly. This pushed out
any trapped air and raised the water level in both tubes
evenly because the bypass valve was open. Both tubes were
filled to a level somewhere below 55 in, and the pressure
tap valve was then closed. A voltmeter was used to measure
the output of the carrier demodulator. The carrier
demodulator has a zero knob and a span knob. The zero knob
was adjusted until the voltmeter read 0 volts. Next, the
bypass valve was closed, and the pressure tap valve on the
high pressure side was opened slightly to raise the water
level in the tube. The isolation valve was closed when the
water level on the high pressure side was 55 in higher than
the water level on the low pressure side. A voltmeter was
again used to measure the output of the carrier demodulator.
The span knob was then adjusted until the voltmeter read 10
volts. The pressure was then equalized by loosening the
connection between the bleed valve on the high pressure side
and the tube bank and letting the water drain into a

34

container until both water levels were approximately the same height. The bypass valve was then opened to completely equalize the pressure. Once again the zero knob was adjusted until the voltmeter read 0 volts. Then the data acquisition card was attached to the carrier demodulator. A total of 13 calibration points were taken over the range of pressures by using the method described earlier to raise or lower the water level in the tubes. The calibration points are shown in Table 3 in the order in which they were taken. Each voltage represents the average of 2000 samples taken by the data acquisition card at 500 Hz. The calibration points and calibration line are shown below with error bars.
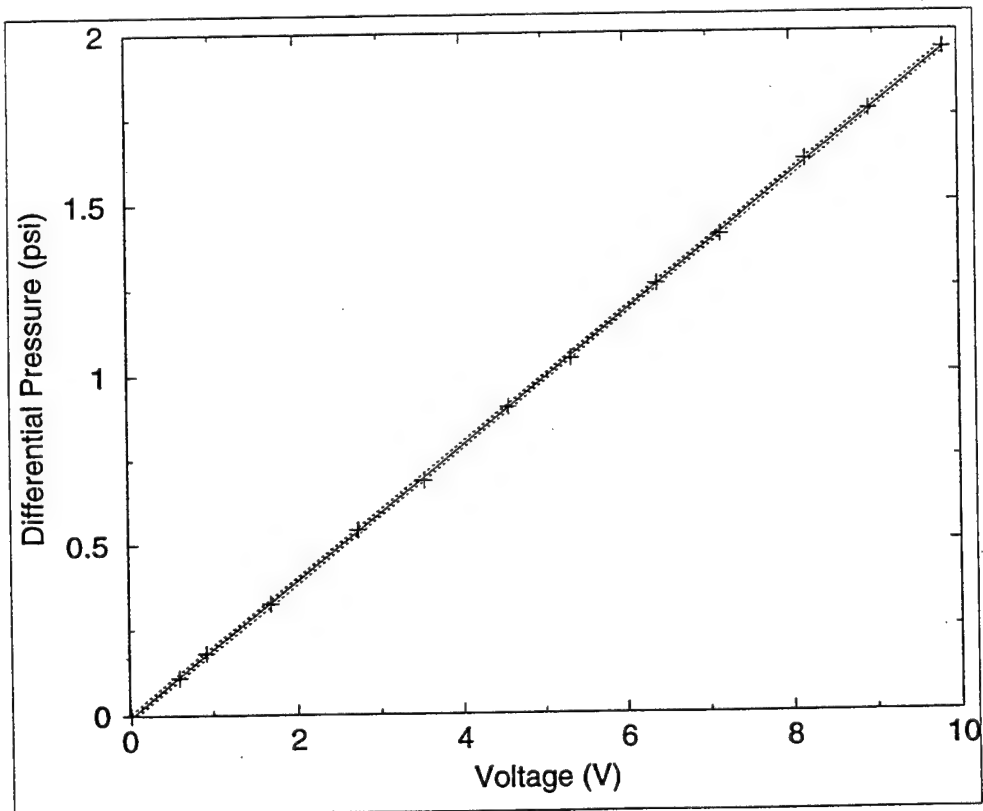

Figure 8 Calibration Plot.

Data Acquisition Procedure

To facilitate pressure measurements from the different pressure taps, a pressure manifold was constructed. The pressure manifold has isolation valves for each pressure tap. A bypass valve is also provided which connects both sides of the pressure transducer. Opening this valve allows the pressure on both sides of the transducer to be equalized. Two bleed valves were also included which allow air to be removed from the system and were also used in the calibration process.

To begin each test, all pressure tap valves and bleed valves were closed. The bypass valve was opened. The motor was started and the desired speed was entered. After the motor reached this speed, a few minutes were allowed to pass before any pressure readings were taken. This allowed the circulating water to reach a steady state. The pressure drop across the contraction was recorded to be used in computing the test section velocity. The pressure upstream of the contraction was also recorded. To take measurements with the differential pressure transducer, first the reference pressure tap valve was opened. The bypass valve was then closed, and the valve connected to the desired pressure tap was opened to the low side of the pressure transducer. At this point, the data acquisition card was used to record the voltage from the carrier demodulator. To read the differential pressure to another pressure tap,

first the pressure tap valve on the low pressure side was closed. Then the bypass valve was opened to allow the pressure to equalize. After the pressure had equalized, the bypass valve was then closed and the next pressure tap valve on the low pressure side was opened. The voltage corresponding to this pressure difference was then recorded. Before stopping the motor, all pressure tap valves were closed, and the bypass valve was opened. Following this procedure ensured that the pressure transducer was never overpressured.

Noise and Noise Reduction Efforts

After the first set of data was taken, it was apparent that the electrical signal from the transducer contained a significant amount of noise. An oscilloscope was attached to the carrier demodulator to determine the approximate frequency of the noise. Low frequency noise would be a problem if its frequency was so low that very few cycles occurred in the 4-s sampling period of the data acquisition card. On the other hand, high frequency noise would be a problem if the data acquisition card did not sample at least a few samples per cycle of the noise. However, it is desirable to reduce all noise at any frequency as much as possible. The noise could be caused by electrical noise or actual pressure fluctuations. It was discovered that if the pressure lines were allowed to touch any part of the tunnel

while the motor was running, the noise level increased. This was caused by vibrations in the tunnel being transmitted through the pressure tubing. To eliminate this noise, the tubes were supported away from the tunnel by stands which were placed on the floor. The pressure manifold was originally mounted on a tunnel support. However, it was discovered that the noise level could be reduced if the manifold was removed and placed on a table with foam between the manifold and the table. The motor controller was found to be a source of electrical noise. Furthermore, the frequency of this noise is above 10,000 Hz which causes a serious problem because it is higher than the sampling rate. To eliminate this noise and still be able to run the tunnel, capacitors were placed across the output of the carrier demodulator. These capacitors act as a low-pass filter. A total capacitance of 0.54 µF was added.

Results

The results from the experiments are shown below. Each set number represents a new orientation of the test section. Multiple tests were carried out for each tunnel orientation and motor speed to determine repeatability.
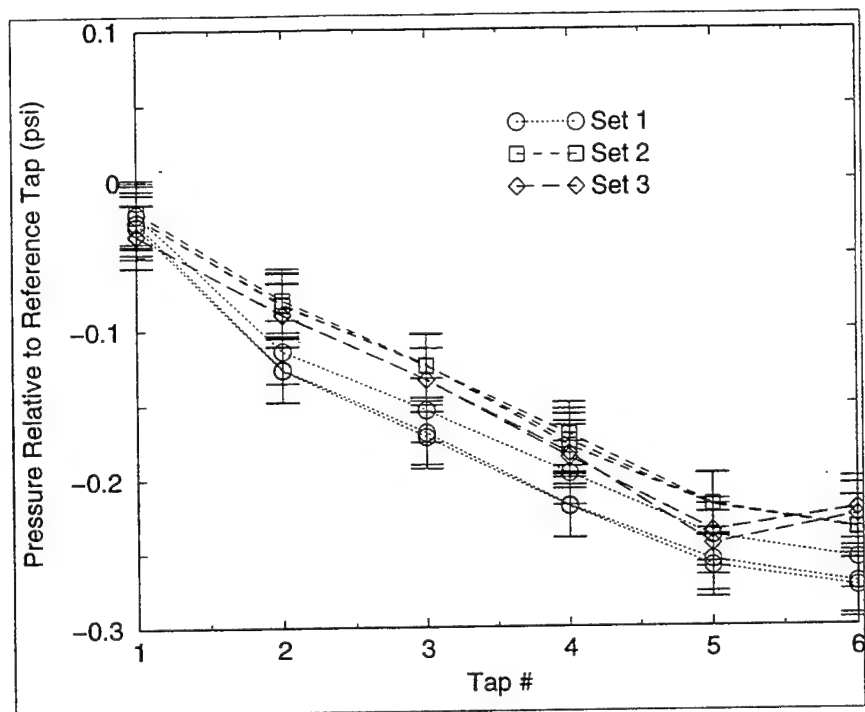
Figure 9 Pressure Distribution at 500 RPM--all test section
   orientations.
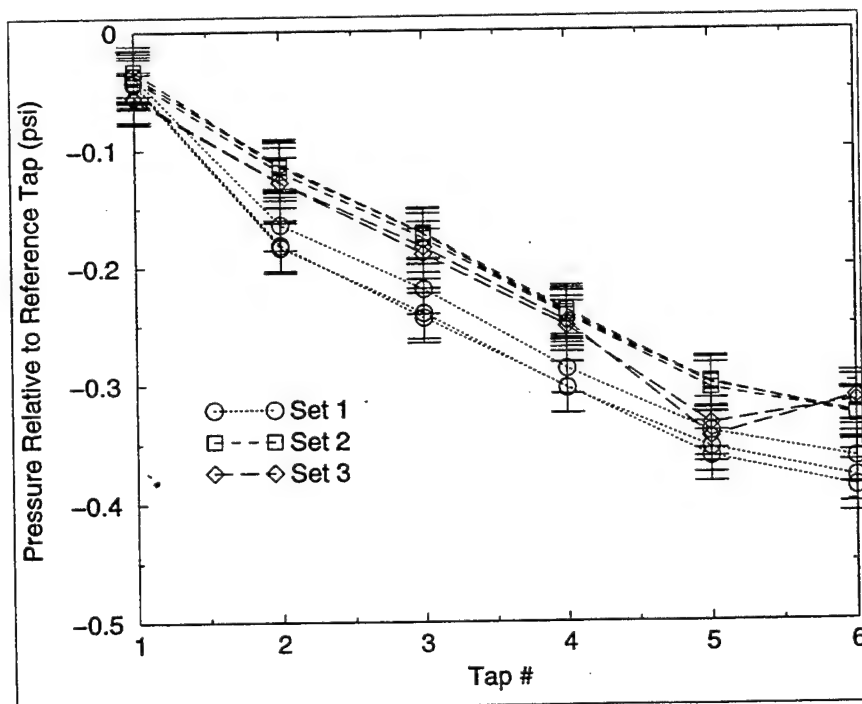
Figure 10 Pressure Distribution at 600 RPM--all test section
   orientations.
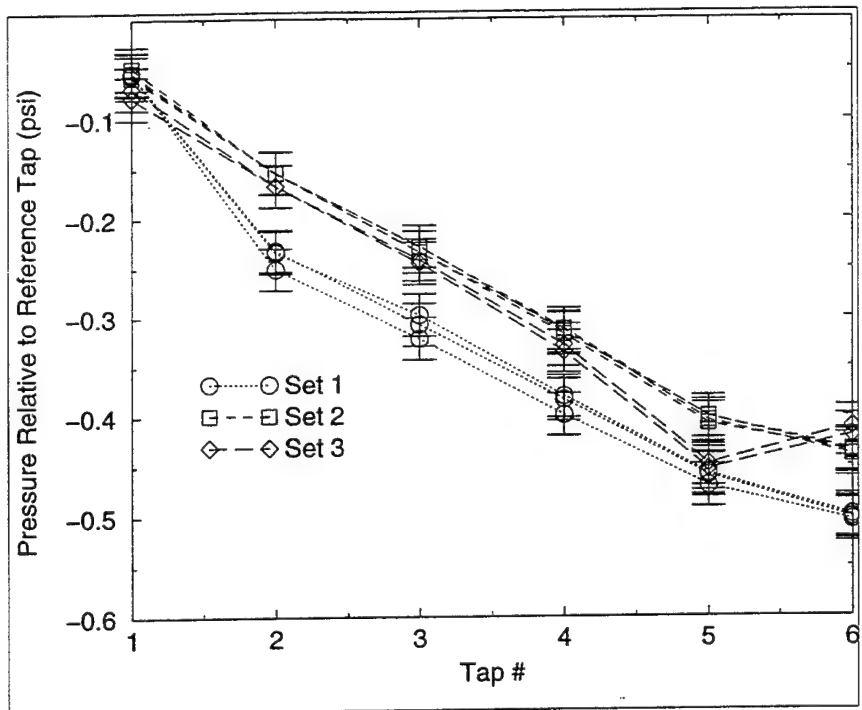
Figure 11 Pressure Distribution at 700 RPM--all test section orientations.

As shown by the plots, there is some shift in curves from one test to the next. Possible causes for this inconsistency include changes in water temperature or slight variations in motor speed. These could cause slight variations in the test section velocity. These inconsistencies should be eliminated if the pressures were changed to coefficients of pressure by dividing by the accurate dynamic pressure. This would require the use of a pressure transducer to more accurately measure the pressure drop across the contraction.

Another problem with the static pressure measurements is differences in pressure readings at the same streamwise location. Originally, this problem was assumed to be caused

by flow nonuniformities not related to the test section. To confirm this assumption, the test section was rotated 180° about a vertical axis. The results are shown below.
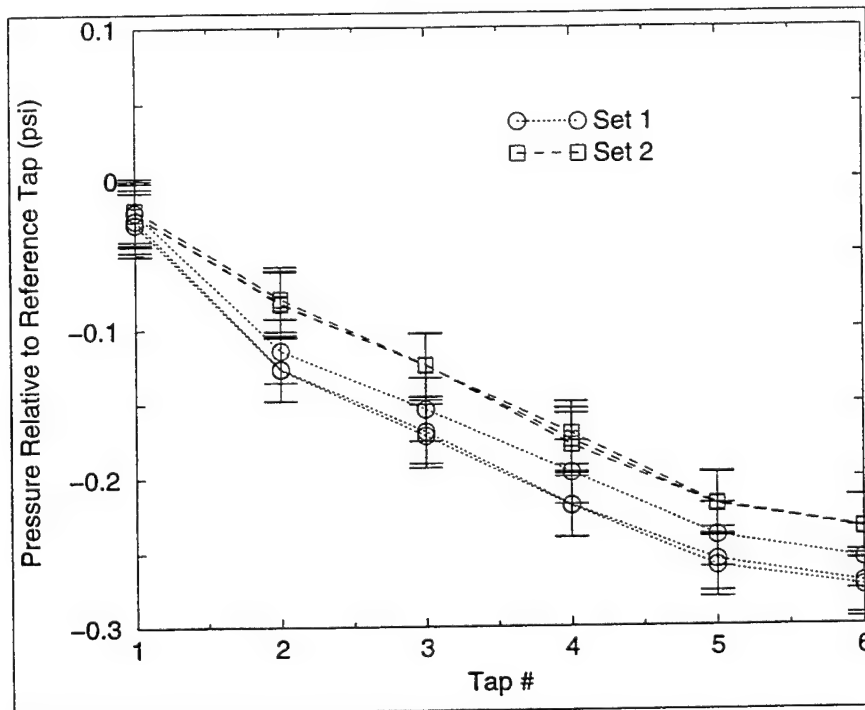

Figure 12 Pressure Distribution at 500 RPM--first and second test section orientations.
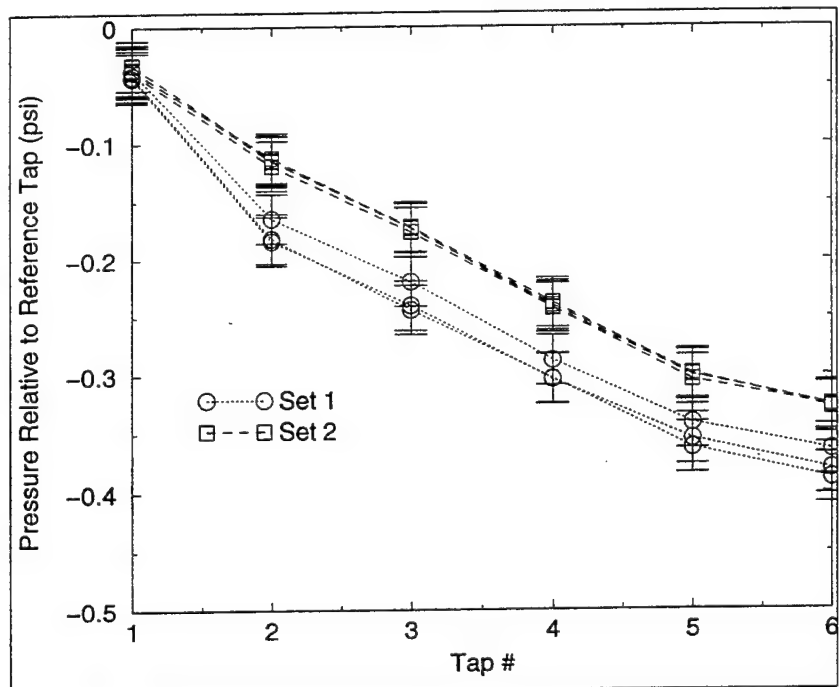
Figure 13 Pressure Distribution at 600 RPM--first and second
    test section orientations.
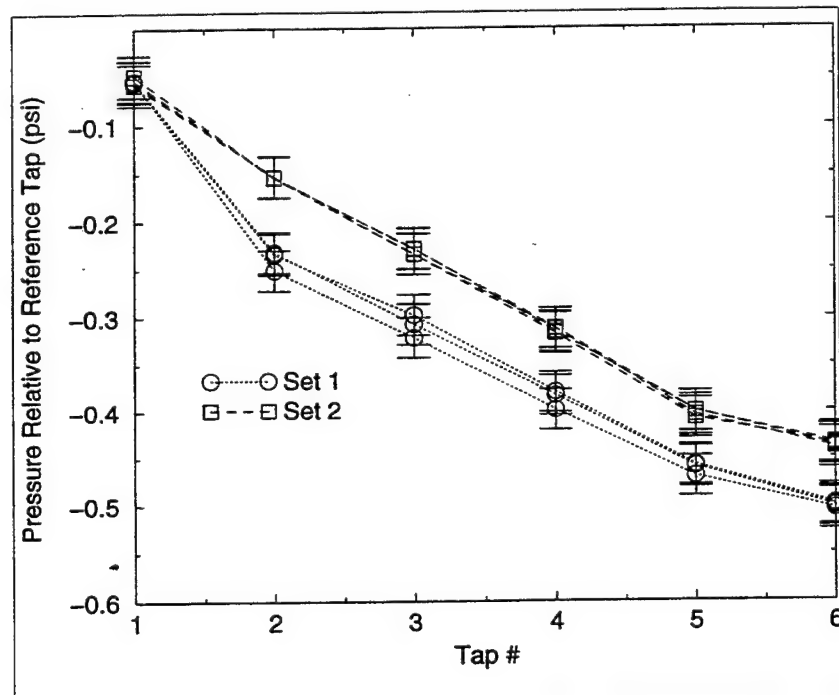
Figure 14 Pressure Distribution at 700 RPM--first and second
    test section orientations.

Instead of confirming this assumption, these results seem to indicate that the pressure problem was fixed to the test section. Next, the test section was rotated 180° about its longitudinal axis. The results from this test are plotted below.
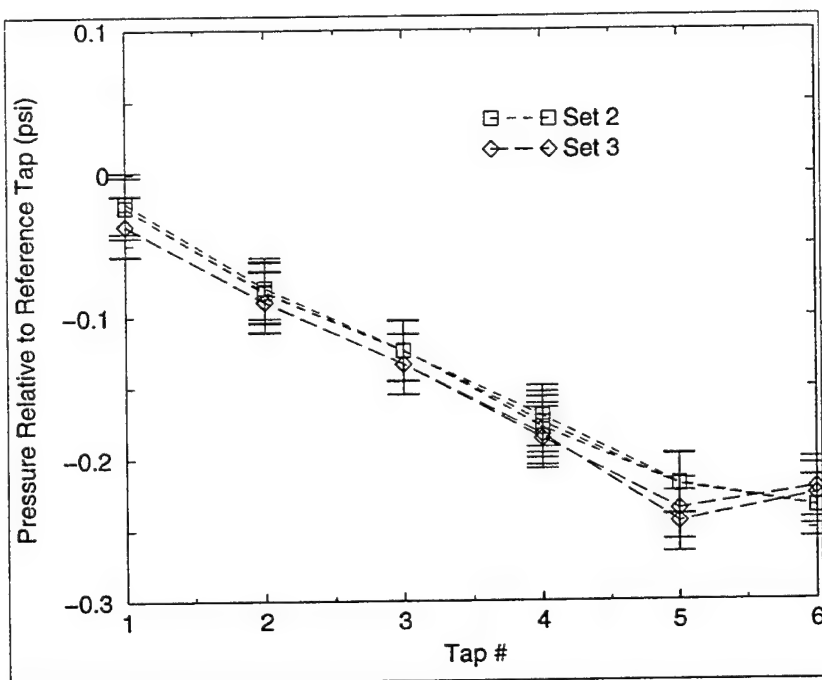
Figure 15 Pressure Distribution at 500 RPM--second and third test section orientations.
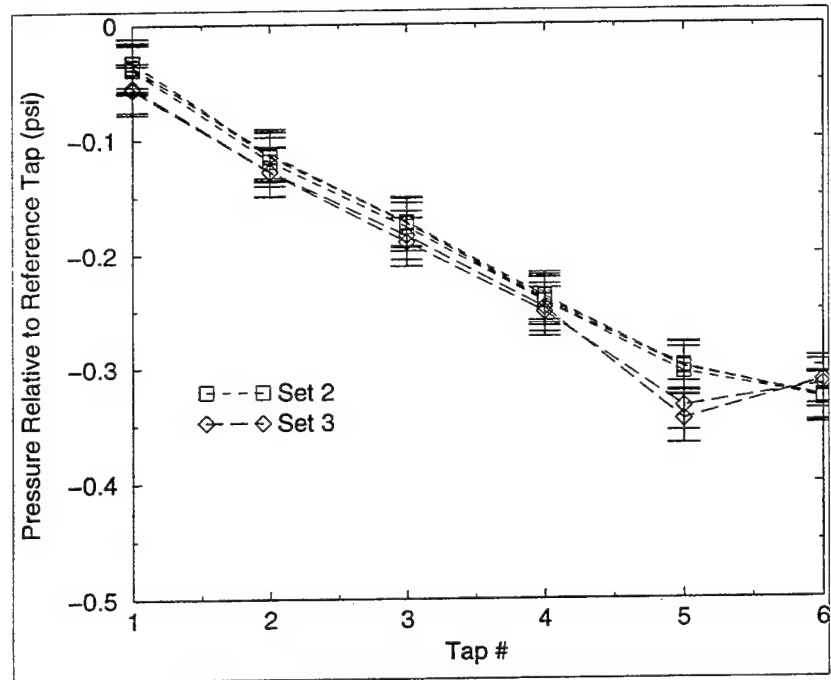
Figure 16 Pressure Distribution at 600 RPM--second and third test section orientations.
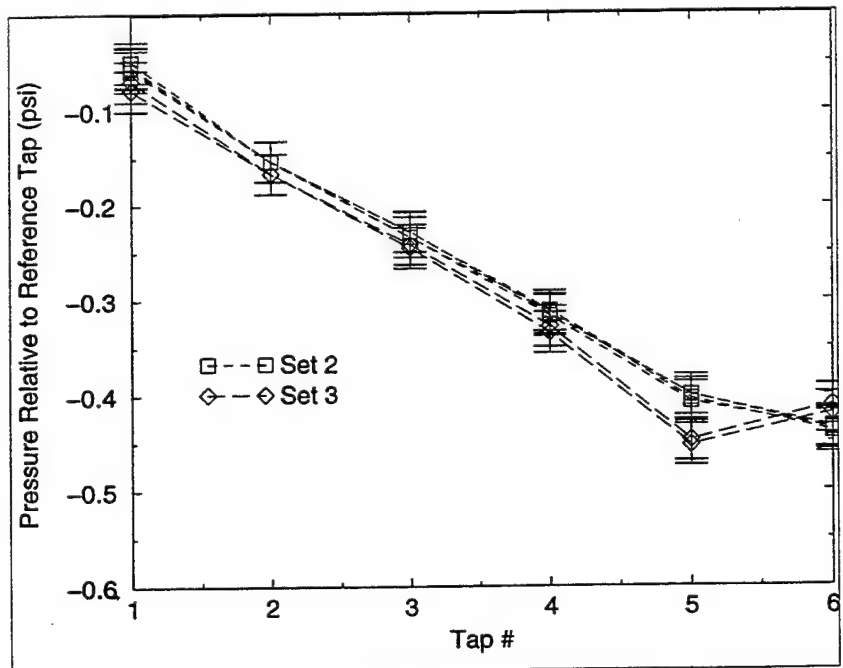

Figure 17 Pressure Distribution at 700 RPM--second and third test section orientations.

In this case, the difference between the pressures from tap 5 and tap 6 changed sign, but stayed roughly the same magnitude. This seems to indicate that the error is caused by flow nonuniformities independent of the test section. However, the pressure from tap 1 is still lower than the pressure from the reference pressure tap which is located directly across the test section. This indicates that this pressure difference is attached to the test section. One possible reason for this pressure difference is misalignment of the test section with the rest of the tunnel. Another possible problem could be the seals at the ends of the test section. If some of the RTV used to make the seals was squeezed out into the flow, it would create a flow disturbance. Also, if there was a gap between the test section and the rest of the tunnel, the flow would be disturbed.

Asymmetric expansion of the test section under pressure could also affect the static pressure measurements. Dial indicators were used to measure this expansion. The maximum expansion of the outer diameter of the test section was measured to be 0.009 in. To get an approximation of how much error this expansion could cause, static pressures were computed for two different diameters. The diameters were 11 and 11.009 in. The sections were assumed to have the same total pressure and the same volumetric flow rate. The velocity in the 11-in diameter section was assumed to be 32

ft/s. This is the test section velocity at the highest

tested speed. Through the use of Bernoulli's equation, the

static pressure difference caused by the change in diameter

was found to be 0.0225 psig. Compared to the expected

pressure errors, this difference is significant.

CHAPTER VI

CONCLUSIONS AND FUTURE WORK

The water tunnel was successfully renovated, reassembled, and operated. The leaks in the tunnel have been found and stopped. The electric motor has also been used to run the tunnel at test section speeds up to 32 ft/s. The tunnel is now ready to conduct further research or to be used for laboratory instruction.

The pressures in the test section were measured using the pressure transducer and data acquisition card. These measurements did not entirely agree with the expected results. The errors did, however, seem to be independent of the techniques associated with the use of the pressure transducer.

The turning vanes on which the coating has begun to flake off should be sanded, cleaned, and recoated. There is also another section in which the coating is beginning to crack. This area should also be sanded, cleaned, and recoated.

There is still a problem with cavitation for motor speeds of greater than about 700 RPM with the tunnel pressure at only 45 or 50 psig. If a lower tunnel pressure was desired, cavitation would become a problem at an even

lower motor speed. One way to solve this problem would be to increase the pressure in the tunnel. To do this, some other means of pressurizing the water tunnel other than waterline pressure would have to be found. Compressed air could possibly be used to accomplish this task. However, the structural integrity of the water tunnel might become a concern if the pressure were raised very much.

A pressure transducer is needed to accurately measure the pressure drop across the contraction. Knowing this pressure drop, the pressure coefficients can be computed. Using pressure coefficients instead of actual pressures should make the results more consistent.

The problem of test section expansion also needs to be addressed. One way to reduce or eliminate test section expansion would be to put metal bands around it in several places along its length. The possible problem of misalignment of the test section also needs to be addressed. A new way to seal the test section needs to be found to prevent disturbances from being introduced to the flow.
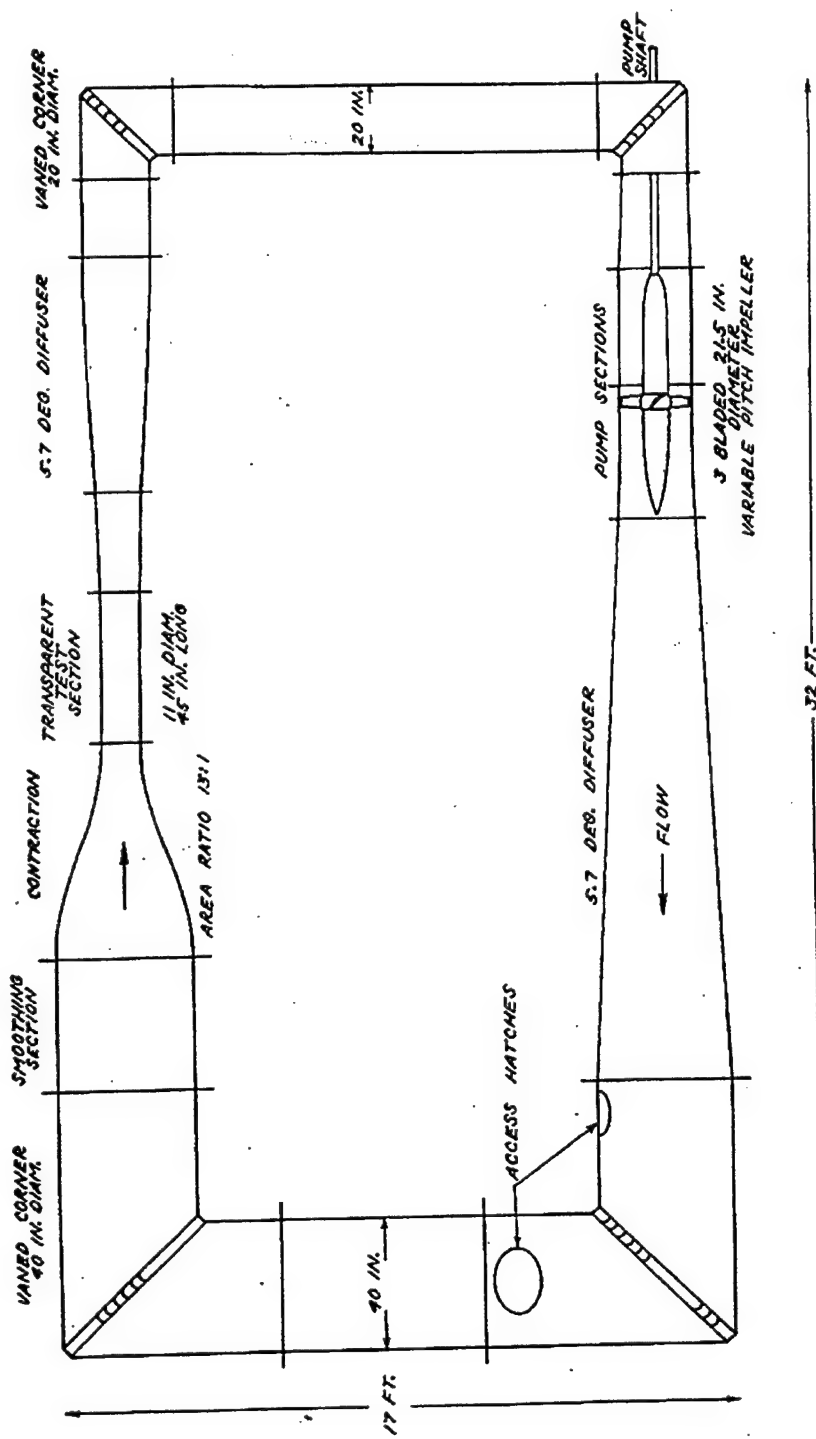
Figure 18 Tunnel Design (figure from Wells[1]).

Table 1

Contraction Geometry

Horizontal Position (in)	Radius (in)
-40	20.000
-38	19.999
-36	19.993
-34	19.970
-32	19.910
-30	19.770
-28	19.473
-26	18.707
-24	17.985
-22	16.752
-20	15.371
-18	13.998
-16	12.714
-14	11.550
-12	10.513
-10	9.599
-8	8.803
-6	8.118
-4	7.537
-2	7.053
0	6.657
2	6.339
4	6.089
6	5.899
8	5.758
10	5.657
12	5.588
14	5.543
16	5.517
18	5.504
20	5.500

Table 2

Diffuser Transition Geometry

Horizontal Position (in)	Radius (in)
0	5.5000
1	5.5001
2	5.5007
3	5.502
4	5.505
5	5.510
6	5.518
7	5.528
8	5.541
9	5.557
10	5.577
11	5.600
12	5.627
13	5.657
14	5.691
15	5.728
16	5.768
17	5.810
18	5.855
19	5.902
20	5.951
21	6.000
22	6.050
23	6.100
24	6.150
25	6.200
26	6.250
27	6.300
28	6.350
29	6.400
30	6.450
31	6.500

Table 3

Calibration Data

Voltage (V)	Precision of Voltage (V)	Pressure Difference (psi)
0.01958411	6.456E-5	0
0.9238139	7.914E-5	0.1804
2.739506	8.741E-5	0.5411
4.5708	8.961E-5	0.9019
6.386338	9.246E-5	1.26266
8.178802	9.403E-5	1.6234
9.832778	9.445E-5	1.9481
8.941816	9.267E-5	1.7677
7.152274	9.216E-5	1.40696
5.342029	9.080E-5	1.0462
3.538024	8.933E-5	0.68544
1.685292	8.547E-5	0.32468
0.6001856	8.278E-5	0.10823

BIBLIOGRAPHY

[1]Wells, Wm. Graham, "Design Principles for a High Speed Fiberglass Water Tunnel," Research Report No. 51, Aerophysics Department, Mississippi State University, April, 1964.

[2]Cohen, M. J., and Ritchie, N. J. B., "Low Speed, Three-Dimensional Contraction Design," Journal of the Royal Aeronautical Society, Vol. 66, No. 616, April, 1962, p. 235.

[3]Szczeniowski, B., "Contraction Cone for a Wind Tunnel," Journal of Aeronautical Sciences, October, 1943.

[4]Tsien, Hsue-Shen, "On the Design of the Contraction Cone for a Wind Tunnel," Journal of Aeronautical Sciences, February, 1943.

[5]Shaw, R., "The Influence of Hole Dimensions on Static Pressure Measurements," Journal of Fluid Mechanics, Vol. 7, No. 4, 1960, pp. 550-564.

[6]Munson, Bruce R., *et al.*, Fundamentals of Fluid Mechanics, John Wiley & Sons, Inc. 1990.

[7]Ducruet, C. and Dyment, A., "The Pressure Hole Problem," Journal of Fluid Mechanics, Vol. 142, 1984, pp. 251-267.

[8]Gatlin, Boyd and B. K. Hodge, "BLACOMP User's Manual," Department of Mechanical & Nuclear Engineering, Mississippi State University, August, 1983.

[9]Coleman, Hugh W. and W. Glenn Steele, Jr., Experimental and Uncertainty Analysis for Engineers, John Wiley & Sons, Inc., 1989.

APPENDIX

The MagneTek® GPD 515 is a menu-driven motor controller. When the power is first turned on to the controller, it comes up to the frequency reference display. The frequency reference is used to set the desired motor RPM. To change this value, press the data/enter key. The first digit of the motor RPM will begin to flash. To change this digit, press the up or down arrows. To move to the right to another digit, press the reset/right arrow key. When the desired RPM has been entered, press the data/enter key again. The entered RPM will then become the frequency reference. The escape button must then be pressed if no further changes to the frequency reference are desired at the current time. Pressing the up arrow at this point will bring up the output frequency. This is the actual speed of the motor. This value is only for monitoring purposes and cannot be changed. The control panel has a run button and a stop button each with LED indicators. When the power is first turned on, the LED on the stop button will be illuminated. To start the motor, press the run button. The LED on the stop button will go out, and the LED on the run button will turn on. The motor will then accelerate to the entered RPM based on the programmed acceleration. The acceleration is currently set to 100 seconds. This is long enough to allow the motor to be brought from stop to any desired RPM directly. The deceleration, however, is set to coast to stop. This was set so that the motor would stop as

rapidly as possible if an emergency occurred. Because of this deceleration rate, the frequency reference was reduced in increments of 100 RPM until 200 RPM was reached for normal stops. At this point, the stop button was pressed. This reduced the deceleration rate of the water and the tunnel loads associated with it.

REPORT DOCUMENTATION PAGE

1. REPORT DATE (DD-MM-YYYY)	2. REPORT DATE	3. DATES COVERED (From - To)
15-05-2001		15-05-1996 to 15-02-2000

4. TITLE AND SUBTITLE
A Detailed Study of the Flow Field of a Submarine at Large Angle of Drift

5a. CONTRACT NUMBER

5b. GRANT NUMBER
N00014-96-1-0911

5c. PROGRAM ELEMENT NUMBER

6. AUTHOR(S)
David H. Bridges

5d. PROJECT NUMBER

5e. TASK NUMBER

5f. WORK UNIT NUMBER

7. PERFORMING ORGANIZATION NAME(S) AND ADDRESS(ES)
Department of Aerospace Engineering
Mississippi State University
P.O. Drawer A
Mississippi State, MS 39762

8. PERFORMING ORGANIZATION REPORT NUMBER
MSSU-ASE-01-1

9. SPONSORING/MONITORING AGENCY NAME(S) AND ADDRESS(ES)
Office of Naval Research
Ballston Centre Tower One
800 North Quincy Street
Arlington, VA 22217-5660

10. SPONSOR/MONITOR'S ACRONYM(S)
ONR

11. SPONSORING/MONITORING AGENCY REPORT NUMBER

12. DISTRIBUTION AVAILABILITY STATEMENT
APPROVED FOR PUBLIC RELEASE

13. SUPPLEMENTARY NOTES

14. ABSTRACT
When a submarine executes a high-speed turn, the sail experiences a cross-flow velocity component. Because the sail is essentially a low-aspect-ratio finite-span wing, it sheds a tip vortex. The flow field induced by the vortex causes higher pressures on the hull deck and lower pressures on the keel, creating a net downward force that leads to an uncommanded nose-up pitching moment. Tests to examine the features of such flows were conducted in the U. S. Navy's Large Cavitation Channel (LCC) in Memphis, TN. A submarine model of length 22.7 ft was mounted in the LCC at angles of drift of 0, 5, and 9.5 degrees and was tested with the sail on and off. Tests were conducted (continued) on reverse

15. SUBJECT TERMS
Submarine, vortex, pitching moment, sail, drift, yaw

16. SECURITY CLASSIFICATION OF:

a. REPORT	b. ABSTRACT	c. THIS PAGE	17. LIMITATION OF ABSTRACT	18. NUMBER OF PAGES	19a. NAME OF RESPONSIBLE PERSON
Unclass.	Unclass.	Unclass.	None.	210	David H. Bridges

19b. TELEPONE NUMBER (Include area code)
662-325-3623

14. ABSTRACT (continued)

at speeds up to 14.9 m/s (27 kts). Circumferential pressure distributions
and laser Doppler velocimeter (LDV) surveys were obtained at two axial
locations for each of the speeds and configurations tested. Body forces
and moments were also measured using a 6-component force balance. The
pressure distributions were integrated to obtain section vertical force
coefficients, and the velocity data obtained from the LDV measurements were
used to estimate the circulation of the tip vortex. The measured pressure
distributions were consistent with the hypothesized mechanism by which
the tip vortex changed the flow around the submarine and created the
nose-up pitching moment. The measured pitching moment and the sectional
vertical force coefficients demonstrated the nonlinear variation with
angle of drift predicted by theory. The measured values of the circulation
were in general agreement with values obtained by other researchers,
although the measured circulation values were consistently somewhat higher.